



The University of  
**Nottingham**

**Department of Mechanical, Materials and Manufacturing Engineering**

**Faculty of Engineering**

# **Design of a Continuum Robot for In-Situ Repair of Aero Engine**

By

**Xin Dong**

Master of Mechanical Engineering

*Thesis submitted to the University of  
Nottingham for the degree of Doctor of  
Philosophy*

September 2015

## DECLARATION OF ORIGINALITY

**Title of Thesis:** *Design of a continuum robot for in-situ repair of aero engine*

I declare that the thesis hereby submitted for the degree of Doctor of Philosophy at the University of Nottingham is my own work except as cited in the references and has not been previously submitted for any degree.

**Name** : Xin Dong

**Signature** :

## Abstract

Unlike conventional rigid-link robots, continuum robot, also known as elephant trunk and snake arm robot, has numerous numbers of degrees of freedom, which enables it to be used for accessing confined places in many fields, e.g. minimally invasive surgery, and safe robot/objective interactions, e.g. rapid handling. Up to now, most of the researches are driven to develop two kinds of continuum robots, i.e. flexible and rigid backbones, which can be structured with either small diameter but short length or long length but large diameter. Further, according to the observation of this work, the conventional flexible backbone has a twisting problem when bending in the horizontal plane with end load, rendering a poor position control. Therefore, designing a 'slender' continuum robot enabling to be employed in in-situ repair of gas turbine engine is still a challenge, since it requires a long length, small diameter, appropriate flexibility and variable stiffness simultaneously.

In the research of this PhD thesis, two unique concepts of continuum robot designs were proposed, i.e. double- and twin-pivot compliant joint constructions. By employing compliant joints, the continuum robot was enabled to be built with small diameter/length ratio, appropriate flexibility, stiffness, and minimised twisting angle. Further, a variable stiffness system was developed in this research, which allows the robot arm able to be articulated in a relatively low stiffness state and dramatically enhance its stiffness in a relatively high stiffness state. With these features, this system was able to be navigated into gas turbine engine (Rolls-Royce Trent XWB) and activate inspection and in-situ repair tasks.

Since the new continuum robot concepts were introduced, the fundamental modelling was developed for both design and control of the new structures. Firstly, position kinematics models were developed: one for double-pivot construction deployed a new derivation approach, which can simplify the procedure; the other for twin-pivot

construction employed a two-sub bending plane model, due to unique construction of the robot, which is different to the conventional method. Secondly, the actuation force analysis was derived, enabling to calculate the action force of an arbitrary section in a multiple-section continuum robot with any bending angle. Further, buckling failure is a major obstacle for designing the compliant joints, since flexible structure can experience buckling. Hence, the analysis of compliant joint critical buckling load was introduced for guiding the hardware design. Also, a general approach for deriving Jacobian and stiffness matrix of continuum robot was presented in this work.

According to the concept and modelling of the new concepts, four demonstrators of continuum robots were built and tested. Comparing with the conventional concept, the double-pivot and twin-pivot concept can decrease the twisting angle by 67% and 98.6%, respectively. Further, in the machining trials, it has been proven that a three-section twin-pivot backbone continuum robot can provide an appropriate stiffness, control accuracy ( $\pm 1$  mm error for sweeping in any  $\pm 5^\circ$  area in the work volume) and repeatability ( $\pm 0.5$  mm error in the whole work volume), enabling the system to blend metal materials, e.g. aluminium and titanium, which are the materials widely employed in aerospace industry. Next, a two-section variable stiffness system was tested on this demonstrator and the TCP displacement caused by end load can be decreased by up to 69%. Finally, accessing in gas turbine engines has been realised by the final full length continuum robot (1266mm). It has been proven that the system has an appropriate control accuracy to be navigated to reach the first stage of LPC (low pressure compressor) of a gas turbine engine (Rolls-Royce XWB) by following a pre-planned path.

Therefore, it can be concluded that the study of this PhD thesis provides a unique continuum robot design concept, which can be utilised for in-situ repair of gas turbine engine.

## Publications

The research in this thesis has contributed in part or full for the following publications:

- [1]. X. Dong, M. Raffles, S. C. Guzman, D. Axinte, and J. Kell, "Design and analysis of a family of snake arm robots connected by compliant joints," *Mechanism and Machine Theory*, vol. 77, pp. 73-91, 2014.
- [2]. Dong, X., et al. (2016). "A Novel Continuum Robot Using Twin-Pivot Compliant Joints: Design, Modeling, and Validation." *Journal of Mechanisms and Robotics* 8(2): 021010.

Patent:

- [1]. X. Dong, M. H. Raffles, D. Axinte, and K. James, "Multi-jointed arm assembly," ed: Google Patents, 2014.
- [2]. D. Axinte, X. Dong, A. Nagy, M. H. Raffles, and K. James, "Flexible tools and apparatus for machining objects", Filed by Rolls-Royce, 2015.

Talk:

MiRoR workshop at the 2015 IEEE/RSJ International Conference on Intelligent Robots and Systems in Hamburg, Germany on 28th of September, 2015.

## Acknowledgments

I would like to sincerely thank my parents for their love and support throughout my life. Thank you for giving me the strength and confidence to chase my dreams.

I would like to sincerely thank the most important person who made me to realise this goal of PhD - my principal supervisor Prof Dragos Axinte. Thank you for the supports in all matters, right from technical discussions, publishing academic papers to your confidence in me. I would also like to thank my co-supervisor Dr Mark Raffles, Dr Salvador Cobos Guzman and industry supervisor James Kell for reviewing my work and participating in technical discussions.

This PhD was funded by the Dorothy Hodgkin International PhD Scholarship from EPSRC UK and Rolls-Royce for the initial three years. I gratefully acknowledge the financial support, without which I could not have completed this thesis.

I would like to thank UTC Manufacturing Lab Technical Staff, Mr Stuart Branston for supporting manufacturing and experimental activities in this work. I also appreciate friendly support provided by all MCM group members and staff.

---

## Table of Contents

Abstract.....	II
Publications .....	IV
Acknowledgments .....	V
Table of Contents.....	VI
List of Figures.....	XI
List of Tables .....	XX
 Chapter 1 Introduction.....	 1
1.1. Background.....	1
1.2. Problem definition .....	4
1.3. Objectives of this study .....	5
1.4. Structure of the thesis .....	6
1.5. Highlights and contributions.....	8
1.5.1. New concepts of continuum robot and variable stiffness system .....	8
1.5.2. Modelling.....	9
 Chapter 2 Literature Review.....	 11
2.1. Introduction .....	11
2.2. An overview of available in-situ repair/maintenance technologies .....	11
2.3. Review of redundant robots.....	13
2.4. Review of continuum robots.....	15
2.4.1. Design of continuum robots.....	15
2.4.2. Kinematics of continuum robots.....	39
2.5. Review of adjustable stiffness systems for continuum robots .....	47

---

2.6. Opportunities for Future Research.....	51
Chapter 3 Innovative concepts of continuum robot design .....	55
3.1. Disadvantages and challenges of the existing continuum robot designs .....	55
3.1.1. Flexibility and stiffness.....	55
3.1.2. Twist problem.....	57
3.1.3. Actuation approach.....	58
3.1.4. Challenge of inverse kinematics.....	60
3.2. Innovative concepts of continuum robot design .....	62
3.2.1. Family of concept A: Double-pivot compliant joint construction .....	62
3.2.2. Family of concept B: Twin-pivot compliant joint construction.....	66
3.2.3. Advantages of the new continuum robot concepts .....	67
3.3. Innovative concept of variable stiffness system .....	69
3.3.1. Basic concept of variable stiffness system .....	69
3.3.2. Two DOFs variable stiffness joint design.....	70
3.4. Conclusions .....	72
Chapter 4 Kinematics analysis.....	73
4.1. Kinematics analysis of family A (Double-pivot construction).....	73
4.1.1. Forward kinematics .....	74
4.1.2. Inverse kinematics .....	77
4.1.3. Cable tension analysis.....	79
4.1.4. Simulation validation of kinematics analysis .....	82
4.2. Kinematics analysis of family B (Twin-pivot construction).....	85
4.2.1. Forward kinematics .....	85

---

4.2.2. Inverse kinematics .....	91
4.2.3. Cable tension analysis.....	97
4.3. Workspace analysis .....	98
4.3.1. Max bending angle of single joint .....	99
4.3.2. Work volume of multiple sections.....	101
4.5. Conclusions .....	103
Chapter 5 Modelling of continuum robots.....	105
5.1. Force Analysis .....	105
5.1.1. Mathematical model of actuation force .....	105
5.1.2. Force calculation interface.....	111
5.2. Buckling Analysis.....	112
5.3. Jacobian Analysis .....	113
5.6. Stiffness Analysis .....	118
5.4. Conclusions .....	125
Chapter 6 Prototypes of the continuum robots .....	126
6.1. Prototype 1 (continuum robot with segmented single backbone pivot) .....	126
6.1.1. Evaluation of backbone materials.....	127
6.1.2. Actuation system .....	129
6.2. Prototype 2 (full length double-pivot continuum robot).....	133
6.2.1. Continuum arm .....	133
6.2.2. Variable stiffness system .....	138
6.3. Prototype 3 (Three-section continuum robot with twin-pivot backbone).....	139
6.3.1. Continuum arm .....	140

---

6.3.2. Variable stiffness system .....	142
6.4. Prototype 4 (full length continuum robot with twin-pivot backbone) .....	144
6.4.1. Continuum arm and variable stiffness constructions .....	144
6.4.2. Actuation system .....	152
6.5. Conclusions .....	154
Chapter 7 Experimental on the prototypes .....	156
7.1. Test of prototype 1 .....	156
7.2. Test of prototype 2 .....	157
7.3. Test of prototype 3 .....	162
7.3.1. Accuracy and repeatability measurements .....	162
7.3.2. Work volume validations .....	166
7.3.3. Twisting angle measurements .....	168
7.3.4. Load carrying capability measurements .....	169
7.3.5. Machining trails .....	172
7.4. Test of prototype 4 .....	174
7.4.1. Navigation trails of the twin-pivot demonstrator .....	174
7.4.2. Work volume validation .....	177
7.4.3. Coiling and uncoiling trails .....	178
7.4.4. Load carrying capability measurements .....	179
7.5. Conclusions .....	181
Chapter 8 Conclusion and future works .....	183
8.1. Discussing challenges in continuum robots vs project objectives .....	183
8.2. Academic findings and engineering validations .....	186

---

8.2.1. Unique designs of continuum robots .....	187
8.2.2. Modelling of continuum robots .....	189
8.2.3. An unique design of variable stiffness system as ancillary for continuum robots .....	192
8.3. Future work.....	192
8.3.1. Towards next-generation design of continuum robots.....	193
8.3.2. Modelling.....	194
8.3.3. Control and calibration .....	195

## List of Figures

Figure 2-1 Available conventional in-situ repair tools: (a) repair of injection pump landing surface on a diesel engine [42]; (b) Laser cladding by an industry robot arm [43]; (c) industrial invasive tooling [44].....	12
Figure 2-2 A group of serial redundant robots: (a) DLR lightweight robot III [47]; (b) Mitsubishi PA-10 Robot [48]; (c) Dexter arm [49];.....	14
Figure 2-3 A series of rigid backbone continuum robot with U joints: (a) the tensor arm manipulator;(b) elephant’s trunk robot;.....	17
Figure 2-4 (a) Continuum robot for aerospace assembly [69]; (b) continuum robot for maintenances of tunnel boring machines [70];.....	18
Figure 2-5 (a) Concept of spherical joint integrated with rubber layer [71]; (b) concept of spherical joint integrated with spring [72]; (c) continuum robot developed by Beihang University [73]; .....	19
Figure 2-6 Several rigid backbone continuum robots: (a) CT Arm [57, 59, 74, 75]; (b) a stiffness-adjustable hyper redundant manipulator [76]; (c) steering mechanism [77]; .....	20
Figure 2-7 Continuum robot HARP (a) the prototype [33]; (b) two concentric continuum robots construction of HARP [79, 80]; (c)working principle of the mechanism[79];.....	21
Figure 2-8 Single Motor Driven Hyper-Redundant Manipulator: (a) the prototype [81]; (b) the mechanism of special universal joint [82]; .....	22
Figure 2-9 i-Snake robot (a) the demonstrator of i-snake [83]; (b) schematic of the bending mechanism [84]; (c) mechanism of the universal joint [84]; (d) the JPL Serpentine Robot [85]; (e) Medusa [86];.....	24
Figure 2-10 (a) A novel hyper redundant robot arm [91]; (b) section mechanism of the arm [91, 92]; (c) a pneumatic driven elephant's trunk (TAK) [93]; (d) section mechanism of TAK [94];.....	25

Figure 2-11 (a) Robot MINIR [96]; (b) working principle of single joint [97]; (c) the prototype of BRAID [98]; (d) one parallel section of BRAID; (e) a 2-DOF cannula prototype [99, 100]; .....	26
Figure 2-12 (a) A curvilinear continuum robot [106]; (b) elephant trunk type elastic manipulator [107]; (c) EMMA™ manipulator; (d) KSI tentacle manipulator; .....	28
Figure 2-13 (a) Flexible surgical continuum robot [112]; (b) Clemson tentacle manipulator [108]; (c) Bionic Tripod 3.0 [111]; .....	29
Figure 2-14 (a) Concentric pre-curved tube robot [113]; (b) the working principle [114].....	29
Figure 2-15 (a) Flexible Microactuator (FMA) (b) AMADEUS phase I prototype gripper [115] (c) array of fin mechanism with multiple hydraulic continuum actuators .....	30
Figure 2-16 A group of pneumatic continuum robots (a) Octarm IV [120]; (b) Octarm VI [121] ; (c) FESTO elephant trunk [122, 123]; (d) Instrument for keyhole surgery actuated by McKibben actuators [124]; (e) MALICA [125]; .....	32
Figure 2-17 (a) D-H coordinates for single section curve (b) geometry approach for the single section kinematics .....	40
Figure 2-18 Schematic of conventional kinematic model (a) a three-cable driven section model; (b) top view of the tip plane; (c) side view of the bending plane .....	43
Figure 2-19 Side view of the bending plane of a three-continuously bending actuator section.....	45
Figure 2-20 Adjustable stiffness solutions based on phase-change material: (a) jamming of granular media [143]; (b) innovative soft robots based on electro-rheological fluids [145]; (c) thermally activated joint (solder-based locking mechanism) [147]; .....	49
Figure 2-21 Various Stiffness mechanisms (a) Retroflex [149]; (b) HARP [33]; (c) lawyer jamming mechanism (negative air pressure) [150]; .....	50

Figure 2-22 Rigidizing solution based on mechanical interlocking mechanism (a) prototype A [151, 152]; (b) prototype B [153, 154];.....	50
Figure 3-1. Accessibilities of different continuum robots (a) single universal joint model (b) multi universal joints model (c) flexible backbone model.....	56
Figure 3-2. Schematic representation of the parasitic twist of continuum robot utilizing a central located flexible backbone design: (a) original configuration (affected by gravity); (b) twisting configuration (affected by gravity + end load).....	58
Figure 3-3. Different actuation types of continuum robots: (a) triple actuation (b) double actuation concepts.....	59
Figure 3-4. Kinematic challenge for two actuations concept: (a) flexible backbone model (b) rigid backbone model.....	59
Figure 3-5. Schematic showing the difference between section bending angle and tip disk orientation: (a) continuous backbone without the segmented disks [157] (b) segmented backbone.....	61
Figure 3-6. A plot of differences between section' overall bending angle and tip disk orientation for a 100mm long section (e.g. as shown in Figure 3-5 (b), flexible backbone length and disk thickness are 20 mm and 5mm, respectively); At 0° section bending, the difference is 0°. And the max angle difference is 8° at section bending angle 90°, direction angle 0°.....	62
Figure 3-7. Continuum robot construction using two actuations concept: (a) general view; (b) one segment.....	63
Figure 3-8. Compliant joints: (a) elastic-rod compliant universal joint; (b) notch compliant universal joint ; (c) leaf spring compliant joint; (d) compliant universal joint continuum robot segment; (e) notch compliant universal joint continuum robot segment; (f) leaf spring compliant joint continuum robot segment;.....	65
Figure 3-9. Schematic of double-pivot compliant joint construction .....	65
Figure 3-10. (a) General view of twin-pivot compliant joints robot; (b) one segment of twin-rod concept one (c) one segment of twin-sheet concept.....	67

Figure 3-11. The general approach for increasing the work volume (a) universal joint+ springs; (b) flexible backbone; .....	68
Figure 3-12. Two DOFs variable stiffness joint .....	70
Figure 3-13. Work principal of the variable stiffness system.....	71
Figure 4-1. Kinematics model of a single segment .....	74
Figure 4-2. Configuration of continuum robot (a) unit vector and parameters of single segment configuration (b) one section of continuum robot.....	76
Figure 4-3. Precision kinematics model of single segment: (a) general and (b) bending section views.....	79
Figure 4-4 Gaps in one section .....	81
Figure 4-5. An example of cable tension plot in work volume: The stiffness of 400mm cable (200mm in continuum robot and 200mm in actuation system) is 37.5 N/mm (0.75mm diameter steel cable).....	82
Figure 4-6. FEA model in ANSYS: (a); a section model (b) a single segment;.....	83
Figure 4-7. Comparisons between computation/simulation:(a) in workspace; (b) direction angle $0^\circ$ .....	84
Figure 4-8. Error between computation/simulation: (a) Position error (b)Angular error .....	85
Figure 4-9. Schematic for kinematic model of single twin-pivot segment.....	87
Figure 4-10. (a) Joint 1 bending section view (b) Top view of disk B ( $\beta_{segment}$ and $\alpha_{segment}$ are denoted as bending and direction angles, respectively).....	88
Figure 4-11. Denavit-Hartenberg frames for one single segment (Coordinate 0 and 3 locate at the centre of the top surface of the disks A and C; Coordinate 1 locates at the intersection point of central axes of disks A and B; Coordinate 2 locates at the intersection point of central axes of disks B and C; bending plane $\beta_1$ is vertical with bending plane $\beta_2$ ; $Z_1$ and $Z_2$ are the rotation axes for joint 1 and 2, respectively).....	90

Figure 4-12. Difference between section bending angle and tip disk orientation (twin-pivot backbone continuum robot).....	92
Figure 4-13. Parameters of single section configuration .....	92
Figure 4-14. Iteration method for inverse kinematics.....	95
Figure 4-15. An example of cable tension plot in work volume of single section (stiffness $k= 37.5$ N/mm of a 0.75mm diameter steel cable of 400mm length: 200mm in continuum robot and 200mm in actuation system) ; In the work volume, the original tension is 100N at $0^\circ$ bending; The min tension is 95N at bending angle $131.8^\circ$ , direction angle $\pm 46.4^\circ$ & $\pm 133.5^\circ$ .....	98
Figure 4-16. Strain model of single compliant joint.....	99
Figure 4-17. Max bending of one joint considering the limitation of geometry.....	100
Figure 4-18. (a) 3D single section work volume;(b) case1: 2D section view of three sections work volume (XZ); (c) case2: 2D section view of three sections work volume (XZ); .....	102
Figure 5-1. (a) Schematic of a single-segment section; (b) the force model of case 1; .....	107
Figure 5-2. (a) Schematic of segment force model; (b) general view of multiple-segment section; (c) the forces acting on the length of cable 1 between disk 1 and 2; .....	109
Figure 5-3. MATLAB GUI of the actuation force calculation .....	111
Figure 5-4. (a) FEA validation of a single compliant joint in ANSYS ; (b) the FEA simulation result; .....	113
Figure 5-5. Velocity of point B <sub>1</sub> and linear velocity of actuation cable.....	114
Figure 5-6. Verification method for Jacobian matrix; .....	117
Figure 5-7. (a) Calculation error of the bending velocity comparing with the FEA model (b) the calculation error of the direction velocity comparing with the FEA model (the specifications of the model are presented in Figure 4-6).....	118
Figure 5-8. Stiffness of one section: (a) direction angle $0^\circ$ ; (b) direction angle $45^\circ$	121

---

Figure 5-9. Verification method for stiffness matrix .....	122
Figure 5-10. Simulation models for validating the stiffness analysis .....	122
Figure 5-11. Stiffness of a one-section continuum robot vs different section's bending angles .....	123
Figure 5-12. Deflection of one section continuum robot vs different section's bending angles .....	124
Figure 6-1. CAD model of the 1st demonstrator (the details are explained in Figure 6-2 & Figure 6-3).....	126
Figure 6-2. (a) Concept one: spring-style compliant backbone (mono-coil tube); (b) concept two: multiple elastic backbones; (c) concept three: single elastic backbone; (d) kinematic performance of spring-style backbone; (e) kinematic performance of elastic rod actuation; .....	127
Figure 6-3. Actuation system of the two-section continuum robot: (a) actuation mechanism; (b) linear motor; (c) the six-motor actuation system; .....	129
Figure 6-4. Stroke & force test of NiTi wire: (a) the original position; (b) the activated wire contracts to the max stroke position; (c) the inactivated wire is pulled back to the original position by the weight; .....	130
Figure 6-5. NiTi actuated demonstrator utilising concept one .....	131
Figure 6-6. NiTi actuated demonstrator utilising concept two .....	132
Figure 6-7. Linear NiTi actuation system.....	133
Figure 6-8. (a) Schematic illustration of the full length continuum; (b) photograph of the full length continuum; (c) CAD of a single segment design; (d) schematic of single section design; .....	134
Figure 6-9. Disk designs of four stages .....	135
Figure 6-10. (a) actuation pack of full length continuum robot; (b) concept of the spool employed in the 2 <sup>nd</sup> demonstrator;.....	137
Figure 6-11. Variable stiffness system prototypes: (a) schematic of variable stiffness system; (b) prototype 1; (c) prototype 2; .....	139

Figure 6-12. (a) General view of the continuum robot; (b) one segment construction; (c) working channel of the continuum robot; (d) the continuum robot equipped with a machining tool and motor;.....	140
Figure 6-13. (a) CAD of the actuation system (b) concept of the spool employed in the 3 <sup>rd</sup> demonstrator;.....	141
Figure 6-14. (a) one segment construction; (b) the prototype of the variable stiffness system; (c) the rigid state of variable stiffness system; (d) the soft state of variable stiffness system;.....	143
Figure 6-15. (a) Cad of the 4th prototype; (b) the tip stage; (c) the middle stage; (d) the base stage;.....	145
Figure 6-16. Middle stage of the continuum robot: (a) the combination of the internal disk and outer nylon layer; (b) the general view of a single section; (c) the forces acting on the disk; (d) the variable stiffness system of middle stage; .....	147
Figure 6-17. (a) Bottom view of concentric layout of the base stage; (b) detail design of the base stage;.....	148
Figure 6-18. Simulation evaluation of the disk design for different sections: (a) the stress analysis of the disk of section 12 (the base stage); (b) the stress analysis of the disk of section 9 (the middle stage); (c) the stress analysis of the disk of section 6 (the middle stage); (d) the stress analysis of the disk of section 3 (the tip stage).....	151
Figure 6-19. Trails of the buckling of compliant joint: (a) the setup of the experiment; (b) the test result of bending angle 0°; (c) the test result of bending angle 3°; (d) the test result of bending angle 6° (e)the test result of bending angle 9°; .....	152
Figure 6-20. Coiled & uncoiled modes of the continuum robot;.....	153
Figure 6-21. the assembly of the final full length continuum robot .....	154
Figure 7-1. Twisting test of the first prototype: (a) 90° bend configuration without external load; (b)90° bend with external load (20g);.....	156
Figure 7-2. Navigation control trial of the 2nd prototype [165] .....	159
Figure 7-3. Schematic of the pattern of one actuation cable in polar coordinate .....	160

Figure 7-4. (a) The setup of the measurement system; (b) the arrangement of the markers .....	163
Figure 7-5. Repeatability of the three-section twin-pivot demonstrator: (a): repeatability test with respect to 30° [42.34mm, 98.98mm] bend (b): repeatability test with respect to 60° [60.22mm, 66.34mm] bend (c): repeatability test with respect to 90° [87.62mm, 43.55mm] bend (Note: One bend and return is called one loop) .....	166
Figure 7-6. The 3rd demonstrator performing controlled motions for validating work volume .....	167
Figure 7-7. Twisting measurement of three section demonstrator: configuration for twisting measurement (a) original configuration without end load (b) twisting configuration.....	168
Figure 7-8. The 3rd demonstrator performing large load carrying capability: (a)200g end load; (b)450g end load .....	170
Figure 7-9. A three-section variable stiffness continuum robot .....	171
Figure 7-10. Machining test of the 3rd demonstrator (a) the test on an aluminium plate; (b) the test on a titanium compressor blade .....	173
Figure 7-11. (a) An example of navigation paths in a gas turbine engines; (b) top view of the navigation path (c) front view of the navigation path (d) trial on a engine mock up (Rolls-Royce XWB) .....	175
Figure 7-12. Another example of navigation tails in a gas turbine engines .....	176
Figure 7-13. (a) 30° bend of section three in plane XOZ; (b) 30° bend of section three in plane XOY; (c) 60° bend of section six in plane XOZ; (d) 60° bend of section six in plane XOY; (e)90° bend of section ten in plane XOZ; (f) 90° bend of section ten in plane XOY;.....	178
Figure 7-14. Coiling and uncoiling trials of the 4th demonstrator .....	179
Figure 7-15. End load carrying capability trial.....	179



---

## List of Tables

Table 2-1. TRL in the continuum robot research.....	33
Table 2-2. Summary of the existing continuum robot prototypes .....	35
Table 2-3. D-H parameters table for single section of a continuum robot .....	40
Table 3-1. Melting Temperature table .....	69
Table 4-1. Nomenclature used in this section.....	75
Table 4-2. Gap distances of one section for different configurations.....	81
Table 4-3. Nomenclature used in this section.....	86
Table 4-4. D-H Parameters for Single Segment .....	90
Table 4-5. Strain of NiTi compliant joint against bending angles.....	100
Table 4-6. Max Bending angles against disk sizes .....	101
Table 5-1. Nomenclature used in this section.....	106
Table 5-2. Nomenclature used in this chapter .....	113
Table 6-1 Specifications of the linear motor .....	129
Table 6-2. Max actuation force in each stage .....	135
Table 6-3. Parameters of the compliant joints .....	148
Table 6-4. Actuation force of each section.....	149
Table 7-1. Shape accuracy measurement results .....	159
Table 7-2. Displacements of cables versus rotation angle of spool.....	161
Table 7-3. Position accuracy measurement results.....	164
Table 7-4. Twisting angles of the base section versus end loads.....	168
Table 7-5. Deflections of the arm versus end loads.....	170
Table 7-6. Deflections of the variable stiffness continuum robot versus end loads ..	171
Table 7-7. Deflections of the full length arm versus end loads .....	180

## Chapter 1 Introduction

### 1.1. Background

As defined in Oxford dictionary, robot is a term of “a machine capable of carrying out a complex series of actions automatically, especially one programmable by a computer” [1]. Generally, a robot generally has two main systems, i.e. mechanical and control systems. The former conventionally comprises several mechanical elements (e.g. end effectors, joints and links) and actuators (e.g. electrical, hydraulics or pneumatics motors), performing variable tasks (e.g. transport, assembly, logistics, cleaning, etc.) by the control of the later system, which mostly consisting of actuation controllers, sensors and computers.

The appearance of modern robots can be tracked back to the last forties because of the development of electronics; two decades later, robots started to replace humans in performing repetitive and dangerous tasks in industry, such as metal products and automotive industry. Further, the application areas of robots expanded to serve outside of factories, e.g. hospital, space, ocean and cleaning. The robots developed in the last fifty years can be divided into two broad categories: industrial and service robots [2, 3]. According to the definition of ISO 8373 [4], the former one can be defined as “an automatically controlled, reprogrammable, multipurpose manipulator programmable in three or more axes, which may be either fixed in place or mobile for use in industrial automation applications”. In this category, there are several sub-categories classified by mechanical structure [5], including articulated [6], SCARA [7], linear [8] and parallel robots [9]. Unlike industrial robots utilised for industrial automation applications, service robots perform useful tasks for humans or equipment [10], which have a wider range of applications. According to different applications, these robots can be classified as field (e.g. space [11], underwater [12, 13], aerial [14, 15], mining [16, 17] and rescue robots [18]), educational [19], medical [20, 21], inspection and

maintenance [22, 23] and domestic robots [24], etc. According to the latest survey of IFR (International Federation of Robotics) [3], the total number of industrial robots sold from 2006 to 2013 keeps increasing, except 2009, since the economic and financial crisis. In 2013, the sales reached the highest level ever recorded for one year, which values up to US\$9.5 billion. Regarding service robots, the total number of sold units rose by 4% in the same period, which valued US \$3.57 billion. And based on the report of IFR, the market is expected to keep growing within the next 20 years.

From the mechanical point of view, most of the aforementioned robots share a similar design principle, which comprises of several articulated rigid elements driven by actuators. Advances of rigid robots have been revealed in terms of high stiffness, end load carrying capability and precision. For example, a typical small industrial robot, ABB IRB 140 [25] can pick up to 6kg end load with an good repeatability and absolute position accuracy of 0.03mm and 0.35mm [26], respectively, which enables it suitable for a wide range of applications, e.g. cleaning, spraying, material handling and assembly [27]. Further, rigid-link constructions are also employed in most of the existing service robots. For instance, iRobot (710Kobra [28]) was equipped with a two-link manipulator, which can carry heavy end loads (max 150kg), allowing it equip with a wide range of end-effectors for secure/defense applications, e.g. bomb disposal and check vehicle inspections. Additionally, over the last fifty years, modellings of conventional rigid-link robots with 2 to 6 DoFs have been well developed in terms of kinematics, dynamics, path-planning, navigation and so on. These researches enable rigid-link robots have a good performance (in terms of accuracy and repeatability) for the applications in factories and service in many other fields. However, the rigidity of the conventional robots brings some drawbacks for some specific applications, e.g. it inevitably limits the accessibility for operating in hard-to-access environments and also decreases the safety of human/object-robot interaction when cooperating with humans.

Over the last twenty years, a new brand of robots (continuum robots, also called snake arm or elephant trunk robots) has been created, which are characterized by flexible and hyper-redundant structure. One main advantage of continuum robots over rigid ones is their capability of accessing and operating in confined spaces; the other one is their ability to bump into things without causing damage to themselves or the other party/object, which enables the robot perform safer human/object-robot interaction with a compliance control algorithm. Due to these advantages, many researches focused on developing small scale continuum robot system for medical applications, like minimally invasive surgery (MIS). In last ten years, quite few companies have been found and started to commercialize continuum medical robots to offer the market, which has decreased diameters (generally less than 10 mm) and appropriate articulated lengths (generally less than 300 mm) for accessing to desired organs in human bodies [29-31]. For example, Titan medical INC developed a dual-continuum-arm medical robot, which can be inserted into the patient's body through a skin port of approximately 25mm. The twin continuum robot can be equipped with variable end-effectors, e.g. cautery hook and scissors for operating in desired areas. It can bring the benefits for patients, e.g. quicker recovery, less pain and less blood loss and for surgeons, e.g. improved precision. Regarding large scale of continuum robots, several systems were developed, e.g. Festo elephant trunk, formed with fully flexible construction, which can be utilized for safe rapid handling, however, the position accuracy is not ideal (approximately 15mm position error). Additionally, OC robotics provides commercial hyper-redundant robots to the market, which have been demonstrated able to be deployed for aircraft assembly and nuclear station inspection. Researchers from both academia and industry show a great amount of interests on developing continuum robots for new applications. However, comparing with conventional rigid-link robots, the new brand of robots has its own disadvantages including low stiffness and accuracy, which limits them to be constructed with long lengths and reduced diameters, rendering it difficult to employ large scale continuum

---

robot in highly constrained environments. This requires new solutions to enhance the performances of the new kind of robots.

## 1.2. Problem definition

The main goal of this thesis is to design and build a novel continuum robot for the application of in-situ repair of gas turbine engines (including inspection and machining). With the need to reach the area of the low pressure compressors through the front of the engine (Rolls-Royce Trent XWB), the robot needs to be featured with multi-DoF at reduced dimensions (the tip diameter needs to be no more than 15 mm), appropriate length (no less than 1200 mm) and stiffness (200g end effector needs to be carried at the tip).

However, most of the existing systems are developed for their own specialized applications, e.g. MIS, aircraft assembly and safe rapid handling, which are theoretically unable to be employed for the in-situ repair applications, because of the following constraints:

1. One main limitation is the existing continuum robots do not have the appropriate **diameter/length ratio** or **flexibility**<sup>1</sup> for delivering the end effectors to desired positions in highly confined spaces (e.g. gas turbine engine). For example, the medial systems are generally structured with small diameters (down to 4mm [32]) but short lengths (up to 300mm [33]), which are too short to reach the target position; while other systems [34] are kinematically hyper-redundant and long (up to 3250mm) [35], but employs rigid link/larger diameter pneumatic actuators as the basic unit of the arm, which is difficult to access narrow spaces between the blades.
2. The other constraint is that the **stiffness** of the existing systems cannot support the reaction forces related to desired tasks, e.g. blade mechanical blending. What is even more challenging, the stiffness of continuum robots is

---

<sup>1</sup> In the thesis, flexibility refers to the bending capability of each section of continuum robot.

inversely proportional with the length, but proportional with the diameter. For decreasing the diameter/length ratio, the system stiffness is inevitably reduced, which renders low accuracy and no appropriate end effectors can be carried.

Hence, a slender multi-degree of freedom continuum robots with appropriate stiffness is needed to be developed so that in-situ repair/maintenance can be performed in confined environments. With the development of new concepts of continuum robot, scientific/academic challenges are expected to be addressed.

### **1.3. Objectives of this study**

As a part of FP7 project MiRoR (Miniaturised Robotic systems for holistic in-situ Repair and maintenance works in restrained and hazardous environments), a variable stiffness continuum robot needs to be developed and combined with a walking-hexapod system [36] for performing in-situ repair tasks. The aim of this thesis is to develop a fundamentally novel continuum robot comprising an appropriate diameter/length ratio continuum unit and a tubular variable-stiffness unit<sup>2</sup>. This unit should be able to wave between engine blades to reach desired repair positions and the variable-stiffness system allows the continuum robot have a proper flexibility to navigate into/out from gas turbine engine and increase its stiffness (of particular sections) when activating machining task. The specific objectives of this study are to:

- Propose novel concepts of the mechanism of continuum robots. This allows the designer to design and manufacture a continuum robot capable to navigate (section bending capability: 90 °) and carry active end-effectors (e.g. cutting tools, up to 200g) in confined spaces;
- Develop kinematics models of the proposed multi-section continuum robots for precisely controlling the system (including forward and inverse

---

<sup>2</sup> In this thesis, the variable stiffness unit is called rigidizing system. And the whole articulated unit, including the continuum unit and rigidizing unit, is called semi-rigid continuum robot.

kinematics), since new mechanisms of continuum robot are introduced in this thesis;

- Develop the methodologies of designing continuum robots: 1) obtain an modelling approach for calculating actuation forces depending on number of sections and their orientation angles; 2) investigate the models for buckling force of the key element - compliant joint considering its geometry and material property; 3) model and evaluate the section stiffness of the proposed continuum robot;
- Design and build a variable-stiffness system (rigidizing system) for the continuum robot. With the assistant of the variable stiffness system, the continuum unit is enabled to take the reaction force when activating machining tasks (e.g. blade blending) in the engine;
- Demonstrate a series of evolving concepts (from single to twin compliant joints and from short to long structure) of continuum robots and evaluate their performances measuring the accuracy and repeatability of the system and demonstrate a precision blending repair on different materials.

#### **1.4. Structure of the thesis**

**Chapter 2** provides a review on the exiting in-situ repair/maintenance technologies utilised in the aerospace/nuclear industries and the designs of hyper-redundant robots; this chapter also concludes with a detailed literature review from a wide range of publications covering the key elements for developing a continuum robot including mechanical designs, approaches of computing kinematics and variable stiffness designs. Finally, research gaps/challenges for building a novel continuum robot are identified.

**Chapter 3** introduces the kinematics challenges and disadvantages of the existing continuum robots. Further, regarding these disadvantages, two families of continuum robot are presented, one employing two compliant joints connected in series in a

segment (double-pivot compliant joint); the other one utilizing two orthogonal groups of twin parallel elastic rods as compliant joint (twin-pivot compliant joint). Finally, a stiffening approach is introduced, which renders the continuum robot have two states, relatively low and high stiffness, enabling the robot bend all the sections freely in the low stiffness state and perform machining in the other state.

**Chapter 4** presents the forwards and inverse kinematics for both two proposed families of design concepts. Moreover, with regard to the kinematic challenge presented in chapter 3, an iterative approach is presented, so that the accurate inverse kinematics can be obtained, which enables the continuum robot has precision position control. Further, the cable tension for both families of continuum robots configurations are analysed for validating the tension able to be maintained at a constant value in arbitrary configuration. Furthermore, the method for calculating the work volume of a multiple section continuum robot is developed and a three-section case study is presented.

**Chapter 5** covers fundamental analyses including the static actuation force, joint buckling, Jacobian and stiffness. The auction force analysis of an arbitrary section in a multiple-section continuum robot with a random bending shape is presented. Secondly, the method for calculating the critical buckling load of the compliant joint is derived, which is utilized for guiding the compliant joint designs of the physical demonstrators. Further, the Jacobian of multiple-segment section is investigated, so it allows the stiffness of the multiple-segment section to be analysed. The simulation validations of the analyses are presented at the end of this chapter.

**Chapter 6** details the design of four evolving concepts of prototypes, which employs different concepts introduced in chapter 3. By comparing the mechanical performances of these prototypes (2<sup>nd</sup> and 3<sup>rd</sup> ones), an ‘optimal’ concept is selected to build the final prototype and the design of this demonstrator is presented. This chapter

also introduces two variable stiffness system designs by employing the concepts proposed in chapter 3.

**Chapter 7** introduces the trials undertaken on the four demonstrators. The first demonstrator was setup to evaluate the backbone material and according to the tests, the super-elastic Nitinol is determined to be utilised for the following prototypes. Further, the second demonstrator is utilised to validate the concept of double-pivot compliant joint and the navigation strategy: the tip-following algorithm. Furthermore, the trial results of the third prototype are presented, including position accuracy, repeatability, twisting angle and machining test. Regarding the fourth system, the physical system are finished and under testing.

**Chapter 8** discusses the conclusion of this research work, emphasising the contributions of this thesis and the future work that could support further development in the field.

## **1.5. Highlights and contributions**

### **1.5.1. New concepts of continuum robot and variable stiffness system**

1. Two families of novel continuum robot concepts were proposed (Chapter 3), i.e. double- and twin-pivot compliant joints construction. The concepts are different from the existing continuum robots in having unique compliant joints connection, enabling the system to simultaneously have a small diameter/length ratio, a great flexibility (bend capability) and an appropriate stiffness, thus it can be utilised for in-situ repair applications.
2. The twisting problem of conventional flexible continuum robots (Chapter 3) was identified from experiments. The designs employing the proposed concepts in this research can decrease the twisting angle by up to 98.6% (Chapter 7).

3. A novel variable-stiffness concept utilising thermoplastic material was developed (Chapter 3), which can be integrated with continuum units, rendering a conventional continuum robot into a variable stiffness one.
4. Four prototypes of continuum robots were designed and built (Chapter 6). In the machining trials, it has been proven that three-section twin-pivot backbone continuum robot can provide an appropriate stiffness, control accuracy ( $\pm 1\text{mm}$  error for sweeping in any  $\pm 5^\circ$  area in the work volume) and repeatability ( $\pm 0.5\text{ mm}$  error in the whole work volume), enabling the system to blend metal materials, e.g. aluminium and titanium, which are the materials widely employed in the aerospace industry. (Chapter 7). Accessing in gas turbine engines has been realised by the final full length continuum robot (1266mm). It has been proven that the system has an appropriate control accuracy to be navigated to reach the first stage of LPC (low pressure compressor) of a gas turbine engine (Rolls-Royce XWB) by following a pre-planned path. (Chapter 7)

### **1.5.2. Modelling**

1. Two kinematics models for two families of new continuum robot design concepts were developed (Chapter 4) by using an algebra approach and a combination method of geometry approach and D-H parameters, respectively. The kinematic models are modular, allowing their application to a wide range of double/twin-pivot continuum construction, which were presented in this PhD thesis.
2. A novel approach for evaluating the cable tension was introduced for verifying the tension force capable to be maintained at constant value in arbitrary configuration of the continuum robot (Chapter 4).

3. The work volume was analysed to evaluate the reachable capability of the continuum robot when activating machining capability by considering the geometry limitation and compliant joint material yield (Chapter 4).
4. A general approach for calculating the static action force of an arbitrary section in a multiple-section continuum robot with a random bending shape was developed by considering end load, weight of robot, cable tension, force for bending flexible backbone, and the interaction from distal sections' cables. It was utilised to direct the action system design, particularly to the selection of the motors (Chapter 5).
5. Joint buckling limits the load carrying capability of elastic construction in the longitudinal axis. The method of calculating the critical buckling load for compliant joint was introduced in this thesis for guiding the design of the arm (Chapter 5).
6. A general approach for computing Jacobian and stiffness of the proposed continuum robots were investigated to evaluate the compliant joint design in terms of section stiffness (Chapter 5).

---

## Chapter 2 Literature Review

### 2.1. Introduction

There are nowadays a large number of robots servicing in variable fields across the world, which can be mainly divided in two broad groups, i.e. industrial and service robots<sup>3</sup>. For in-situ repair aero-engines, a service robot needs to be developed, which requires a reduced diameter and long length with a relatively low stiffness when navigating in a cluttered environment and a relatively high stiffness when acting a machining task. It can be found that several off-the-shelf technologies (employing industrial robots or specialist tools) have been employed for repair and maintenance in some sectors of industry, e.g. energy industry and aerospace. However, the existing devices are limited by their DoFs and rigid construction, which disables them to be deployed for the applications in constrained spaces. In the last thirty years, especially last two decades, a new kind of hyper-redundant robots (continuum robot) has been developed, which demonstrated its potential for working in confined spaces [32, 34, 37]. In this chapter, a wide range of literature review about design and kinematics of continuum robots is provided to identify the challenges of developing a robot for in-situ repair. Further, a research of the existing technology was made to figure out the research gaps for developing an adjustable stiffness mechanism to enable a continuum robot have dual stiffness states.

### 2.2. An overview of available in-situ repair/maintenance technologies

Maintenance and repair is critical in some key fields of industry, such as energy, aerospace, marine and other sectors which are directly related to safety [38, 39]. Failing to maintain in good order installations can lead to serious accidents, which can cause large casualty and financial loss [40, 41].

---

<sup>3</sup> A service robot performs useful tasks for humans or equipment, e.g. mining, medical surgery, equipment repair and maintenance.

There are a wide range of off-the-shelf technologies and systems employed to perform the maintenance and repair tasks in these fields [42, 43]. However, since that the constructions of some working environments are very complex (e.g. gas turbine engines), the conventional approach needs to disassemble the system to allow the end-effectors (e.g. inspection and/or cutting tools) reach the target position, which can lead a large additional expenditures:

- For example, for repairing a gas turbine engine, about 10% of the total cost is spent to take it off the wing; the loss in revenue when grounding an aircraft is ca. \$100,000/day.
- In energy industry, the cost of removal and reassembly of a generator is ca. \$250,000 for fossil fuelled plants and ca. \$400,000 for nuclear plants; the loss in revenue for a non-operational plant can amount to €500,000/day.

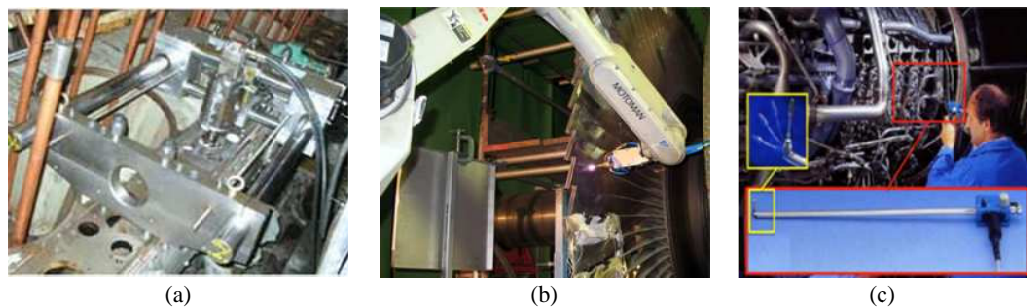


Figure 2-1 Available conventional in-situ repair tools: (a) repair of injection pump landing surface on a diesel engine [42]; (b) Laser cladding by an industry robot arm [43]; (c) industrial invasive tooling [44].

In order to minimise the cost, the delivery system & end effectors that can access cluttered environments and perform repairs & maintenances with requiring less/no disassembly (in-situ repair/maintenance), need to be developed, so it can reduce the consumption of operation time and financial cost significantly.

Conventionally, the solution is to utilise job-customized tooling to execute single in-situ tasks, as shown in Figure 2-1(a). The disadvantage of this approach is that the design is bulky, requiring big operation space and rendering it difficult and inconvenient to handle. Further, more advanced multi-axis systems have started to emerge, which have more degrees of freedom for more complex tasks (Figure 2-1 (b)).

But they are still over-sized and lack of flexibility for operating in cluttered environments.

For in-situ repair/maintenance in confined spaces (e.g. gas turbine engine), up to now, invasive tooling is employed in most cases, as shown in Figure 2-1(c). Through an accessing hole in the side of the engine, it can reach the desired area and inspect/repair the cracked compressors. However, it cannot cover a wide range of repair & maintenance works as the delivery system is lack of degrees of freedom, which limits its reachable range in complex environments.

It can be seen that the existing technologies are lack of degrees of freedom and compact design for in-situ repair/maintenance, which limits the accessing and reachable capability of the systems in restricted environments.

### **2.3. Review of redundant robots**

A kinematically redundant manipulator can be defined as the mechanism which is constructed with more joints than those strictly required to reach a specified position [44]. Generally, a task for serial robots operating in open space requires max 6 DoFs, hence, a robot arm with seven or more joints is considered as a typical redundant robot. The kinematic redundancy provides the robot with increased dexterity, so it enables the robot end-effector can reach a target position with variable orientations and have better capability for avoiding obstacles in cluttered environment (e.g. avoiding collisions with other robots or equipment in a small operation area). Several prototypes have been presented and proven them have a great potential to be employed in complex and hazardous environment, such as space station [45] and surgery operation [46].

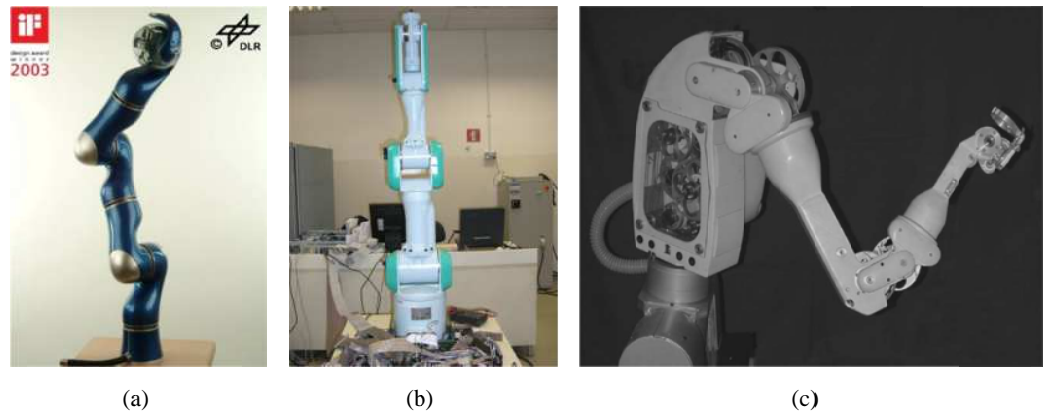


Figure 2-2 A group of serial redundant robots: (a) DLR lightweight robot III [47]; (b) Mitsubishi PA-10 Robot [48]; (c) Dexter arm [49];

As shown in Figure 2-2(a), DLR lightweight robot III consists of seven joints and the joints are actuated by motors which are integrated in each link. It has been demonstrated in some applications, such as picking & handling objects with a robot hand and inserting a piston into motor block. Further, it is planned to be utilized on the space station for repair and maintenance operations in the future. Figure 2-2(b) illustrates Mitsubishi PA-10 robot (7 DoFs), which has similar construction with the previous robot. The researchers made considerable efforts to develop more efficient algorithm for path planning of redundant robots [48, 50]. Furthermore, Dexter arm, a 8-DoF serial robot, is designed for assisting to disabled and elderly people in their daily life environments [49]. For articulating each link, steel cables are employed to transmit the actuation from the motor (located on the base) to the joint. Due to this design, weights of the links are notably decreased, but it makes the mechanical drive system quite complex.

Comparing with the conventional 6-DoF robot, redundant robot has several significant advantages, such as more dexterity in the workspace. However, most of the designs are structured with more articulated links and the motors are integrated in each link, making the system physically bulk, which limits the accessibility of the robot in constrained spaces. Further, the redundancy renders the inverse kinematics complex [51], since there are more than one solutions for the inverse kinematic to execute a

task. Hence, the best one needs to be determined from these solutions based on a method, such as path planning/torque/ error optimization [48, 49, 52-54], which requires longer time to compute. However, for operating in highly restricted environment (e.g. gas turbine engine), the robots need more degrees of freedom than the conventional redundant robots.

## **2.4. Review of continuum robots**

Continuum robots, also known as hyper-redundant, snake arm and elephant's trunk robots, unlike conventional redundant / non-redundant rigid-link robots, can feature a curvature shape with a large number of degrees of freedom [55]. Due to their unique flexibility (bending capability), continuum robots can reach the places that are usually inaccessible for other robots and/or hostile for human beings. Hence, continuum robots can be utilised for operations in highly constrained environments, such as in-situ repair of a gas turbine aero-engine and surgery interventions. In the following sections, two key factors, i.e. mechanical designs and kinematics of continuum robots, will be discussed in detail.

### **2.4.1. Design of continuum robots**

In general, continuum robot consists of a backbone (to support the structure if it is rigid; to enable the bending movement and support the structure if it is flexible), joints (utilized to allow the bending movement), actuation cables (to articulate the construction and keep the stiffness of the system) and disks (constrain the actuation cables). For minimizing the size and weight of the arm, most of the designs locate the actuators on the base of the robot and the actuation power is transmitted by actuation cables/pneumatics tubes to each link. Further, variable end effectors, such as grippers and camera, can be mounted on the tip of the robot for different applications, such as medical surgery [32] and maintenance in nuclear power station [56, 57].

According to the backbone designs, all continuum robots can be divided into two broad categories:

- **Rigid backbone continuum robots:** single/multiple joints (universal/spherical joints) are utilised to connect rigid backbones in one section<sup>4</sup>;
- **Flexible backbone continuum robots:** flexible rod/tubes or pneumatics tubes are employed as backbone, which is made up of materials capable to generate high elastic displacements, such as super-elastic NiTi or rubber.

In the following sections, the designs of continuum robots are discussed in two categories, ‘rigid backbone’ and ‘flexible backbone’, respectively.

### 1) Rigid Backbone Continuum Robots (RBCR)

In the group of RBCR, the system generally consists of multiple rigid sections, which are connected by R/U/S joints (revolute/universal/spherical joints). And each of the sections is constructed with single/multiple segments [34, 37, 58, 59].

According to actuation methods and location of mechanical actuation, all rigid backbone continuum robots can be classified into two sub categories [60]:

- **Rigid backbone continuum robots with ‘extrinsic’ actuations:** extrinsic system uses remote actuations, which generally locate on the base of the system and the actuation power is transmitted into the mechanism via cables.
- **Rigid backbone continuum robots with ‘intrinsic’ actuations:** In an intrinsic system, the actuators (micro motor/pneumatics) are located in each section separately.

#### A) Rigid Backbone Continuum Robots with Extrinsic Actuation

There have been numerous prior attempts to create a rigid backbone continuum robot with extrinsic actuations. The origin concept of continuum robot can be generally traced back to the creation of tensor arm manipulator in the late 1960s. The concept (Figure 2-3 (a)) was presented and patented in 1967 [58, 61]. In this design, the arm has several multiple-segment cable-driven sections. Each section can feature an arc

---

<sup>4</sup> The length between two adjacent disks is termed a segment; the length between two terminate segments is classified as a section; the terminate segments are where the actuation cables are attached (Figure 2-3(a)).

shape by pulling actuation cables which are attached to the terminate disk of this section, allowing the arm generate a complex curvature shape. A physical system (Figure 2-3 (b)) employing this idea was developed in 1999 [37] . U joints are utilised for connecting the disks and four evenly spaced springs are attached to the adjacent disks for making every segment has the same stiffness, so the section can have an evenly bend (it can be also understood as the springs passively reduce hyper-DoFs of a section to two, so two actuators can operate it). The prototype is 838mm in total length and four sections range in diameter from 101.6 mm, 88.9 mm, 76.2 mm, and down to 63.5 mm for the tip section. Two pairs of cables are employed for actuating each single section, and a pulley system is designed for keeping constant tensions of the actuation cables.

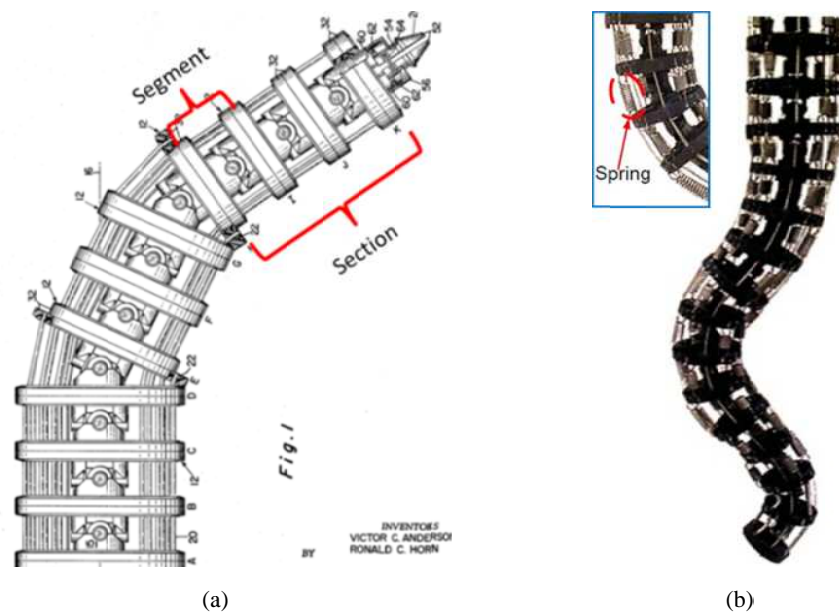


Figure 2-3 A series of rigid backbone continuum robot with U joints: (a) the tensor arm manipulator;(b) elephant's trunk robot;

Since this robot employs a number of joints, it is flexible and suited for both obstacle avoidance and safe human-robot interaction, comparing with conventional rigid link robots. However, the drawbacks of these prototypes are poor position accuracy (the error of the elephant's trunk robot is approximately 10~20mm, it can be found from the experiments presented in [62, 63]) and low payload carrying capability (in the

experiments [63, 64], a football and plastic rod were grasped) , which are caused by the following reasons :

(i): Theoretically, evenly bending of every section is the basic assumption for the kinematics analysis and control [65-67]. It requires identical springs to be employed for making every segment have equal stiffness, so each section can generate an even bending. However, practically, due to the manufacture and assembly errors of springs and other elements, the stiffness of each segment cannot be the same, accusing unevenly bending of the sections which leads to poor position control accuracy.

(ii): The factor limiting the payload carrying capability is the buckling of the articulated arm [68]. Specifically, the force for pulling the actuation cables generates a high load along the length of the arm, which can buckle the joints of the continuum robot. By the constraint of the actuation cables, a section with single U joint can take relatively large buckling load, due to the relatively rigid construction; for a section employing multiple U joints and a number of springs, buckling load mainly depends on the stiffness of the springs, causing it much lower than a single U joint section. Therefore, the concept which employs one U joint for single section is able to be utilised for heavy duty industrial application. Figure 2-4(a) shows a eleven-section continuum robot which can access through a small opening for the job of inspecting, swaging and sealing inside the wing box [69]. A similar system was utilised for cleaning and inspecting the cutting head of a tunnel boring machine [70].

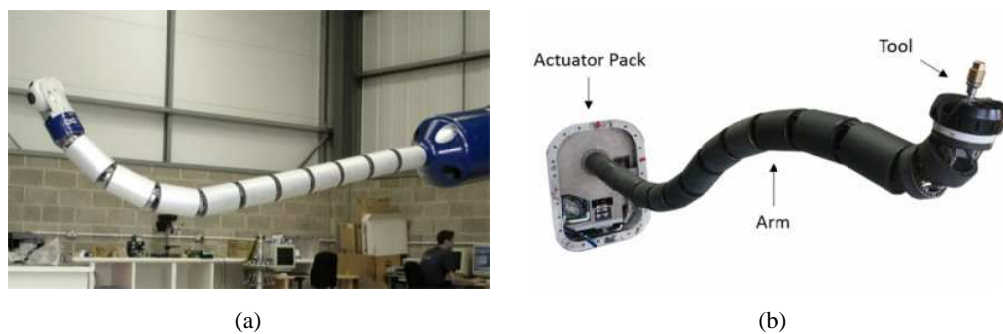


Figure 2-4 (a) Continuum robot for aerospace assembly [69]; (b) continuum robot for maintenances of tunnel boring machines [70];

Further, universal joint can be also replaced by spherical joint, as shown in Figure 2-5. Elastic elements, such as rubber and spring, are needed to be integrated with the joints, which makes the bending angle of single section evenly distributed over every joint.

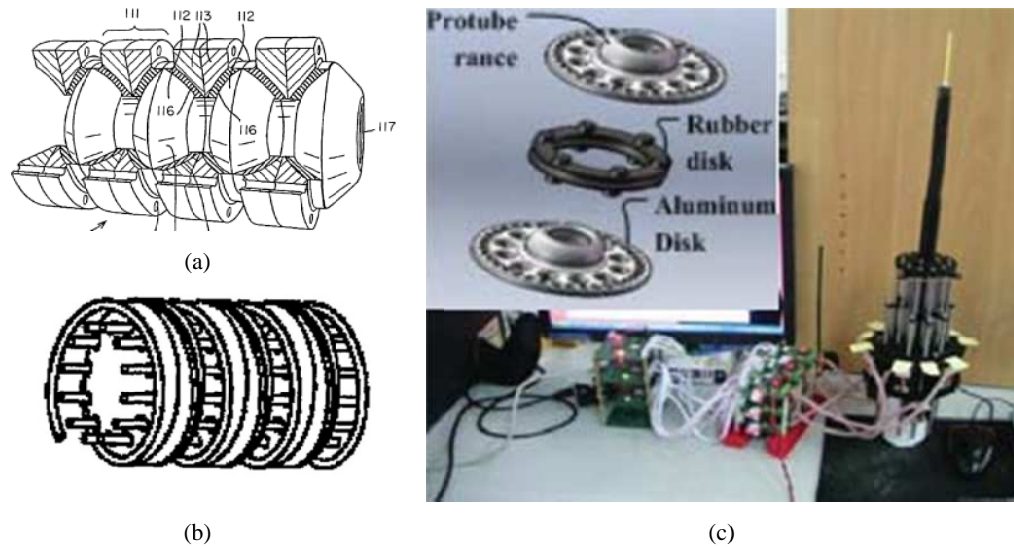


Figure 2-5 (a) Concept of spherical joint integrated with rubber layer [71]; (b) concept of spherical joint integrated with spring [72]; (c) continuum robot developed by Beihang University [73];

Figure 2-6 (a) illustrates a design of a continuum robot connected by revolute joints, which was developed for nuclear reactor maintenance. Since the axes of the revolute joints are all parallel, the arm can only work in one plane with three DoFs, i.e. two translations and one rotation. Similarly, a steering mechanism (Figure 2-6(c)), employs multiple parallel revolute joints in single section; two NiTi rods are coupled in the system along the backbone, which play the same role with the elastic elements (spring/rubber) used in the aforementioned multiple-segment section robots. Figure 2-6(b) presents a continuum robot connected by rolling joints and Teflon flexures (elastic element). And the revolute joint is arranged to be perpendicular to the adjacent one for generating two DoFs rotation.

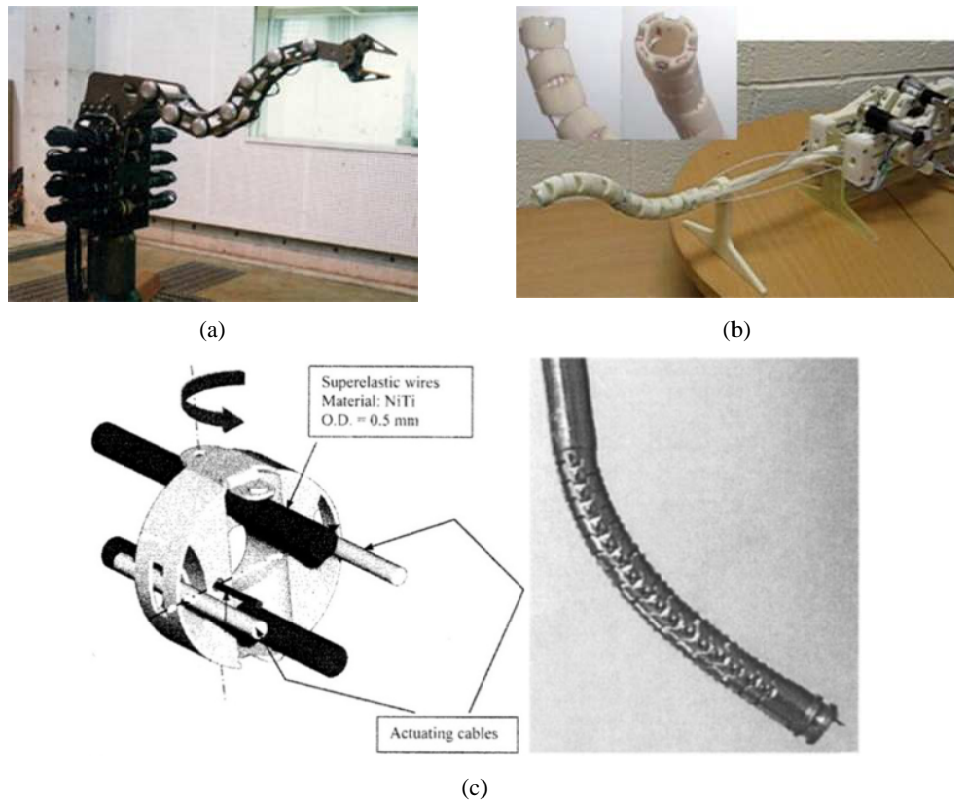


Figure 2-6 Several rigid backbone continuum robots: (a) CT Arm [57, 59, 74, 75]; (b) a stiffness-adjustable hyper redundant manipulator [76]; (c) steering mechanism [77];

According to these examples, the conventional design is generally utilising revolute/universal /spherical joints to connect rigid links with elastic elements for evenly distributing bending angle of each section along the longitudinal direction. However, massive number of motors are needed for the actuation (one actuation per section [59]; two actuations per section [37, 64, 76]; three actuations per section [34, 71, 73, 78]), which cause the actuation system heavy and bulky.

Apart from the aforementioned designs, a novel rigid backbone continuum robot (HARP, as shown in Figure 2-7(a)), was developed in 2006, which has a different working principle comparing with other continuum robots. As shown in Figure 2-7(b), the design consists of two concentric continuum robots. The inner and outer mechanisms are separately connected by spherical joints and actuated by one cable and three cables, respectively. By pulling/releasing the actuation cables, both mechanisms can alternatively switch between rigid or soft state. In particular, by

acting a large amount of forces on the actuation cables, the mechanism can be locked by the friction between the disks; while the mechanism can move freely, when the large amount of forces are realised.

Figure 2-7(c) illustrates the working procedure of this system: assuming the system start with both inner and outer mechanisms as rigid (step a). The outer mechanism turns to be flexible and orientates to a desired direction. In this step, the system maintains most of its shape (except the tip disk of the outer mechanism) because the inner one is rigid (step b). Further, the outer mechanism becomes rigid; then the inner one switches to soft state and next advances till it reaches the same configuration of the outer mechanism (step c). By repeating the procedure (steps d-f), the system can follow an arbitrary three-dimensional curve with min four actuators, which significantly decreases the weight of the actuation system, simplify the arm design and enhances the obstacle avoid capability. However, this design needs an appropriate size of the rigid link to generate enough friction to lock the mechanism for a particular length. It means the diameter of the arm need to be increased when build a long arm with this concept.

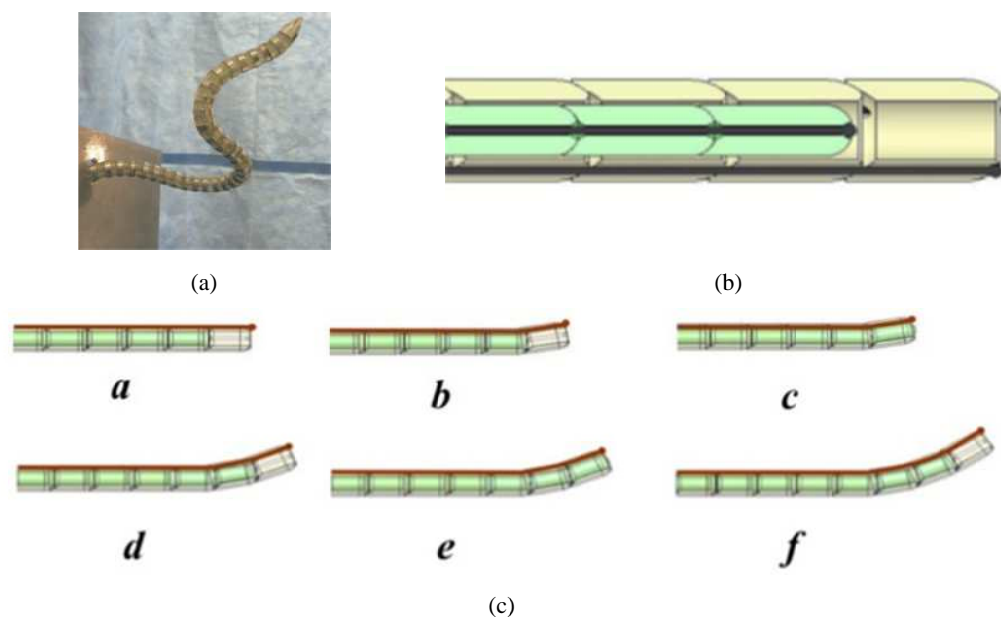
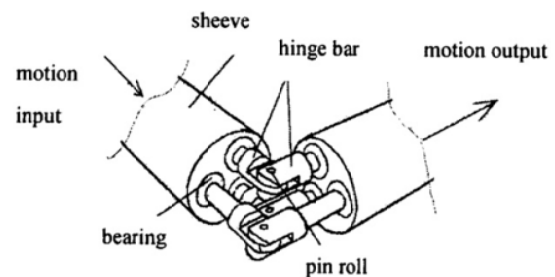


Figure 2-7 Continuum robot HARP (a) the prototype [33]; (b) two concentric continuum robots construction of HARP [79, 80]; (c) working principle of the mechanism [79];

Figure 2-8 shows a 20-DOF continuum robot which is 1.8 meter in length and 0.2 meters in diameter. The whole arm is driven by a motor located on the base of the system. The actuation power is transmitted by the rotational motion of a group of central shafts to each section. All the central shafts are coupled together which performs as a universal joint, as shown in Figure 2-8(b). Specifically, each shaft chain is connected by a number of hinge joints, which can rotate relative to the hinge hole and also slide back and forth, so it allows the pivot points of all the hinges to be maintained in this same plane and the hinges bends in the same direction. Hence, the joint mechanism can generate two DoFs as a universal joint. For bending each section independently, the bending mechanism of each section engages and disengages with the power transmission shaft by electromagnetic clutches. The unique design decreases the weight of the actuation system remarkably. However, each section has to integrate an independent electromagnetic clutches and bending system, making the robot arm quite complex and the size difficult to miniature.



(a)



(b)

Figure 2-8 Single Motor Driven Hyper-Redundant Manipulator: (a) the prototype [81]; (b) the mechanism of special universal joint [82];

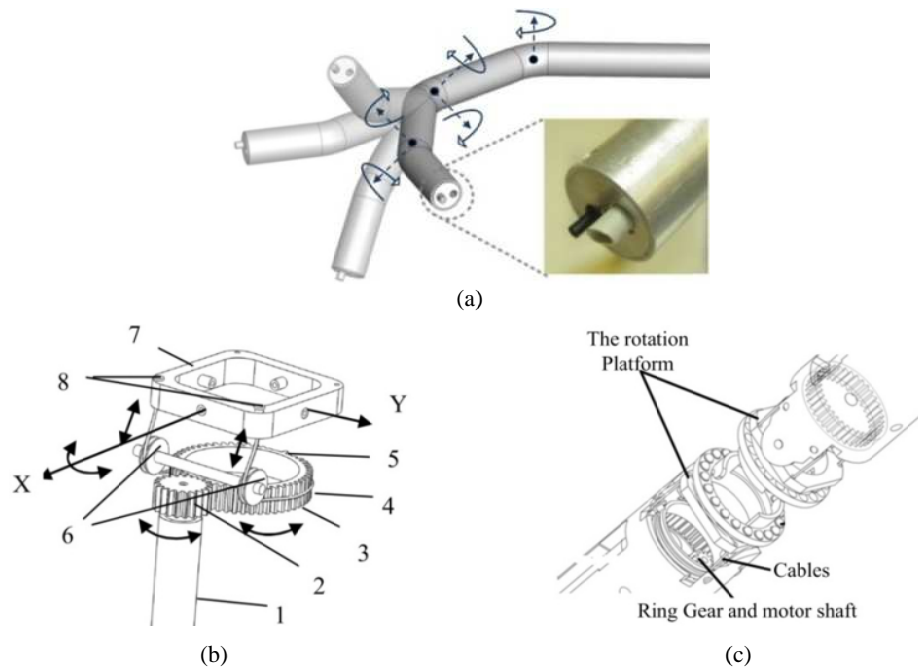
In terms of rigid backbone continuum robots with remotely located actuators, many practical applications have been demonstrated, including aerospace assembly [69], tunnel boring machines maintenance [70] and surgical device [76, 77, 79]. In the future, they may be deployed for more operations requiring high end load carrying

ability in large scale confined spaces, e.g. nuclear reactor maintenance, because of high stiffness and long slender shape comparing with other continuum robots.

### ***B) Intrinsic Actuation (Motor/SMA)***

In this sub-category, the mechanism is generally constructed with rigid backbone and actuated by micro motor or other approaches, e.g. shape memory alloy (SMA) and pneumatics, which are located in the arm. The specific designs will be described separately based on different actuation approaches.

In 2010, a five-DoF continuum robot (i-Snake) was presented (Figure 2-9 (a)), which is actuated by micro motors located in rigid links [83]. The articulated arm is 12.5mm in diameter and 124 mm in length. Two universal joints are serially located at the tip, and one revolute joint is arranged at the tail of the arm. Figure 2-9(b) shows the specifications of the joint design: ring gear (3) is actuated by micro motor shaft (1), which transmits the power to rotation platform (7) by cables (4). Hence, element 7 can be rotated about axis Y. The advantage of micro motor actuated system is good portability, distal dexterity, and enhanced manipulation accuracy and stability [84].



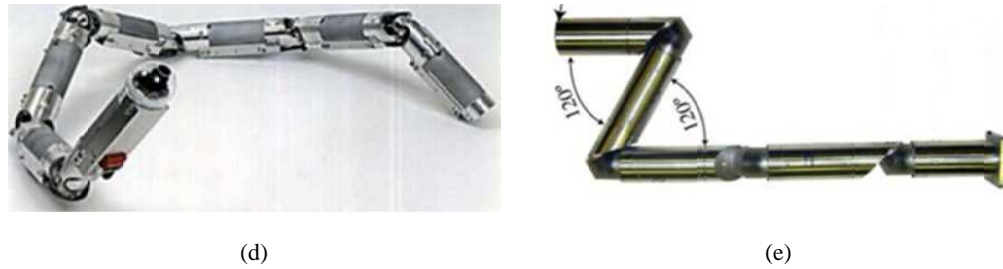
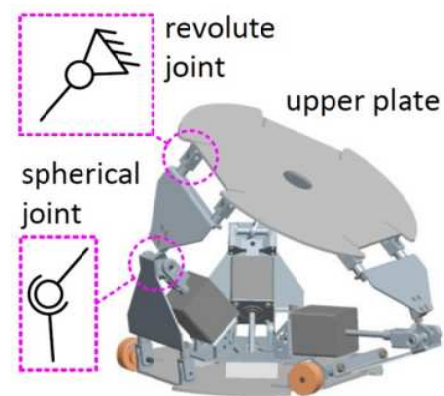


Figure 2-9 i-Snake robot (a) the demonstrator of i-snake [83]; (b) schematic of the bending mechanism [84]; (c) mechanism of the universal joint [84]; (d) the JPL Serpentine Robot [85]; (e) Medusa [86];

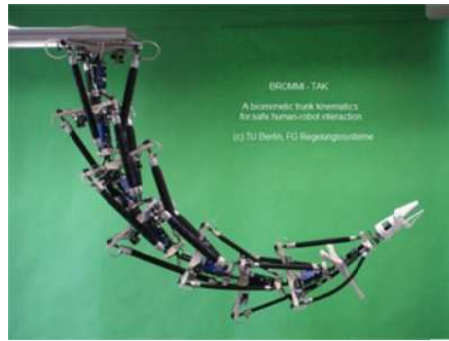
The serial link configuration is also employed in several other prototypes, which makes a remarkable impact in inspection, undersea/ground search and rescue tasks [85-90] (Figure 2-9 (d) & (e)). Additionally, another widely utilised configuration is composed of multiple parallel kinematics mechanism connected in series (Figure 2-10 (a) & (c)). As shown in Figure 2-10(b), the 3-DoF section is constructed with three RSR legs (R-revolute joint; S- spherical joint), each of which is attached to the base via a revolute joint driven by a motor. Figure 2-10(d) illustrates another prototype employing parallel link configuration as the mechanism for single section, which makes use of universal joints for connecting adjacent sections and pneumatic actuators for generating 2-DoF rotation. Comparing with serial link configurations, parallel link configuration continuum robots have better stiffness, accuracy and stability. However, this design cannot be miniaturised easily, since the actuations are located intrinsically in the arm, which takes a relatively large space comparing with other actuation approach, e.g. cables.



(a)



(b)



(c)



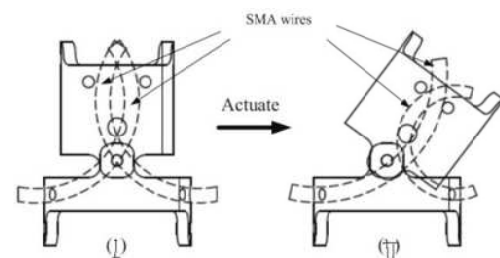
(d)

Figure 2-10 (a) A novel hyper redundant robot arm [91]; (b) section mechanism of the arm [91, 92]; (c) a pneumatic driven elephant's trunk (TAK) [93]; (d) section mechanism of TAK [94];

In terms of actuations, an alternative approach is to use shape memory alloys (SMA), which is an alloy which can be trained to ‘remember’ a shape and returns to its remembered shape from a deformed shape when heated [95]. As shown in Figure 2-11(a), a SMA-actuated continuum robot was developed and presented in 2009. Figure 2-11(b) illustrates the design in detail: two antagonistic SMA wires are brought into service in each revolute joint for generating a 1-DoF rotation; at the initial position, SMA wires are bent to the desired shape in advance to keep the links straight; when activating one SMA wire, the wire is heated and then it recovers its remembered straight shape; as a result, the link will be pushed by the actuated SMA wire, which leads to a rotation of the link. Moreover, a similar concept is used in the 2-DOF steerable cannula, as shown in Figure 2-11(e).



(a)



(b)

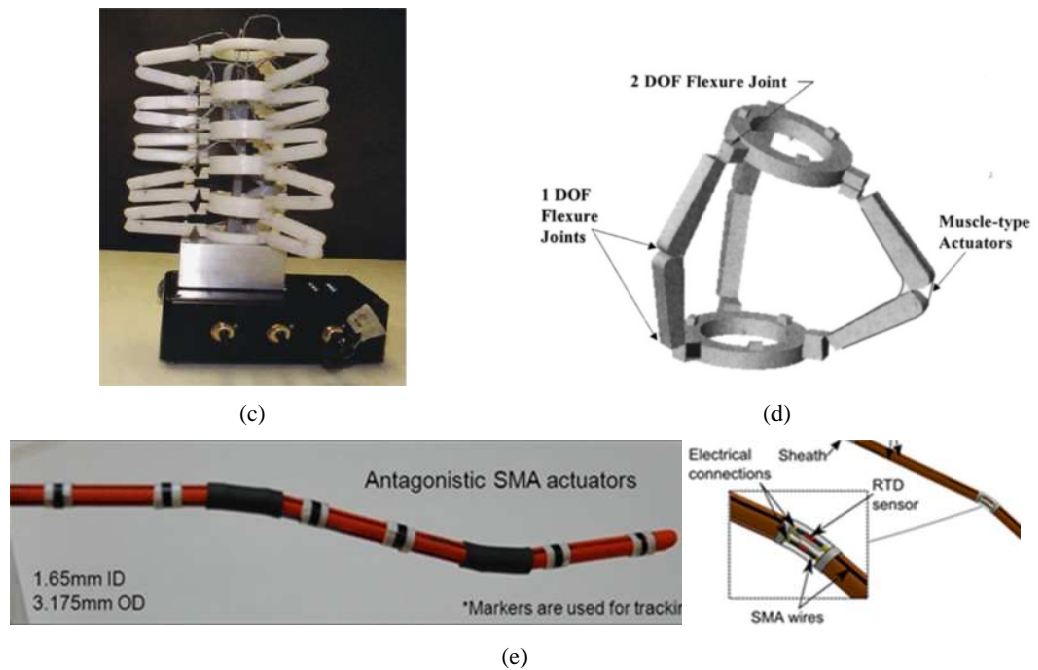


Figure 2-11 (a) Robot MINIR [96]; (b) working principle of single joint [97]; (c) the prototype of BRAID [98]; (d) one parallel section of BRAID; (e) a 2-DOF cannula prototype [99, 100];

Figure 2-11 (c) illustrates a continuum robot made of a serial chain of parallel sections actuated by SMA wires. The detail of single section design is given in Figure 2-11(d). Since NiTi wire contracts when electrically activated, a pair of oppositely located wires is deployed for rotating the middle revolute joint of each leg. Employing SMA as actuations can make the design compact, lightweight and portable. However, the drawback at the present time is poor accuracy and stability of the system, mainly because the ratio of strain to temperature is nonlinear making it difficult to control.

According to a wide range of literature review, it can be concluded that rigid backbone continuum robots generally have the advantages of better dexterity and accessibility in crowd environments, comparing with conventional rigid link robots, and good stiffness, simple kinematic model, good accuracy and stability, comparing with other types of continuum robots. Based on these advantages, they have been deployed for the operations in large scale confined spaces, e.g. tunnel boring machines maintenance and aircraft wing assembly. However, since the backbone elements are rigid, the human-robot interaction is less safe than flexible backbone continuum robot, which

limits it to be utilised in the applications directly related to human safety, e.g. minimally invasive surgery (MIS).

## **2) Flexible Backbone Continuum Robot (FBCR)**

Flexible backbone continuum robots, as the names suggests, utilise elastic materials (elastic rod or pneumatic actuator) as the backbone, which can obtain continuously bending shape. According to actuation methods and location of mechanical actuation, all flexible backbone continuum robots can be also classified into two sub category: 'extrinsic' and 'intrinsic' (the same with the category of FBCR).

### ***A) Extrinsic actuation***

In the early works, steel spring/flexible coupling was deployed for generating a true continuum bend. Figure 2-12(a) and (b) illustrate two systems constructed with spring backbones. In 1997, a 3 meter long robotic manipulator (EMMA) (using flexible couplings as the joints) was developed and demonstrated for inspection and remediation of high level radioactive waste in waste storage tanks [56, 101] (Figure 2-12 (c)). Another early prototype, KSI tentacle manipulator [102-104], employs two serial connected pneumatic actuators as the backbone, and each section is controlled by three cables (Figure 2-12 (d)). It was utilised for nuclear decontamination of a hot cell by vacuuming radioactive detritus from the floor. These designs demonstrated good capabilities of flexibility. However, the spring-like backbone makes it difficult to estimate/control the length of the arm, since the varying actuation force along the longitudinal direction compress the backbone to variable lengths in the process of operation, which leads to poor accuracy and stiffness [105].

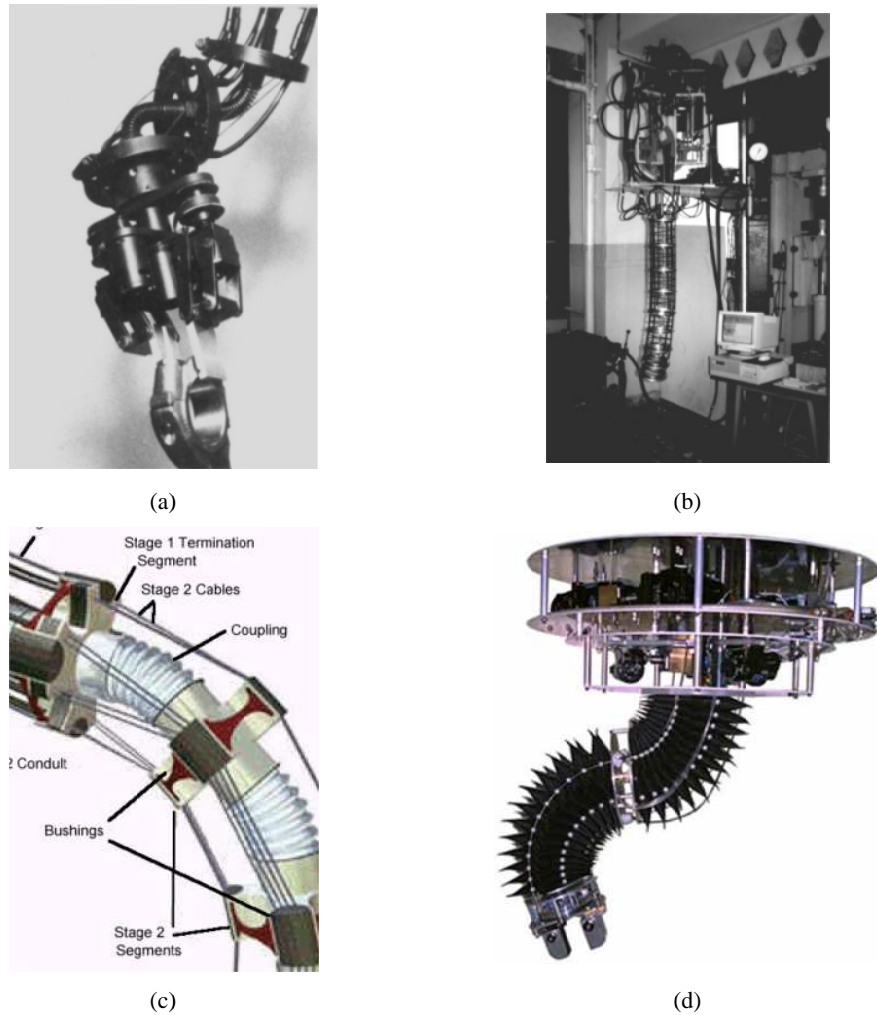


Figure 2-12 (a) A curvilinear continuum robot [106]; (b) elephant trunk type elastic manipulator [107]; (c) EMMA™ manipulator; (d) KSI tentacle manipulator;

This problem can be easily solved by employing incompressible elastic rods as backbone, such as super elastic NiTi /spring steel rod. A large number of prototypes have been built based on this concept. In particular, a series of super elastic NiTi (e.g. ASTM F 2633) backbone continuum robots has been presented since 2004, which can be described as “continuum-style” segmented backbone designs (Figure 2-13 (a)). In these designs, one NiTi rod is located at the centre of the arm and mounted with the disks as the main backbone. Another three NiTi rods, instead of cables, are symmetrically placed around the backbone for transmitting the actuation power. Spring steel backbone continuum robots were also designed for kinematic study [108-110] and rapid handling [111] (Figure 2-13 (b) and (c)).

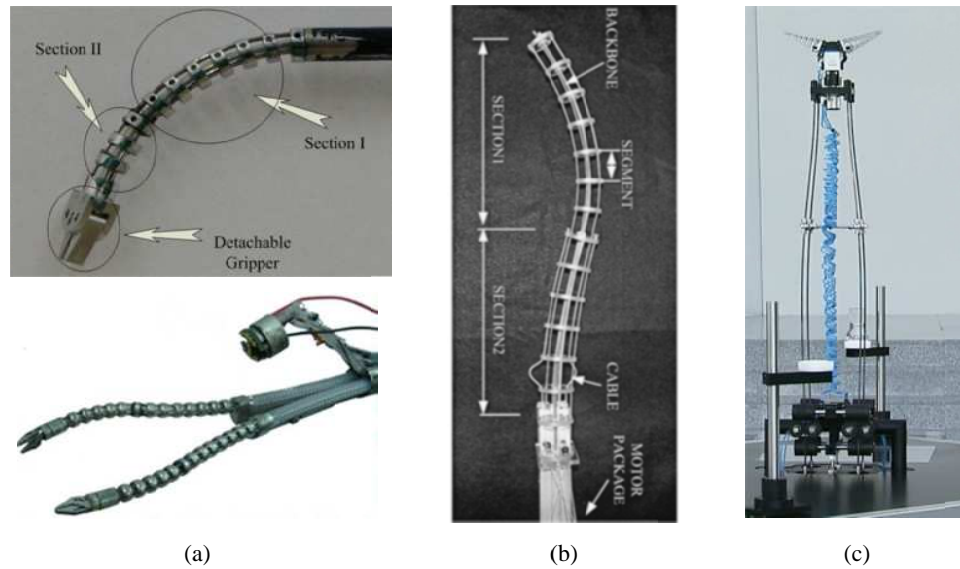


Figure 2-13 (a) Flexible surgical continuum robot [112]; (b) Clemson tentacle manipulator [108]; (c) Bionic Tripod 3.0 [111];

Apart from the previous concepts, a concentric-tube robot was presented, which utilizes three concentric pre-curved NiTi tubes as backbone (Figure 2-14 (a)). All the tubes are pre-curved to different curvatures, which can extend and rotate axially with respect to one another. The shape of each section is dominated by those tubes retracted inside it. Specifically, since the outer and inner tubes have different curvatures, when they are in the same direction, the curvature of the combined configuration can be formed between two tubes (Figure 2-14 (b)); when they are in the opposite directions, a straight configuration can be obtained. Due to the novel actuation solution, this system has small diameter (1.6 mm) and high dexterity, but no load is claimed to be able to take at the tip.

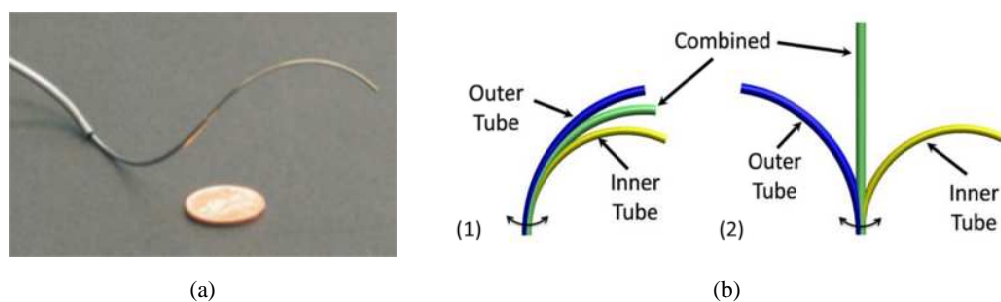


Figure 2-14 (a) Concentric pre-curved tube robot [113]; (b) the working principle [114]

Flexible backbone continuum robots with extrinsic actuations, especially super-elastic NiTi backbone, have great flexibility and small dimensions in diameter, allowing it have an appropriate ability to access small scale cluttered environment and safer human-robot interaction, comparing with RBCR. According to these features, most of the continuum robots employed in MIS take flexible backbone designs for their hardware.

### ***B) Intrinsic actuation (Pneumatics/ hydraulics)***

This type of continuum robots typically forms the backbone from its hydraulic/pneumatic actuators [105], which can be considered as pure continuum backbone. The concept couples triple hydraulic/pneumatic actuators as one section to generate three DoFs (one-translation-DoF, two-rotation-DoF) by adjusting the pressures of the actuators.

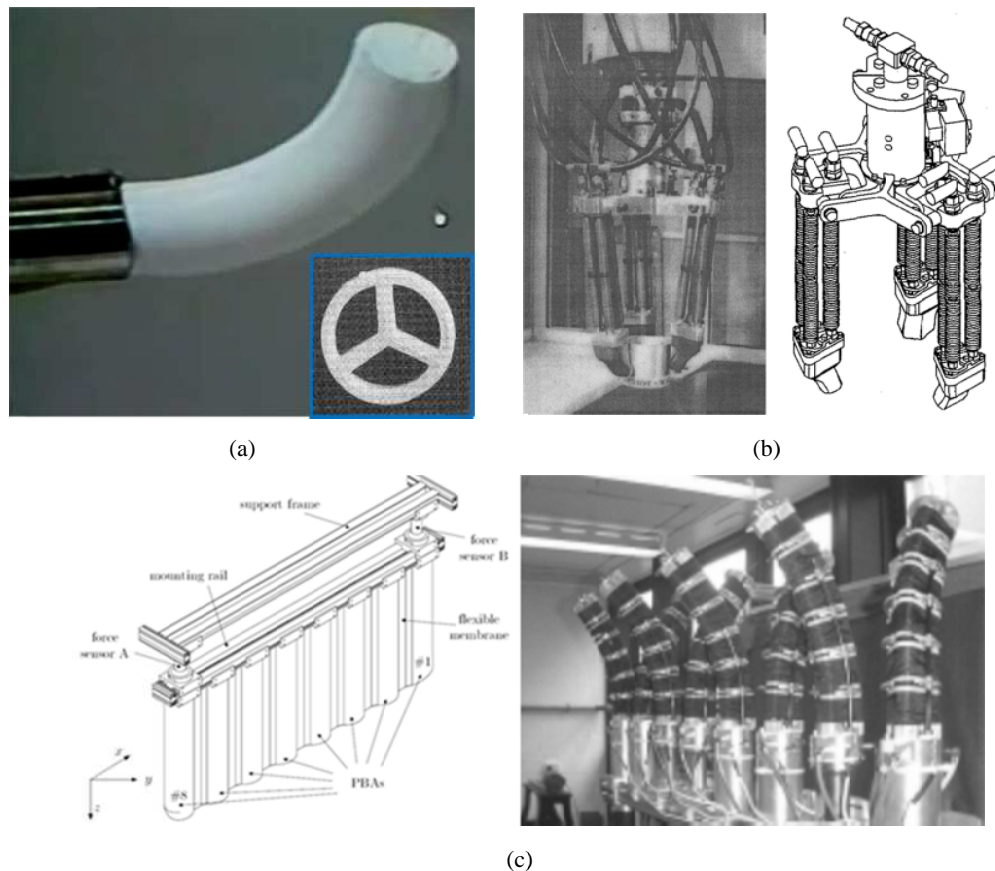


Figure 2-15 (a) Flexible Microactuator (FMA) (b) AMADEUS phase I prototype gripper [115] (c) array of fin mechanism with multiple hydraulic continuum actuators

The first demonstrator employing this concept, flexible Micro actuator (FMA), was presented in 1991 (Figure 2-15 (a)). This system demonstrated a great flexibility and dexterity, but the challenge was precise control for accurate operations. By combining several bespoke 3-DoF continuum manipulators, a flexible gripper can be constructed with passive compliant fingers to avoid damaging complex geometry objects by inevitable positioning inaccuracies when grasping [116]. In 1994, a three-flexible-finger gripper was developed for subsea applications [117], as shown in Figure 2-15(b), because of the bespoke reason and its simplify of design. Then, it was used to build a fin biomimetic propulsion mechanism by employing an array of parallel arranged hydraulic continuum actuators for man-made underwater vehicles. Unlike the conventional propulsion, e.g. propeller, the fin mechanism can generate a nature wave by moving in coordinate, bringing the advantages of minimal sediment disturbance (improving the visibility when working close to the seabed) and smooth moment in the water [118, 119]. Also, larger scale of continuum robots were also suggested able to be formed by connecting multiple 3-DoF continuum manipulators in serial [118].

Since 2006, a series of OctArm continuum robots (Figure 2-16 (a) & (b)) has been developed, which utilised the aforementioned concept. Each section generally integrates three independent pneumatic actuators. Single section can extend/extract by equally adjusting the air pressure of the actuators in this section; while the orientation can be modified by applying different pressures to the actuators. In particular, the four sections of OctArm IV (Figure 2-16 (a)) range in diameter from 40 mm (the base two sections) and down to 34 mm for the final two sections. Further, the vertical loading capability of arm is 90 N at the end. This allows the arm handle relatively heavy object, such as a large piece of wood and traffic Cone [120].

In 2010, FESTO utilised the same concept to build a pneumatic flexible trunk for handling assistant, which can generate larger longitudinal movement and bending

angle (Figure 2-16 (c)). The arm is 0.75 m length (maximum extension: 1.1 m) and able to handle 500 g weight at the tip. According to the same working principle, some other designs are built in small size (Figure 2-16 (d) & (e)), which is suggested for the surgical applications.

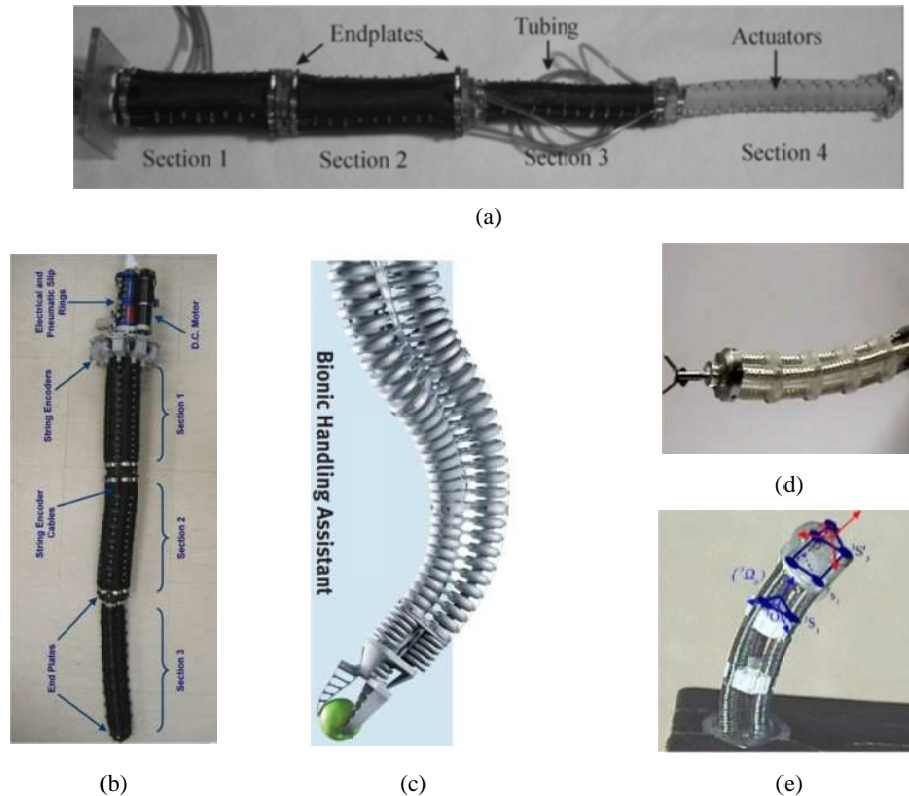


Figure 2-16 A group of pneumatic continuum robots (a) Octarm IV [120]; (b) Octarm VI [121]; (c) FESTO elephant trunk [122, 123]; (d) Instrument for keyhole surgery actuated by McKibben actuators [124]; (e) MALICA [125];

In summary, as we discussed in this section, variable continuum robot designs have been seen from the previous works. The designs can be divided into two main categories:

- Rigid backbone continuum robot: single/multiple joints (universal/spherical joints) are utilised to connect rigid backbones in one section;
- Flexible backbone continuum robots: flexible rod/tubes are employed as backbone, which is made up of materials capable to generate high elastic displacements, such as super-elastic NiTi or rubber.

It can be seen that single rigid link was employed as one section for most of large-dimension continuum robots. However, it limits the flexibility and accessibility of the robot for some applications. Hence, a solution was developed to enable more joints to be coupled in single section, which integrates elastic material into the joint mechanism in order to passively reducing hyper-DoFs of a single section to 2 DoFs. Most of small scale ones developed in recent years generally take flexible backbone as support constructions. This design can bring many advantages, e.g. better accessibility and safer human-robot interaction. But the disadvantage is that flexible backbone has lower stiffness and it is more difficult to control, which makes it hard to take large end load, comparing with rigid backbone continuum robots.

Finally, Technology Readiness Levels (TRL: a method of estimating technology maturity of Critical Technology Elements (CTE) of a program during the acquisition process) of the continuum robot research are discussed. Specifically, TRL is based on a scale from 1 to 9 and the description of each level is presented in Table 2-1.

Table 2-1. TRL in the continuum robot research

<b>TRL</b>	<b>Description</b>
1	Basic principles observed and reported
2	Technology concept formulated (e.g. patent)
3	Analytical and experimental critical function and/or characteristic proof of concept
4	robot prototype validated in laboratory environment (e.g. prototype tested in mock up environment)
5	robot prototype validated in relevant environment
6	robot prototype demonstrated in a relevant environment
7	robot prototype system prototype demonstration in operational environment (e.g. surgical continuum robot demonstrated in surgery on animals)
8	Robot system complete and qualified
9	Robot system proven in operational environment (e.g. surgical continuum robot)

---

	demonstrated in surgery on human)
--	-----------------------------------

---

Table 2-2. Summary of the existing continuum robot prototypes

Backbone	Actuation Location	Robot Name	Year	Image	TRL*	Features
<b>Rigid backbone Continuum robot</b>	<b>Extrinsic actuation</b>	Tensor arm manipulator [61]	1967	Figure 2-3(a)	2	Mutiple <b>U joints</b> per section
		Elephant's Trunk [37]	1999	Figure 2-3 (b)	3	Mutiple <b>U joints</b> per section + four <b>springs</b> coupled in every segment (8 DoF); diameter/length ration:0.10;
		OC robotics [34]	2007	Figure 2-4 (a)	9	Single <b>U joint</b> per section (22 DoF); diameter/length ration: 0.04;
		OC robotics [70]	2014	Figure 2-4 (b)	9	Single <b>U joint</b> per section (24 DoF); diameter/length ration: 0.05;
		Snake-Arm Robot [73]	2012	Figure 2-5(c)	3	Mutiple <b>S joints</b> per section + <b>rubber dick</b> located between two adjacent disks (6 DoF); diameter/length ration: 0.11;
		CT ARM-I [59]	1992	Figure 2-6(a)	4	Single <b>R joint</b> per section (11 DoF);
		A stiffness-adjustable hyper redundant manipulator [76]	2014	Figure 2-6 (b)	3	Mutiple <b>R joints</b> per section + <b>Teflon flexure</b> intergrated between two adjacnt joints (4 DoF)
		Steering mechanism [77]	2000	Figure 2-6 (c)	4	Mutiple <b>R joints</b> per section + two <b>super elastic NiTi rod</b> intergrated along the backbone (2 DoF); diameter/length ration: 0.16;

		HARP [79]	2006	Figure 2-7	5	<b>two concentric continuums construction</b> which can generate Arbitrary curvature (3 DoF); diameter/length ration: 0.03;
		Single Motor Driven Hyper-Redundant Manipulator [81]	2003	Figure 2-8	3	20 DoF driven by <b>single motor</b> ; diameter/length ration: 0.11;
Intrinsic actuation		i-Snake [84]	2010	Figure 2-9 (a)	5	<b>Serial</b> configuration: <b>Micro motor</b> coupled in every articulated link (5 DoF); diameter/length ration: 0.03;
		The JPL Serpentine Robot [85]	1995	Figure 2-9 (d)	3	<b>Serial</b> configuration: 2-DoF joint actuated by <b>miniature motors</b> located in the arm (12 DoF); diameter/length ration: 0.04;
		Medusa [86]	2006	Figure 2-9 (e)	3	<b>Serial</b> configuration: a spatial hyper-redundant robot constructed by four 3-DoF joints ( <b>miniature motor</b> intergrated in the arm; 12 DoF); diameter/length ration: 0.06;
		a novel hyper redundant robot arm [91]	2012	Figure 2-10 (a)	4	<b>Parallel</b> configuration: a chain of mutiple 3-RSR mechanism connected in series (motor; 15 DoF)
		TAK [94]	2013	Figure 2-10 (c)	4	<b>Parallel</b> configuration: a serial chain of parallel section driven by <b>pneumatic actuators</b> (12 DoF)

		MINIR [97]	2011	Figure 2-11 (a)	3	<b>Serial</b> configuration: 6 DoF continuum robot actuated by the bend force of pairs of antagonistic <b>pre-bent SMA wires</b> ; diameter/length ratio: 0.13;
		BRAID [126]	2001	Figure 2-11 (b)	3	<b>Parallel</b> configuration: a serial chain of parallel section driven by the contraction force of SMA wires when heated
		A steerable cannula [99]	2012	Figure 2-11 (c)	3	<b>Serial</b> configuration: 2-DoF cannula actuated by the bend force of two antagonistic pre-bent SMA wires
<b>Flexible backbone continuum robot</b>	Extrinsic actuation	a curvilinear continuum robot [106]	1983	Figure 2-12 (a)	3	<b>Spring-based backbone</b>
		Elephant trunk type elastic manipulator [107]	1999	Figure 2-12 (b)	3	<b>Spring-based backbone</b>
		Flexible surgical continuum robot [127]	2004	Figure 2-13(a)	5	One main <b>NiTi rod</b> as backbone; another three NiTi rods /section for transmitting the actuation power; diameter/length ratio: 0.15;
		The Clemson tentacle manipulator [109]	2002	Figure 2-13(b)	4	One main <b>spring steel rod</b> as backbone; three cables/section for transmitting the actuation power;

		Bionic Tripod 3.0 [111]	2011	Figure 2-13(c)	4	Four <b>spring steel rods</b> as backbones
		Concentric pre-curved tube robot [113]	2006	Figure 2-14	5	three <b>concentric pre-curved NiTi tubes</b> ; the shape of each section is dominated by those sections retracted inside it
	Intrinsic actuation	Octarm [128]	2005	Figure 2-16(a) & (b)	4	Three independent <b>pneumatic</b> actuators per section for controlling the length and orientation of the system; diameter/length ration: 0.16;
		FESTO elephant trunk [122]	2010	Figure 2-16 (c)	7	The same as Octarm; diameter/length ration: 0.33;
		Instrument for keyhole surgery actuated by McKibben actuators [124]	2011	Figure 2-16 (d)	3	The same as Octarm;
		MALICA [129]	2004	Figure 2-16 (e)	3	The same as Octarm; diameter/length ration: 0.25;

\*The TRL level presented in this table represents Author's opinion;

### 2.4.2. Kinematics of continuum robots

Kinematics studies the relation between geometry and movement of multi-degree of freedom kinematic chains that form the structure of robotic systems. The purpose of forward kinematics (FK) analysis is to calculate the configuration (i.e. position and orientation) of robot TCP with given actuation displacements (e.g. radial displacement of motor and linear displacement of linear actuator). In comparison, inverse kinematics (IK) determines the actuation displacements for a known position of robot TCP.

In order to precisely control a multi-section continuum robot to reach a desired position, two levels of IK are needed in general. The first is from task space to configuration space of each independent articulated unit, which calculates the shape and orientation of each section with the given TCP position [130, 131]. The second is from this configuration space to joint/actuation space, which computes the actuation displacements (e.g. lengths of cable, flexible rods or pneumatic actuations) for each section to reach the desired configurations [62, 65, 66, 108, 132]. In contrast, regarding forwards kinematics (FK), the TCP position of continuum robot can be obtained from configuration space of each section, which is determined by the displacement of actuations.

#### 1) Forward kinematics

In the previous works [65, 133], constant curvature of single bending section is the most fundamental assumption for the kinematics analysis. Based on this assumption, two most widely exploited approaches of forwards kinematics are expressed in this sub-section.

##### A) Denavit–Hartenberg Approach

In this approach, D-H model is built by utilising ‘virtual rigid link’ connected three joints (universal joint, prismatic joint and universal joint) to describe the curve [62,

134]. As shown in Figure 2-17(a), the transformation from one end of the curve to the other can be divided into four steps: first, rotate the bending plane to the desired direction (from coordinate 0 to 1); then, the vector tangent to the curve at the end is rotated to orientate to the tip of the curve (point  $O'$ ) by a virtual revolute joint (from coordinate 1 to 2); next the vector is translated to the tip by a virtual prismatic joint (from coordinate 2 to 3); finally, the vector is rotated to be normal to the tip plane of the curve by another virtual revolute joint (from coordinate 3 to 4).

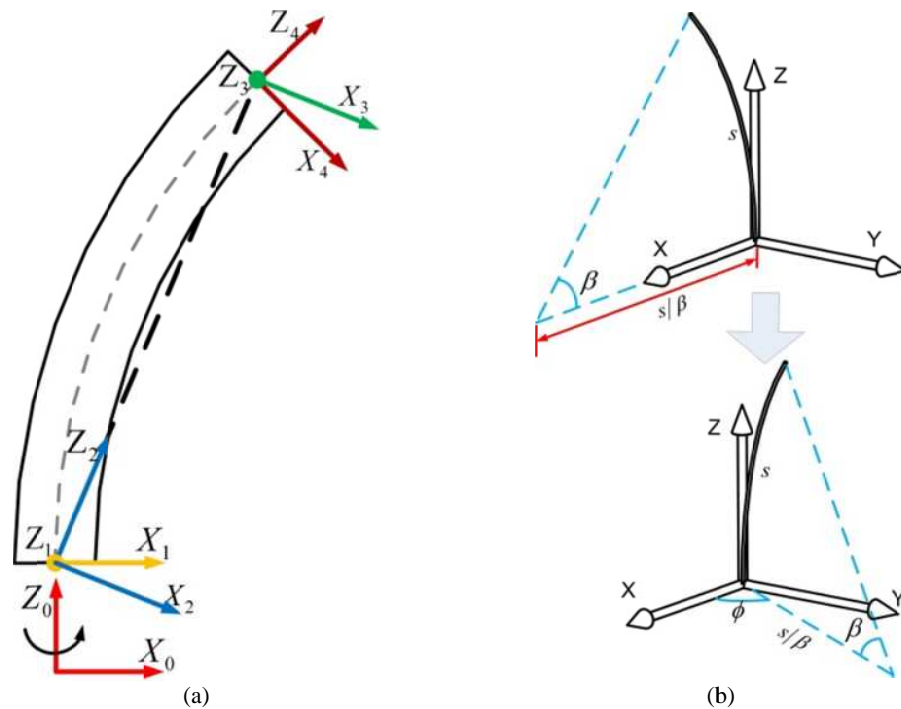


Figure 2-17 (a) D-H coordinates for single section curve (b) geometry approach for the single section kinematics

Let the length of a section (the curve) be  $S$ . Bending and direction angles are denoted as  $\beta$  and  $\phi$ , respectively. Hence, D-H parameters of a single section are given in Table 2-3, which can be written in terms of  $S$ ,  $\beta$  and  $\phi$ .

Table 2-3. D-H parameters table for single section of a continuum robot

Link	$\theta$	$d$	$r$	$\alpha$
1	$\phi$	0	0	$\pi/2$
2	$-\beta/2$	0	0	$-\pi/2$

3	0	$2 \cdot S/\beta \cdot \sin(\beta/2)$	0	$\pi/2$
4	$-\beta/2$	0	0	$-\pi/2$

Further, according to D-H parameters, the transformation matrix for single section can be obtained in Eq.2.1 [135].

$$T = \begin{bmatrix} \cos(\phi)\cos(\beta) & -\sin(\phi) & \cos(\phi)\sin(\beta) & \frac{S \cdot \cos(\phi) \cdot (1 - \cos(\beta))}{\beta} \\ \sin(\phi)\cos(\beta) & \cos(\phi) & \sin(\phi)\sin(\beta) & \frac{S \cdot \sin(\phi) \cdot (1 - \cos(\beta))}{\beta} \\ -\sin(\beta) & 0 & \cos(\beta) & \frac{s \cdot \sin(\beta)}{\beta} \\ 0 & 0 & 0 & 1 \end{bmatrix} \quad (2.1)$$

This approach is first presented in [62], and utilised in the following researches [64, 67, 134].

#### B) Geometry approach

Comparing with the D-H approach, the geometry approach is more direct to describe a single section movement. It can be considered as rotating point  $O$  at bending angle  $\beta$  about vector  $v (S/\beta, 0, 0)$  in plane  $XOZ$ , thus the trajectory of the point is a curve of the section; then rotating the curve at direction angle  $\phi$  about  $Z$ -axis, as shown in Figure 2-17(b). Hence, the orientation and position of the tip of the section can be derived as:

$$T = \begin{bmatrix} R_z(\phi) & 0 \\ 0 & 1 \end{bmatrix} \begin{bmatrix} R_y(\beta) & p \\ 0 & 1 \end{bmatrix} \quad (2.2)$$

Where  $p = [\frac{S}{\beta}(1 - \cos(\beta)), 0, \frac{S}{\beta}\sin(\beta)]$ ;  $R_y(\beta)$  is the rotation matrix with respect to vector  $v (S/\beta, 0, 0)$ ;  $R_z(\phi)$  is the rotation matrix with respect to  $Z$  axis.

Finally, substituting the details into Eq. 2.2 gives the same result with Eq.2.1. This approach is also widely used in the previous works [133, 136, 137].

In spite of these two main approaches, there are several other methods, such as Frenet-serret frames (differential geometry) [67] and integral representation [131], developed for FK, which can obtain the same results with the aforementioned approaches. However, comparing with DH and geometry approaches, these two methods are more complex and hard to understand.

## 2) Inverse kinematics

Since variable actuation approaches were utilised for articulating continuum robots, an approach of IK for each specific type of actuation was developed. Cable and continuously bending actuations (e.g. flexible rods and pneumatic actuators) are two of the most widely used actuation approaches, thus, inverse kinematics for these two types of actuations are discussed in detail in the following chapter. Here, the first level of IK for continuum robots is not discussed in detail, since it is not in the scope of this thesis; while the second level of IK (from configure space to actuation space) is discussed.

### A) *Inverse kinematics for cable actuations*

As discussed in previous part of this chapter (2.4.1 design of continuum robot), three or four cables are generally utilised for articulating a single section, which are equally spaced about the central longitudinal axis. In most of the previous works [134, 135], the following procedure was employed to derivate IK:

- Project the cables to the bending plane of the section;
- Calculate the cable lengths on the bending plane according to the configuration parameters (e.g. bending and direction angle, section length and diameter);

Here, a simplified derivation of inverse kinematics for three-cable driven continuum robots is presented as an example (Figure 2-18(a)). Specifically, section length and PCD of cable-guide holes are  $S$  and  $d$ , respectively. Let bending and direction angles

be  $\beta$  and  $\phi$ , respectively. The centre of the base plane is attached to the origin of coordinate  $XYZ$ . Cable one is on axis  $X$  and all of three cables are equally spaced by  $120^\circ$  axially.

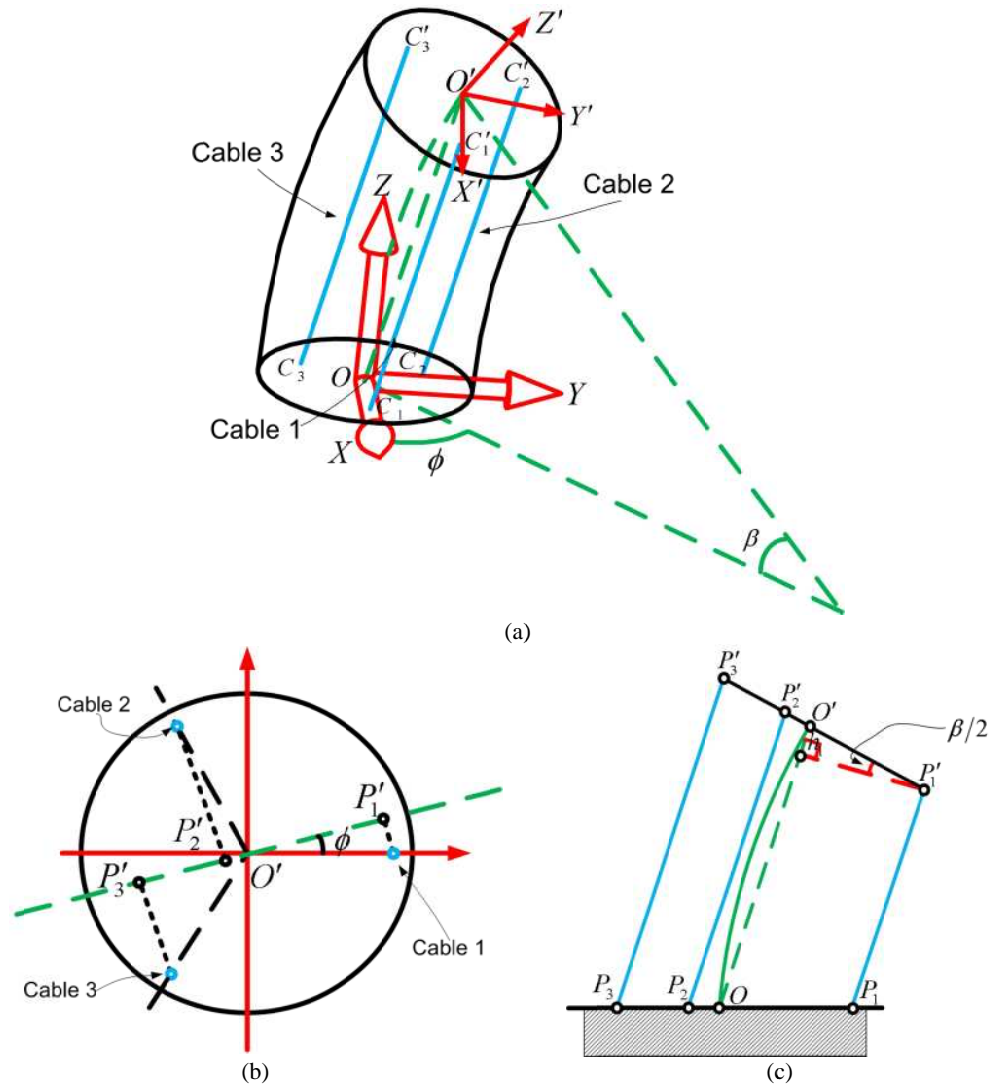


Figure 2-18 Schematic of conventional kinematic model (a) a three-cable driven section model; (b) top view of the tip plane; (c) side view of the bending plane

Since point  $O$  and  $O'$  are located at the centres of the base and tip planes, respectively,

the magnitude of vector  $\vec{OO'}$  can be described as:

$$\left| \vec{OO'} \right| = 2 \cdot \frac{S}{\beta} \cdot \sin\left(\frac{\beta}{2}\right) \quad (2.3)$$

As shown in Figure 2-18(b), the magnitudes of vectors  $\vec{O'P'_1}$ ,  $\vec{O'P'_2}$  and  $\vec{O'P'_3}$  can be obtained as, which are the projections of vectors  $\vec{O'C'_1}$ ,  $\vec{O'C'_2}$  and  $\vec{O'C'_3}$  on vector  $\vec{OO'}$  :

$$\begin{cases} \left| \vec{O'P'_1} \right| = \frac{d}{2} \cdot \cos(\phi) \\ \left| \vec{O'P'_2} \right| = \frac{d}{2} \cdot \cos\left(\frac{\pi}{3} + \phi\right) \\ \left| \vec{O'P'_3} \right| = \frac{d}{2} \cdot \cos\left(\frac{\pi}{3} - \phi\right) \end{cases} \quad (2.4)$$

As shown in Figure 2-18(c), the projection of vector  $\vec{O'P'_1}$  on vector  $\vec{OO'}$ ,  $h_1$ , can be expressed as:

$$h_1 = \left| \vec{O'P'_1} \right| \cdot \sin\left(\frac{\beta}{2}\right) \quad (2.5)$$

Hence, the length of cable 1,  $l_1$ , can be written as:

$$l_1 = \left| \vec{OO'} \right| - \left| \vec{O'P'_1} \right| \cdot \sin\left(\frac{\beta}{2}\right) \quad (2.6)$$

Likewise, the lengths of the other two cables, cable 2 and 3, can be obtained as:

$$\begin{cases} l_2 = \left| \vec{OO'} \right| + \left| \vec{O'P'_2} \right| \cdot \sin\left(\frac{\beta}{2}\right) \\ l_3 = \left| \vec{OO'} \right| + \left| \vec{O'P'_3} \right| \cdot \sin\left(\frac{\beta}{2}\right) \end{cases} \quad (2.7)$$

Therefore, IK for a three-cable section of a continuum robot is derived. The kinematics for four-cable section can be considered in a very similar procedure to the derivation above.

### B) Inverse kinematics for continuously bending actuators

Another widely utilised continuum robot actuation is composed of actuators which can be bent continuously, e.g. flexible rods and pneumatic actuator. The only difference between these two types of actuators is that the cable is straight, while the

continuously bending actuators are curved. It features a slightly different kinematics solution, which can be derived in the same procedure, as shown in Figure 2-19.

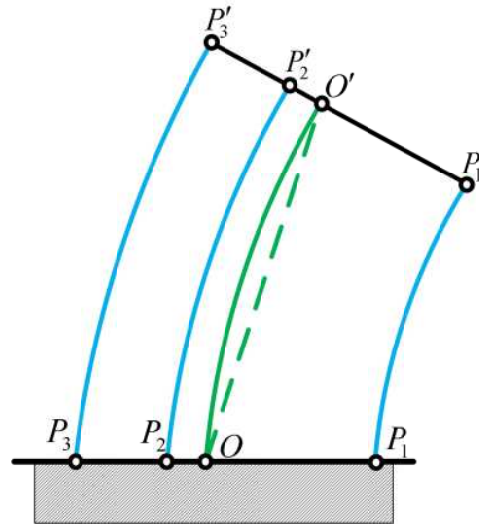


Figure 2-19 Side view of the bending plane of a three-continuously bending actuator section

Hence, the lengths of cable 1, 2 and 3 can be expressed as:

$$\begin{cases} l_1 = \left( \frac{S}{\beta} - \left| \vec{O'P'_1} \right| \right) \cdot \beta \\ l_2 = \left( \frac{S}{\beta} - \left| \vec{O'P'_2} \right| \right) \cdot \beta \\ l_3 = \left( \frac{S}{\beta} - \left| \vec{O'P'_3} \right| \right) \cdot \beta \end{cases} \quad (2.8)$$

In summary, the assumption of constant curvature of single bending section is applied for both forward and inverse kinematics for most of the methods. Based on this assumption, kinematics of continuum robots can be divided into two levels, i.e. one is the mapping between task and configuration spaces; the other is between configuration and actuation spaces. For FK, Denavit-Hartenberg and geometry approaches are utilised by majority of the previous works. Further, some other methods, e.g. Frenet-serret frames and integral representation were also employed in the previous researches for calculating FK of continuum robots. Regarding IK, the actuations are projected on the bending plane to simplifying the 3D problem to a 2D one, which makes the derivation very easy and the solution very straightforward. This

approach can be applied on most of cases, e.g. cable actuations and continuous bending actuations. Apart from these methods, concentric continuum robot has its own for calculating its FK and IK. However, since it can just be utilised to this particular design, it is not discussed in detail.

### 3) Jacobian

Jacobian is important and heavily used throughout robotics and control theory. Jacobian matrix can be calculated by differentiating with respect to time of the forward position kinematics equations:

$$v_N = J \dot{q} \quad (2.9)$$

Where  $v_N$  is the spatial velocity of the end-effector;  $\dot{q}$  is an N-dimensional vector composed of the joint velocity.

According to the Jacobian matrix, the velocity of the continuum arm can be obtained and the force/torques applied on the robot joint (actuators) can be described by:

$$\tau = J^T f \quad (2.10)$$

Where  $f$  is the force and torques acting on the end-effector.

Kinematics of continuum robots are divided into two levels. One is studying the relation from task space to configuration space of each independent articulated unit, which calculates the shape and orientation of each section with the given TCP position; the other one is from this configuration space to joint/actuation space, which computes the actuation displacements for each section to reach the desired configurations. Therefore, the research of continuum robot Jacobian has also been studied in these two levels.

With regard to the first level kinematics, the end-effector configuration can be obtained by the positions and orientations of all the section:

$$T_p = T_1 T_2 T_3 \cdots T_n \quad (2.11)$$

Where  $T_p$  is the orientation and position matrix of the end-effector;  $T_i$  ( $i=1, 2, \dots, n$ ;  $n$  is the number of section) is the orientation and position matrix of each section. Therefore, the Jacobian can be described by differentiating both sides of the previous equation. By utilising the first level of Jacobian, the end-effector velocity can be obtained, based on the given bending and direction velocities of sections [138].

Since the second level kinematics describes the relation from configuration space to actuation space, the Jacobian can be calculated by differentiating the section position matrix (e.g. **Eq. 2.6** and **2.7**), which is in terms of cable lengths  $l_1, l_2, l_3$  and section parameters ( $S, r$ ) [134, 139]. According to the second level of Jacobian, the section velocity can be described by given actuation velocity (e.g. speed of linear actuator, velocity of pneumatics actuator).

Therefore, the Jacobian of continuum robot has been obtained.

## 2.5. Review of adjustable stiffness systems for continuum robots

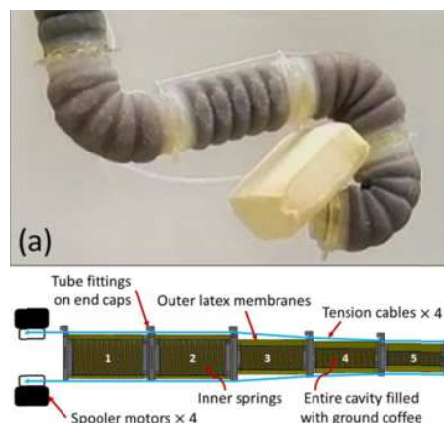
Continuum robots have been investigated by many researchers for industrial [69, 70, 140], medical [32, 141], and security applications [86-88], due to their unique features and advantages: high flexibility, high dexterity, obstacle-avoidance capability and so on. However, compared with rigid link robots, the main drawback of continuum robots is low stiffness, which limits the capability for carrying efficient end load/force. In order to overcome this drawback, some solutions for enabling the backbone have adjustable stiffness been developed, which allowing continuum robots move freely when in a relatively low stiffness state and lock the arm when in a relatively high stiffness state.

Firstly, the research started to make use of the phase-change material to obtain variable backbone stiffness property. One widely utilised approach is to use granular material, such as dry sand, to lock/unlock the backbone mechanism by applying

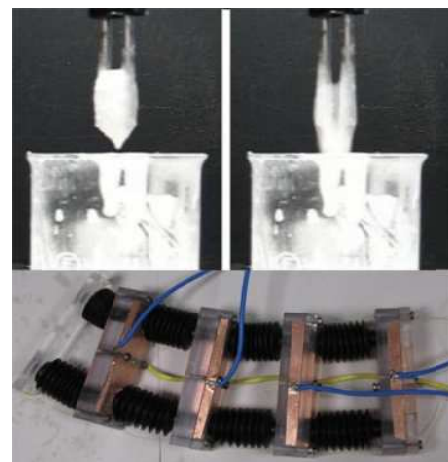
negative pressure [142-144]. In particular, ground coffee was deployed to fill the inside space of spring-based backbone. By applying a vacuum to squeeze grains via the chamber, the grains switch from liquid-like state to solid-like state, which makes the backbone has controllable backbone stiffness (Figure 2-20 (a)). However, this approach requires a relatively large volume for reaching an appropriate stiffness, making it difficult to be miniature.

Further, Electro-rheological (ER) fluids were exploited for novel variable stiffness worm robot (Figure 2-20 (b)). By applying an electric field, ER fluids can transform into ‘gel’ phase from the liquid-like one. Based on this concept, each section of worm robot can be blocked at an arbitrary configuration when a voltage applied. However, the drawback of this concept is that high voltage (500V) and large volume of ER fluids need to be applied for blocking a large scale construction [145].

Figure 2-20 (c) illustrates a more efficient approach, based on the phase-change material. In the worm robot, solder-alloy mixture is integrated into joint mechanism, which can be thermally activated to selectively “lock” or “unlock” the joint, thereby modulating the overall robot stiffness [146-148].



(a)



(b)

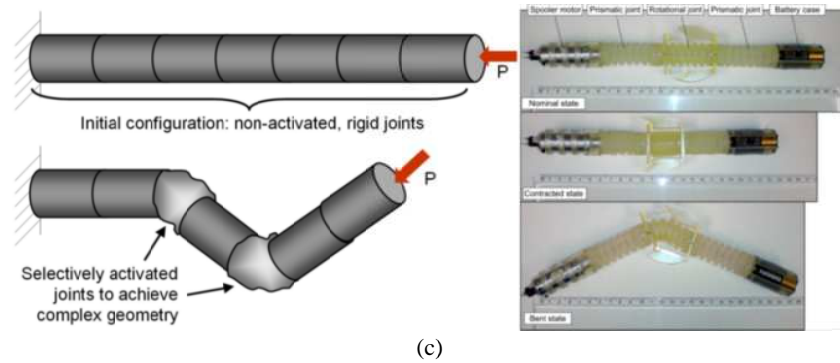
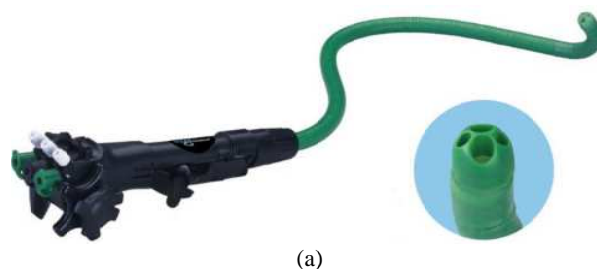


Figure 2-20 Adjustable stiffness solutions based on phase-change material: (a) jamming of granular media [143]; (b) innovative soft robots based on electro-rheological fluids [145]; (c) thermally activated joint (solder-based locking mechanism) [147];

Apart from phase-change material concepts, the other main approach is to control the friction between rigid links for varying stiffness [149]. As shown in Figure 2-21(a) & (b), the friction is controlled by adjusting wire tension, so the mechanisms can switch between rigid and flexible modes rapidly. But due to the fact that the stiffness is depended on the friction which is determined by the size of the contact area between the adjacent links, thus, the links must be large enough to sustain the load and generate enough friction to lock the system. Hence, it is difficult to create a long and compact manipulator based on this approach.

More recently, a novel approach is presented which utilise “layer jamming” mechanism to obtain variable stiffness [150]. Figure 2-21(c) illustrates the backbone of a “layer jamming” continuum robot consisting of multiple coupled rubber layers, which is wrapped by latex rubber skin. The friction between layers can be enhanced significantly by applying vacuum pressure, so it renders the backbone become rigid. But the mechanism still needs a large contacting area between layers for generating appropriate friction to interlock the elements of the backbone.



(a)

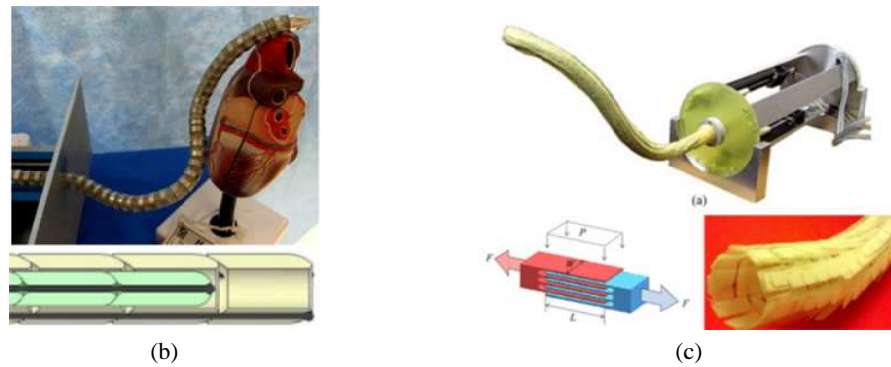


Figure 2-21 Various Stiffness mechanisms (a) Retroflex [149]; (b) HARP [33]; (c) lawyer jamming mechanism (negative air pressure) [150];

Another mechanical ‘rigidizing’ solution is to employ interlocking mechanism, which can generate greater ‘locking’ force. Figure 2-22 illustrates the construction details of two designs. Both of them utilised a toothed link to lock the mechanism, which can be controlled to engage/disengage pneumatically.

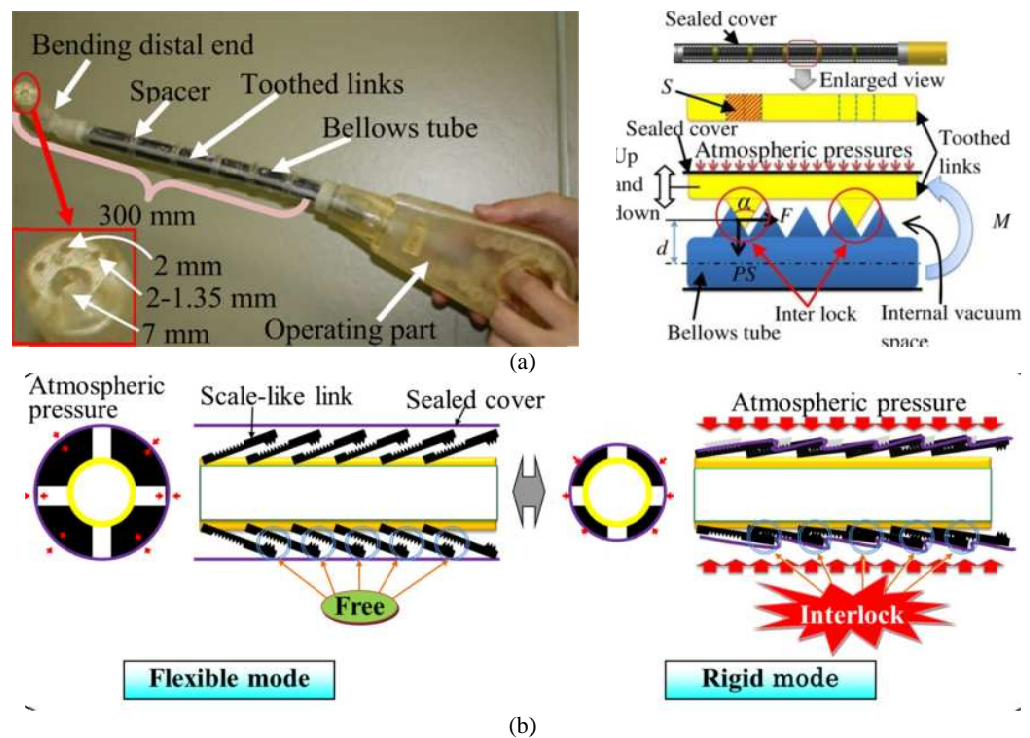


Figure 2-22 Rigidizing solution based on mechanical interlocking mechanism (a) prototype A [151, 152]; (b) prototype B [153, 154];

In summary, several efficient solutions have been developed, which can be divided into two main categories:

- Phase-changing materials: granular material, Electro-rheological (ER) fluids and thermally activated material (e.g. solder-alloy mixture)
- Mechanical approaches: pneumatic and mechanical locking mechanism (e.g. cable locking and toothed link mechanisms).

However, it seems most of them require a relatively large volume for generating enough stiffness, making it difficult to miniature. Among these solutions, the approach of thermally activated material seems more promising, since it can provide a better stiffness when it gets cold, allowing to build an adjustable stiffness at a reducing dimension. However, it needs to identify a lightweight material which can switch between rigid and soft states at a low temperature (between 40° and 100°). And the material needs to provide efficient stiffness in rigid state and be really flexible in the soft state.

## **2.6. Opportunities for Future Research**

During the last thirty years, the researches made a significant contribution on the development of continuum robots in design, kinematics, and application. However, comparing with conventional rigid link robots, there are still some challenges needs to be addressed, which are discussed in the following part of this chapter.

### ***1) Design of continuum robots***

As we discussed in Chapter 2.4.1, variable continuum robot designs have been seen from the previous works. All the designs can be divided into two main categories, i.e. rigid and flexible backbones. It can be found that most of large scale continuum robots employed rigid backbone (single rigid link/section) as supporting construction, since its good stiffness and accuracy. However, this construction limits the flexibility and accessibility of the arm, making it difficult to be employed for highly constrained environments, e.g. gas turbine engine. A solution, which integrates elastic material into the joint mechanism in order to passively reducing DoFs of a single section to two, was developed to enable more joints to be coupled in single section, making each

section more flexible and have better accessibility. However, most of small scale ones developed in last decade generally takes flexible backbone, especially elastic rod and pneumatics actuator, as support construction, which is very promising for working in a confined space, since flexible constructions can bring many advantages as better accessibility and safer human-robot interaction and so on. But comparing with rigid backbone continuum robot, it has less stiffness, limiting it to be utilized for building a long slender continuum robot (the max length of the existing flexible backbone continuum robot with efficiently accuracy is 1.1meter, but the diameter is larger than 300mm [122]).

In summary, there are some challenges still remaining:

- A solution for constructing a long flexible backbone continuum robot with a reduced diameter, an appropriate stiffness and end load carrying capability needs to be found, which requires the design have the advantages of rigid and flexible backbone designs simultaneously.
- A relatively large amount of force needs to be acted on the backbone for carrying an appropriate weight of end load, which brings the challenges of avoiding buckling of flexible backbone and requires enhancing the joint stiffness.

## ***2) Design of an adjustable stiffness system***

Comparing with conventional rigid link robots, continuum robots generally have better flexibilities as an advantage for accessing a crowded space, but less stiffness as a drawback for carrying appropriate end load and control accuracy. Therefore, several adjustable stiffness methods were considered for enabling continuum robots have a relatively high stiffness for taking reaction force/torque and a relatively low stiffness when moving.

The approaches can generally be classified into two broad groups, i.e. phase-change material and mechanical locking mechanism. Among these solutions, the approach of

phase-change material seems more promising, since more stiffness can be provided with a relatively small volume. However, the following research gaps need to be filled:

- A lightweight material which can switch between rigid and soft states at a low temperature (between 40° and 100°) needs to be identified, so it requires less power for melting the material and allows the melt material get rigid above the room temperature;
- A material needs to provide efficient stiffness in rigid state and be really flexible in soft state, so it does not require a large actuation force to articulate continuum robots in the low stiffness state.

### 3) *Modelling*

The kinematics of continuum robots (forward and inverse kinematics) has been quite well developed since numerous approaches were presented in this field. However, the following challenges are remaining:

- New kinematics model maybe needs to be developed for new designs. Further, since continuum robot is generally constructed with multiple sections, it requires the kinematics model for a new construction to be simple and precise, in order to reduce the computing time to enable real-time control for a hyper redundant robot;
- Since the actuation transmission mechanism of distal sections, e.g. cable or elastic rods, influences the shapes of the proximal ones, it requires to be considered in kinematics model.
- The models considering external effects on the kinematics, such as gravity and end load, have been built. But it includes additional complex computation, so it also needs some simple models for simplifying the calculation.

Further, dynamic modelling is also a very active research area. Various methods of dynamics have been developed [110, 155, 156] . However, most of the researches require complex computation. In the future, they need to be more efficient and stable

for real-time application. In summary, each of the aforementioned factors is offering an opportunity for the new researching areas.

---

## **Chapter 3 Innovative concepts of continuum robot design**

Continuum robots have been demonstrated in several critical areas, like minimally invasive surgery [32, 113] and security [140], and also show the capability for the potential application in industry, such as aerospace assembly [69] and inspection/repair in power station [57]. However, there are some disadvantages of the existing designs limiting continuum robots to be utilised in more applications. In this chapter, the drawbacks of the existing continuum robot systems are summarized and presented. Further, regarding the disadvantages, several new concepts of continuum robot designs are introduced.

### **3.1. Disadvantages and challenges of the existing continuum robot designs**

In general, continuum robots consist of backbone (rigid backbone: support the structure; flexible backbone: enable the bending movement and support the structure), rigid universal or spherical joints (utilized to allow the bending movement), cables (to actuate the construction) and disks (to constrain the cables). The critical parameters of continuum robot design are diameter/length ratio, flexibility, stiffness and actuation approach, which are discussed in the following part of this chapter. Further, the kinematics challenge of continuum robots with single central located flexible backbone is presented in this chapter.

#### **3.1.1. Flexibility and stiffness**

The flexibility determines the obstacle avoidance capability of continuum robots. For rigid backbone continuum robots, the flexibility is determined by the number of joints (universal or spherical joints) in a single section. Due to the degrees of freedom (DoF) of a single section (2 DoF), rigid backbone continuum robots can only employ one universal joint (2 DoF) in single section [69, 70], as shown in Figure 3-1 (a). The solution for employing multiple rigid joints in single section is to utilize springs or

other elastic material (Teflon flexure/rubber) to make all these joints have the same stiffness so that the section can be bent evenly [37] (it can be also understood as the springs passively reduce hyper-DoFs of a section to two, so two actuators can operate it), as shown in Figure 3-1(b); nevertheless, these designs cause the continuum robot to be bulky / low stiffness, which makes it difficult to access confined places / carry appropriate weight end effectors. For flexible backbone robots, due to the elastic property, the whole backbone performs as an elastic universal joint, resulting in continuous bending of a single section. Therefore, it allows continuum robots to be designed light-weight and small size, Figure 3-1 (c), thus having great obstacle avoidance capability in cluttered environment [32]. However, the long flexible backbone leads to low stiffness and hence, low position accuracy. Hence, it requires a solution able to enhance the stiffness, meanwhile provides an appropriate flexibility.

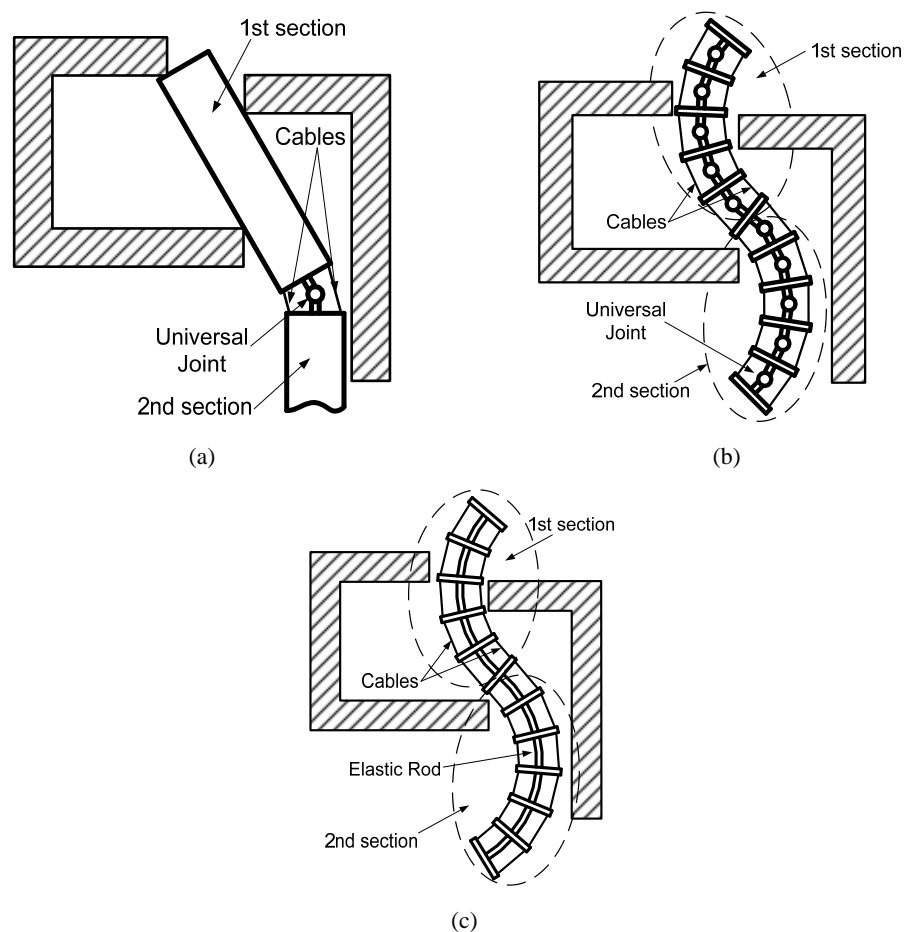


Figure 3-1. Accessibilities of different continuum robots (a) single universal joint model (b) multi universal joints model (c) flexible backbone model

### 3.1.2. Twist problem

Compared with rigid backbone continuum robot, flexible backbone design has good flexibility making them more suitable for operating in tight environments. However, it was found from the follow-up experiments that the flexible backbone is twisted along its length due to the torque generated by the weight of the system and end load, as shown in Figure 3-2. Only the bend movement about Y and Z axes (2 DoF), as shown in Figure 3-2, can be controlled by the actuations in single section, as a result, the twist angle about X axis cannot be controlled, which makes difficult in kinematic modeling and control.

The twisting angle of segment backbone (without cables constraint) can be expressed as:

$$\phi = \frac{TL}{GI_x} \quad (3.1)$$

Where T is the twisting torque; L is the length of the flexible backbone;  $I_x$  is the moment of inertia; G is the shear modulus of elasticity, which can be written as  $G = E/2(1+\nu)$ ; E is elastic modulus;  $\nu$  is Poisson's ratio.

For example, assuming the super-elastic NiTi rod (length of a single segment,  $L=15\text{mm}$ ; diameter,  $\Phi=1\text{mm}$ ) on which a torque  $T = 0.1\text{Nm}$  is applied at its end, refer to **Eq. 3.1**, the twisting angle  $\phi = 58.22^\circ$ . (The twisting angles are not constant against different end loads and configurations). Due to the fact that the twisting angle cannot be controlled by actuations, it makes extremely difficult to build kinematics model and control the system. Therefore, the best solution in such instance is to design the backbone which can mechanically minimize the twisting angle.

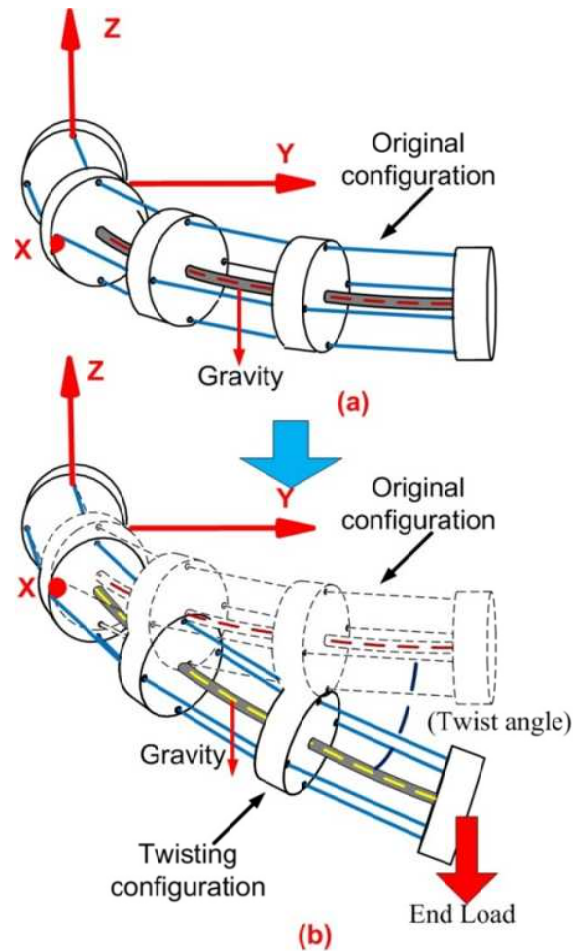


Figure 3-2. Schematic representation of the parasitic twist of continuum robot utilizing a central located flexible backbone design: (a) original configuration (affected by gravity); (b) twisting configuration (affected by gravity + end load)

### 3.1.3. Actuation approach

In terms of actuation, there are two different concepts, one employs three independent cables and actuators for driving a single section, as shown in Figure 3-3 (a), and the other one utilizes two actuators and pairs of cables, as seen in Figure 3-3 (b). The former concept is applied in most of the existing designs of continuum robots, whilst the other designs which applies the latter concept has to employ a pulley system/other tensioning system for compensating the internal tension of the cables, which makes the actuation system complex and bulky.

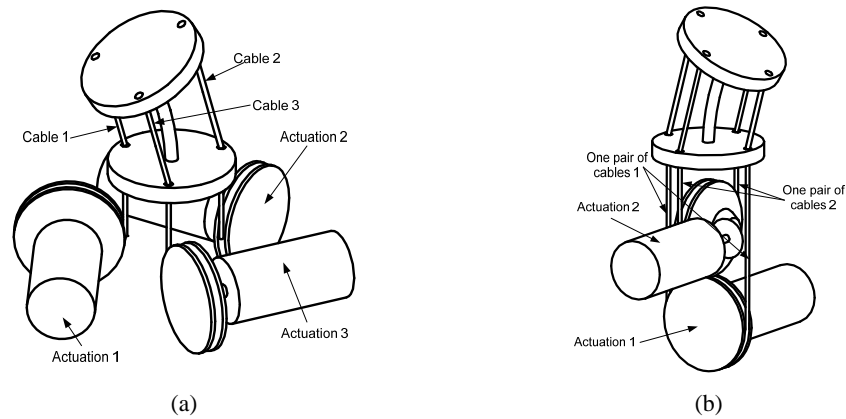


Figure 3-3. Different actuation types of continuum robots: (a) triple actuation (b) double actuation concepts

Although the double actuation design concept (Figure 3-3 (b)) can significantly minimize the weight and size of the actuation packing system, neither flexible backbone (Figure 3-1 (c)) nor rigid universal joint continuum robots (Figure 3-1 (a)&(b)) can apply double actuations for one section directly, due to the kinematics problem caused by the cable tension (Figure 3-4) discussed below.

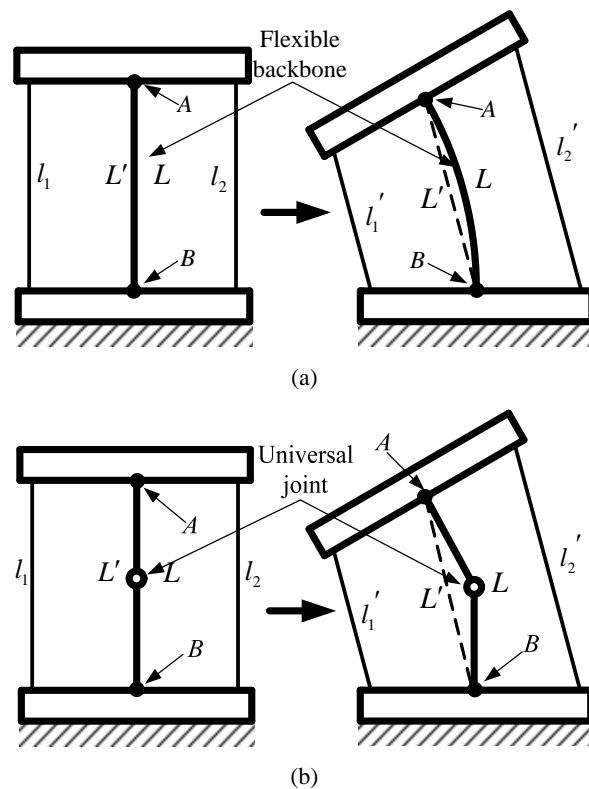


Figure 3-4. Kinematic challenge for two actuations concept: (a) flexible backbone model (b) rigid backbone model

Figure 3-4 (a) shows the kinematic model of one segment of flexible backbone continuum robot. Let  $L$  and  $L'$  be the length of flexible backbone and the distance between points A and B, respectively. Then let  $l_1, l_2$  and  $l'_1, l'_2$  be the cable lengths in different configurations. Hence, an equation can be obtained from initial configuration (the left one of Figure 3-4 (a)) :

$$l_1 + l_2 = 2 \cdot L = 2 \cdot L' \quad (3.2)$$

From the right configuration of Figure 3-4 (a), an equation can be obtained

$$l'_1 + l'_2 = 2 \cdot L' < 2 \cdot L \quad (3.3)$$

According to **Eq. 3.2 and 3.3**, an equation can be obtained

$$l'_1 + l'_2 < l_1 + l_2 \quad (3.4)$$

Based on the **Eq. 3.4**, this pair of cables cannot keep a constant tension when the continuum robot is bent. Similarly with the presented problem, the pair of cables of a rigid backbone continuum robot shown in Figure 3-4 (b) cannot maintain a constant tension either. Therefore, neither the existing rigid backbone concept nor the flexible one can apply this novel actuation concept without other additional systems, such as cable tension compensation system.

#### 3.1.4. Challenge of inverse kinematics

The purpose of inverse kinematics is to determine the displacements of actuation cables for a desired TCP position in order to control the shape of continuum robot. According to the desired position ( $X_p, Y_p$  and  $Z_p$ ), the section's overall bending and directional angles can be expressed in terms of  $X_p, Y_p$  and  $Z_p$  (i.e. bending angle =  $2 \cdot \arctan\left(\sqrt{X_p^2 + Y_p^2} / Z_p\right)$ ; direction angle =  $\arctan(Y_p / X_p)$ ). In the previous work [66, 134], the tip disk orientation angle with respect to the base disk is considered being

equal with the section's overall bending angle. This assumption can simplify the calculation, but brings errors to the position control.

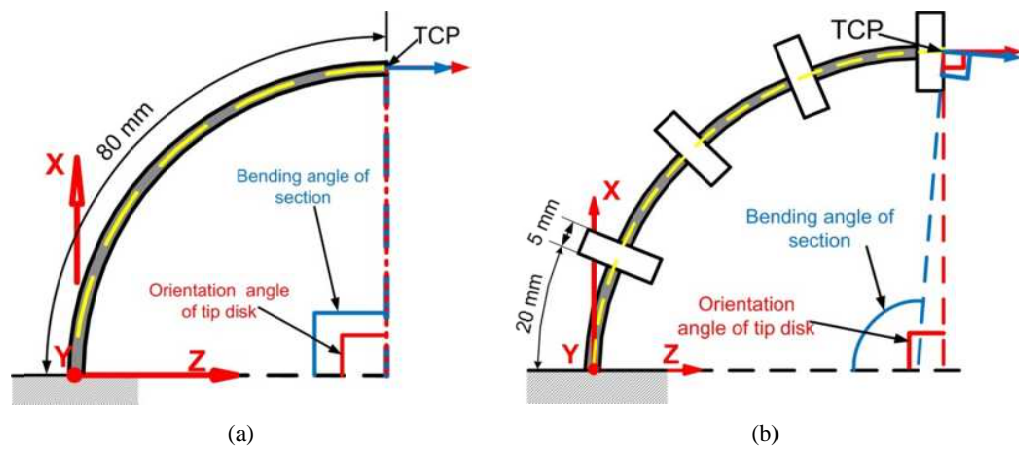


Figure 3-5. Schematic showing the difference between section bending angle and tip disk orientation: (a) continuous backbone without the segmented disks [157] (b) segmented backbone

For example, Figure 3-5 (a) illustrates a fully continuous section and the section's overall bending angle is equal to the tip disk orientation, which is  $90^\circ$ . As shown in Figure 3-5 (b), the section is divided into four pieces and they are connected by 5 mm disks. Now the tip disk orientation is still  $90^\circ$ , but the section's overall bending angle is  $94.5^\circ$ .

Hence, it can be found that, regarding segmented backbone (e.g. flexible segmented backbone/multi universal-joint continuum robot), these two bespoke angles are not equal with each other, as shown in Figure 3-5 (b), unless the thickness of the disk is infinitesimal small. In other words, these two angles of continuum robot are equal, only when the section is entirely continuous (without anything unbendable in a section). Figure 3-6 shows a case study for calculating the angle difference between these two angles in the work volume of a single section.

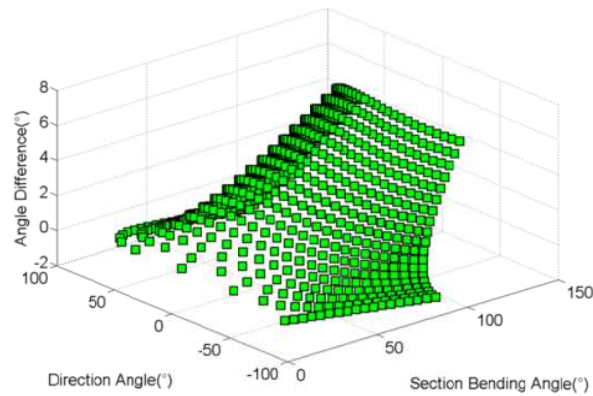


Figure 3-6. A plot of differences between section' overall bending angle and tip disk orientation for a 100mm long section (e.g. as shown in Figure 3-5 (b), flexible backbone length and disk thickness are 20 mm and 5mm, respectively); At  $0^\circ$  section bending, the difference is  $0^\circ$ . And the max angle difference is  $8^\circ$  at section bending angle  $90^\circ$ , direction angle  $0^\circ$ .

Therefore, this simplification causes an error for continuum robot position control, but to date, there is limited information reported on addressing this problem.

### 3.2. Innovative concepts of continuum robot design

As aforementioned, the critical parameters of continuum robot design are diameter/length ratio, flexibility, stiffness and actuation approach. To date, the existing systems can just give consideration to one or two of these factors in their designs simultaneously. Hence, the challenge of the design is to construct a continuum robot that can carry an appropriate payload, while having small diameter/length ratio, great flexibility (bending capability) and a compact actuation system. In this section, several innovative concepts are developed for overcoming the aforementioned disadvantages, which can be classified into two families of robot designs, one is double-pivot compliant joints construction and the other one consists of twin-pivot compliant joints.

#### 3.2.1. Family of concept A: Double-pivot compliant joint construction

Regarding the drawback of the low stiffness and twisting problem of flexible backbone continuum robot, a novel family of double-pivot compliant joint continuum

robots is developed, which can improve stiffness, reduce twisting angles, have an appropriate flexibility and employ two actuations for each section.

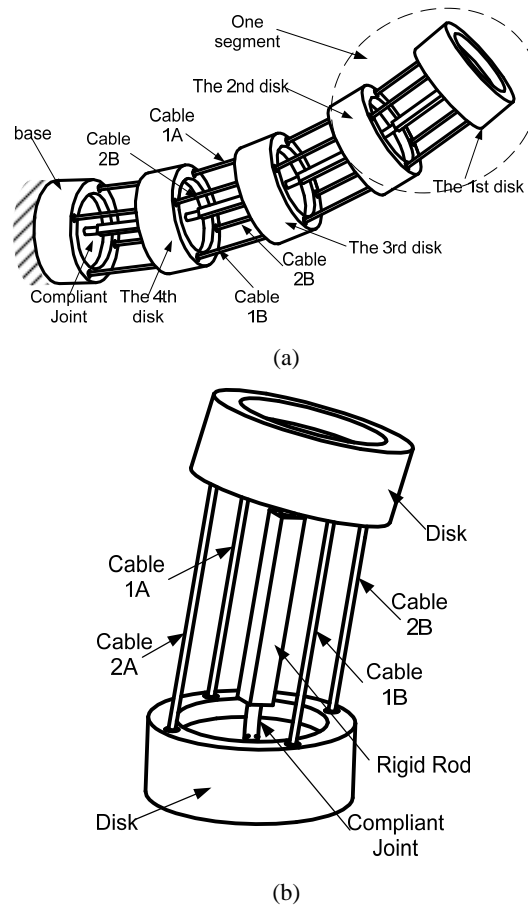


Figure 3-7. Continuum robot construction using two actuations concept: (a) general view; (b) one segment

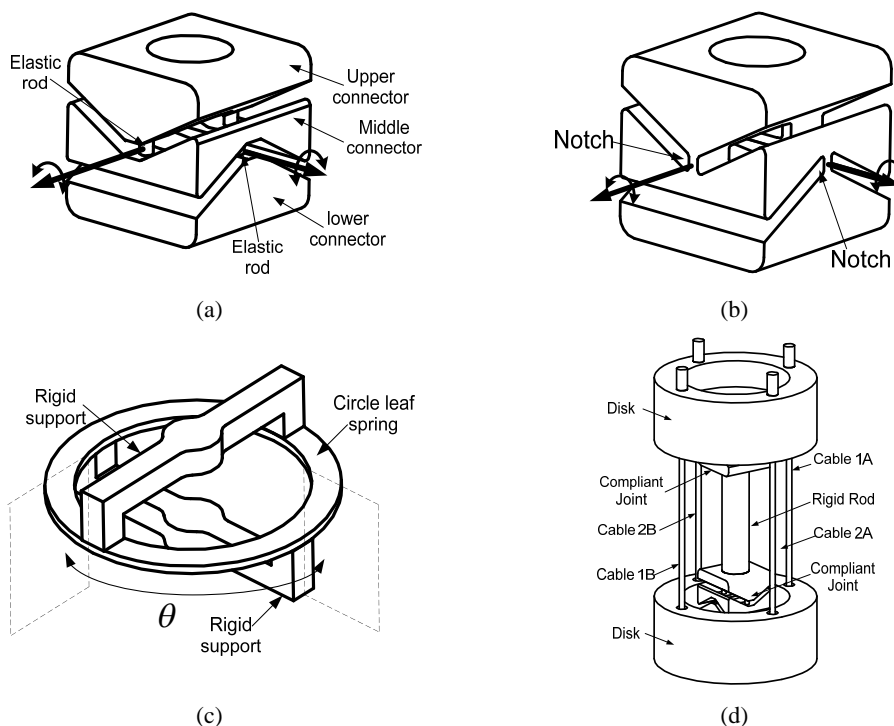
As shown in Figure 3-7 (a), the continuum robot consists of disks, actuation cables, compliant joints and rigid rods/tubes. The disks are connected by compliant joints and rigid rods/tubes; the continuum robot bent is caused by the torque generated through actuation cables.

Figure 3-7 (b) shows the construction of a continuum robot which consists of the following elements:

- **Compliant joint** is made of a material which is flexible and able to be bent with little residual plastic deformation. As shown in Figure 3-7 and Figure 3-8

(a), the compliant joint can be made by a single elastic rod/ tube, e.g. super-elastic Nitinol, or a universal joint construction connected by elastic rods/tubes. This construction makes rotation axes of these two pairs of elastic rods coincide with each other. Therefore, it can perform as a universal joint. Further, the compliant joint also can be a flexible hinge or leaf spring construction, as shown in Figure 3-8 (b) and (c), which can also perform as a universal joint. Figure 3-8 (d), (e) and (f) present several continuum robot designs, which replace single elastic rod with other universal joint designs.

- **Rigid rod/tube** is made of a material that is significantly stiffer than the elastic rod;
- **Disks** are utilized for constraining the cables; Note that pivot point of compliant joint is on the top plane of the disk bulge, as shown in Figure 3-9 (left configuration).
- **Cables** consist of two pairs of cables (1A and 1B; 2A and 2B) each being actuated by a single motor.



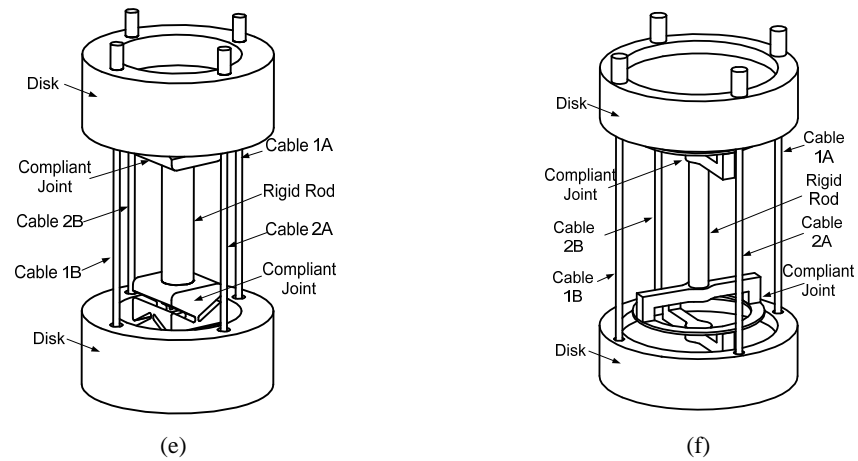


Figure 3-8. Compliant joints: (a) elastic-rod compliant universal joint; (b) notch compliant universal joint ; (c) leaf spring compliant joint; (d) compliant universal joint continuum robot segment; (e) notch compliant universal joint continuum robot segment; (f) leaf spring compliant joint continuum robot segment;

Comparing with flexible backbone continuum robots, compliant joints are much stiffer. Due to the elastic property of compliant joints, the robot can obtain an evenly distributed bending shape, a relatively small size and simple design, which cannot be achieved by multiple rigid universal joints concept. Further, based on the double-pivot compliant joints construction, a twin actuation design can be applied for the continuum robot. And the verification is given below (taking elastic rod concept as an example):

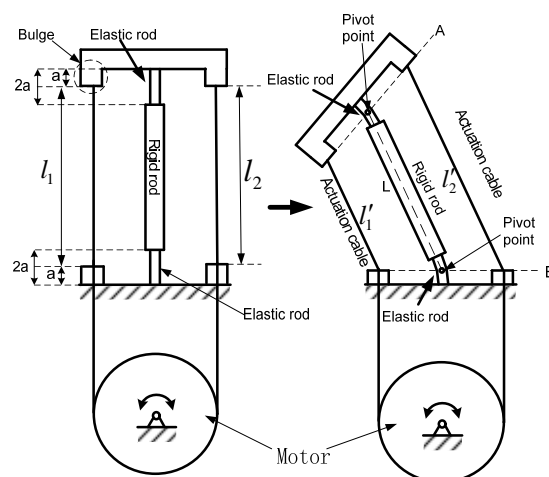


Figure 3-9. Schematic of double-pivot compliant joint construction

Assuming compliant joint performs as a rigid universal joint and the pivot points coincide with the top of bulges (planes A and B – see Figure 3-9), the following identity can be assumed:

$$l'_1 + l'_2 = 2 \cdot L' = 2 \cdot L \quad (3.5)$$

Hence, **Eq. 3.6** can be obtained

$$l'_1 + l'_2 = l_1 + l_2 \quad (3.6)$$

The error caused by this approximation is calculated in the Chapter 4.1. Based on **Eq. 3.6**, one cable pulls a length and the other cable extends the same length, which causes a bending deformation of compliant joints and keeps the pair of cables a constant tension in an arbitrary configuration. Due to this construction, the novel two actuations for one section design concept can be applied to the continuum robot.

Based on this design, a continuum robot can have an appropriate stiffness and reduced twisting angle with a unique twin actuation design, while giving the possibility to be constructed with a small diameter/length ratio and great flexibility so that it can carry an appropriate end load and access confined spaces thus be applicable for a variety of machining tasks, like visual inspection, laser cutting and laser deposition.

### **3.2.2. Family of concept B: Twin-pivot compliant joint construction**

For enhancing the stiffness and minimizing the twisting problem, another novel family of twin-pivot compliant joint continuum robots is developed, which also provides an appropriate flexibility and employs double actuations for each section.

As shown in Figure 3-10 (a), the continuum robot consists of disks, actuation cables and twin-pivot compliant joints. The disks are connected by compliant joints; a bend is caused by the torque generated through actuation cables. Figure 3-10 (b) and (c) show twin-pivot compliant joint construction of a continuum robot which consists of the following elements:

- **Compliant Joint (rod/tube/sheet)** is made of a material which is flexible and able to be bent with little residual plastic deformation (e.g. super-elastic Nitinol). As shown in Figure 3-10 (b), two rods/tubes are located in plane A-A; and the other two are located in plane B-B. The angle  $\theta$  is 90 degrees. So arbitrary direction (two DoF) bend can be generated.
- **Disks** are utilized for constraining the cables;
- **Cables** consist of two pairs of cables, each being actuated by a single motor.

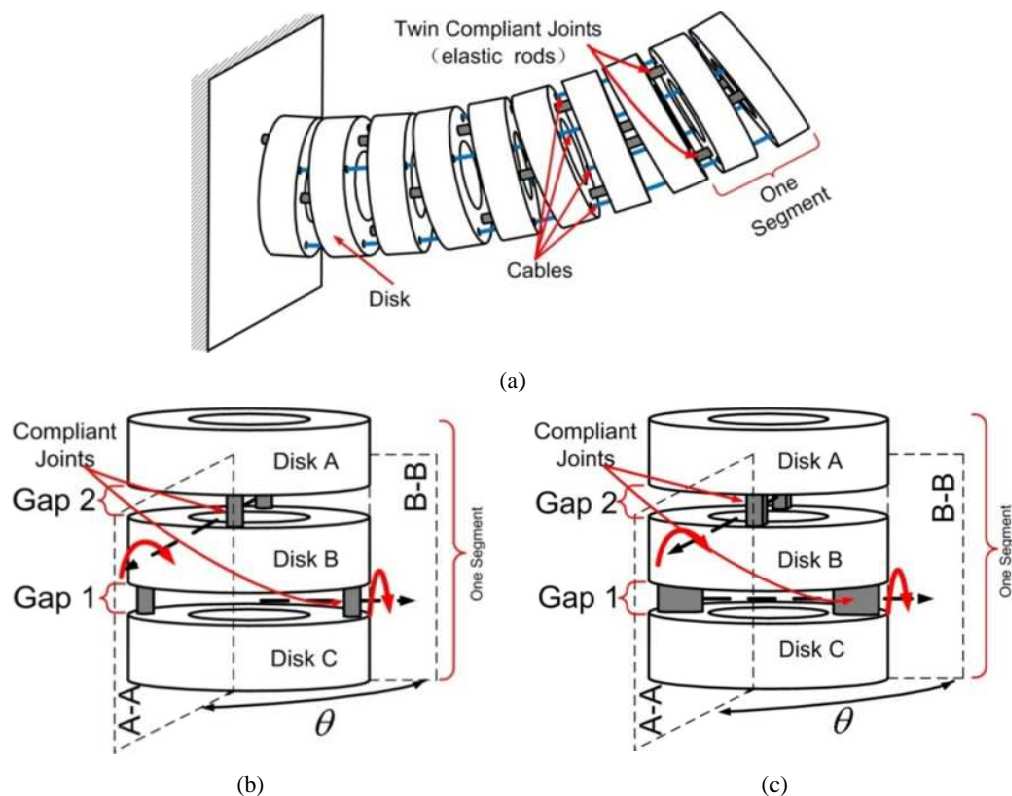


Figure 3-10. (a) General view of twin-pivot compliant joints robot; (b) one segment of twin-rod concept one (c) one segment of twin-sheet concept

### 3.2.3. Advantages of the new continuum robot concepts

Based on the compliant joint construction, two families of novel continuum robot designs are presented, which can carry an appropriate payload with double actuations per section, while giving the possibility to construct the arm with a small diameter/length ratio, great flexibility and minimized twisting, so that the robot can access confined spaces thus be applicable for a variety of machining and visual inspection tasks.

Further, another significant advantage of new concepts is the system can obtain appropriate flexibility without sacrificing the stiffness and accessibility in complex environments. For the existing continuum robots, the general approach for increasing the flexibility is to increase the length of flexible backbone/ universal joint, which enables the section have a greater bending and obstacles avoiding capability. However, due to the increase of the backbone length, the stiffness of the system is decreased. Specifically, as shown in Figure 3-11(a), the length increase of a universal joint makes the springs longer, which is the key element for bending stiffness. It renders stiffness reduced, which has to be compensated for by an increase in spring size, causing a decreased accessibility in cluttered environments. Similarly, for flexible backbone continuum robots, as shown in Figure 3-11 (b), stiffness compensation is achieved by increasing the flexible backbone size.

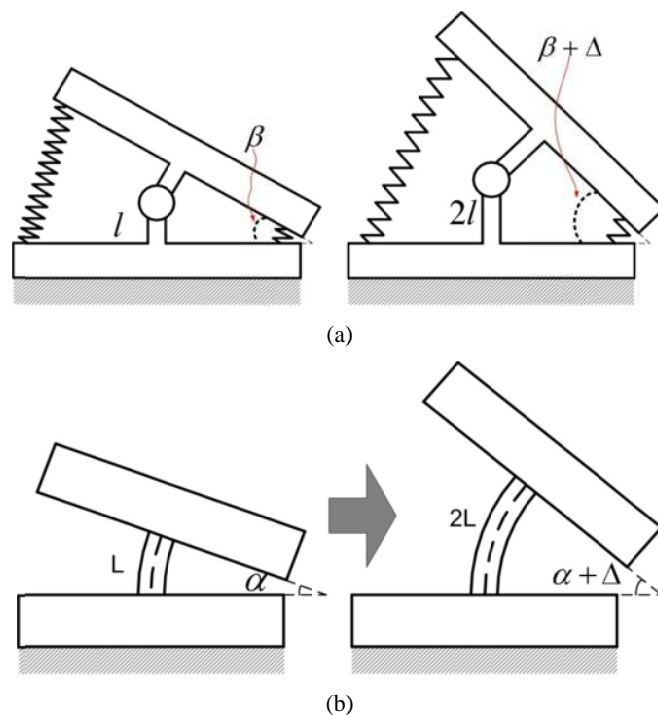


Figure 3-11. The general approach for increasing the work volume (a) universal joint+ springs; (b) flexible backbone;

But for the new concepts (Figure 3-8 (a) & (b)), the flexibility can be easily enhanced by decreasing the NiTi rods diameter/ sheet thickness, while compensating the

stiffness by increasing NiTi rods quantity/ NiTi sheet length, which does not make the section size increase. Therefore, the flexibility can be adjusted to meet the requirements of the application without sacrificing stiffness and accessibility of the design proposed in this chapter.

### 3.3. Innovative concept of variable stiffness system

Continuum robots have been utilized for several light duty applications, such as minimally invasive surgery in medical field and inspection in industry. However, the existing design solutions still offer a limited range of system stiffness [105]. To overcome this disadvantage, a novel concept is developed to ‘rigidize’ continuum robot for enhancing the stiffness, which enables the system take greater reaction force/torque when acting tasks and allow the robot flexible to move when navigating in a confined space.

#### 3.3.1. Basic concept of variable stiffness system

The basic concept is to utilize stiffening material, which can repeatably switch between relatively low and high stiffness, to allow continuum robot have variable stiffness. The stiffening material can be either thermoplastic material or low-melting-point alloy, which can melt at a low temperature (below 100 °C) and get solidified above room temperature. Table 3-1 shows specifications of several stiffening materials.

Table 3-1. Melting Temperature table

Material	Melting temperature (°)
Polymorph	60
Field's alloy (Bi 32.5, In 51.0, Sn 16.5)	62
Wood's metal (Bi 49.5, Pb 27.3, Sn 13.1, Cd 10.1)	70

### 3.3.2. Two DOFs variable stiffness joint design

The concept of 2-DOF variable stiffness system is shown in Figure 3-12. This structure (one segment) is composed of three disks, two orthogonal groups of compliant joints, heating element (Nichrome wire) and stiffening material (thermoplastic), which fills the gaps between two adjacent disks. Nichrome wire can generate heat when it connects to power, which can heat up and melt the thermoplastic material. After turning off the power, the material can be cooled by air and get stiff. Therefore, the variable stiffness system can have two states, one is rigid and the other is soft.

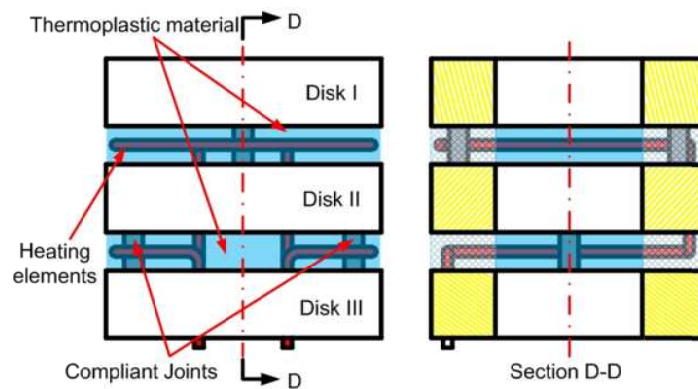


Figure 3-12. Two DOFs variable stiffness joint

For stiffening continuum robot, variable stiffness system (comprise of multi two DOF segments) is mounted to the outside of the robot, as shown in Figure 3-13 (a). Specifically, in the soft state, the system can be bent to an arbitrary configuration due to the movement of the continuum robot. The thermoplastic material is constrained by rubber tube from outside, and the rubber covered continuum robot from inside. Hence, the material can be pressed from left side to right side, as shown in Figure 3-13 (b), which allows the stiffness of the system keep constant. Subsequently, when the power is turned off, the thermoplastic mater gets cooled and solidified, so that the continuum robot is rigidized, as shown in Figure 3-13 (c). By switching between the soft and rigid states, the continuum robot can bend and get rigidized at an arbitrary configuration.

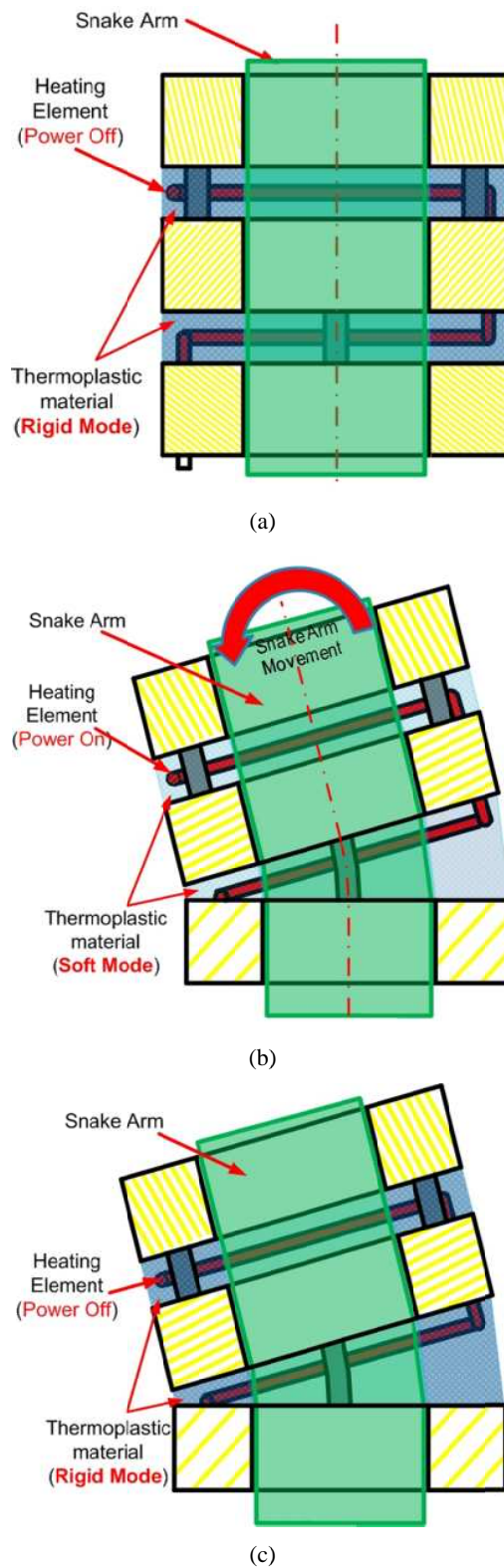


Figure 3-13. Work principal of the variable stiffness system

---

### 3.4. Conclusions

This chapter presents the design challenges and disadvantages of the existing continuum robots, such as the twist problem, how to balance the flexibility and stiffness, and kinematic challenge. Further, regarding these disadvantages, two families of continuum robots are developed, one employs two compliant joints connected in series in a segment, which is called double-pivot compliant joint; the other one utilizes two orthogonal groups of two parallel elastic rods as compliant joint, which is called twin-pivot compliant joint. By employing the new concepts, the continuum robots are able to carry an appropriate payload with double actuations per section, while giving the possibility to be constructed with a small diameter/length ratio, great flexibility and minimized twisting angle. Finally, a variable stiffness system is introduced, which renders the continuum robot have two states, relatively low and high stiffness. Hence, the robot can bend all the sections freely in the low stiffness state and is allowed to do some machining tasks in the other state.

## Chapter 4 Kinematics analysis

Kinematics studies the relation between geometry and the movement of multi-degree of freedom kinematic chains that form the structure of robotic systems [158]. Regarding continuum robots, kinematics can be divided into two levels, the first one is the mapping between task space to joint space (e.g. computing the positions and orientations of each section tip by a given desired position for robot TCP) and the second one is the mapping between joint to actuation space (e.g. calculate the actuation displacements by the configurations of each section obtained from the first mapping, according to the section geometry) [135]. In this paper, the research focused on the second mapping of kinematics. Since new structures of continuum robots are introduced in this research, so their kinematics models are valuable to be investigated to enable the precise control for them. Further, as mentioned in chapter 3.1, the orientation of tip disk is assumed to be equal with section's overall bending angle for solving inverse kinematics, accusing positioning control errors. In this chapter, a iterative approach is presented for minimising this error. Further, cable tension is analysed for verifying that the cable can maintain a constant tension in arbitrary configurations. Finally, work volume is presented to evaluate the reachable capability of the continuum robot by considering geometry limitation and material yielding.

### 4.1. Kinematics analysis of family A (Double-pivot construction)

For the family of double-pivot compliant joint continuum robots, a model is developed for computing the kinematics, which assumes that the compliant joint performs as a rigid universal joint; this is a situation in which the continuum robot is likely to work when backbone is not buckling under compression forces acted by the actuation cables and no parasitic twist of the structure occurs. The previously stated condition can be achieved by a careful control of the continuum robot once adequate models are developed. Further, in this analysis, assume the length of a section is far more than that of a segment (number of segments in single section is 5 or more), which renders

the section bending angle extremely close to tip disk orientation angle, so it can avoid the kinematics error mentioned in Chapter 3 and simplify the kinematics model.

#### 4.1.1. Forward kinematics

The purpose of forward kinematics analysis is to determine the tip position of the continuum robot with known lengths of cables. The kinematics of the entire arm depends on that of a single segment. Thus, a kinematics model of one segment is expressed for calculating the forward kinematics (Figure 4-1). In this method, the compliant joint is assumed to perform as a rigid universal joint and the cables are directly projected on the backbone, unlike the conventional approach which projects on bending plane, leading to simpler derivation.

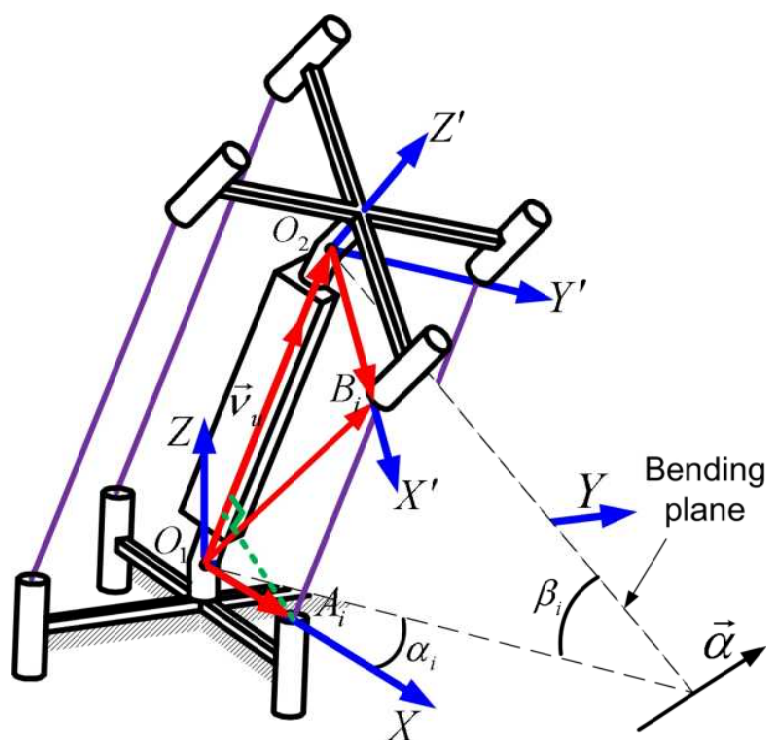


Figure 4-1. Kinematics model of a single segment

In Figure 4-1,  $O_1$  and  $O_2$  are the pivot points of two compliant joints, respectively. The coordinate system  $O_1XYZ$  and  $O_2X'Y'Z'$  attaches on the pivot points  $O_1$  and  $O_2$ .

Table 4-1. Nomenclature used in this section

$\vec{\mu} (x_u, y_u, z_u)$	unit vector of the orientation of backbone $O_1O_2$ .
$l_i (i=1, 2,3,4)$	lengths of cables in single segment
$L_i (i=1, 2,3,4)$	total lengths of cables in single section
$l_{disk}$	thickness of the disks
$l_{backbone}$	length of backbone $O_1O_2$
$A_i (x_i, y_i, 0)$	anchor points for the cables on the base disk, $i=1, 2$
$\alpha_{segment}, \beta_{segment}$	direction and bending angle of the $i^{th}$ segment.
$\alpha_{section}, \beta_{section}$	direction and bending angles respectively of a single section
$\vec{\alpha}$	vector of rotation axis
n	number of segments in single section

Since the length of one pair of cables is constant, the kinematics of a segment can be determined by the lengths of two cables, which are in different pairs. The projection of vector  $\vec{O_1A_i}$  on vector  $\vec{O_1O_2}$  is  $(l_i - S)/2$ . Therefore, the equation can be obtained as:

$$\vec{O_1A_i} \cdot \vec{\mu} = \frac{l_i - S}{2} \quad (4.1)$$

Substituting vector  $\vec{\mu} (x_u, y_u, z_u)$  and  $\vec{O_1A_i} (x_i, y_i, 0)$  into **Eq. 4.1** produces **Eq. 4.2**,

$$x_u x_i + y_u y_i = \frac{l_i - S}{2} \quad (i=1, 2) \quad (4.2)$$

Where  $A_1(x_1, y_1, 0)$ ,  $A_2(x_2, y_2, 0)$  and backbone length  $S$  are known from the design of the system and cable length  $l_1$  and  $l_2$  are given. Therefore, based on the **Eq. 4.2**, parameters  $x_u$  and  $y_u$  can be described in terms of  $l_1$ ,  $l_2$  and  $A_i(x_i, y_i, 0) (i=1 \text{ and } 2)$ , so that  $\vec{\mu} (x_u, y_u, z_u)$  can be obtained.

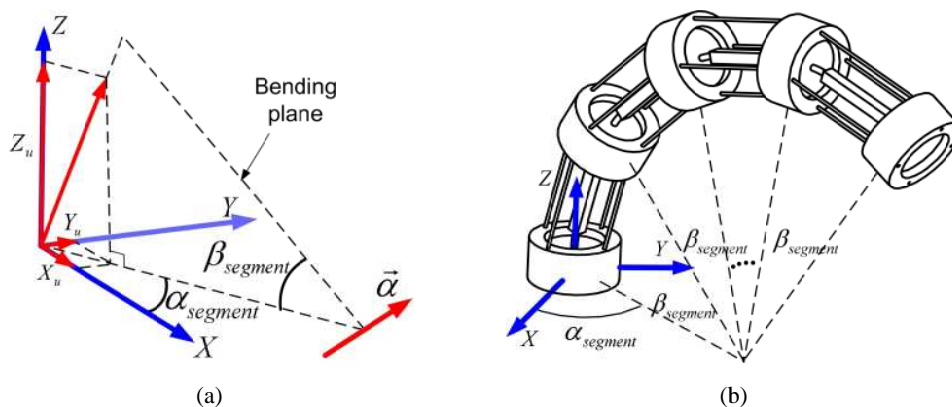


Figure 4-2. Configuration of continuum robot (a) unit vector and parameters of single segment configuration (b) one section of continuum robot

Further, based on the obtained vector  $\vec{\mu}(x_u, y_u, z_u)$ , as shown in Figure 4-2 (a), the segment's direction and bending angles can be expressed as

$$\begin{cases} \alpha_{segment} = \tan^{-1}\left(\frac{y_u}{x_u}\right) \\ \beta_{segment} = \pi - 2 \tan^{-1}\left(\frac{z_u}{\sqrt{x_u^2 + y_u^2}}\right) \end{cases} \quad (4.3)$$

It can be found that if  $x_u=0$ , the equation is infinite. Hence, in the real control program, direction angle  $\alpha_{segment}$  is set to be  $90^\circ$ , if  $x_u=0$  and  $y_u>0$ ;  $\alpha_{segment}$  is set to be  $270^\circ$ , if  $x_u=0$  and  $y_u<0$ .

According to the bending and direction angles of the  $i^{th}$  segment, as shown in Figure 4-2 (b), the orientation of one section (when the continuum robot bends, the whole construction of one section is in one bending plane, so all segments of this section are in the same plane) can be expressed as

$$\begin{cases} \alpha_{section} = \alpha_{segment} \\ \beta_{section} = n \cdot \beta_{segment} \end{cases} \quad (4.4)$$

Hence, bending and direction angle  $\alpha_{section}$  and  $\beta_{section}$  can be written in terms of the elements of vector  $\vec{O_1A_i}(x_i \text{ and } y_i)$ , backbone length  $S$ , cable length  $l_1$  and  $l_2$ , which

can describe the orientation of a section. Therefore, the forward kinematics of double-pivot joint continuum robots is obtained.

#### 4.1.2. Inverse kinematics

The purpose of inverse kinematics analysis is to determine the lengths of cables for a known position in order to manipulate the tip of a continuum robot to the desired position. The inverse kinematics can be derived in two steps: as shown in Figure 4-1, First, by given the bending and direction angles, the position of the upper anchor points  $B_i$  can be obtained. Then, the length of each cable can be derived by the magnitude of vector  $\vec{A_i B_i}$ .

Referring to Figure 4-1, a vector-loop equation can be written for each cable as given below:

$$\vec{O_1 B_i} = \vec{O_1 O_2} + \vec{O_2 B_i} \quad (4.5)$$

According to the kinematics model shown in Figure 4-1, the orientation of vector  $\vec{O_2 B_i}$  can be obtained by rotating  $\vec{O_1 A_i}$  through bending angle  $\beta_i$  with respect to vector  $\vec{\alpha}$ . Firstly, the rotation axis, vector  $\vec{\alpha}$ , can be expressed as:

$$\vec{\alpha} = \begin{bmatrix} k_x \\ k_y \\ k_z \end{bmatrix} = \begin{bmatrix} \cos(\pi/2 + \beta_i) \\ \sin(\pi/2 + \beta_i) \\ 0 \end{bmatrix} \quad (4.6)$$

And the rotation matrix  $R_T$  can be expressed as

$$R_T = \begin{bmatrix} k_x \cdot k_x \cdot (1 - cs) + cs & k_y \cdot k_x \cdot (1 - cs) - k_z \cdot sn & k_z \cdot k_x \cdot (1 - cs) + k_y \cdot sn \\ k_x \cdot k_y \cdot (1 - cs) + k_z \cdot sn & k_y \cdot k_y \cdot (1 - cs) + cs & k_z \cdot k_y \cdot (1 - cs) - k_x \cdot sn \\ k_x \cdot k_z \cdot (1 - cs) - k_y \cdot sn & k_y \cdot k_z \cdot (1 - cs) + k_x \cdot sn & k_z \cdot k_z \cdot (1 - cs) + cs \end{bmatrix} \quad (4.7)$$

Where  $cs = \cos(\beta_i)$  and  $sn = \sin(\beta_i)$ .

According to **Eq. 4.6** and **4.7**, vector  $\vec{O_2 B_i}$  can be written as

$$\vec{O_2B_i} = R_T \cdot \vec{O_1A_i} \quad (4.8)$$

As shown in Figure 4-1(b), vector  $\vec{O_1O_2}$  can be expressed as

$$\vec{O_1O_2} = \begin{bmatrix} S \cdot \cos(\varphi) \cdot \cos(\alpha) \\ S \cdot \cos(\varphi) \cdot \sin(\alpha) \\ S \cdot \sin(\varphi) \end{bmatrix} \quad (4.9)$$

Where  $\varphi = (\pi - \beta_i)/2$

Substituting **Eq. 4.8** and **4.9** into **4.5** produce **4.10**,

$$\vec{O_1B_i} = \vec{O_1O_2} + R_T \cdot \vec{O_1A_i} \quad (4.10)$$

Therefore, vector  $\vec{A_iB_i}$  can be written as

$$\vec{A_iB_i} = \vec{O_1O_2} + R_T \cdot \vec{O_1A_i} - \vec{O_1A_i} \quad (4.11)$$

Hence, the cable length  $l_i$  ( $i=1, 2, 3, 4$ ) can be computed by the following equation

$$l_i = \left| \vec{A_iB_i} \right| = \left| \vec{O_1O_2} + R_T \cdot \vec{O_1A_i} - \vec{O_1A_i} \right| \quad (4.12)$$

By given bending and direction angles, cable lengths ( $L_i$ ), for a single section, can be expressed as [134]

$$L_i = n \cdot l_i \quad (4.13)$$

Where considering there is no extra cable elongation caused by the bending of the continuum robot.

Hence, inverse kinematics of a single section for double-pivot compliant joint construction is obtained. It was utilized for calculating the max displacement of the control cables, which helped the designer select the motor and design the spool system employed in prototype 2. Further, it was utilized for controlling prototype 2.

### 4.1.3. Cable tension analysis

In this family, each section employs two pairs of cables, which are connected to two motors respectively, as shown in Figure 3 (b) (Chapter 3.2); as mentioned, although challenging to materialize, this offers an advantage of compact design and lighter system that makes it portable and applicable for the scope of the project. For maintaining the constant stiffness of continuum robot sections in arbitrary configuration, two cables of each pair need to keep persistent tensions. For double-pivot compliant joint continuum robot robots, a kinematics model is developed to calculate the cable tension in an arbitrary configuration, as shown in Figure 4-3.

In this model, the compliant joint is considered to bend as a pure arc which is the real kinematic performance of the joint and different with the assumptions for inverse and forwards kinematics. Points  $E_1$ ,  $E_2$  and points  $E_3$ ,  $E_4$  are the ends of two compliant joints, respectively. The coordinate system XYZ attaches on the point  $E_1$  (lower end of the compliant joint). The parameters  $l_{joint}$  and  $l_{rod}$  are the lengths of compliant joint (elastic rod) and rigid rod  $E_2E_3$ .

By comparing the gap distance  $A_iB_i$  ( $i=1, 2, 3, 4$ ) with the original total cable length of one pair of cables, the tension condition can be obtained.

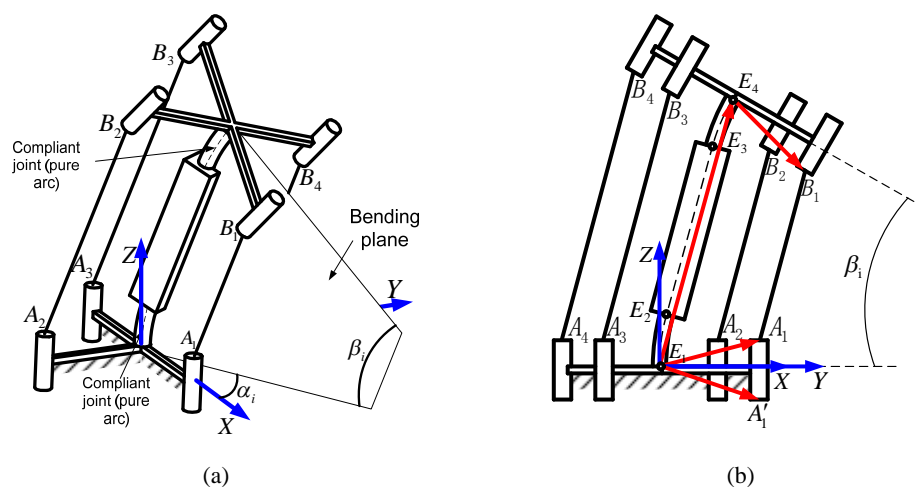


Figure 4-3. Precision kinematics model of single segment: (a) general and (b) bending section views

Specifically, if the length of cables actuated by the same motor satisfies **Eq. 4.14**, it can be concluded that this pair of cables can maintain constant tensions well in any configuration:

$$A_i B_i + A_{i+2} B_{i+2} \geq 2l_{original} \quad (i=1, 2) \quad (4.14)$$

where  $l_{original}$  is the original length of cable between two disks at the straight configuration.

If **Eq. 4.14** is not fulfilled, the pair of cables gets slack when the continuum robot bends. When the section is in the initial configuration (straight), the gaps distance  $A_i B_i + A_{i+2} B_{i+2}$  is obviously equal to  $2l_{original}$ . Hence, in this analysis, the bending angle of the section is assumed greater than  $0^\circ$ .

Referring to Figure 4-3 (b), a vector-loop equation can be written for each cable as given below:

$$\vec{A_i B_i} = \vec{E_1 E_4} + \vec{E_4 B_i} - \vec{E_1 A_i} \quad (4.15)$$

Vector  $\vec{E_1 A_i}$  can be expressed as

$$\vec{E_1 A_i} = \left[ \begin{array}{cc} x_{Ai} & y_{Ai} \\ \frac{l_{joint}}{2} \end{array} \right]^T \quad (4.16)$$

The magnitude of vector  $\vec{E_1 E_4}$  can be written as

$$m = \left| \vec{E_1 E_4} \right| = l_{rod} + \frac{4l_{joint}}{\beta_i} \cdot \sin\left(\frac{\beta_i}{2}\right) \quad (4.17)$$

Therefore, vector  $\vec{E_1 E_4}$  can be written as

$$\vec{E_1 E_4} = \left( \begin{array}{c} m \cdot \cos(\varphi) \cdot \cos(\alpha_i) \\ m \cdot \cos(\varphi) \cdot \sin(\alpha_i) \\ m \cdot \sin(\varphi) \end{array} \right) \quad (4.18)$$

Where  $\varphi = (\pi - \beta_i)/2$ .

And vector  $\vec{E}_4 B_i$  can be expressed as

$$\vec{E}_4 B_i = R_T \cdot \vec{E}_1 A'_i = R_T \cdot [x_{Ai}, y_{Ai}, -l_{joint}/2]^T \quad (4.19)$$

Substituting Eq. 4.16, 4.18 and 4.19 into 4.15 produces 4.20,

$$\vec{A}_i B_i = \begin{bmatrix} m \cdot \cos(\varphi) \cdot \cos(\alpha_i) \\ m \cdot \cos(\varphi) \cdot \sin(\alpha_i) \\ m \cdot \sin(\varphi) \end{bmatrix} + R_T \cdot \begin{bmatrix} x_{Ai} \\ y_{Ai} \\ -\frac{l_{joint}}{2} \end{bmatrix} - \begin{bmatrix} x_{Ai} \\ y_{Ai} \\ \frac{l_{joint}}{2} \end{bmatrix} \quad (4.20)$$

Therefore, the gap distance  $A_i B_i$  is obtained.

Regarding different bending angles, the gap distance of one section, as shown in Figure 4-4, is calculated and shown in Table 4-2.

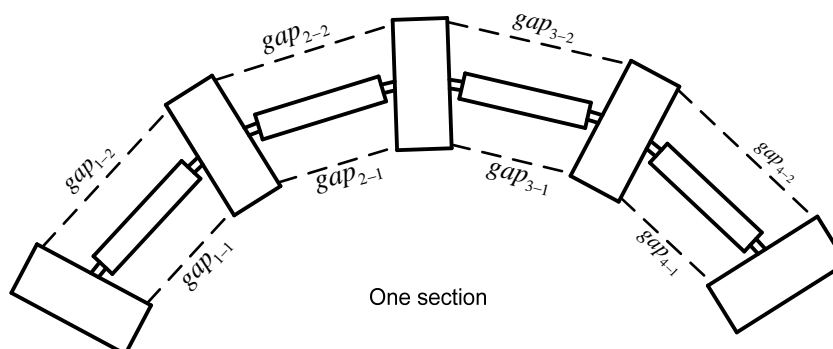


Figure 4-4 Gaps in one section

Table 4-2. Gap distances of one section for different configurations

Section bending angle	Sum of gaps for one pair of cables	Note
0°	144mm	The gap distance $\geq$ original length of one pair of cables (144mm)
30°	144.02mm	
60°	144.07mm	
90°	144.15mm	

**Note:** the gap distances are calculated at a configuration of direction angle 0°.

Table 4-2 indicates that the sum of gaps in one section (required cable length) is greater than or equal to the original length of one pair of cables in these configurations. Therefore, an elongation of one pair of cables generates for compensating the length difference between gap distance (required cable length) and original cable length, when the section bends. So, the cable can be kept tensioned in any configuration.

Since direction and bending angles rang in  $(-\pi, \pi)$  and  $(0, \pi/2)$ , respectively, the cable tension in the work volume is calculate and shown in Figure 4-5. Let the pre-tension of cable be 100 N at the original position (bending angle is 0). It can be found that the max tension force is 105.74N, when the section bends  $90^\circ$  ( $\pi/2$  in radian). Therefore, the cable tension can be maintained in arbitrary configuration. Based on this fact, twin actuation can be applied in the design, which decreases the weight and size of actuation system.

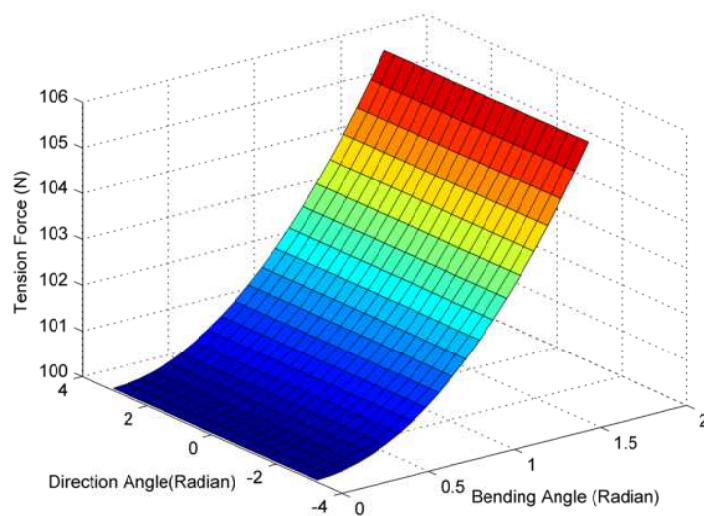
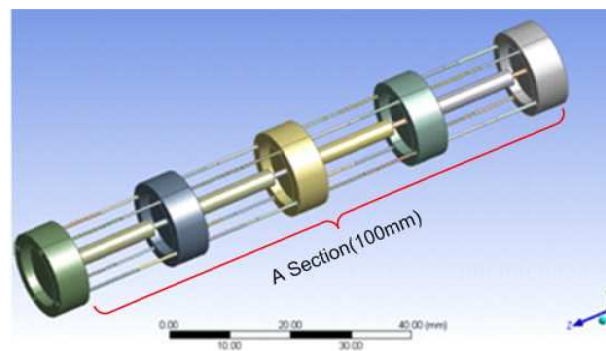


Figure 4-5. An example of cable tension plot in work volume: The stiffness of 400mm cable (200mm in continuum robot and 200mm in actuation system) is 37.5 N/mm (0.75mm diameter steel cable)

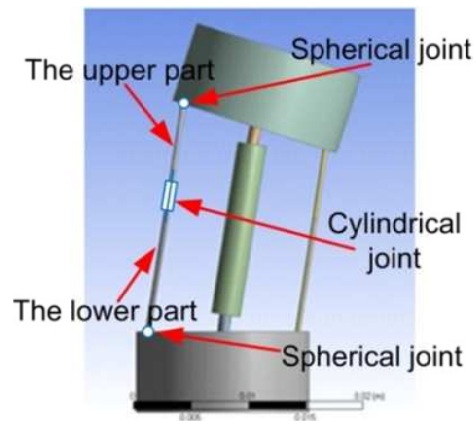
#### 4.1.4. Simulation validation of kinematics analysis

In this section, the validation method for kinematics of double-pivot compliant joint continuum robots is presented. A FEA model is built in ANSYS (100mm in length,

and 15mm in diameter), as shown in Figure 4-6. In the model, there are four segments in a section and two pairs of actuation cables. The cable in each segment is constructed with two separate parts, upper and lower part, which are both attached to the disks with spherical joints in one end; and the other ends of the upper and lower part are constrained by a cylindrical joint defined, which can simulate the stretch/contract of the cable. The joints are flexible to be bent and all of the other parts are rigid, e.g. cables, disks and rigid connector between two adjacent joints.



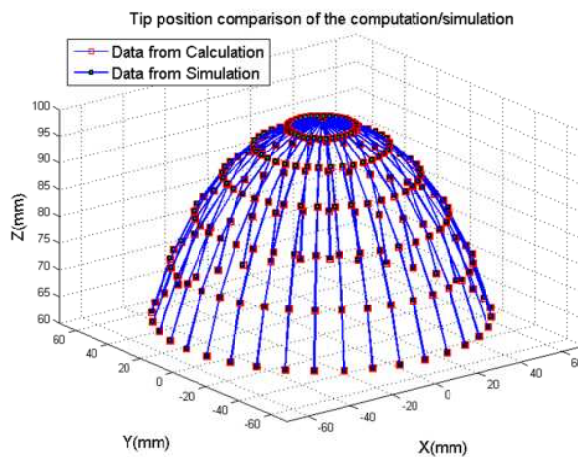
(a)



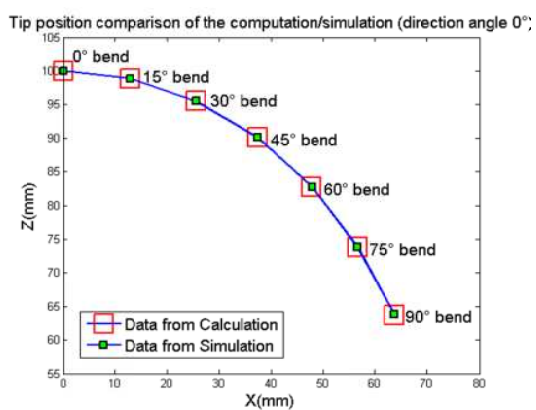
(b)

Figure 4-6. FEA model in ANSYS: (a); a section model (b) a single segment.

For comparing the error between simulation and calculation, the results of the tip position of one section computed by forward kinematics and simulation are shown in Figure 4-7 and the errors between these two approaches are shown in Figure 4-8.

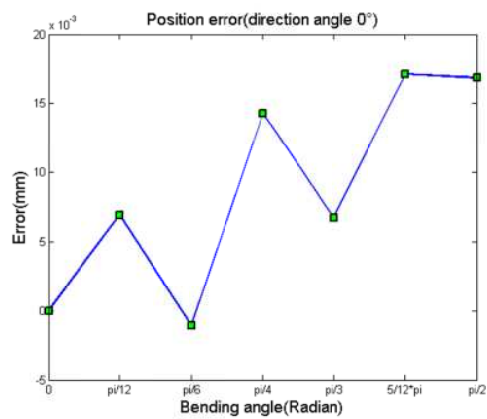


(a)

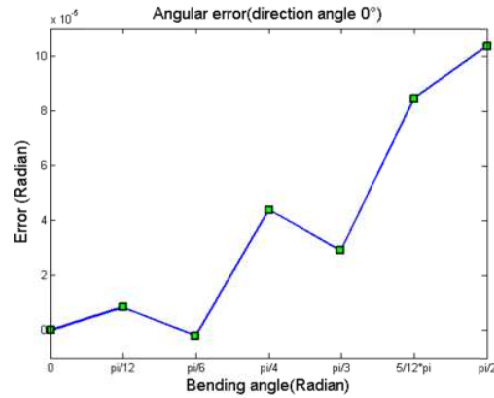


(b)

Figure 4-7. Comparisons between computation/simulation:(a) in workspace; (b) direction angle  $0^\circ$



(a)



(b)

Figure 4-8. Error between computation/simulation: (a) Position error (b) Angular error

It can be found that the tip position of the section computed by the kinematics model coincides with the value obtained by the FEA model. The max position and angular errors are 0.017 mm and less than  $1.04 \times 10^{-4}$  radian, respectively, so it can be concluded that the kinematics model presented here can be used to present the kinematics of a continuum robot with double-pivot compliant joint construction.

## 4.2. Kinematics analysis of family B (Twin-pivot construction)

Since a twin-pivot compliant joint construction is introduced, a kinematic model needs to be studied for this specific concept. In this model, two sub-bending planes are employed for investigating forwards kinematics, different with the existing researches which utilized single bending plane. Further, regarding the kinematic error of inverse kinematics presented in Chapter 3, the model also considers minimizing it by an iterative method.

### 4.2.1. Forward kinematics

As each section includes identical segments, forward kinematic model of twin-pivot compliant joint construction is expressed, based on the analysis of a single segment (Figure 4-9) on which the compliant joint is assumed to perform as a pure arc. The initial configuration of the section is straight, where the cable lengths  $l_1$  and  $l_2$  are equal to the initial lengths. In the real control system, the solution is directly set up for

this configuration. Hence, in the following analysis, the bending angle is assumed equal to greater than  $0^\circ$ .

Table 4-3. Nomenclature used in this section

$XYZ$	coordinate system located at the center of disks A
$X'Y'Z'$	coordinate system located at the center of disks B
$X''Y''Z''$	coordinate system located at the center of disks C
$A_i$	guide points for the cables on the disk A, $i=1, 2,3,4$
$B_i$	guide points for the cables on the disk B, $i=1, 2,3,4$
$C_i$	anchor points for the cables on the disk C, $i=1, 2,3,4$
$l_{joint}$	length of the compliant joints (given)
$l_{disk}$	thickness of the disks (given)
$\beta_1$	bending angle of joint_1
$\beta_2$	bending angle of joint_2
$\beta_{segment}$	bending angle of segment
$\beta_{section}$	bending angle of section
$\alpha_{segment}$	direction angle of segment
$\alpha_{section}$	direction angle of section
$l_1, l_2$	total lengths of cable 1 ( $l_1 = l'_1 + l''_1$ ) and 2 ( $l_2 = l'_2 + l''_2$ ), respectively
$\theta_1$	angle between $B_1B_3$ and axis $Y'$ (given, as shown in Figure 4-10(b))
$(X_p, Y_p, Z_p)$	The tip position of single section
$r$	distance from center of the disk to the cable anchor point (given)
$n$	number of segments in single section (given)
$l_{original}$	original length of one pair of cables in one section
$l_{gap}$	gap distance for one pair of cables in one section
$K_{cable}$	stiffness of a cable

---

$F_{original}$  original cable tension force

---

**Note:** Cables 1 and 3 are attached to the same motor; and cables 2 and 4 are attached to another motor.

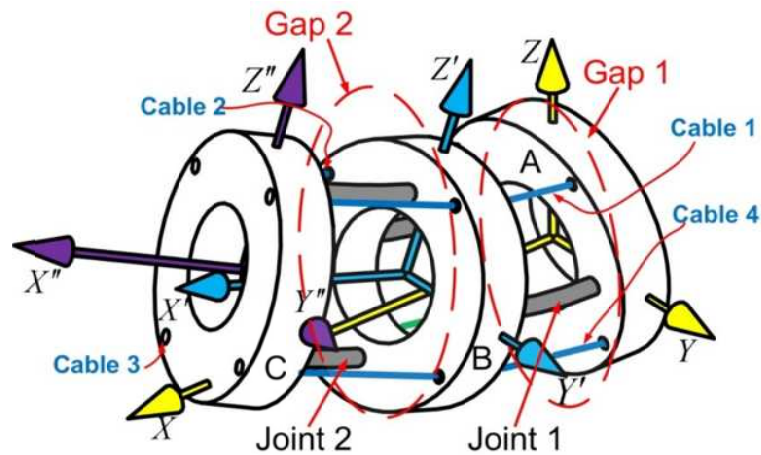
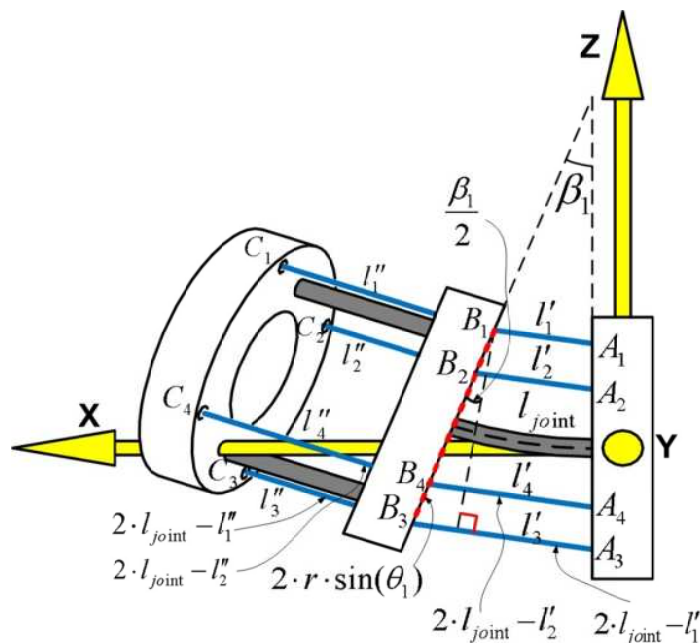
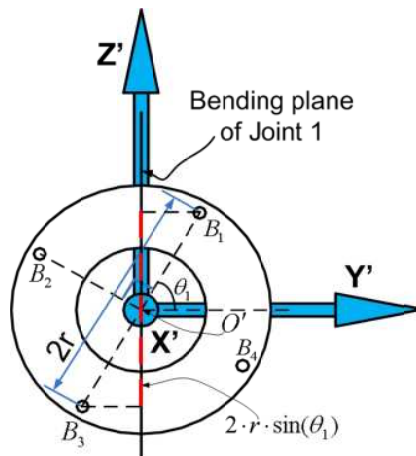


Figure 4-9. Schematic for kinematic model of single twin-pivot segment

TCP position and orientation of a single section can be derived via Denavit-Hartenberg method, after obtaining DH parameters of a segment ( $\beta_1$  &  $\beta_2$ ) with given cable lengths ( $l_1$  and  $l_2$ ). **Step A:** based on  $l_1$  and  $l_2$ , compute bending angles  $\beta_1$  &  $\beta_2$ . As show in Figure 4-10 (a), the difference between  $l'_1$  and  $l'_3$  can be obtained, due to the length of one pair of cables in one gap is constant to  $2l_{joint}$  (the compliant joint in this concept is short, (e.g. 1.5mm) and bending angle of each joint is small (up to 9 degrees for 90 degrees section bend), so the distance between two ends of the joint is extremely close to joint length (0.1% difference)). In one segment, two groups of twin-pivot complaint joints are arranged orthogonally and each group can only bend in one direction. It renders section' overall bending plane does not couple with that of each joint, which is different with the conventional designs (central located backbone performance as a universal joint, thus section's overall bending angle couples with joint bending plane). Hence, the kinematics derivation needs to be divided, by projecting the cables in the bending planes of joint 1 and 2, separately. Firstly, the kinematics of joint 1 is studied.



(a)



(b)

Figure 4-10. (a) Joint 1 bending section view (b) Top view of disk B ( $\beta_{segment}$  and  $\alpha_{segment}$  are denoted as bending and direction angles, respectively)

$$l'_3 - l'_1 = (2 \cdot l_{joint} - l'_1) - l'_1 \tag{4.21}$$

Where  $l_{joint}$  is given.

As shown in Figure 4-10 (b), the projection of line  $B_1B_3$  on bending plane of joint 1 can be expressed as:

$$m_{B_1B_3} = 2 \cdot r \cdot \sin(\theta_1) \tag{4.22}$$

Where  $r$  and  $\theta_1$  are given.

Hence, from Joint 1 bending section view, the following equation can be given by:

$$(2 \cdot l_{joint} - l'_1) - l'_1 = 2 \cdot m_{B_1, B_3} \cdot \sin(\beta_1/2) = 2 \cdot [2 \cdot r \cdot \sin(\theta_1)] \cdot \sin(\beta_1/2) \quad (4.23)$$

Similarly, the difference between  $l'_2$  and  $l'_4$  can be obtained:

$$(2 \cdot l_{joint} - l'_2) - l'_2 = 2 \cdot [2 \cdot r \cdot \sin(\pi/2 - \theta_1)] \cdot \sin(\beta_1/2) \quad (4.24)$$

Likewise, another two equations can be obtained by projecting the cables on the bending plane of joint 2:

$$(2 \cdot l_{joint} - l''_1) - l''_1 = 2 \cdot [2 \cdot r \cdot \cos(\theta_1)] \cdot \sin(\beta_2/2) \quad (4.25)$$

And

$$(2 \cdot l_{joint} - l''_2) - l''_2 = 2 \cdot [2 \cdot r \cdot \cos(\pi/2 - \theta_1)] \cdot \sin(\beta_2/2) \quad (4.26)$$

Further, in order to eliminate parameters  $l'_1$  and  $l''_1$ , adding the left and right side of **Eq. 4.23** with those of **Eq. 4.25**, respectively, yields

$$2 \cdot l_{joint} - l_1 = 2 \cdot r \cdot \sin(\theta_1) \cdot \sin(\beta_1/2) + 2 \cdot r \cdot \cos(\theta_1) \cdot \sin(\beta_2/2) \quad (4.27)$$

Where  $l_1$  is given.

Likewise, according to **Eq. 4.24** & **4.26**, another equation can be obtained:

$$2 \cdot l_{joint} - l_2 = 2 \cdot r \cdot \cos(\theta_1) \cdot \sin(\beta_1/2) + 2 \cdot r \cdot \sin(\theta_1) \cdot \sin(\beta_2/2) \quad (4.28)$$

Where  $l_2$  is given.

Hence, based on **Eq. 4.27** and **4.28**, the bending angles  $\beta_1$  and  $\beta_2$  can be written in terms of cable lengths  $l_1$  and  $l_2$ ,  $\theta_1$  ( $\theta_1 \neq 45^\circ \pm n \cdot 90^\circ$ ),  $r$  and joint length  $l_{joint}$  as:

$$\begin{cases} \beta_1 = \sin^{-1} \left( \frac{2l_{joint} (\sin(\theta_1) - \cos(\theta_1)) - l_1 \sin(\theta_1) + l_2 \cos(\theta_1)}{2r(\sin^2(\theta_1) - \cos^2(\theta_1))} \right) \\ \beta_2 = \sin^{-1} \left( \frac{2l_{joint} (\sin(\theta_1) - \cos(\theta_1)) + l_1 \cos(\theta_1) - l_2 \sin(\theta_1)}{2r(\sin^2(\theta_1) - \cos^2(\theta_1))} \right) \end{cases} \quad (4.29)$$

**Step B:** In step A, parameters  $\beta_1$  and  $\beta_2$  are derived with given lengths of cables  $l_1$  and  $l_2$ . Hence, as shown in Figure 4-11, all D-H parameters are obtained from design and step A, which are shown in Table 4-4. By using Denavit-Hartenberg (DH) method, TCP position and orientation of a segment can be described. Since one pair of compliant joints can bend in a single direction, it is assumed to perform as a revolute joint, which can bend as a pure curve.

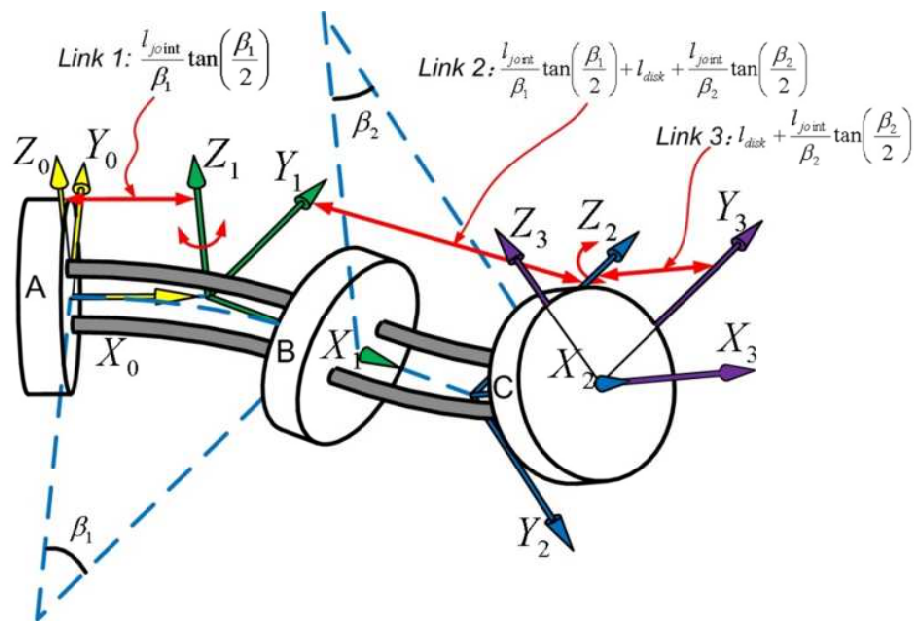


Figure 4-11. Denavit-Hartenberg frames for one single segment (Coordinate 0 and 3 locate at the centre of the top surface of the disks A and C; Coordinate 1 locates at the intersection point of central axes of disks A and B; Coordinate 2 locates at the intersection point of central axes of disks B and C; bending plane  $\beta_1$  is vertical with bending plane  $\beta_2$ ;  $Z_1$  and  $Z_2$  are the rotation axes for joint 1 and 2, respectively)

Table 4-4. D-H Parameters for Single Segment

Link	$\theta$	a	d	$\alpha$
1	0	$\frac{l_{joint}}{\beta_1} \tan\left(\frac{\beta_1}{2}\right)$	0	0
2	$\beta_1$	$\frac{l_{joint}}{\beta_1} \tan\left(\frac{\beta_1}{2}\right) + l_{disk} + \frac{l_{joint}}{\beta_2} \cdot \tan\left(\frac{\beta_2}{2}\right)$	0	$-\frac{\pi}{2}$
3	$\beta_2$	$l_{disk} + \frac{l_{joint}}{\beta_2} \cdot \tan\left(\frac{\beta_2}{2}\right)$	0	$\frac{\pi}{2}$

Using the above D-H table, the matrix for each links can be expressed as, respectively:

$$T_0 = \begin{bmatrix} 1 & 0 & 0 & l_{joint}/\beta_1 \cdot \tan(\beta_1/2) \\ 0 & 1 & 0 & 0 \\ 0 & 0 & 1 & 0 \\ 0 & 0 & 0 & 1 \end{bmatrix} \quad (4.30)$$

$$T_1 = \begin{bmatrix} \cos(\beta_1) & 0 & -\sin(\beta_1) & (\frac{l_{joint}}{\beta_1} \tan(\frac{\beta_1}{2}) + l_{disk} + \frac{l_{joint}}{\beta_2} \cdot \tan(\frac{\beta_2}{2})) \cdot \cos(\beta_1) \\ \sin(\beta_1) & 0 & \cos(\beta_1) & (\frac{l_{joint}}{\beta_1} \tan(\frac{\beta_1}{2}) + l_{disk} + \frac{l_{joint}}{\beta_2} \cdot \tan(\frac{\beta_2}{2})) \cdot \sin(\beta_1) \\ 0 & -1 & 0 & 0 \\ 0 & 0 & 0 & 1 \end{bmatrix} \quad (4.31)$$

$$T_2 = \begin{bmatrix} \cos(\beta_2) & 0 & \sin(\beta_2) & (l_{disk} + \frac{l_{joint}}{\beta_2} \cdot \tan(\frac{\beta_2}{2})) \cdot \cos(\beta_2) \\ \sin(\beta_2) & 0 & -\cos(\beta_2) & (l_{disk} + \frac{l_{joint}}{\beta_2} \cdot \tan(\frac{\beta_2}{2})) \cdot \sin(\beta_2) \\ 0 & 1 & 0 & 0 \\ 0 & 0 & 0 & 1 \end{bmatrix} \quad (4.32)$$

Then, the tip position and orientation of segment can be calculated as

$$T_0^2 = T_0 \cdot T_1 \cdot T_2 \quad (4.33)$$

As all segments of single section share the same construction, the forward kinematics for one section can be written in terms of bending angles of  $\beta_1$ ,  $\beta_2$ ,  $n$ ,  $l_{joint}$  and  $l_{disk}$  as:

$$T_{section} = (T_0^2)^n = (T_0 \cdot T_1 \cdot T_2)^n \quad (4.34)$$

Therefore, the section forwards kinematics is obtained, which includes the position and orientation of section tip. Likewise, the forward kinematics of other sections can be obtained based on the given cable lengths.

#### 4.2.2. Inverse kinematics

For computing the inverse kinematics of Family B, the bending angles  $\beta_1$  and  $\beta_2$  are the critical parameters, which can be derived based on the orientation angle of tip disk [134]. However, regarding inverse kinematics analysis, the position of section tip is given, hence, only the section bending and direction angles can be derived (**Eq. 4.35**).

As mentioned in Chapter 3, section bending angle and tip disk orientation are not identical, as shown in Figure 4-12. Therefore, an iterative method is developed for calculating accurate inverse kinematics, which is based on the section bending and direction angles.

The approach consists of two steps: **Step 1**: assuming the orientation of tip disk is equal with section bending angle to initial approximation for  $\beta_1$  and  $\beta_2$ , which can be obtained from the position of section tip;; **Step 2**: utilize the initial approximation values to compute the inverse kinematics by an iteration method.

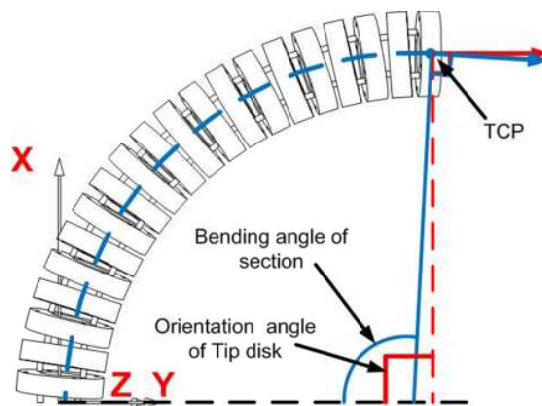


Figure 4-12. Difference between section bending angle and tip disk orientation (twin-pivot backbone continuum robot)

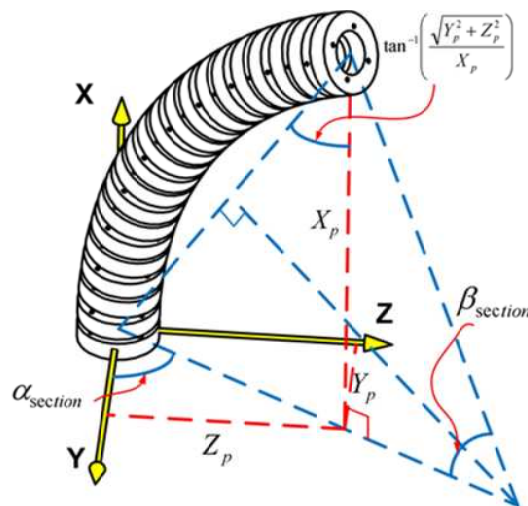


Figure 4-13. Parameters of single section configuration

Specifically, **Step 1**: due to the fact that all the segments share the same construction, the kinematics of single section depends on single segment, hence, kinematic model of a segment is developed for calculating  $\beta_1$  and  $\beta_2$ .

As shown in Figure 4-13, assuming the tip disk orientation is equal with the section bending angle, thus, the bending and direction angles of segment can be written in terms of the position of section tip  $(X_p, Y_p, Z_p)$  and  $n$  (number of segments in single section):

$$\left\{ \begin{array}{l} \alpha_{segment} = \alpha_{section} = \tan^{-1}\left(\frac{Z_p}{Y_p}\right) \\ \beta_{segment} = \frac{\beta_{section}}{n} = \frac{2}{n} \cdot \tan^{-1}\left(\frac{\sqrt{Y_p^2 + Z_p^2}}{X_p}\right) \end{array} \right. \quad (4.35)$$

It can be found that if  $Y_p=0$ , the equation is infinite. Hence, in the real control program, direction angle  $\alpha_{segment}$  is set to be  $90^\circ$ , if  $Y_p=0$  and  $Z_p > 0$ ;  $\alpha_{segment}$  is set to be  $270^\circ$ , if  $Y_p=0$  and  $Z_p < 0$ .

The bending angles of joint 1 and 2 in single segment can be expressed as:

$$\left\{ \begin{array}{l} \beta_1 = \tan^{-1}\left(\cos(\alpha_{segment}) \cdot \tan(\beta_{segment})\right) \\ \beta_2 = \sin^{-1}\left(-\sin(\alpha_{segment}) \cdot \sin(\beta_{segment})\right) \end{array} \right. \quad (4.36)$$

**Step 2:** Since the actual bending angle of single section is different with tip disk orientation, an iteration method is utilized to compute the inverse kinematics, which applies the initial approximations obtained from Step 1, as shown in Figure 4-14.

The proposed iteration method can be described as following:

**Sub-step i:** substituting  $\beta_1$  and  $\beta_2$  into forward kinematics equation (refer to **Eq. 4.34**, the tip position of the section is obtained;

**Sub-step ii:** Then comparing this position with the desired position, the distance differences (diff) in X, Y and Z axis ( $diff_x$ ,  $diff_y$  and  $diff_z$ ) are calculated;

**Sub-step iii:** comparing the distance difference  $\Delta_{distance} = \sqrt{diff_x^2 + diff_y^2 + diff_z^2}$

with the desired distance error  $\delta$  ;

**Sub-step iv:** if  $\Delta_{distance}$  is not greater than  $\delta$  , the program moves to calculate the cable lengths, based on current value of  $\beta_1$  and  $\beta_2$  ;

**Sub-step v:** if  $\Delta_{distance}$  is greater than  $\delta$  , the iteration starts. The angles  $\beta_1$  and  $\beta_2$  are assigned with eight combinatorial paired values that are assigned using their nominal values and  $\Delta_\beta$  , and then the distance difference  $\Delta_i$  ( $i = 1\sim 8$ ) are calculated, according to these eight pairs of values. Compare  $\Delta_i$  and assign  $\beta_1$  and  $\beta_2$  new values, which obtains the minim valve of  $\Delta_{distance}$  ;

**Sub-step vi:** then repeat the procedure until the  $\Delta_{distance}$  is not greater than  $\delta$  .

**Note:** Value 1: ( $\beta_1 + \Delta_\beta$  ,  $\beta_2$ ); Value 2: ( $\beta_1 + \Delta_\beta$  ,  $\beta_2 + \Delta_\beta$ ); Value 3 :( $\beta_1 + \Delta_\beta$  ,  $\beta_2 - \Delta_\beta$ ); Value 4 :( $\beta_1 - \Delta_\beta$  ,  $\beta_2$ ); Value 5 :( $\beta_1 - \Delta_\beta$  ,  $\beta_2 + \Delta_\beta$ ); Value 6 :( $\beta_1 - \Delta_\beta$  ,  $\beta_2 + \Delta_\beta$ ); Value 7 :( $\beta_1$  ,  $\beta_2 + \Delta_\beta$ ); Value 8 :( $\beta_1$  ,  $\beta_2 - \Delta_\beta$ );

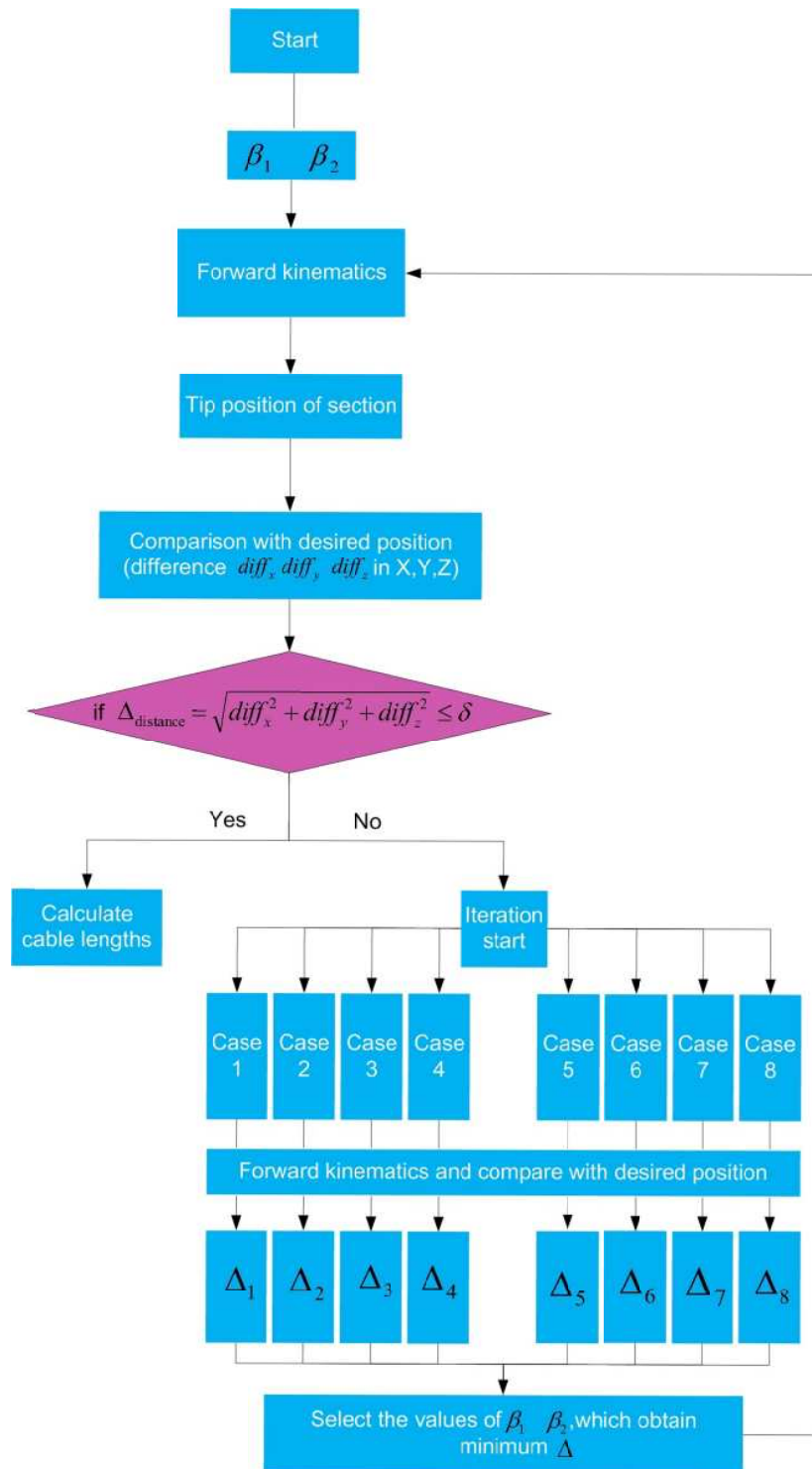


Figure 4-14. Iteration method for inverse kinematics

Based on the angle values  $\beta_1$  obtained from the iteration program, cable lengths  $l'_1, l'_2, l'_3$  and  $l'_4$  in gap 1 can be written as, as shown in Figure 4-10:

$$\begin{cases} l_1' = 2 \cdot \left( \frac{l_{joint}}{\beta_1} - r \cdot \sin(\theta_1) \right) \cdot \tan\left(\frac{\beta_1}{2}\right) \\ l_2' = 2 \cdot \left( \frac{l_{joint}}{\beta_1} - r \cdot \cos(\theta_1) \right) \cdot \tan\left(\frac{\beta_1}{2}\right) \\ l_3' = 2 \cdot \left( \frac{l_{joint}}{\beta_1} + r \cdot \sin(\theta_1) \right) \cdot \tan\left(\frac{\beta_1}{2}\right) \\ l_4' = 2 \cdot \left( \frac{l_{joint}}{\beta_1} + r \cdot \cos(\theta_1) \right) \cdot \tan\left(\frac{\beta_1}{2}\right) \end{cases} \quad (4.37)$$

Similarly, according to the angle values  $\beta_2$ , cable lengths  $l_1''$ ,  $l_2''$ ,  $l_3''$  and  $l_4''$  in gap 2 can be described as:

$$\begin{cases} l_1'' = 2 \cdot \left( \frac{l_{joint}}{\beta_2} - r \cdot \cos(\theta_1) \right) \cdot \tan\left(\frac{\beta_2}{2}\right) \\ l_2'' = 2 \cdot \left( \frac{l_{joint}}{\beta_2} - r \cdot \sin(\theta_1) \right) \cdot \tan\left(\frac{\beta_2}{2}\right) \\ l_3'' = 2 \cdot \left( \frac{l_{joint}}{\beta_2} + r \cdot \cos(\theta_1) \right) \cdot \tan\left(\frac{\beta_2}{2}\right) \\ l_4'' = 2 \cdot \left( \frac{l_{joint}}{\beta_2} + r \cdot \sin(\theta_1) \right) \cdot \tan\left(\frac{\beta_2}{2}\right) \end{cases} \quad (4.38)$$

According to **Eq. 4.37** and **4.38**, the lengths of cables for a known position of section tip can be calculated as:

$$\begin{cases} l_1 = 2n \cdot \left( \frac{l_{joint}}{\beta_1} - r \cdot \sin(\theta_1) \right) \cdot \tan\left(\frac{\beta_1}{2}\right) + 2n \cdot \left( \frac{l_{joint}}{\beta_2} - r \cdot \cos(\theta_1) \right) \cdot \tan\left(\frac{\beta_2}{2}\right) \\ l_2 = 2n \cdot \left( \frac{l_{joint}}{\beta_1} - r \cdot \cos(\theta_1) \right) \cdot \tan\left(\frac{\beta_1}{2}\right) + 2n \cdot \left( \frac{l_{joint}}{\beta_2} - r \cdot \sin(\theta_1) \right) \cdot \tan\left(\frac{\beta_2}{2}\right) \\ l_3 = 2n \cdot \left( \frac{l_{joint}}{\beta_1} + r \cdot \sin(\theta_1) \right) \cdot \tan\left(\frac{\beta_1}{2}\right) + 2n \cdot \left( \frac{l_{joint}}{\beta_2} + r \cdot \cos(\theta_1) \right) \cdot \tan\left(\frac{\beta_2}{2}\right) \\ l_4 = 2n \cdot \left( \frac{l_{joint}}{\beta_1} + r \cdot \cos(\theta_1) \right) \cdot \tan\left(\frac{\beta_1}{2}\right) + 2n \cdot \left( \frac{l_{joint}}{\beta_2} + r \cdot \sin(\theta_1) \right) \cdot \tan\left(\frac{\beta_2}{2}\right) \end{cases} \quad (4.39)$$

Therefore, the inverse kinematics for the family of twin-pivot point compliant joint continuum robot is obtained. It was utilized for calculating the max displacements of

the control cables, which helped the designer select the motor and design the spool system employed in prototype 3 & 4. Further, it was utilized for controlling those porotypes.

### 4.2.3. Cable tension analysis

In this part, cable tension of twin-pivot compliant joint construction is analyzed for validating the tension can be maintained at arbitrary configuration. Similarly to the method utilized for family A, by comparing the gap distance  $A_iB_i + B_iC_i$  ( $i=1, 2, 3, 4$ ) with the original total cable length of one pair of cables (Figure 4-10), the tension condition can be obtained. Similar to the cable tension analysis of double-pivot construction, the gaps distance  $A_iB_i + B_iC_i$  ( $i=1, 2, 3, 4$ ) is obviously equal to  $2l_{original}$ , when the section is in the initial configuration (straight). Hence, in this analysis, the bending angle of the section is assumed to be greater than  $0^\circ$ .

Referring to Figure 4-10 (a), the gap distances for cable  $l'_1$  and  $l'_3$  in gap 1 can be calculated as:

$$\begin{cases} A_1B_1 = 2 \cdot \left( \frac{l_{joint}}{\beta_1} - r \cdot \sin(\theta_1) \right) \cdot \sin\left(\frac{\beta_1}{2}\right) \\ A_3B_3 = 2 \cdot \left( \frac{l_{joint}}{\beta_1} + r \cdot \sin(\theta_1) \right) \cdot \sin\left(\frac{\beta_1}{2}\right) \end{cases} \quad (4.40)$$

And likewise, the gap distances for cable  $l''_1$  and  $l''_3$  in gap 2 can be expressed as:

$$\begin{cases} B_1C_1 = 2 \cdot \left( \frac{l_{joint}}{\beta_2} - r \cdot \cos(\theta_1) \right) \cdot \sin\left(\frac{\beta_2}{2}\right) \\ B_3C_3 = 2 \cdot \left( \frac{l_{joint}}{\beta_2} + r \cdot \cos(\theta_1) \right) \cdot \sin\left(\frac{\beta_2}{2}\right) \end{cases} \quad (4.41)$$

Therefore, the gap distance in one section for one pair of cables can be written as:

$$l_{gap} = n \cdot \sum_{i=1,3} (A_iB_i + B_iC_i) = 2 \cdot n \cdot l_{joint} \left( \frac{\sin(\beta_1/2)}{\beta_1} + \frac{\sin(\beta_2/2)}{\beta_2} \right) \quad (4.42)$$

Hence, the cable tension force can be obtained as

$$F = F_{original} + K_{cable} \cdot (l_{gap} - l_{original}) \quad (4.43)$$

Where  $K_{cable}$  is denoted as the stiffness of a cable.

Figure 4-15 shows a case study of the cable tension in work volume of a section. Let the pretension of cable be 100 N at the original position (bending angle is  $0^\circ$ ). In the work volume, the tension force modifies when the continuum robot bends, and the minimum tension force is 95N, when the section bends  $131.8^\circ$  at direction angle  $\pm 46.4^\circ$  &  $\pm 133.5^\circ$ .

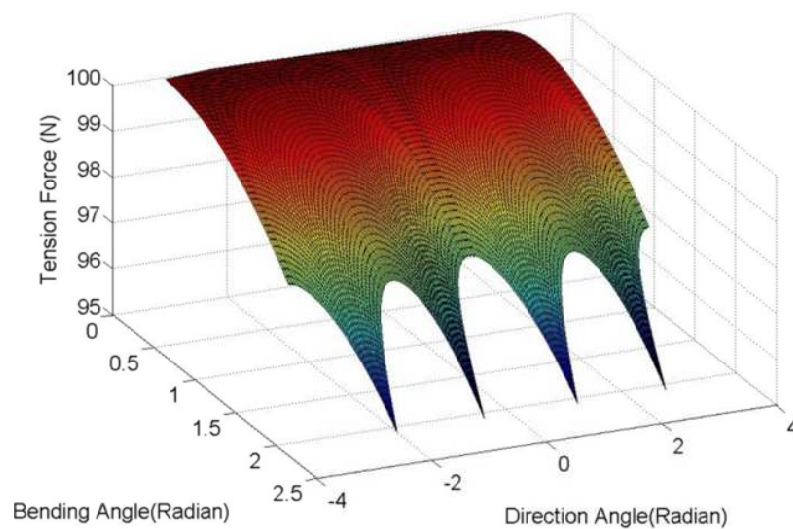


Figure 4-15. An example of cable tension plot in work volume of single section (stiffness  $k = 37.5$  N/mm of a 0.75mm diameter steel cable of 400mm length: 200mm in continuum robot and 200mm in actuation system); In the work volume, the original tension is 100N at  $0^\circ$  bending; The min tension is 95N at bending angle  $131.8^\circ$ , direction angle  $\pm 46.4^\circ$  &  $\pm 133.5^\circ$ .

Therefore, the cable tension can be maintained in an arbitrary configuration, which remains at least 95% of original tension. Based on this fact, twin actuation is applied in the design, which eliminates the weight and size of actuation system.

### 4.3. Workspace analysis

For performing 3D movements (e.g. machining, inspection) with the continuum robot, work volume is critical to be evaluated. This section addresses the problem of determining the reachable region by the tip of a multiple-section continuum robot.

Firstly, the max bending angle of a single joint is evaluated, and then the work volume of single and multiple sections are analysed subsequently to evaluate the reachable capability of a three-section continuum robot.

#### 4.3.1. Max bending angle of single joint

Regarding continuum robots, the max bending angle of single joint ( $\theta_{\max}$ ) depends on two factors: 1) yield of compliant joint material caused by bending movement; 2) geometry limitation.

Firstly, the motion range is discussed in terms of yield of compliant joint material caused by bending movement. Super-elastic NiTi has greater recoverable elastic strain (~8%) than other alloys (e.g. stainless steel: approximately 0.5%), hence, it is employed as compliant joints.

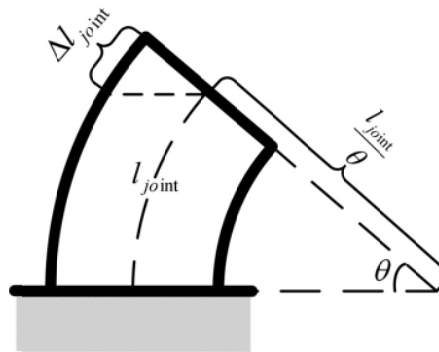


Figure 4-16. Strain model of single compliant joint

As shown in Figure 4-16, the strain of a joint can be expressed as:

$$\text{Strain}_{\text{edge}} = \frac{\Delta l_{\text{joint}}}{l_{\text{joint}}} = \frac{\left( \frac{l_{\text{joint}}}{\theta} + \frac{d}{2} \right) \cdot \theta - l_{\text{joint}}}{l_{\text{joint}}} = \frac{\frac{d}{2} \cdot \theta}{l_{\text{joint}}} = \frac{d \cdot \theta}{2 \cdot l_{\text{joint}}} \quad (4.44)$$

Where  $d$  is the diameter of super elastic NiTi rod. Based on **Eq. 4.44**, strain for different bending angles is calculated and shown in Table 4-5.

Table 4-5. Strain of NiTi compliant joint against bending angles

Max bending angle $\theta_{\max}$	9°	12°	Note
Strain	5.24%	6.98%	Ø1 mm; joint length 1.5mm;

Secondly, the other factor, geometry limitation is studied. Specifically, the motion range depends on the max bending angle where the adjacent disks collide. The bending radius is described as:

$$R_{bending} = \frac{l_{joint}}{\theta} \quad (4.45)$$

Since the adjacent disks of family B are closer than those of family A, family B is used as an example in this part. As shown in Figure 4-17, when the bending radius is equal to the radius of the disk, the disk collides with the adjacent one and the joint gets the max bend.

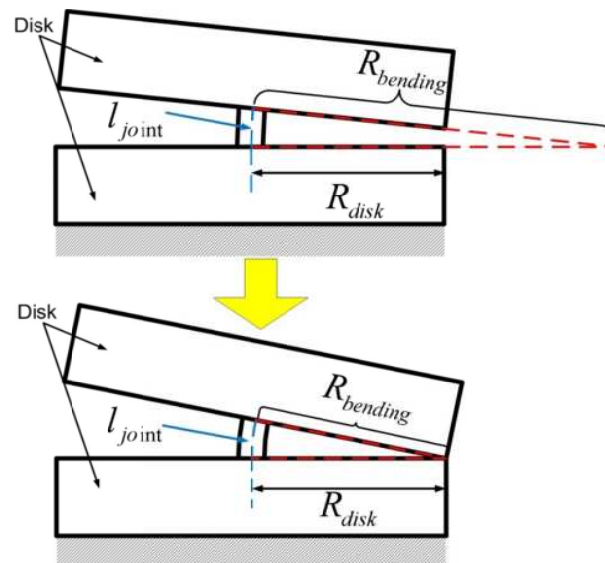


Figure 4-17. Max bending of one joint considering the limitation of geometry

Hence, the max bending angle with respect to geometry limitation is expressed as:

$$\theta_{\max} = \frac{l_{joint}}{R_{disk}} \quad (4.46)$$

According to **Eq. 4.46**, the max single joint bending angles against different disk sizes

are calculated, as shown in Table 4-6.

Table 4-6. Max Bending angles against disk sizes

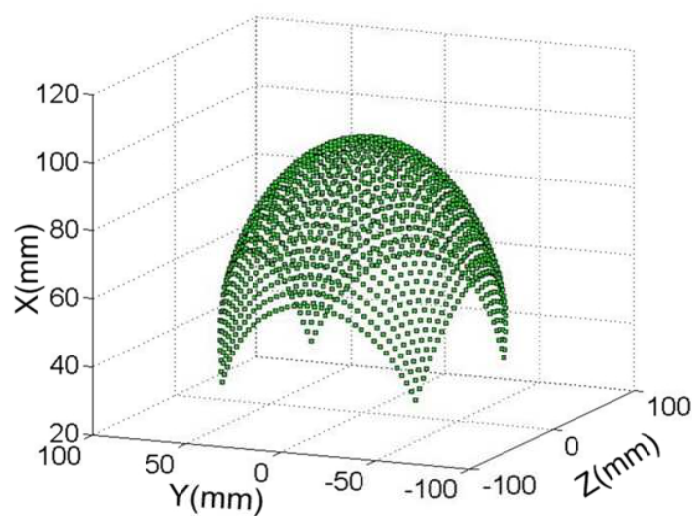
Disk sizes	10 mm	15mm	20mm	Note
Max bending angle $\theta_{\max}$	17.19°	11.46°	8.59°	Ø 1 mm; joint length 1.5mm;

Finally, by comparing the values calculated from these two factors, the max bending angle for single joint can be obtained.

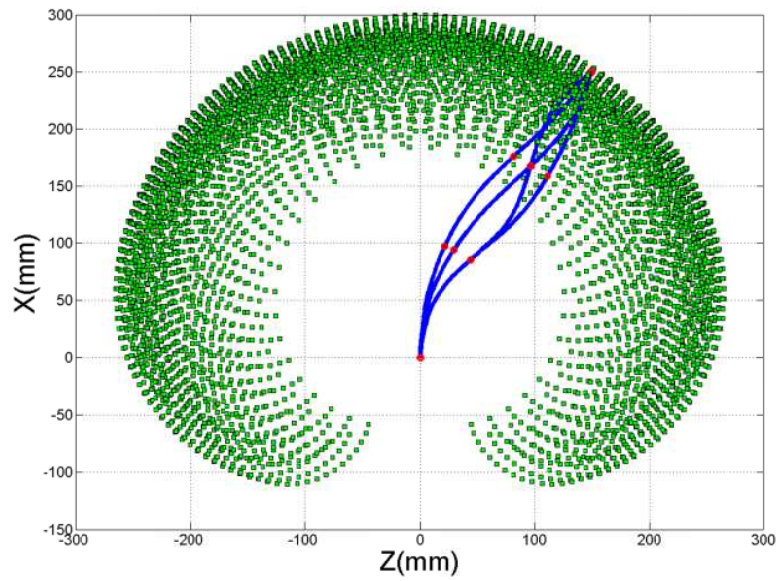
#### 4.3.2. Work volume of multiple sections

Further, a case study for a three-section twin-pivot compliant joint continuum robot (Figure 3-10) is presented. In the case study, each section contains 10 segments. Each segment is 10 mm long and composed of two pairs of cables (attached to the tip of each section), three disks (lower, middle and upper) and the disks are connected by double 1.5mm long, 1mm diameter super-elastic NiTi rods.

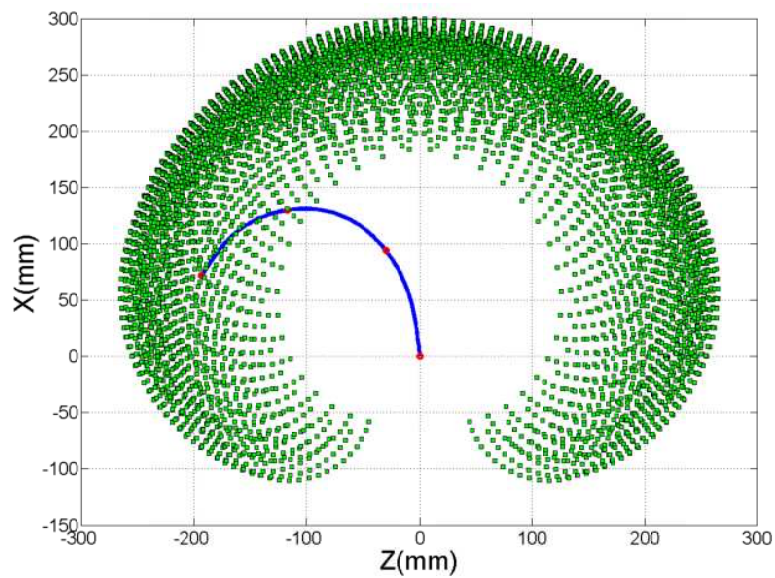
Based on the single joint max bending angle, the work volume of multiple sections is presented. For avoiding the collision between the adjacent disks, single joint is allowed to be bent up to 9°, and then the points on the work volume is calculated by an algorithm, which is based on forward kinematics. As shown in Figure 4-18 (a), it can be found that single section can bend at least 90° in arbitrary direction.



(a)



(b)



(c)

Figure 4-18. (a) 3D single section work volume;(b) case1: 2D section view of three sections work volume (XZ); (c) case2: 2D section view of three sections work volume (XZ);

Likewise, the work volume of the three-section continuum robot is presented in Figure 4-18 (b). For example, in order to reach point  $[X, Y, Z] = [250, 0, 140]$ , there are four different configurations can be utilised:

$$\begin{bmatrix} \beta_1 \\ \beta_2 \\ \beta_3 \end{bmatrix} = \begin{bmatrix} 25.0^\circ \\ 25.0^\circ \\ -15.0^\circ \end{bmatrix}$$

and

$$\begin{bmatrix} \beta_1 \\ \beta_2 \\ \beta_3 \end{bmatrix} = \begin{bmatrix} 35.0^\circ \\ 15.0^\circ \\ -35.0^\circ \end{bmatrix}$$

and

$$\begin{bmatrix} \beta_1 \\ \beta_2 \\ \beta_3 \end{bmatrix} = \begin{bmatrix} 56.0 \\ -45.0 \\ 45.0 \end{bmatrix}$$

and

$$\begin{bmatrix} \beta_1 \\ \beta_2 \\ \beta_3 \end{bmatrix} = \begin{bmatrix} 56.0 \\ -25.0 \\ -15.0 \end{bmatrix}$$

In order to reach point  $[X, Y, Z] = [250, 0, 140]$ , one configure can reach this point:

$$\begin{bmatrix} \beta_1 \\ \beta_2 \\ \beta_3 \end{bmatrix} = \begin{bmatrix} -35.0^\circ \\ -65.0^\circ \\ -55.0^\circ \end{bmatrix}$$

It can found that for some positions, the end of the arm can reach the desired places with different configurations, which can allow the robot operate on that point with variable orientations (dexterous workspace); while regarding the other positions, the arm can reach the desired places with one configuration (reachable workspace).

## 4.5. Conclusions

Over the last twenty years, there have been variable methods presented in the kinematics study of continuum robot, e.g. Denavit-Hartenberg and geometry approaches. However, since new continuum robot concepts were introduced, kinematics models for them were needed to be discussed, including both inverse and forward kinematics. Based on an algebra approach, a straightforward kinematic model for the family of double-pivot compliant joint concepts was presented in this chapter. Unlike the conventional approach making a projection on section's bending plane which transfers the 3D problem to 2D, the new method directly projects cables on the backbone and remarkably simplifies the derivation. Regarding the concept of twin-

pivot compliant joint construction, a new kinematic model was also developed based on a combination of D-H method and geometry approach. Two sub-bending planes were utilised for deriving forward kinematics, since the conventional geometry approach cannot be deployed here by projecting on section's overall bending plane, due to the construction. Moreover, an iterative approach was utilised for minimising the kinematic error causing by assuming section bending angle equal with tip disk orientation, so that an accurate inverse kinematics can be obtained, which enables the continuum robot have precision position control. The kinematics is simple and precise, which enables real-time control for continuum robots. The follow-up experiments (chapter 7) proved the kinematics models are reasonable (the trails of a three-section twin-pivot continuum robot showed that the max position error is  $\pm 1\text{mm}$  for sweeping in any  $\pm 5^\circ$  operation area by using the bespoke kinematics).

Further, the cable tension for both two families are analysed: double-pivot compliant joint construction can increase the cable tension up to 105.74% of its original tension when bends in its work volume, while a structure employing twin-pivot compliant joints can maintain at least 95% of its original tension force at an arbitrary configuration in its work volume. Finally, the method for calculating the work volume of a multiple-section continuum robot is developed by considering the yield of compliant joint material and geometry limitation. A case study of a three-section twin-pivot continuum robot is presented.

---

## Chapter 5 Modelling of continuum robots

In the last twenty years, a large amount of continuum robot researches have been presented from academia and industry. However, most of the work is related to kinematics, navigation and control algorithm of continuum robots [66, 134, 136]. In order to guide the design of the prototypes, some fundamental analyses including actuation force, joint buckling, Jacobian and stiffness were made to evaluate the new concepts presented in the chapter 3.

### 5.1. Force Analysis

In the previous researches, the principle of virtual work was utilized for analyzing the static actuation force of rod-driven continuum robot [32, 159], which neglects actuation force, twisting of the backbone, weight of robot and friction and considers the energy of flexible rods determining the section's shape. Since different actuation media is employed in this research, a general static method was developed for calculating actuation forces of cable-driven continuum robots, which built the static equilibrium by considering end load, weight of robot, cable tension, force for bending flexible backbone and the interaction from distal sections' cables. Specifically, actuation force analysis for single section with one and multiple segments was developed successively. Based on this analysis, the actuation forces acting on each cable for an arbitrary continuum robot bending shape can be obtained, so it allows the designer to select the motor and the (steel) cables for the physical demonstrators while being useful to the further compliant joint design (the force acting on the compliant joint can be determined).

#### 5.1.1. Mathematical model of actuation force

Firstly, the force model of a single-segment section was built. Secondly, according to the previous model, the mathematical force model for a multiple-segment section was developed. Based on this analysis, the force model for a multiple-section continuum

robot can be obtained. Since a modular force model was developed in this analysis, it allows it to be deployed for both A & B families (double-pivot and twin-pivot compliant joint structures) of the continuum robot concepts.

Table 5-1. Nomenclature used in this section

$r$	pitch circle radius of the actuation cable holes
$S$	the length of single section
$\beta_{segment}$	the bending angle of single segment
$G_{Load}$	the end load acting on a continuum robot section
$G_{robot}$	the weight of a continuum robot section
$F_{active}$	the active actuation force
$F_{tension}$	the cable tension force
$k_{joint}$	the stiffness of the compliant joint (Nmm/ °)
$F_{backbone}$	the force acting on the backbone of the tip segment
$Arm_{backbone}$	the moment arm of $F_{backbone}$ with respect to point O
$F_{base}$	the actuation net force acting on the cable lengths in the base segment
$F_{rad}$	the component of $F_{base}$ in the radial direction
$Arm_{rad}$	the moment arm of $F_{rad}$ with respect to point O

### ***Case 1: single-segment section***

In order to simplify the modelling, the analysis starts with the case of a single-segment continuum robot section, as shown in Figure 5-1(a). The model is constructed with two pairs of cables which are attached on disk 1; one is in the horizontal plane and orthogonal with the other one. And the adjacent disks are connected by a flexible backbone. Further, an extra end load is applied on disk 1 of the section.

Since the max actuation force for single cable is acting on cable 1, when the section bends in vertical plane, as shown in Figure 5-1(b), hence, the moment equation of this configuration (with respect to point O ) can be expressed as:

$$\begin{aligned}
 F_{active} \cdot r \cdot \cos\left(\frac{\beta_{segment}}{2}\right) + F_{tension} \cdot r \cdot \cos\left(\frac{\beta_{segment}}{2}\right) &= G_{Load} \cdot \frac{S}{\beta_{segment}} \cdot \sin(\beta_{segment}) \\
 &+ G_{robot} \cdot \frac{S}{\beta_{segment}} \cdot \sin\left(\frac{\beta_{segment}}{2}\right) \quad (5.1) \\
 &+ F_{tension} \cdot r \cdot \cos\left(\frac{\beta_{segment}}{2}\right) \\
 &+ k_{joint} \beta_{segment}
 \end{aligned}$$

Where  $F_{active} \cdot r \cdot \cos(\beta_{segment}/2)$  is the moment generated by active actuation forces for bending the section;  $G_{Load} \cdot S/\beta_{segment} \cdot \sin(\beta_{segment}) + G_{robot} \cdot S/\beta_{segment} \cdot \sin(\beta_{segment}/2)$  is the moment generated by the gravity of the section and end load;  $k_{joint} \beta_{segment}$  is the moment utilised to bend flexible backbone;  $F_{tension} \cdot r \cdot \cos(\beta_{segment}/2)$  is the moment caused by cable tension.

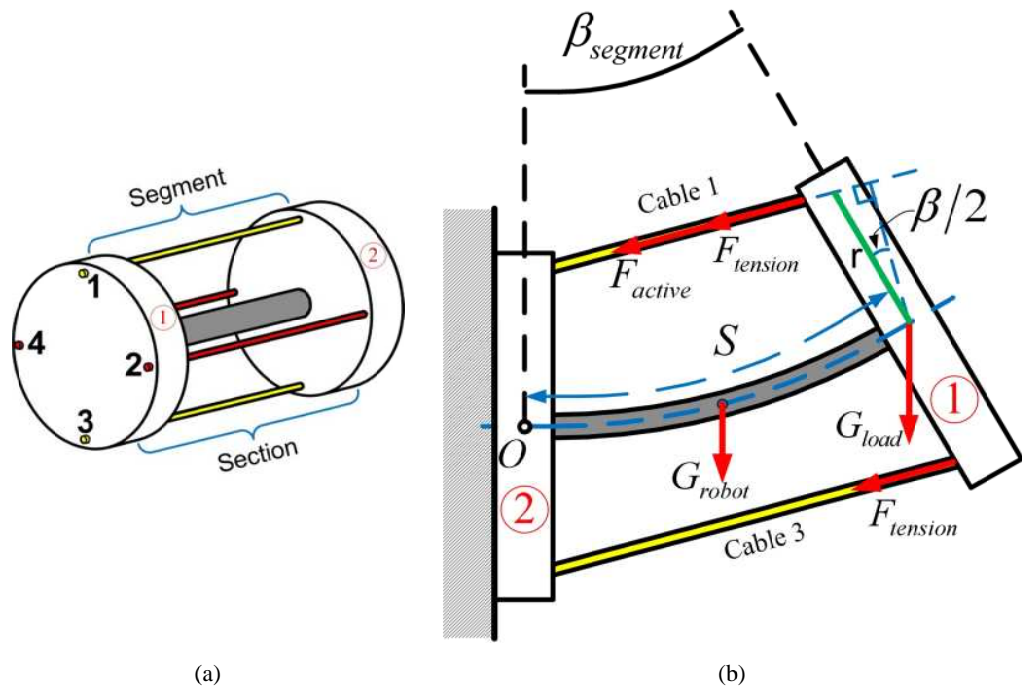


Figure 5-1. (a) Schematic of a single-segment section; (b) the force model of case 1;

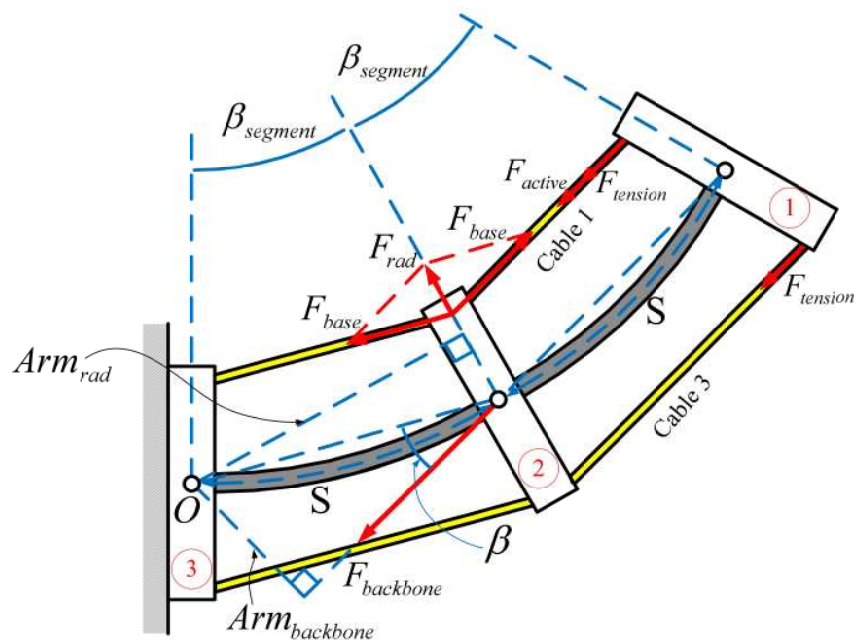
Since identical cable tension forces are applied on two cables of each pair individually, the moments generated by tension forces can be omitted from both sides of **Eq.5.1**.

Hence, the actuation force for a single section can be calculated as:

$$F_{active} = \frac{\left( G_{Load} \sin(\beta_{segment}) + G_{robot} \sin\left(\frac{\beta_{segment}}{2}\right) \right) \cdot \frac{S}{\beta_{segment}} + k_{joint} \beta_{segment}}{r \cdot \cos\left(\frac{\beta_{segment}}{2}\right)} \quad (5.2)$$

### Case two: multiple-segment section

Further, the force analysis of a multiple-segment section is presented. In particular, a two-segment section is utilised as an example, as shown in Figure 5-2. With regard to the tip segment, the force model is as the same as that of single-segment section, which is presented in the previous case. In respect of the base segment, there are two independent forces acting on it: (1) the load on the backbone  $F_{backbone}$ ; (2) the interaction from the cables in radial direction  $F_{rad}$  (including four cables), as shown in Figure 5-2(a).



(a)

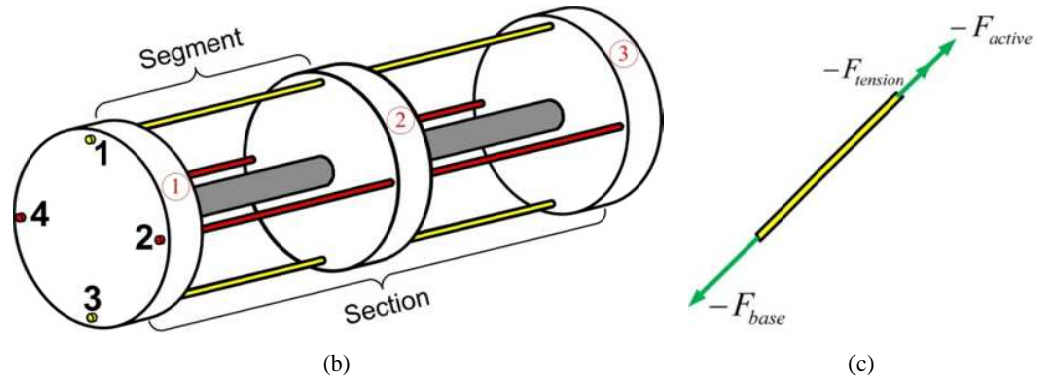


Figure 5-2. (a) Schematic of segment force model; (b) general view of multiple-segment section; (c) the forces acting on the length of cable 1 between disk 1 and 2;

Firstly, the load acting on the backbone is studied. Specifically, since four cables (two pairs) are applying force in the axial direction on disk 1, the load acting on the backbone, which is parallel with the cables between disk 1 and 2, can be expressed as:

$$F_{backbone} = F_{active} + 4F_{tension} \quad (5.3)$$

Hence, the moment generated by  $F_{backbone}$  with respect to point O can be obtained as:

$$\begin{aligned} M_{backbone} &= F_{backbone} \cdot Arm_{backbone} \\ &= 2 \cdot (F_{active} + 4F_{tension}) \cdot \frac{S}{\beta_{segment}} \cdot \sin(\beta_{segment}) \cdot \sin\left(\frac{\beta_{segment}}{2}\right) \end{aligned} \quad (5.4)$$

Where  $Arm_{backbone} = 2 \cdot S / \beta_{segment} \cdot \sin(\beta_{segment}) \cdot \sin(\beta_{segment} / 2)$ .

Secondly, the force in radial direction  $F_{rad}^1$  of cable 1 is analysed. Since a cable needs to be pulled from its two ends to tension it, three forces act on cable 1 between disk 1 and 2 as shown in Figure 5-2 (c), which can be described as:

$$F_{base} + F_{active} + F_{tension} = 0 \quad (5.5)$$

Thus

$$F_{base} = -F_{active} - F_{tension} \quad (5.6)$$

Due to the fact that cable 1 pulls disk 2 from both two directions with the same amount force  $|F_{base}|$ , the resultant force in the radial direction  $F_{rad}$ , can be obtained as:

$$\begin{aligned}
F_{rad}^1 &= 2 \cdot F_{base} \cdot \sin\left(\frac{\beta_{segment}}{2}\right) \\
&= 2 \cdot (-F_{active} - F_{tension}) \cdot \sin\left(\frac{\beta_{segment}}{2}\right)
\end{aligned} \tag{5.7}$$

Hence, the moment generated by  $F_{rad}^1$  can be written as:

$$M_{cable\_1} = F_{rad}^1 \cdot Arm_{rad} \tag{5.8}$$

Where  $Arm_{rad} = S / \beta_{segment} \cdot \sin(\beta_{segment})$ .

Likewise, the moments generated by the other cables (cable 2, 3 and 4) can be obtained. Therefore, the total moment acting on disk 2 with respect to point O, which is caused by the cables, can be expressed as:

$$\begin{aligned}
M_{cable} &= -2(F_{active} + 4F_{tension}) \cdot \sin\left(\frac{\beta_{segment}}{2}\right) \cdot Arm_{rad} \\
&= -2 \cdot (F_{active} + 4F_{tension}) \cdot \sin\left(\frac{\beta_{segment}}{2}\right) \cdot \frac{S}{\beta_{segment}} \cdot \sin(\beta_{segment})
\end{aligned} \tag{5.9}$$

It is very clear that  $M_{cable}$  and  $M_{backbone}$  are equal in magnitude and opposite in direction, which are counteracted with each other completely, so the resultant moment is zero and does not affect the calculation of the actuation force in this section. Hence, along the full length of the cable, the same magnitude of actuation forces acts on cables in the multiple-segment section.

According to **Eq. 5.1**, the actuation force for a section with multiple segments can be expressed as:

$$F_{active} = \frac{\left( G_{Load} \sin(n\beta_{segment}) + G_{robot} \sin\left(\frac{n\beta_{segment}}{2}\right) \right) \cdot \frac{S}{\beta_{segment}} \cdot nk_{joint} \beta_{segment}}{r \cdot \cos\left(\frac{n\beta_{segment}}{2}\right)} \tag{5.10}$$

Where n denotes number of segments in a single section

Further, assuming Figure 5-2 shows a schematic of two single-segment sections of a continuum robot, according to the analysis, it can be concluded that the interaction of

distal sections' cables does not influence on the actuation forces of the proximal sections. Hence, based on Eq. 5.10, the actuation force of multiple sections can be derived. Therefore, the actuation force of an arbitrary section in a multiple-section continuum robot with a random bending shape can be calculated, which helps the designer determine the specifications of the actuation employed in the physical demonstrators.

### 5.1.2. Force calculation interface

In order to make the actuation force calculation user friendly, a MATLAB GUI<sup>5</sup>, as shown in Figure 5-3, was developed based on the multiple-section force model.

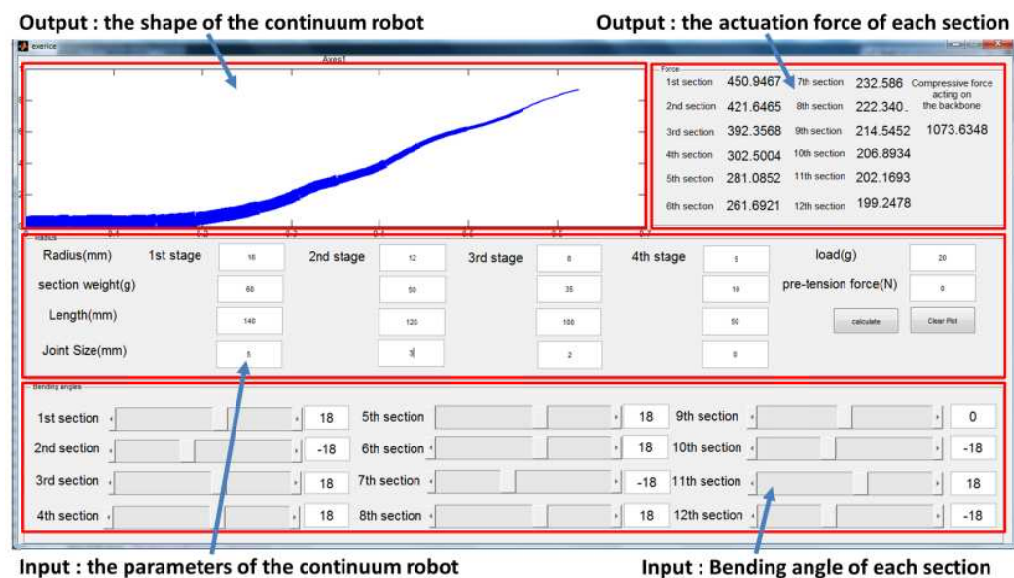


Figure 5-3. MATLAB GUI of the actuation force calculation

Using this interface, the parameters of continuum robot including length, diameter, weight, bending angle, joint size of each section and end load, can be set by the operator, and thus the actuation force of each section can be calculated accordingly. As the output, the shape of the continuum robot can be also shown in the interface, according to the bending angles. And the follow-up experiments (presented in Chapter

<sup>5</sup> graphical user interface

7) indicate that the actuations of the physical demonstrators based on the force calculation of the interface are reasonable.

## 5.2. Buckling Analysis

Buckling failure is a major obstacle for designing the compliant joints of continuum robots, since flexible structure can experience buckling, especially when it is acted by the axial compressive load and constructed with relatively high length to cross-section dimensions ratio [160]. In this section, Euler buckling theory is employed for the evaluation of the buckling problem and the critical buckling load can be calculated as:

$$P_{cr} = \frac{\pi^2 EI}{(KL)^2} \quad (5.11)$$

Where E = Young's modules; I = area moment of inertia; L = unsupported length of column; K = column effective length factor, whose value depends on the conditions of end support of the column: for both ends pinned (hinged, free to rotate), K = 1.0; for both ends fixed, K = 0.50; for one end fixed and the other end pinned, K = 0.699; for one end fixed and the other end free to move laterally, K = 2.0.

Regarding a compliant joint of the continuum robot, it is in the case of one end fixed and the other end free to move laterally, K of which is 2. According to **Eq. 5.11**, a case study of 1mm diameter and 2mm long aluminium rod is given in **Eq. 5.12**.

$$P_{cr} = \frac{\pi^2 EI}{(KL)^2} = \frac{3.14^2 \times 6.9 \cdot 10^{10} \times 4.9 \cdot 10^{-14}}{(2 \cdot 0.02)^2} = 2089 \text{ N} \quad (5.12)$$

As shown in Figure 5-4, the critical buckling load of the aforementioned aluminium rod is 2049.6 N, which is obtained from the FEA simulation (ANSYS).

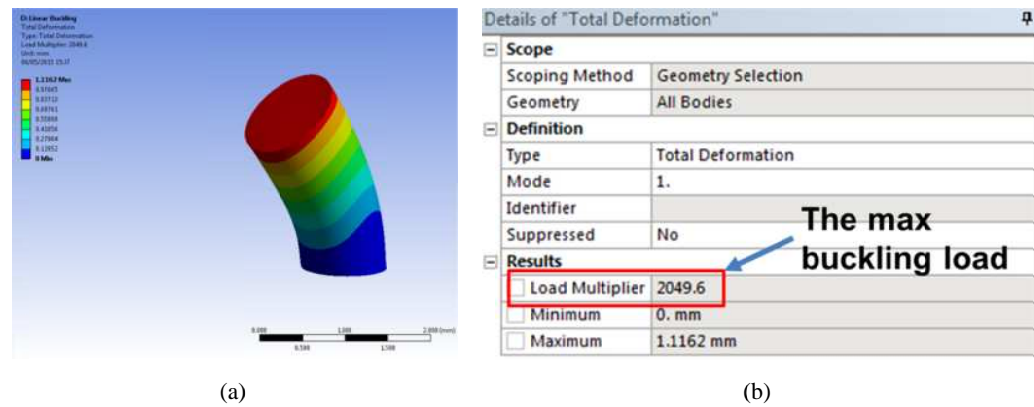


Figure 5-4. (a) FEA validation of a single compliant joint in ANSYS ; (b) the FEA simulation result;

It is found that the error between the calculation and the simulation is 1.5%, which proves that the calculation is appropriate to be applied for guiding the further physical system design. And the follow-up experiments validates the calculation is reasonable, since no buckling problem happened to the joints of the hardware system.

### 5.3. Jacobian Analysis

Jacobian is the mapping between the velocities of the end-effector to those of the actuators. In this section, a general method for deriving Jacobian of the continuum robots proposed in this research is introduced. Further, Jacobian is also utilised in the next section of stiffness analysis, which relates the element stiffness (the actuators & compliant joints) to the system stiffness [2].

Table 5-2. Nomenclature used in this chapter

$V_i$	the linear velocity of the $i^{th}$ pair of cable ( $i=1$ and $2$ )
$V_{B_i}$	the linear velocity of point $B_i$ ( $i=1$ and $2$ )
$J_{segment}$	$2 \times 2$ matrix of the Jacobian of a single-segment section
$\dot{\alpha}_i$	the angular direction velocity of a single segment
$\dot{\beta}_i$	the angular bending velocity of a single segment
$K_{segment}$	the stiffness matrix of a single segment

**Case 1: single-segment section**

Generally, Jacobian of a robot can be obtained by differentiating position kinematic equations with respect to time. Regarding to the geometry and actuation approach of a continuum robot, the analysis of a single-segment section is given firstly in order to simplify the derivation. Jacobian of one segment can be written as [161]:

$$V = J \cdot \dot{\theta} \quad (5.13)$$

Where  $\dot{\theta} = [\dot{\alpha}, \dot{\beta}]$  is the angular velocity of the segment;  $V = [V_1 \ V_2]$  is the linear velocities of the actuators,  $V_1$  and  $V_2$  are the linear velocities of each pair of cables in the segment, respectively.

Differentiating **Eq. 4.5** with respect to time, yields the linear velocity of point  $B_i$ :

$$V_{B_i} = \begin{bmatrix} V_{xi} \\ V_{yi} \\ V_{zi} \end{bmatrix} = (J_{O_1O_2} + J_{O_2B_i}) \cdot \begin{bmatrix} \dot{\alpha}_i \\ \dot{\beta}_i \\ 0 \end{bmatrix} \quad (5.14)$$

Where  $J_{O_1O_2} + J_{O_2B_i}$  is a  $3 \times 3$  Jacobian matrix for point  $B_i$ .

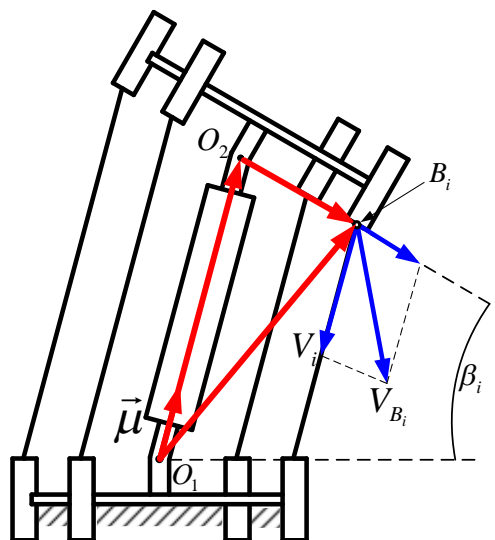


Figure 5-5. Velocity of point  $B_i$  and linear velocity of actuation cable

As shown in Figure 5-5, since the linear velocity of the cable is along the direction of the backbone, thus, dot-multiplying both sides of **Eq. 5.14** by the unit vector  $\bar{\mu}$  yields:

$$V_i = \bar{\mu} \cdot V_{B_i} = \bar{\mu} \cdot \begin{bmatrix} V_{xi} \\ V_{yi} \\ V_{zi} \end{bmatrix} = \bar{\mu} \cdot (J_{O_1O_2} + J_{O_2B_i}) \cdot \begin{bmatrix} \dot{\alpha}_i \\ \dot{\beta}_i \\ 0 \end{bmatrix} \quad (5.15)$$

Therefore, it can be found that the matrix

$$J_i = [J_{i1} \quad J_{i2} \quad J_{i3}] = \bar{\mu} \cdot (J_{O_1O_2} + J_{O_2B_i}) \quad (5.16)$$

is a  $1 \times 3$  matrix for the Jacobian of the  $i^{th}$  pair of cables.

Writing **Eq. 5.16** two times yields Jacobian matrix for two pairs of cables, which can be written as

$$J' = \begin{bmatrix} J_{11} & J_{12} & J_{13} \\ J_{21} & J_{22} & J_{23} \end{bmatrix} \quad (5.17)$$

Since the last element of the angular velocities in **Eq. 5.17** is zero (each segment of the continuum robot has two DoFs), therefore, the Jacobian matrix of one segment can be obtained as

$$V = J_{segment} \cdot \dot{\theta} \quad (5.18)$$

Where

$$J_{segment} = \begin{bmatrix} J_{11} & J_{12} \\ J_{21} & J_{22} \end{bmatrix} \quad (5.19)$$

is a  $2 \times 2$  matrix for the Jacobian of a single-segment section.

### ***Case 2: multiple-segment section***

Further, according to the previous analysis, Jacobian matrix for multiple-segment section is derived. Let the cable displacement of a single segment be  $\Delta l$  in a time  $\Delta t$ . Since all the segments share the same construction and connect serially, the total

stretch in one section is  $n \cdot \Delta l$ , direction and bending velocities are  $n \cdot \dot{\alpha}$  and  $n \cdot \dot{\beta}$ , respectively. Hence, the cable velocity matrix  $V_{section}$  can be expressed as:

$$V_{section} = \frac{n \cdot \Delta l}{\Delta t} = J_{section} \cdot \theta_{section} = J_{section} \cdot \begin{bmatrix} n \dot{\alpha}_i \\ n \dot{\beta}_i \end{bmatrix} \quad (5.20)$$

According to **Eq. 5.20**, omitting  $n$  from both sides, the following equation can be obtained, which is single segment cable velocity:

$$\frac{\Delta l}{\Delta t} = J_{section} \cdot \begin{bmatrix} \dot{\alpha}_i \\ \dot{\beta}_i \end{bmatrix} \quad (5.21)$$

And the linear velocity matrix of cables in one segment  $V_{segment}$  can be expressed as:

$$\begin{aligned} V_{segment} &= \frac{\Delta l}{\Delta t} \\ &= J_{section} \cdot \begin{bmatrix} \dot{\alpha}_i \\ \dot{\beta}_i \end{bmatrix} = J_{section} \cdot \theta_{segment} \end{aligned} \quad (5.22)$$

Where  $\theta_{segment}$  denotes the tip angular matrix of one segment and  $J_{section}$  denotes the Jacobian matrix of one section.

According to **Eq. 5.13** and **5.22**, the following equation can be obtained:

$$J_{section} = J_{segment} \quad (5.23)$$

Therefore, it can be found that the Jacobian matrix of one section is equal to that of one segment in this section. By following the same approach (i.e. differentiation with respect to time of position kinematics equations), Jacobian matrix of other continuum robot structures proposed in this research can be obtained.

Further, a FEA model was utilised for validating the Jacobian matrix and the velocity calculation in ANSYS, as shown in Figure 4-6.

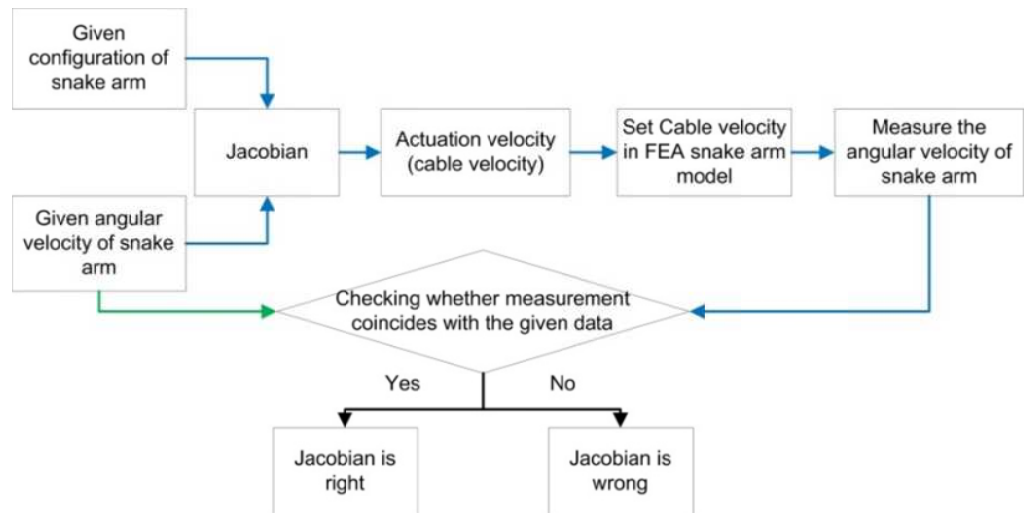
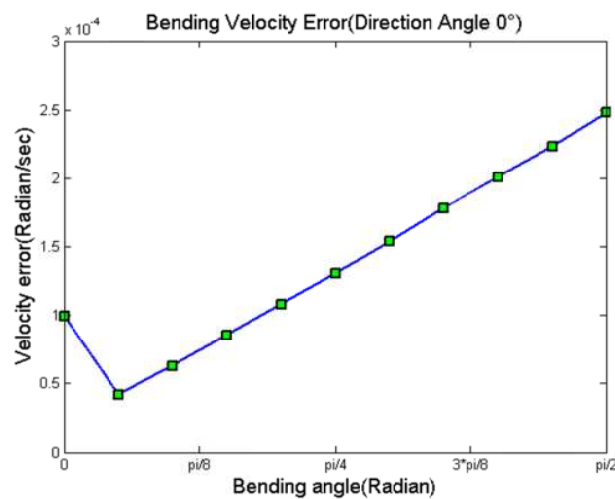
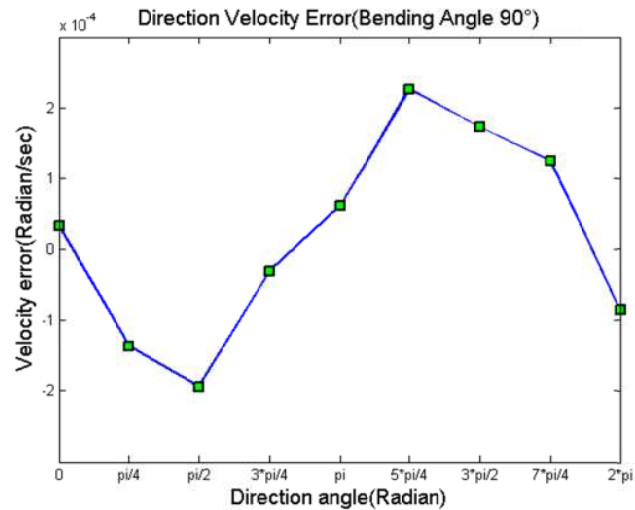


Figure 5-6. Verification method for Jacobian matrix;

Figure 5-6 illustrates the procedure for validating the Jacobian analysis. Specifically, based on Eq. 5.14 and 5.23, actuation velocities (cable velocities) at an arbitrary configuration can be calculated with regard to a given angular velocity of the continuum robot, and then those velocities of the FEA simulation model are set accordingly. Further, the angular velocities of the continuum robot are measured from the FEA model. Comparing the measured data with the given angular velocities, the bending and direction errors are obtained, as shown in Figure 5-7.



(b)



(c)

Figure 5-7. (a) Calculation error of the bending velocity comparing with the FEA model (b) the calculation error of the direction velocity comparing with the FEA model (the specifications of the model are presented in Figure 4-6)

It can be clearly found the max bending and direction errors are  $2.7 \times 10^{-4}$  and  $2.5 \times 10^{-4}$  radian/sec, when the given bending and direction velocities are 0.35 radian/s (20 degrees/s) and 0.63 radian/sec (36 degrees/s), respectively. The max bending and direction velocity errors between simulation and calculation are 0.08% and 0.04%, which proves the analysis reasonable and the approach can be employed to analyse the Jacobian matrix of continuum robots.

## 5.6. Stiffness Analysis

Stiffness is a key parameter for evaluating the design of a robot system. In this part, a 2DoF stiffness matrix of continuum robot will be presented. The stiffness of a robot depends on several factors, including size and material of the links and joints, actuators, control system. In this thesis, the relative flexibility of the compliant joint and steel cable is assumed to be the major sources of the compliance.

Theoretically, in respect of a conventional robot, the stiffness can be expressed as:

$$F = K \cdot \Delta X \quad (5.24)$$

Where  $F$  is the vector of force or moment applied on the tip of the robot;  $\Delta X$  is the displacement of the tip; the stiffness matrix  $K$  can be mathematically expressed as [161]:

$$K = J^T k J^T \quad (5.25)$$

Where  $J$  is the Jacobian matrix of the robot and  $k$  denotes a stiffness matrix, which contains the stiffness information of the compliant elements of the robot, e.g. the joints and the actuations cables.

Since the stiffness of the entire continuum robot depends on the stiffness of a single segment, single segment stiffness is presented firstly. With regards to the proposed concept of the continuum robot, the links are connected by compliant joints and driven by cables, thus the segment stiffness matrix  $K_{segment}$  can be written as [162]:

$$K_{segment} = J_{cable}^T k_{cable} J_{cable} + J_{joint}^T k_{joint} J_{joint} \quad (5.26)$$

Where  $J_{cable}^T k_{cable} J_{cable}$  denotes the stiffness matrix caused by the actuations (cables),  $J_{joint}^T k_{joint} J_{joint}$  denotes the stiffness matrix provided by the compliant joints.  $k_{cable}$  and  $k_{joint}$  are the stiffness matrixes of steel cables and compliant joints in a single segment.  $J_{cable}$  &  $J_{joint}$  are the Jacobian matrixes relating the segment angular velocities to the cable and compliant joint velocities.

**Eq. 5.27** represents the cable stiffness matrix and each element represents the stiffness constant of a cable.

$$k_{cable} = \begin{bmatrix} k_1 & 0 \\ 0 & k_2 \end{bmatrix} \quad (5.27)$$

Where  $k_1$  and  $k_2$  are the cable stiffness constant in X and Y direction. As aforementioned, Jacobian matrix  $J_{segment}$  maps the angular velocities of a segment to

those of the actuations, which is as the same as  $J_{cable}$ , hence,  $J_{cable}$  is equal to the Jacobian matrix  $J_{segment}$ .

**Eq. 5.28** represents the stiffness matrix determined by the compliant joints in a single segment. Each element of the matrix represents the compliant joint stiffness constant in different axes.

$$k_{joint} = \begin{bmatrix} EI/(2l_{joint}) & 0 \\ 0 & EI/(2l_{joint}) \end{bmatrix} \quad (5.28)$$

Since the resultant angular velocities of the compliant joints are equivalent to those of a segment, the joint Jacobian  $J_{joint}$  is an identity matrix ( $J_{joint} = I$ ).

Therefore, the stiffness matrix of a single segment of continuum robot can be obtained:

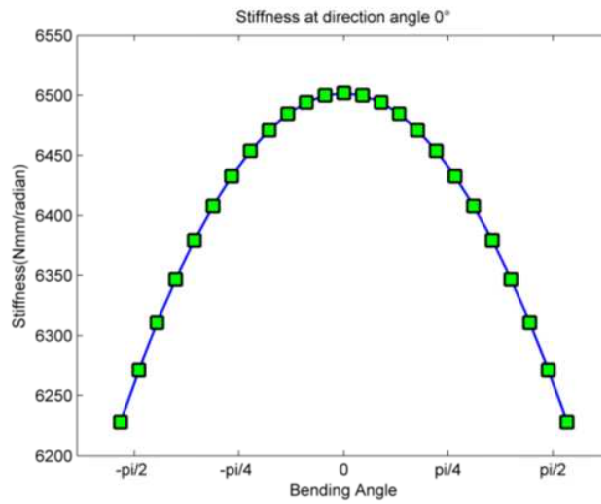
$$K_{segment} = J_{segment}^T k_{cable} J_{segment} + k_{joint} \quad (5.29)$$

Due to the fact that all segments in one section share the same construction, thus, the stiffness matrix of a section can be express as:

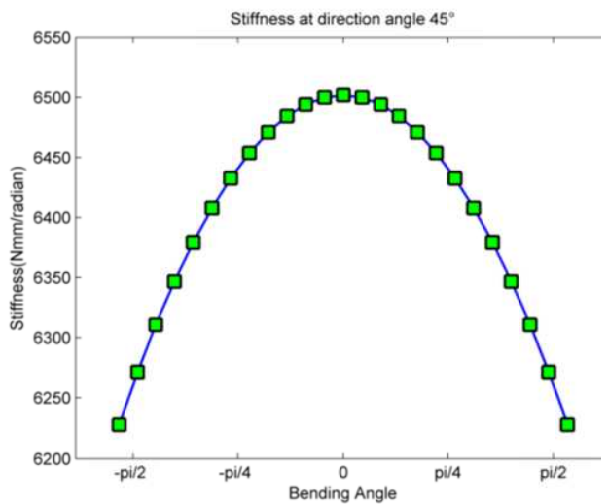
$$K_{section} = \frac{K_{segment}}{n} \quad (5.30)$$

Where number of segments in one section is denoted as n.

With regard to bending angle range  $(-\pi/2, \pi/2)$ , the stiffness of one section at direction angle  $0^\circ$  and  $45^\circ$  are shown in Figure 5-10. For example, the stiffness of 0.75mm diameter 100mm long steel cable is 150 N/mm. The stiffness of 3mm elastic rod is 1314 Nmm/radian. It can be found that the max and min stiffness are 6501 and 6227 Nmm/radian. Hence, the stiffness matrix on one section of continuum robot is obtained.



(a)



(b)

Figure 5-8. Stiffness of one section: (a) direction angle 0°; (b) direction angle 45°

As shown in Figure 5-9, the procedure for validating the stiffness matrix is presented. Specifically, based on **Eq. 5.30**, the deflection of one segment at a configuration is calculated with regard to a given moment applied on the tip. The stiffness matrix is proved by comparing the calculation to the simulation (FEA).

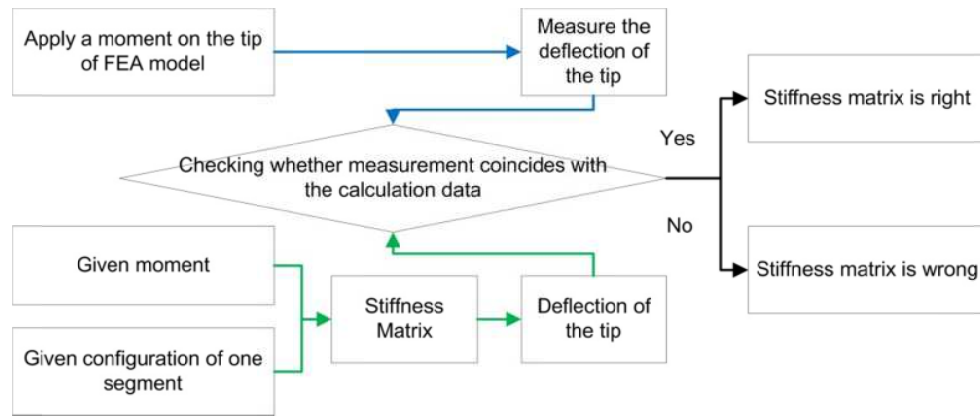


Figure 5-9. Verification method for stiffness matrix

As shown in Figure 5-10, a simulation model is built in ANSYS. Comparing with the model using for validating kinematics model (Figure 4-6), the only difference is that cables are replaced by springs in this model, so that they can generate elongations for simulating the real performance of steel cables when they are pulled. All of the other parameters share the same dimensions and property with the previous simulation model.

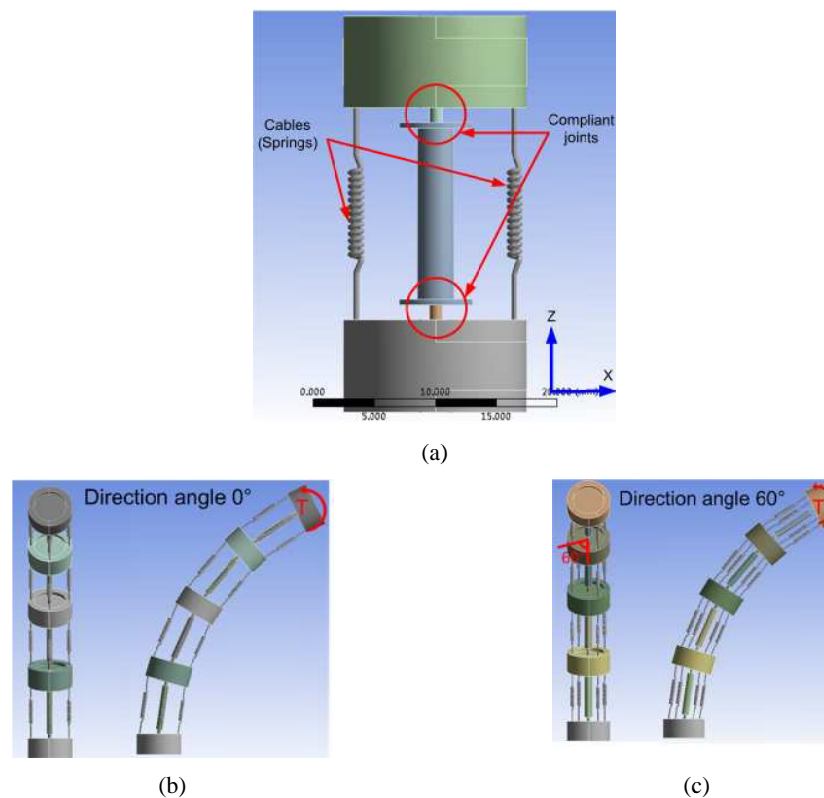
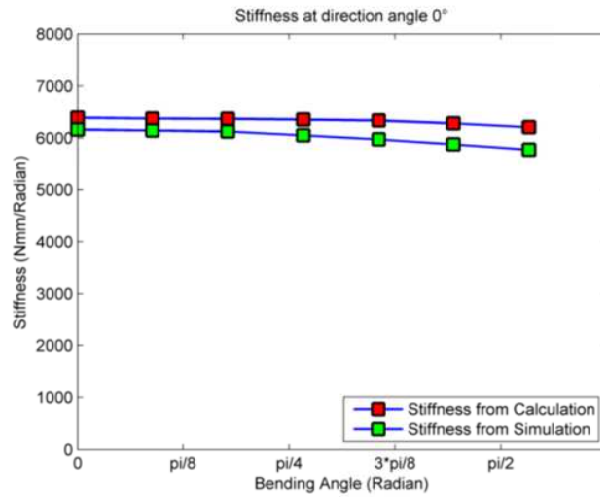
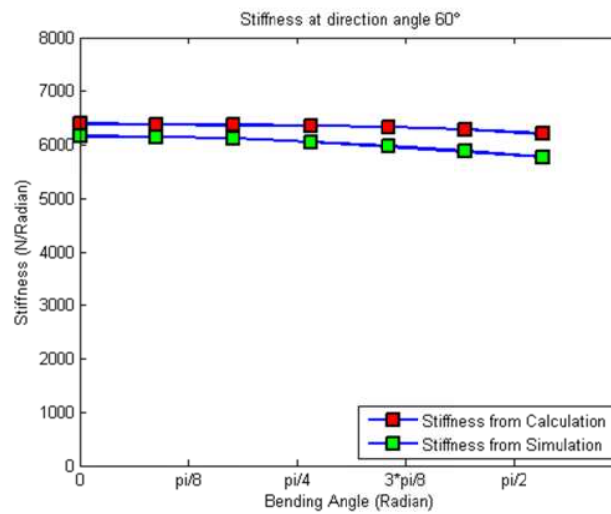


Figure 5-10. Simulation models for validating the stiffness analysis

Set the stiffness of spring is 600 N/mm, which is equal to that of 25mm long and 0.75mm diameter commercial steel cable (one segment). And set the stiffness of a 3mm elastic rod is 1314 Nmm/radian, which is that of a 3mm long, 1mm diameter aluminium rod. Finally, a moment is applied on the tip, which is 200Nmm.

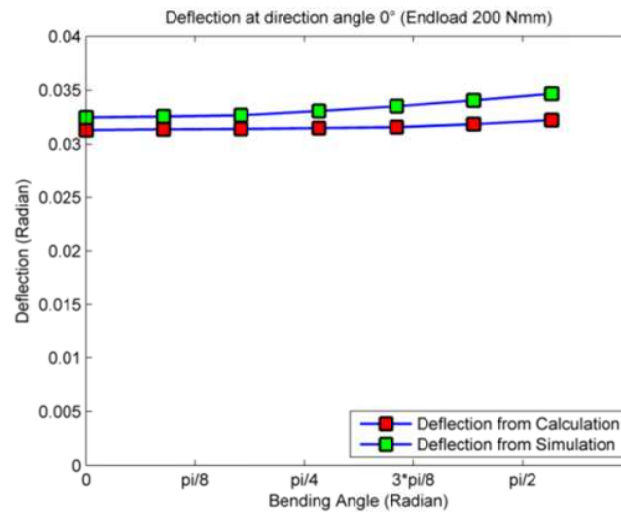


(a)

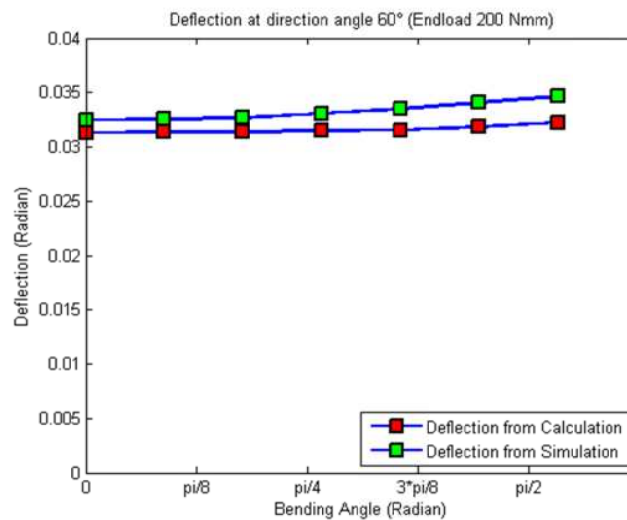


(b)

Figure 5-11. Stiffness of a one-section continuum robot vs different section's bending angles



(a)



(b)

Figure 5-12. Deflection of one section continuum robot vs different section's bending angles

Figure 5-11 presents the stiffness of one section continuum robot (at the bending angles  $0^\circ$ ,  $20^\circ$ ,  $40^\circ$ ,  $60^\circ$ ,  $80^\circ$ ,  $100^\circ$  and  $120^\circ$ ; the direction angles  $0^\circ$  and  $60^\circ$ ) is obtained by calculation and simulation models, respectively. And the deflections caused by 200Nmm end load (at direction angle  $0^\circ$  and  $60^\circ$ ) are presented in Figure 5-12. The max deflection is 0.0344 in radian ( $1.9710^\circ$ ), which happens at  $90^\circ$  bend. It can be found that the max error between simulation and calculation is 7% in a bending range  $(0, \pi/2)$ . Therefore, the stiffness matrix presented in this paper is proved and can be used to present the stiffness of a continuum robot. In the design process, the

---

stiffness analysis and simulation was utilised to estimate the performance of the hardware and to optimize the design.

## 5.4. Conclusions

In this chapter, several fundamental modelling including actuation force, joint buckling, Jacobian and stiffness are presented. Based on the force analysis, unlike the conventional approach utilized in the actuation analysis of rod-driven continuum robot (principle of virtual work), a static analysis of cable-driven continuum robot is developed, by considering gravity, end load, cable tension, force for bending flexible backbone and the interaction from distal sections' cables. Hence, the actuation force of an arbitrary section in a multiple-section continuum robot with a random bending shape can be calculated, which helped the designer determine the specifications of the motors and steel cables utilized in the physical demonstrators. The following experiments prove the actuation selections of the demonstrators are reasonable.

Since compliant joint is relatively flexible comparing with conventional rigid joint, the joint can be buckled if overloaded, which can cause poor control accuracy and even physically fail the whole system. Hence, a method for calculating the critical buckling load of compliant joints is presented, which was utilized for guiding the compliant joint designs of the physical demonstrators and validated on the following trials.

Further, the Jacobian of multiple-segment section is presented, so it allows the actuation velocities able to be calculated according to the given angular velocities of a section. Finally, based on the Jacobian analysis, the stiffness of the multiple-segment section is analyzed and validated by the simulation with a max 7% error.

## Chapter 6 Prototypes of the continuum robots

In order to evaluate the aforementioned continuum robot design concepts, four prototypes were designed and built, which utilised both of the two families of design concepts, i.e. double-pivot and twin-pivot compliant joint constructions. Firstly, a two-section prototype was developed to evaluate the best elastic material for building continuum robot backbones. Further, the 2<sup>nd</sup> (full length continuum robot with single double-pivot backbone) and 3<sup>rd</sup> (three-section continuum robot with twin-pivot backbone) prototypes were built. It was found that twin-pivot compliant joint construction (family B) has better stiffness and less twisting (rotation around its axis of symmetry) problem than double-pivot compliant joint construction (family A). Finally, based on twin-pivot compliant joint construction, the final full length continuum robot (length > 1200mm) was designed and built.

### 6.1. Prototype 1 (continuum robot with segmented single backbone pivot)

In order to select the backbone material (the material is required to have an appropriate elastic modulus, which allows the backbone to have a proper stiffness and bending capability), the first prototype, as shown in Figure 6-1, was constructed that consists of two articulated sections with the total length of 200 mm and the diameter of 15 mm.

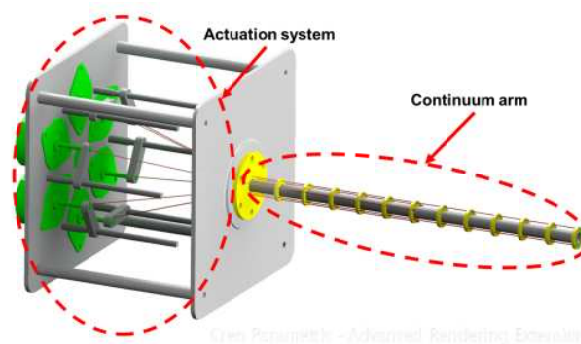


Figure 6-1. CAD model of the 1st demonstrator (the details are explained in Figure 6-2 & Figure 6-3)

In each section, there are 5 segments which are constructed with six evenly spaced through holes in each disk for guiding cables along to the attached. The continuum arm is driven via cables connected to an actuation pack (150x150x144mm) consisting of six stepper motor non-captive linear actuators (three for each section) that are able to produce a thrust force of 55N and stroke length of 75mm (LP3575S0504).

### 6.1.1. Evaluation of backbone materials

The two-section prototype was used to evaluate the design concepts before building a full scale system. The following backbone concepts were tested on this system:

- 1) Concept one: spring-style compliant backbone (mono-coil tube [163]) (Figure 6-2(a));
- 2) Concept two: multiple elastic backbones (super-elastic NiTi rod) (Figure 6-2(b));
- 3) Concept three: single elastic backbone (super-elastic NiTi rod) with cable actuations (Figure 6-2(c)).

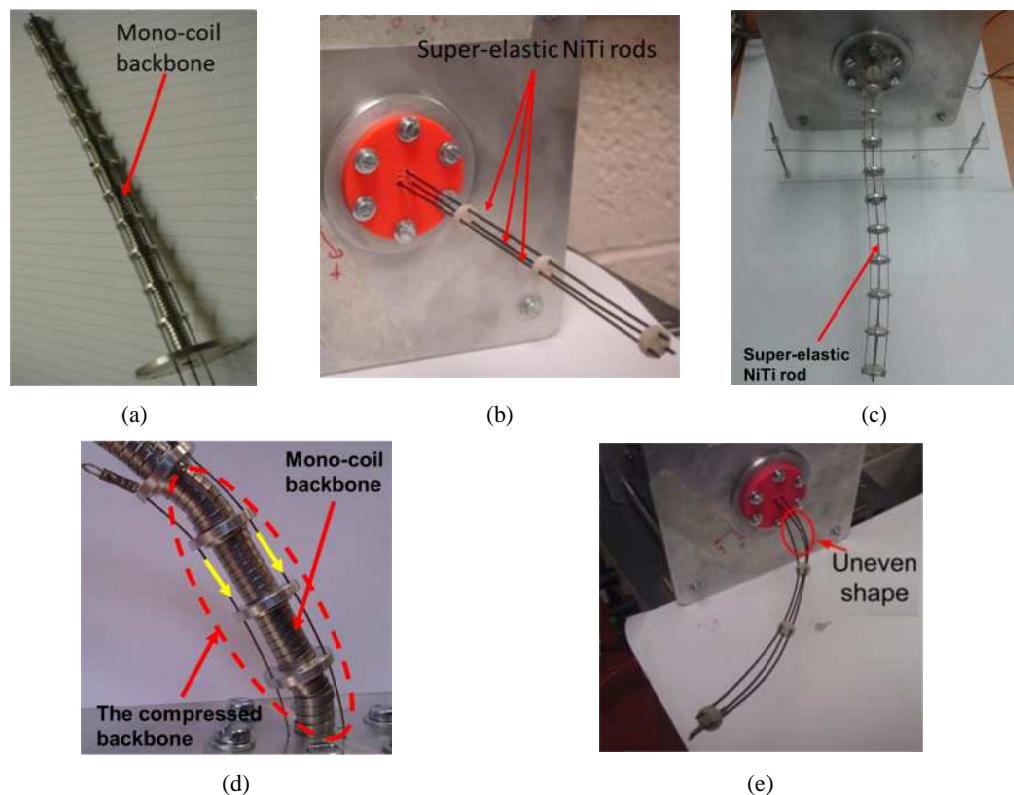


Figure 6-2. (a) Concept one: spring-style compliant backbone (mono-coil tube); (b) concept two: multiple elastic backbones; (c) concept three: single elastic backbone; (d) kinematic performance of spring-style backbone; (e) kinematic performance of elastic rod actuation;

Specifically, the first design utilizes a piece of mono-coil tube as the backbone (Figure 6-2(a)), which provides a working channel for the machining tools to be delivered to the tip of the continuum robot along the axial direction. Concept one demonstrated a good capability of flexibility. However, the spring-like construction makes it difficult to evaluate/control the backbone length, since the varying actuation force along the longitudinal direction compress the backbone to variable lengths in the process of operation, as shown in Figure 6-2(d), which causes a poor accuracy and stiffness of the continuum robot [105].

The second system consists of three super-elastic NiTi rods as the backbone and the mechanism for transmitting the actuation force. All the disks are mounted to one rod by glue, while the other two rods are attached to the tip disk and can run through the holes of other disks along the longitudinal axis (Figure 6-2(b)). Unlike steel cables, the elastic rod can push and pull for adjusting the orientation of the tip disk. Hence, two linear actuators are theoretically needed for single section, which allows fewer actuations than the other two concepts. However, since the rods bend in an uneven shape rather than a circle arc (Figure 6-2(e)) when it is pushed, a complex algorithm of actuation compensation is required for the precise position control [132].

The third concept (Figure 6-2 (c)) employs a single central located super-elastic NiTi rod as the backbone. Comparing with the other two concepts, it has following advantages:

- 1) NiTi rods have good stiffness in longitudinal direction, thus they do not have the variable backbone length problem, comparing with the concept 1;
- 2) This system uses steel cable as the actuation, which is much easier to build a kinematic model for it, comparing with the concept 2;

Therefore, super-elastic NiTi rod was determined to be utilized as the backbone of the next prototype.

### 6.1.2. Actuation system

Figure 6-3(a) illustrates the mechanism for a single linear motor: there is an intermediary action lever fixed to the lead screw of the motor, which is able to move along the action bar (this is utilized to stop the rotation of the lead screw, so that the motor can generate a linear movement). Six linear motors are evenly spaced around the longitudinal axis in the actuation system for controlling two sections, as shown in Figure 6-3(c). The specifications of the linear motor are shown in Table 6-1.

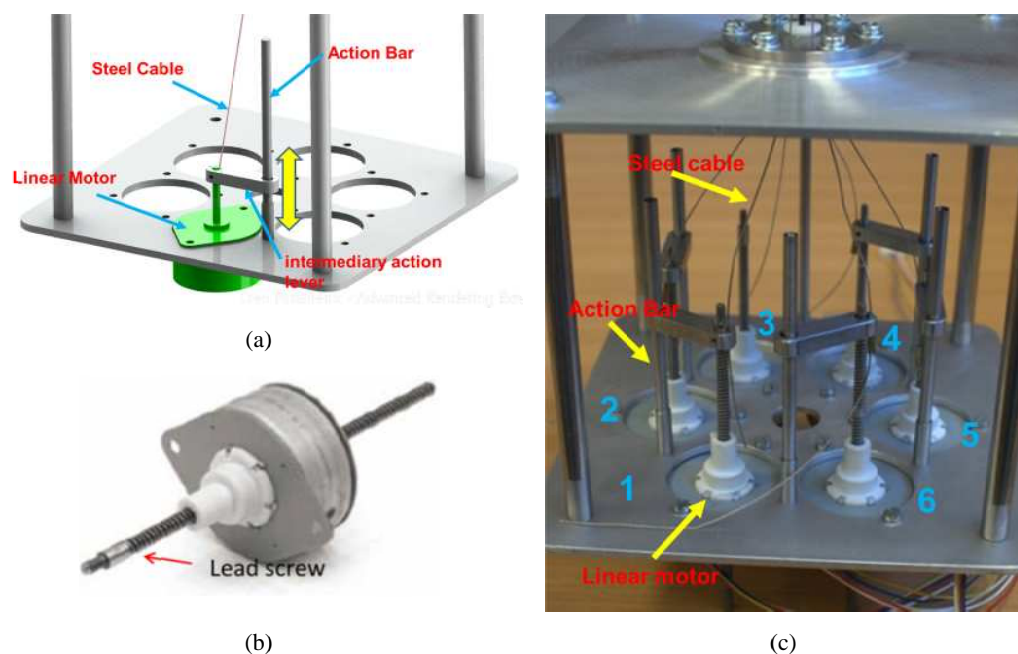


Figure 6-3. Actuation system of the two-section continuum robot: (a) actuation mechanism; (b) linear motor; (c) the six-motor actuation system;

Table 6-1 Specifications of the linear motor

Type	Thrust	Resolution	Pitch	Current	Weight	Stroke
	N	Mm/step	mm	A	kg	Mm
LP3575S0504	55	0.0254	1.22	0.46	0.086	17.5

The actuation system enables each cable to be tensioned and controlled individually, but it requires relatively large space for placing the electrical motors. Since the

continuum robot needs to be carried by a walking hexapod, the size and weight of the actuation system needs to be minimised. Therefore, apart from the conventional actuation method (electrical motor), Shape Memory Alloy was also tested for validating a new actuation approach. Shape Memory Alloy (Nitinol wire [164]) contracts and generates a pulling force when activated and stretches back to its original length by a counter force applied to it in the opposite direction when inactivated, which shows the potential to achieve a large actuation force whilst reducing the size and weight of an actuation pack. For example, a test was performed by using 0.3mm diameter wires (100mm in length), which can contract around 5% of its length and generate a pulling force of 12N per wire when it is heated, as shown in Figure 6-4.

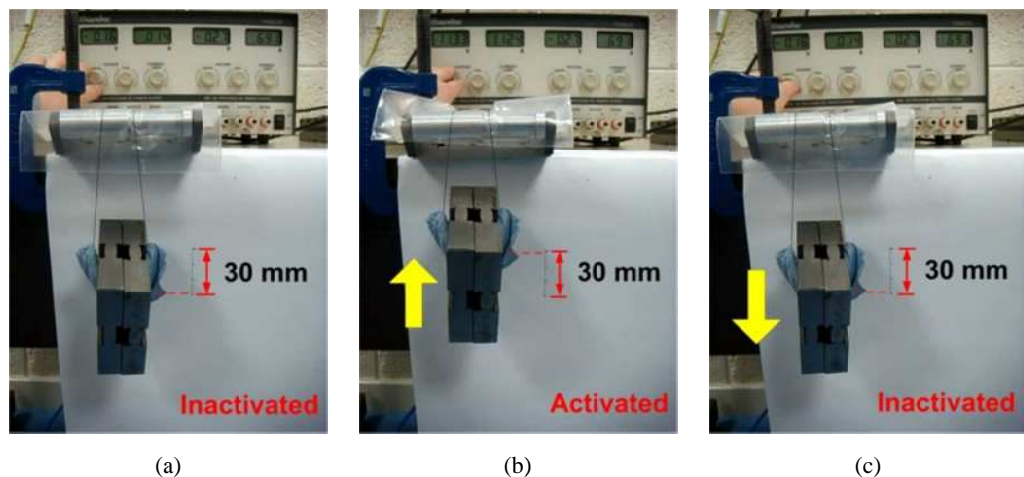


Figure 6-4. Stroke & force test of NiTi wire: (a) the original position; (b) the activated wire contracts to the max stroke position; (c) the inactivated wire is pulled back to the original position by the weight;

According to the initial experiment, two concepts were generated and evaluated: concept one: using long SMA NiTi wires that run from the base to the attached point on the disks and replace steel wires for driving a continuum robot (Figure 6-5); concept two: using SMA as replacements to the motors in the actuation pack where the SMA wire coils on a spool and drives the continuum manipulator (Figure 6-6).

Firstly, a one-DoF prototype was designed to test concept one, as shown in Figure 6-5(a). In this demonstrator, two pairs of NiTi wires were connected to a power

supplier separately, which individually attach to the end of the pivot joint (Figure 6-5(b)). By alternatively activating one pair of the NiTi wires, the system can generate a one DoF rotation, which has the advantage of light weight and high power-to-weight ratio (comparing with the motor actuated demonstrator), as shown in Figure 6-5 (c)&(d). However, the linear arrangement of NiTi wires takes more space than the electrical motors in longitudinal direction, thus it requires a more compact way to arrange the wires.

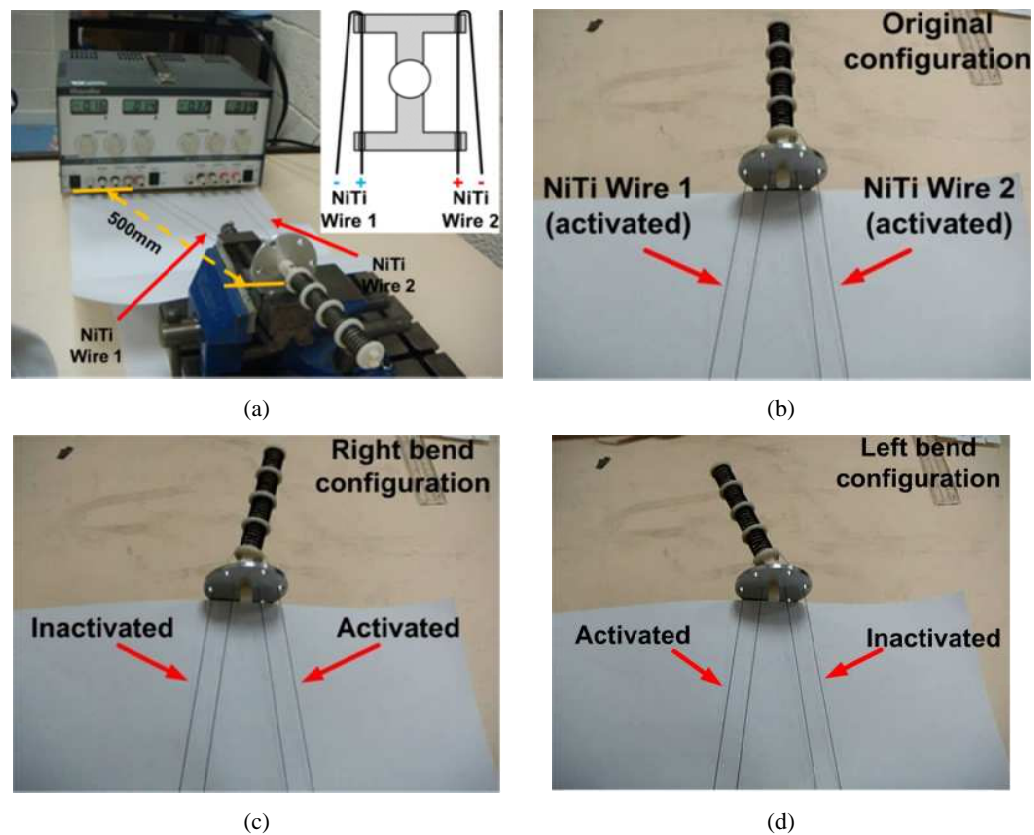


Figure 6-5. NiTi actuated demonstrator utilising concept one

In concept two, as shown in Figure 6-6(a), a NiTi wire (0.3 mm in diameter, 600 mm in length) was coiled on a spool (36 mm in diameter) for measuring the stroke of the wire in the coiling arrangement (since the spool and SMA NiTi wires are all black in colour, it is not easy to identify the coiled wires from the photos). In this experiment, a load (500g) can be lifted by the activated NiTi wire (Figure 6-6(a)), but the stroke ratio decreased (from 5% to around 4% (24 mm/600mm: 4% of its length)) comparing

with the first concept, due to the friction between the wire and the spool. Further, a one-DoF prototype was built for demonstrating the second concept, as shown in Figure 6-6(b), (c) & (d). However, the decreased stroke ratio of the NiTi wire makes the precise position control of the one-DoF mechanism difficult.

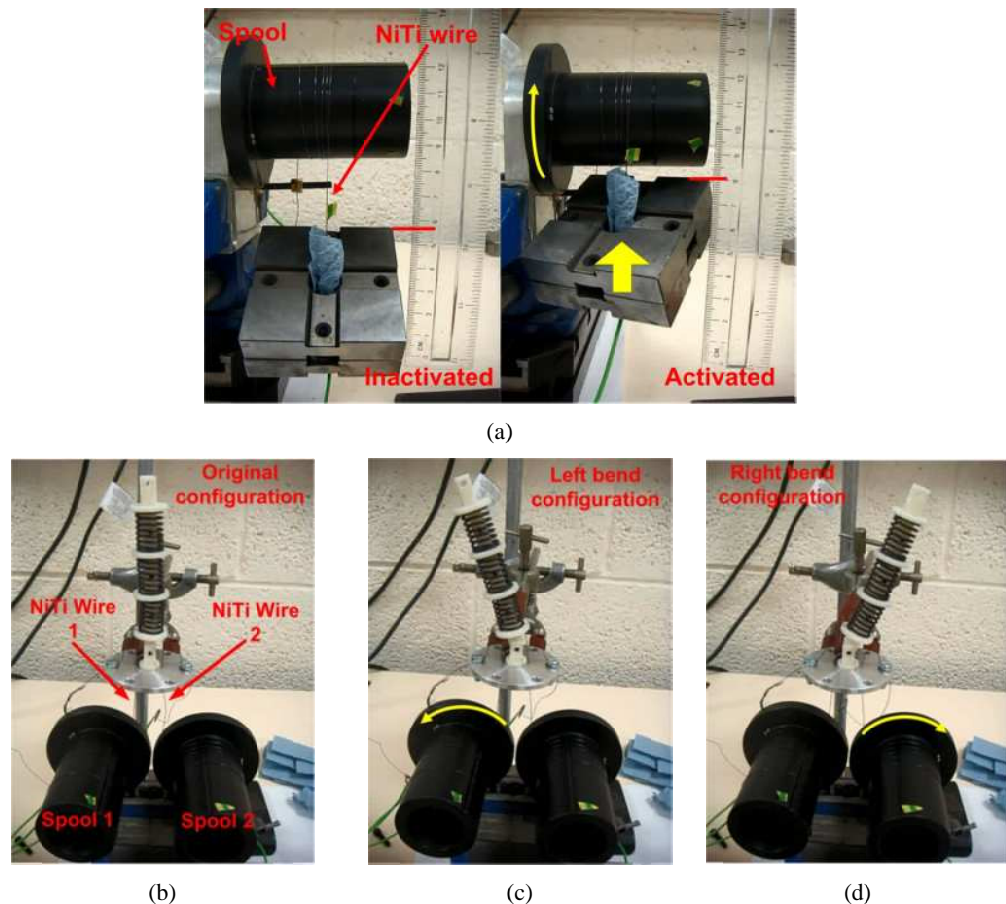


Figure 6-6. NiTi actuated demonstrator utilizing concept two

For studying the NiTi wire control, a linear NiTi actuation demonstrator was built to test the control solution, as shown in Figure 6-7. The system consists of a 0.3 mm diameter and 200 mm long NiTi wire, a slider and a bias steel spring, which can drive the slider back the original position when the NiTi is cooling down. And a linear sensor is combined into the system to feedback the position of the slider. However, the test results show the accurate position control is even difficult to achieve and maintain in the linear cable arrangement. Specifically, the shape memory alloy NiTi wire has a high power-to-weight ratio, which can help to minimise the size and weight of the

actuation system. However, it was found that the precise control is difficult to be achieved, since the nonlinear Temperature/ Strain characteristic of NiTi wire. Therefore, the conventional actuation (the electrical motor) was utilised in the following prototypes.

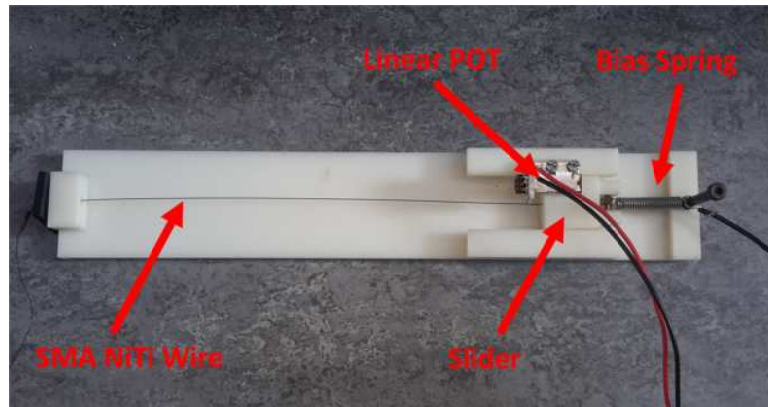


Figure 6-7. Linear NiTi actuation system

## 6.2. Prototype 2 (full length double-pivot continuum robot)

Following the two-section prototype, a full length demonstrator was developed to validate the concepts at the scale of 1.2 m in length. In order to increase the stiffness, the family of the double-pivot compliant joint construction (see Chapter 3.2.1.) was employed, and the concept utilising a single short flexible rod as the compliant joint (Figure 3-7) was selected to be deployed for building this demonstrator, because of the simple construction.

### 6.2.1. Continuum arm

According to the requirement of reaching the first stage of LPC (low pressure compressor) from the front of a gas turbine engine, the full length demonstrator (Figure 6-8 (a) & (b)) is designed to have a length of 1200mm and consists of twelve articulated sections (100 mm long per section), each capable of being bent 90 degrees. In the demonstrator, every section comprises of four segments, each having two compliant joints and a non-flexible steel tube connected in series, as shown in Figure 6-8 (c) & (d). In particular, super-elastic NiTi rods (3mm in length; 1 mm in diameter)

are utilised as the compliant joints and the non-flexible steel tube is utilised to reduce the propensity for joint buckling. In each section, two pairs of steel cables are attached to the tip disk and go through all the following sections, while the other end of the cables attach to the spool mechanism.

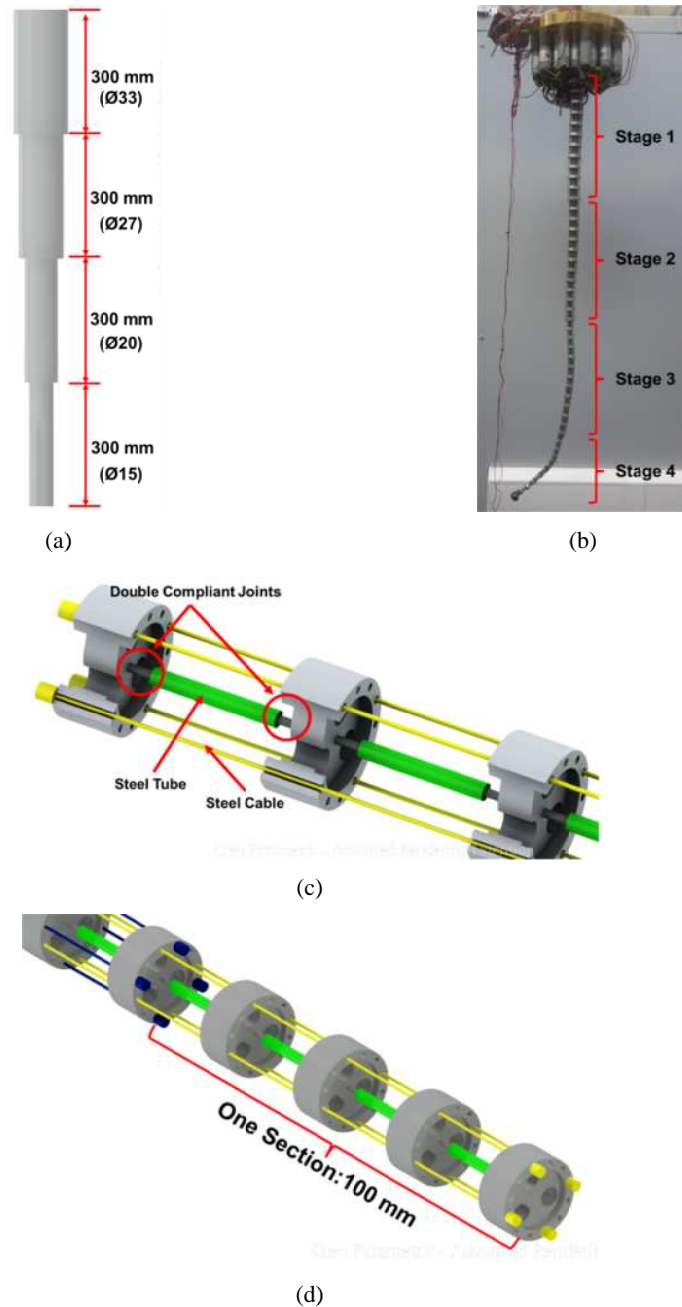


Figure 6-8. (a) Schematic illustration of the full length continuum; (b) photograph of the full length continuum; (c) CAD of a single segment design; (d) schematic of single section design;

The continuum arm has a tapered design with 4 stages of lessening diameters (33mm, 27mm, 20mm and 15mm and the average diameter/length of the arm is 0.02), in order to balance the extremes of actuation force (Figure 6-9). Three 3.5mm diameter working channels are contained within the separating disks that guide and attach the control wires of the end effectors.

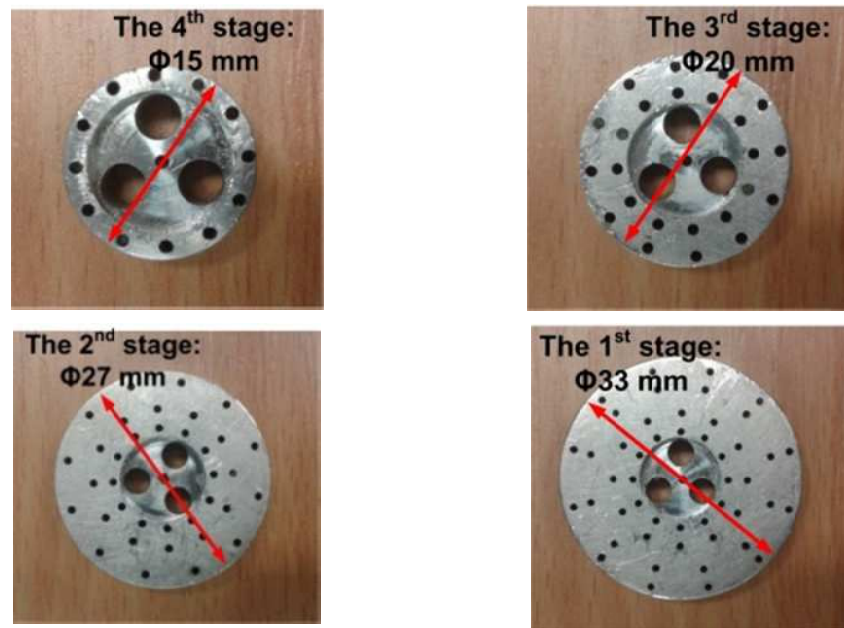


Figure 6-9. Disk designs of four stages

According to **Eq. 5.11**, the critical buckling load of compliant joint (3mm in length; 1mm in diameter; material: superelastic NiTi) was calculated in order to avoid the joint buckling (551.8N). Further, by using the force calculation program (Chapter 5.1), the max actuation force for every section was computed and the details are presented in Table 6-2. (Note that the prototype was designed to be hanged on the ceiling for demonstrating the tip-following control [165].)

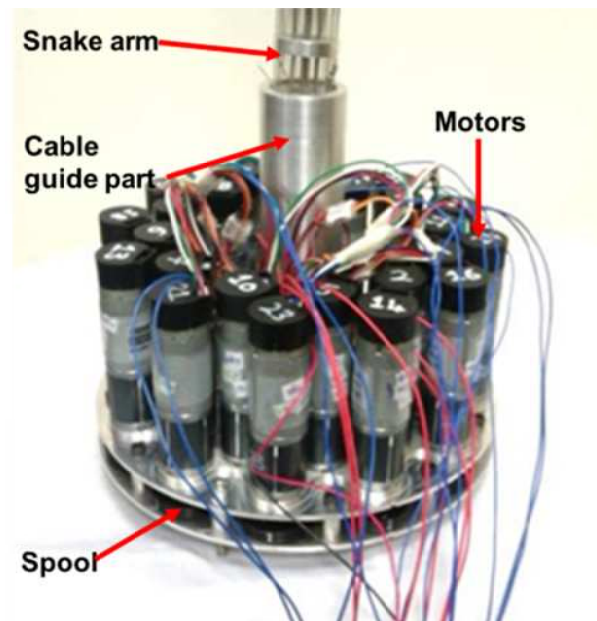
Table 6-2. Max actuation force in each stage

		Max actuation force	Section Mass	Diameter
Stage 1	Section 1	34 N	74 g	33mm
	Section 2	31 N		

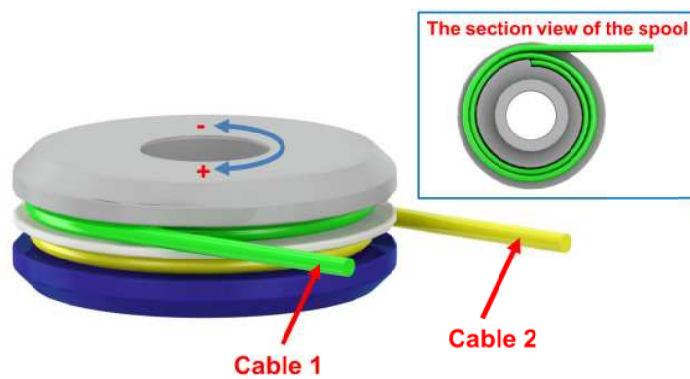
	Section 3	28 N		
	Section 4	27 N		
Stage 2	Section 5	25 N	48 g	27mm
	Section 6	22 N		
	Section 7	22 N		
Stage 3	Section 8	19 N	26 g	20mm
	Section 9	17 N		
	Section 10	18 N		
Stage 4	Section 11	17 N	17 g	15mm
	Section 12	15 N		
Total		275 N	495 g	

In order to provide sufficient electrical motor transmission to meet the arm articulation requirements, DC motors with high ratio gears (304:1) are used that produce 2.4Nm of torque. This gives a max cable pull force of 143N each which is carried in additional bearings mounted to the spools. As the actuation systems are somehow the results of an ordinary design exercise that has been the work of an experienced engineering designer associated to MiRoR project, they were not the focus of this thesis and therefore, they are presented very briefly as they allow the realisation and the demonstration of proposed continuum arm designs. As shown in Figure 6-10(a), this electromechanical actuation pack is designed to be light (7.5Kg) and compact (O/D 235mm x 126mm total height), with planned design improvements (more torque, lower weight) making it suitable to be coupled and carried by the walking hexapod proposed in MiRoR (Chapter 1.3) when required. Figure 6-10(b) illustrates the concept of the spool mechanism which makes two cables coiled in the pattern of Archimedean spirals. However, in the experiment, it was found that when the spool rotates an arbitrary angle, the displacement of the cable in one side is not equal to that

of the other cable attached on the same spool, thus it cause one cable is not tensioned, which renders the decrease of the stiffness. In order to solve this problem, another cable coiling approach was employed to build the spool mechanism for the 3<sup>rd</sup> demonstrator.



(a)



(b)

Figure 6-10. (a) actuation pack of full length continuum robot; (b) concept of the spool employed in the 2<sup>nd</sup> demonstrator;

The following trial (see detail in Chapter 7.2) proves this system have great bending capability, high length/diameter ratio, lightweight construction and an appropriate navigation accuracy. However, the twisting problem of the central located backbone needs to be addressed, which drastically affects the control of the system. Further,

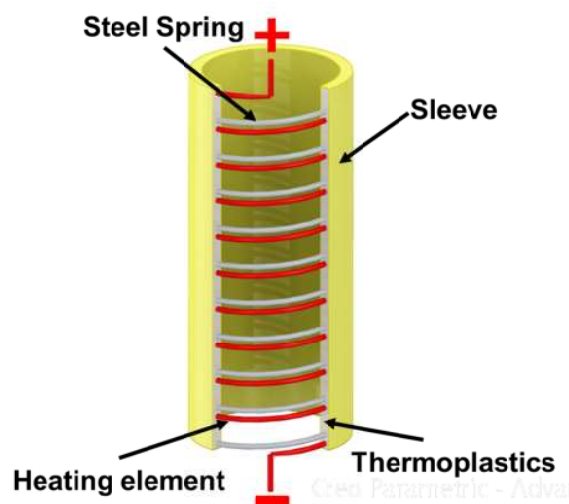
regarding the actuation system, the design of the spool needs to be modified in order to keep the tensions for both cables in a spool.

### 6.2.2. Variable stiffness system

For evaluating the stiffening concept, several variable stiffness systems have been built and tested on the second continuum robot demonstrator, which can turn an ordinary continuum manipulator into a variable-stiffness continuum robot. These non-articulated, tubular constructions consist of:

- (1) A power supplier (up to 24V);
- (2) Heating elements (Nichrome wires);
- (3) Thermoplastics (polymorph: liquid-like, when melt);
- (4) External & internal sleeve (rubber/Kevlar tube) for constraining the thermoplastics.

Prototype (1): As shown in Figure 6-11(a) & (b), the system comprises a compression steel spring in polymorph covered by Kevlar sleeve. The system can be heated up by activated NiCr wire and softened at the temperature of 60 °C. However, it was found that the max bend of the continuum robot (approx. 30°) is limited by the spring (great force is required for bending the spring) and Kevlar tube (low elongation ratio).



(a)

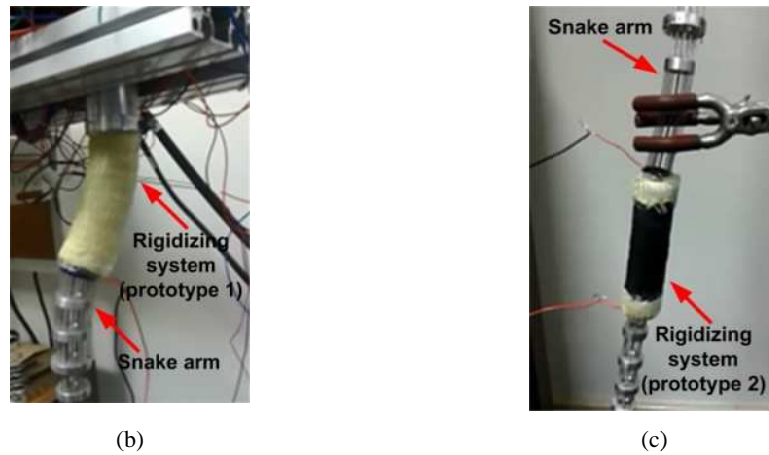


Figure 6-11. Variable stiffness system prototypes: (a) schematic of variable stiffness system; (b) prototype 1; (c) prototype 2;

Prototype (2): This system is constructed along the same principles but with alternative sleeve material (rubber which has a great elongation ratio) and does not use steel spring for increasing the stiffness. The demonstrator was built and integrated with the continuum robot to test the bending capability of the variable-stiffness system, as shown in Figure 6-11(c). It was found that, comparing with prototype 1, this system allows the continuum robot generate greater bending angle in the soft state while still having a good stiffness in the rigid state.

Based on the experiments of these two variable stiffness systems, the main elements of the system (thermoplastic: polymorph; heating element: NiCr wire; sleeve: rubber) were determined and utilised in the next prototype.

### 6.3. Prototype 3 (Three-section continuum robot with twin-pivot backbone)

The second prototype has great bending capability and high length/diameter ratio. However, in the experiments, it was found that the construction has a twisting problem and the stiffness needs to be enhanced during the “moving” mode. Therefore, the aforementioned twin-compliant joint concept was employed in the 3<sup>rd</sup> demonstrator (three sections) used as a stepping stone towards the final design, which was built

within the design remit to closely follow the intention for the final continuum robot design.

### 6.3.1. Continuum arm

The prototype (as shown in Figure 6-12(a)) was constructed with twin-pivot compliant joint and twin actuation per section (Chapter 3.2). The system consists of three sections and each section contains 10 segments. Each section is 100 mm long and composed of two pairs of cables (attach to the tip of each section), and all the disks are connected by twin 1.5mm long, 1mm diameter super-elastic NiTi rods, which has greater single joint buckling load (2207 N) than previous design and gives the construction better stiffness, as shown in Figure 6-12(a) &(b). The whole arm weight is 62 g.

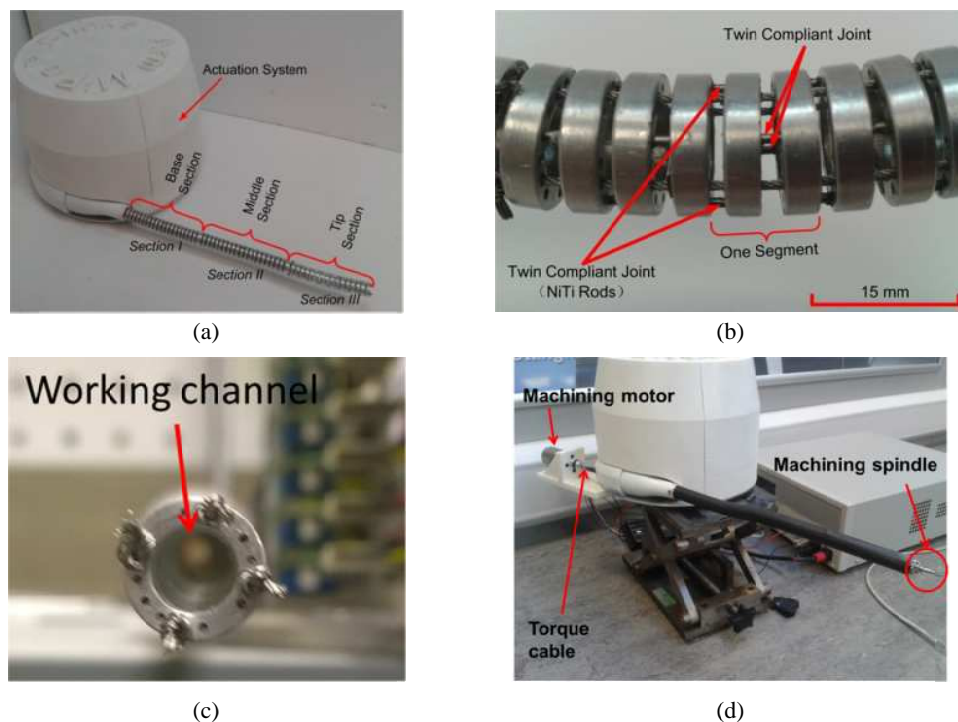


Figure 6-12. (a) General view of the continuum robot; (b) one segment construction; (c) working channel of the continuum robot; (d) the continuum robot equipped with a machining tool and motor;

By actively changing the lengths of two out of the four steel cables, each section can be bent at least  $90^\circ$  in an arbitrary direction. The design of disks is 15 mm in diameter and PCD (pitch circle diameter) of the cable guide holes is 12 mm. For delivering the

torque cable and electrical cables of end-effectors (e.g. camera & illumination) to the tip of the robot, a 9mm diameter hole is made at the center of each disk along the entire length of the manipulator, as shown in Figure 6-12(c). For machining, a motor is attached at the end of the actuation system, which can drive a spindle via a torque cable (Figure 6-12(d)).

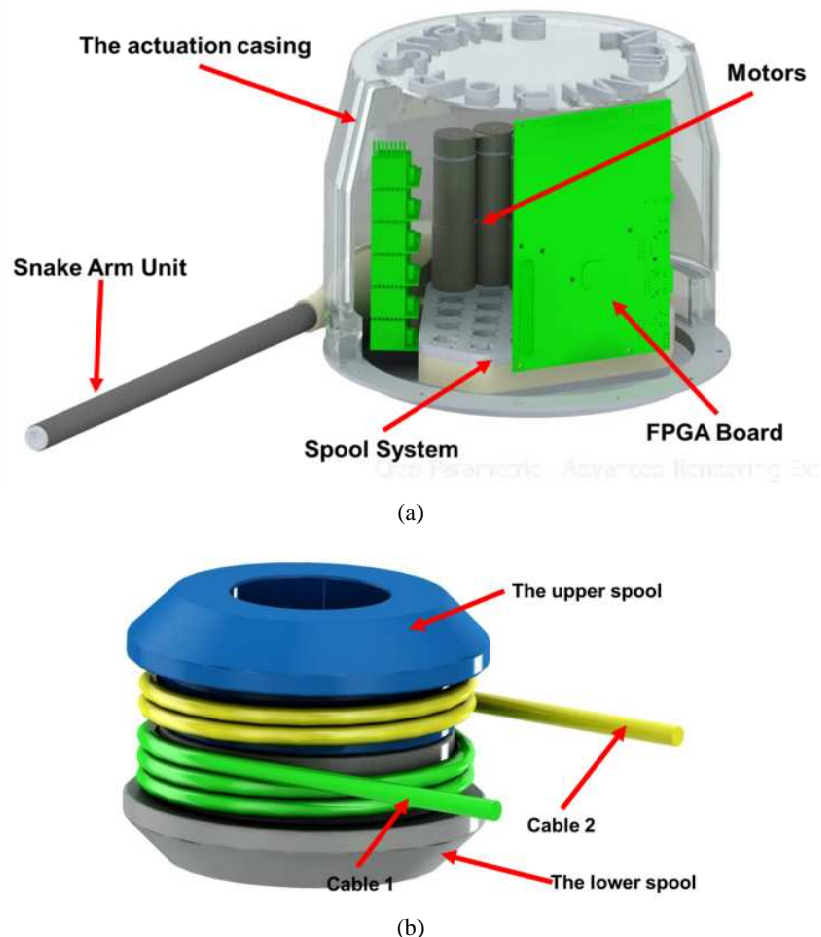


Figure 6-13. (a) CAD of the actuation system (b) concept of the spool employed in the 3<sup>rd</sup> demonstrator;

Figure 6-13(a) shows the actuation system of this prototype, which uses 6 high torque motors (4.5 Nm) to prove out the finer details of this close pack arrangement, which can provide 600N actuation force. This system was designed to accommodate 24 individually controllable of motors, on which here only 6 motors are included, as a pre-test of the final full length demonstrator design. In the prototype, each motor is attached to an individual spool for actuating a pair of control cables, which serially

runs through the spool system and the manipulator, and then separately attaches to the tip of every individual section.

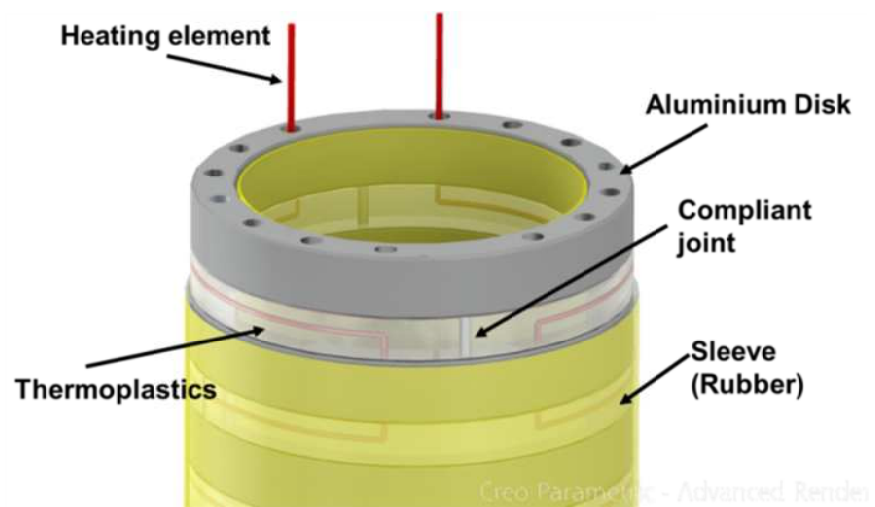
In particular, Figure 6-13(b) illustrates the concept of the spool system, which is the key modification comparing with the previous actuation system. The upper spool attaches to the motor and the lower spool can make a concentric rotation relative to the upper one. Two cables, which are individually mounted on the upper and lower spools, can be mechanically adjusted the tension by rotating the upper/lower spools relative to each other. Unlike the spool utilized in the previous demonstrator, the cables are helically coiled on the spool at the same diameter in this design. Therefore, by rotating the spool an angle, the same length of cables can be simultaneously stretched and contracted from either the upper or lower spool, which can help the continuum manipulator keep a constant cable tension when it is bending. And it can achieve a constant proportional relationship between actuator motion and manipulator motion.

### **6.3.2. Variable stiffness system**

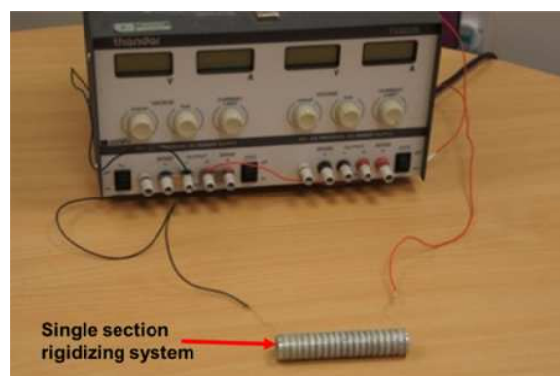
According to the previous experience, this system was constructed with along the similar principle. However, a supporting construction was utilised for keeping thermoplastics at the original position when it melt (Figure 6-14(a)).

The construction consists of compliant joints (1 mm diameter, 2.5 mm long), disks (20 mm outer diameter, 16 mm inner diameter and 2.5 mm high), which are connected serially. The gaps between the disks are filled with polymorph material, which can either block the movement of the compliant joints when it is solid or does not limit the flexibility of the construction when it is melt. And a NiCr wire is integrated in the thermoplastics as the heating element, which is connected to a power supply, as shown in Figure 6-14(a) & (b). And both sides of the variable stiffness system are covered by latex rubber tubes for avoiding the melt polymorph leaking into the continuum manipulator, which can jam the actuation cables. Further, the disks and compliant

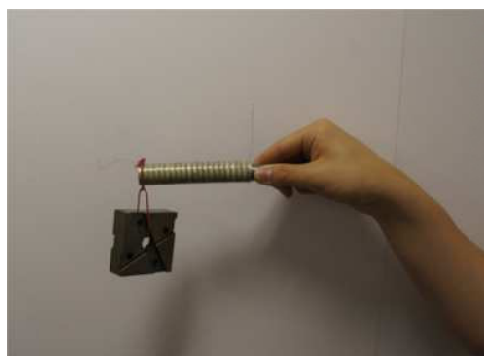
joints are coated by electrical insulating varnish for avoiding short circuit of the NiCr wire.



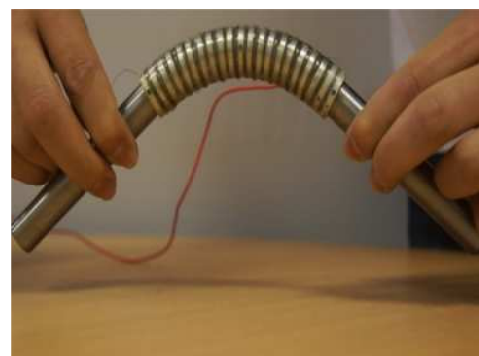
(a)



(b)



(c)



(d)

Figure 6-14. (a) one segment construction; (b) the prototype of the variable stiffness system; (c) the rigid state of variable stiffness system; (d) the soft state of variable stiffness system;

The design has the following characteristics:

- 1) Dual state of stiffness - the rigid state (Figure 6-14(c)), it remarkably increases the stiffness of the system comparing with a pure twin-pivot compliant joint construction; the soft state (Figure 6-14(d)), it does not limit the flexibility of the system;
- 2) Lightweight and compact (40g /100 mm in length; 2mm thickness in radius);
- 3) The construction can be mounted on the outside of arbitrary section of a continuum manipulator, which can turn an ordinary continuum robot into a variable-stiffness continuum robot having variable stiffness.

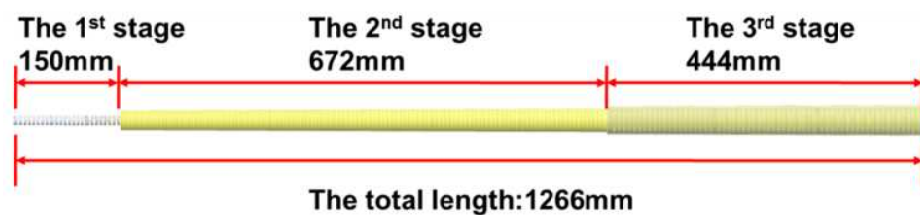
Therefore, the construction with along the same design principle was utilised in the design of the final variable-stiffness continuum robot demonstrator.

#### 6.4. Prototype 4 (full length continuum robot with twin-pivot backbone)

As the final design of the variable-stiffness continuum robot, the prototype comprises three main mechanical units: the continuum construction, the variable stiffness system and the actuation pack. According to the successful experiments of the 3<sup>rd</sup> prototype, the final demonstrator still utilised the same design principle (twin compliant joint) with the previous system.

##### 6.4.1. Continuum arm and variable stiffness constructions

The continuum arm has a total length of 1266mm, a tapered diameter from 42mm at its base to 13mm at its tip (the average diameter/length ratio of the arm is 0.023), as shown in Figure 6-15(a). Each of the twelve articulated sections (24 DoFs) was designed to be able to bend 90 degrees.



(a)

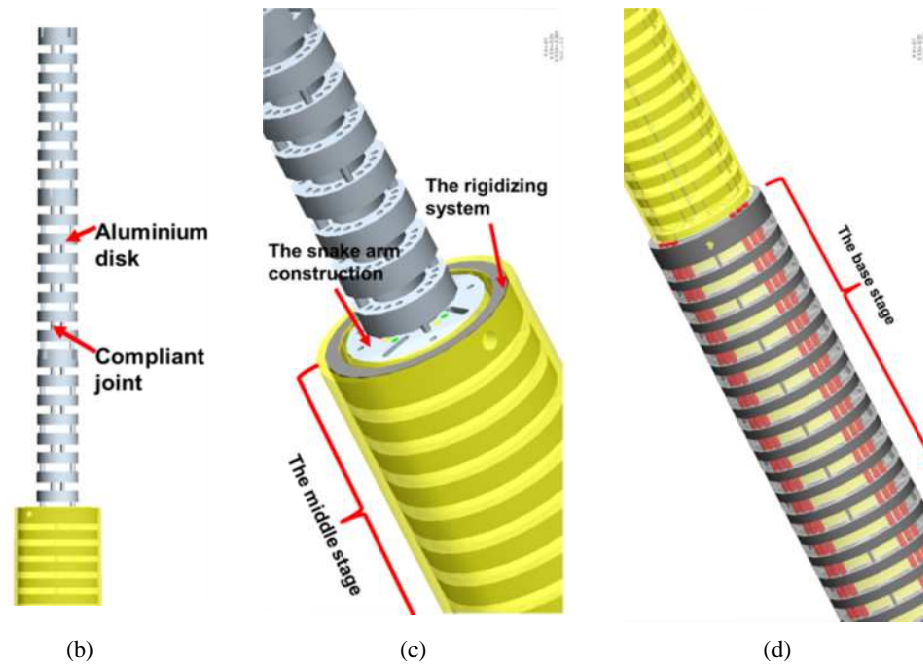
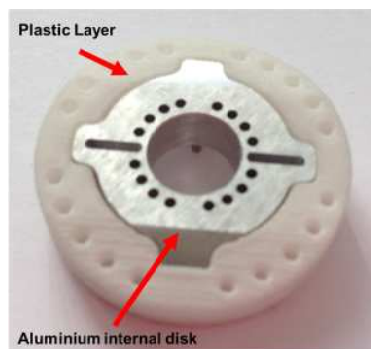


Figure 6-15. (a) Cad of the 4th prototype; (b) the tip stage; (c) the middle stage; (d) the base stage;

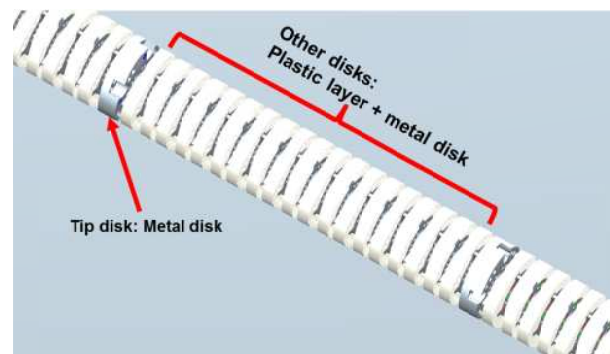
The continuum arm consists of 3 stages. As shown in Figure 6-15(b), the tip stage (3 sections) is 150mm long, and it is made from aluminum disks and NiTi compliant joints. This stage does not include a variable stiffness system and when the continuum manipulator reaches the target position, the 3-section stage can be manipulated for machining in confined environments.

The middle stage is constructed with two systems: the continuum arm and the variable stiffness system. The former is concentrically covered by the latter, which is mounted to the former externally, as shown in Figure 6-15(c). There are 6 sections in this stage and each of the upper and lower three sections are 102 mm and 122mm long, respectively. The continuum construction comprises a combination of aluminum internal disks to resist the compressive forces along the longitudinal axis and a lightweight Nylon outer layer to guide the steel cables (only a force in the radial direction is acting on the Nylon part by the cable when the continuum robot bends (Figure 6-16(c))), as shown in Figure 6-16(a). This combination design can significantly save the weight of the continuum construction, thus it allows smaller size motors to be utilized, which helps to minimize the weight and size of the actuation

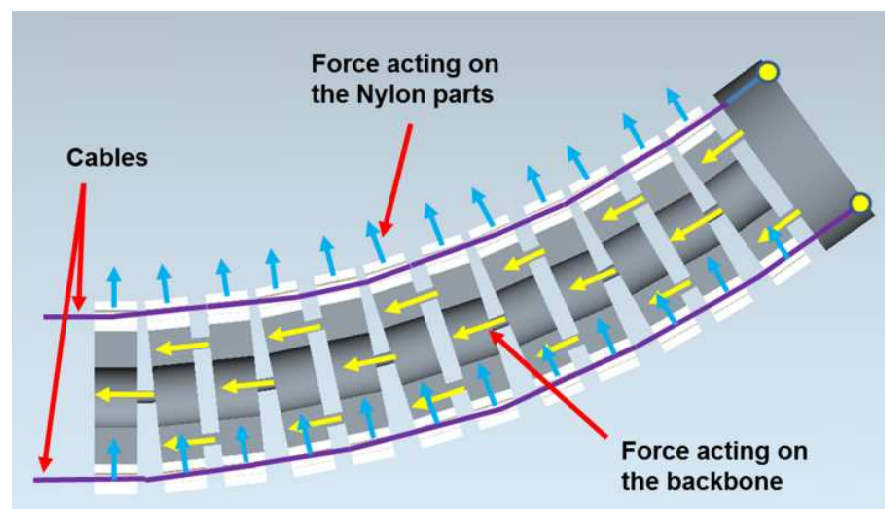
system. But the tip disk of each section is fully made of aluminum which can give it better stiffness, since the control cables are attached on these disks and the actuation force in the longitudinal axis are acting on them, as shown in Figure 6-16(b). Further, the variable stiffness system was designed along the same principle with the previous prototype, as shown in Figure 6-16(d). Specifically, the variable stiffness system is fully covered by rubber tubes, so it avoids the melt polymorph leak into the continuum arm and also constraint the melt stiffening media in the gaps between adjacent disks; the Aluminum disks are manufactured with four internal slots, so it allows the stiffening material filling the adjacent gaps integrally connect and provide better stiffness in the rigid state; a NiCr wire and thermocouple are separately integrated in the variable stiffness construction for heating up the polymorph and monitoring the temperature.



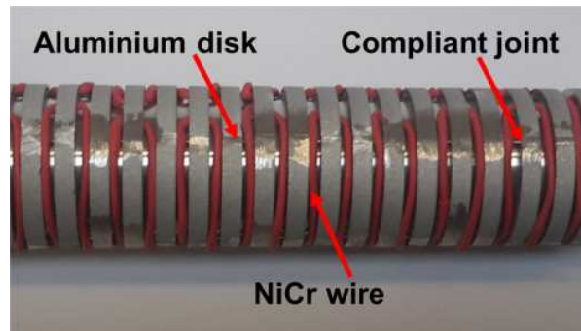
(a)



(b)



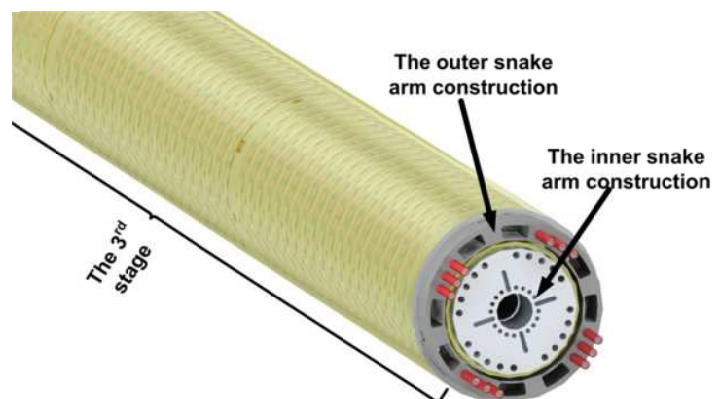
(c)



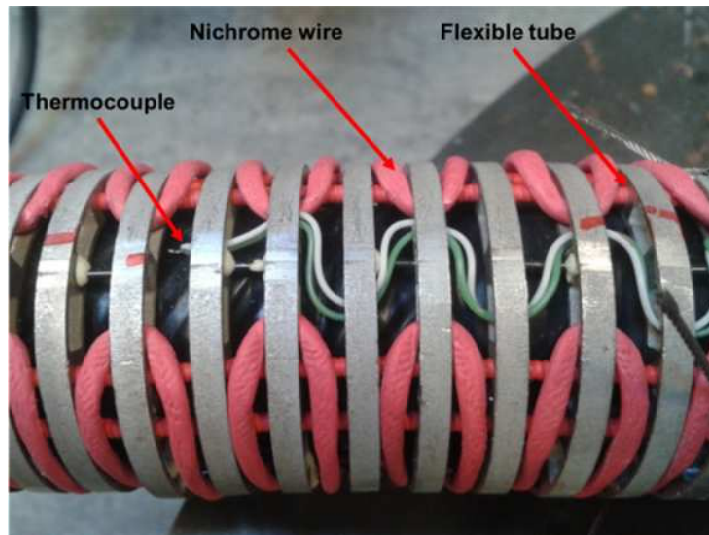
(d)

Figure 6-16. Middle stage of the continuum robot: (a) the combination of the internal disk and outer nylon layer; (b) the general view of a single section; (c) the forces acting on the disk; (d) the variable stiffness system of middle stage;

In the base stage (consisting of 3 sections), a different design principle was utilized to save space on the total diameter. This stage comprises two separated constructions, as shown in Figure 6-17(a), the inner & outer continuum constructions. The inner construction is built along the same design principle with the middle stage continuum construction, while the variable stiffness system is integrated into the outer construction, as shown in Figure 6-17(b). For avoiding the melt thermoplastics blocking the movement of the cable, the actuation cables are covered by flexible tubes. The flexible tubes are able to stretch and contract along the longitude axis, thus they do not limit the bending of the continuum robot, as it was utilized in the previous variable stiffness system. Further, for heating and controlling the stiffening material, one thermocouple and Nichrome wire is integrated into the base stage.



(a)



(b)

Figure 6-17. (a) Bottom view of concentric layout of the base stage; (b) detail design of the base stage;

During the design process, two key elements of the continuum arm (the compliant joint and disk) were considered and tested, since that the load along the backbone is taken by the continuum arm.

Firstly, the parameters of the compliant joints (Table 6-3) were determined based on the calculation (e.g. buckling analysis) and the experience of the previous prototype. Further, the designs of the compliant joints were validated on a one-segment demonstrator (see details in page 146).

Table 6-3. Parameters of the compliant joints

Section	Compliant joint parameters (mm)			The buckling load of single joint (N)
	Width	Length	Thickness	
1	1.25			993
2	1.5	2.5		1192
3	1.5			1192
4	3		1	6621
5	3	1.5		6621
6	3.75			8276

7	4	8828
8	4.5	9931
9	4.5	9931
10	5	11035
11	5	11035
12	5	11035

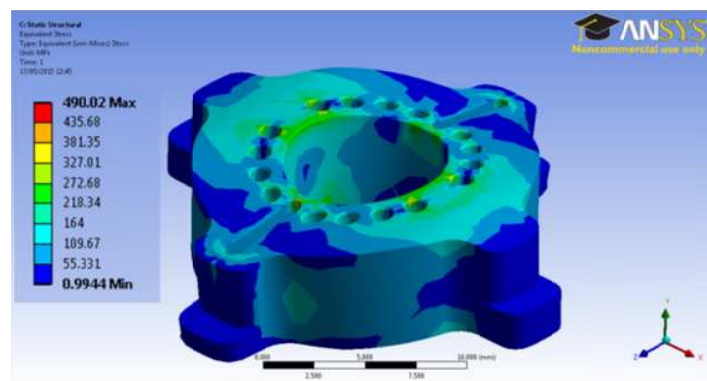
Secondly, the disks (diameter & thickness) of the continuum arm and variable stiffness system were designed. Hence, the weight of the system can be calculated, and then the PCD of the actuation holes can be determined accordingly. Further, the action forces for each section (Table 6-4) was calculated and the force applying on the backbone (compliant joints& disks), was obtained. It was found the max actuation force for single section is 439 N (the section bends 90) and the max force applying on the backbone is 2956 N, which acts on the end section.

Table 6-4. Actuation force of each section

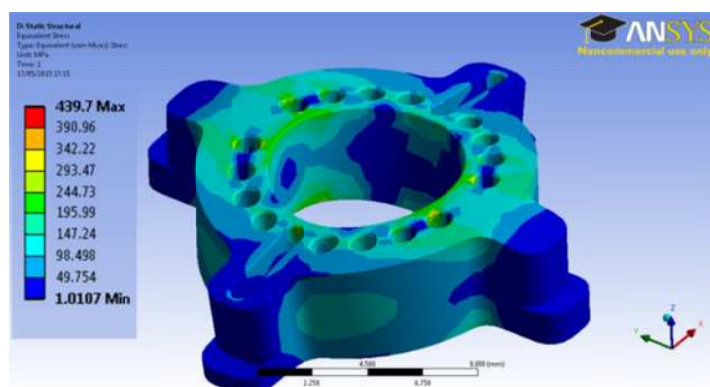
Section	Actuation force (N)	Weight (g)		Diameters (mm)	Notes
		Continuum arm	Variable stiffness		
1	58	5		12.0	
2	76	6		12.4	
3	93	6		12.7	
4	146	22		25	End load:
5	196	27	78	25.7	200g
6	240	29		26.4	
7	293	45		27	
8	348	47	98	27.7	

9	391	53	28.5
10	307	111	41
11	367	116	147
12	439	124	44
<b>Total force</b>	<b>2956</b>	<b>914g</b>	

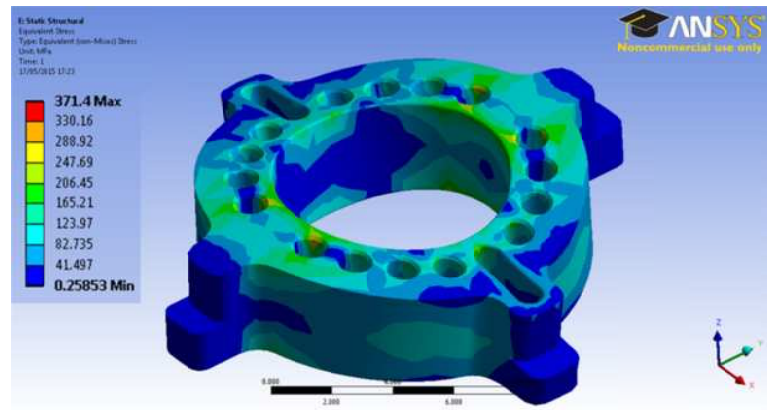
After the initial design, the disk of each section was tested by FE simulation for validating the design, as shown in Figure 6-18 (a), and it was found that the max stress of the disks is 490.02MPa, when they are applied by the corresponding max backbone forces. Therefore, Aluminum 2099T83 (UTS 595 MPa) was selected for manufacturing the disks, which is for use in aerospace and high strength applications requiring low density and high stiffness.



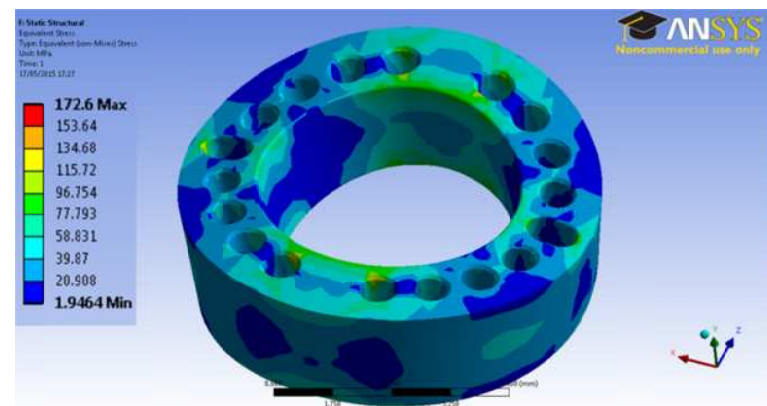
(a)



(b)



(c)

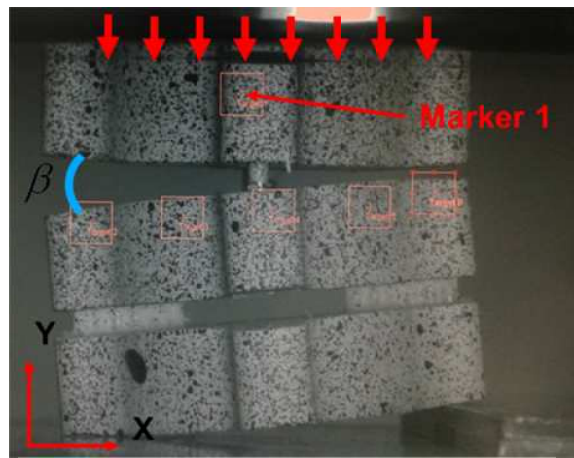


(d)

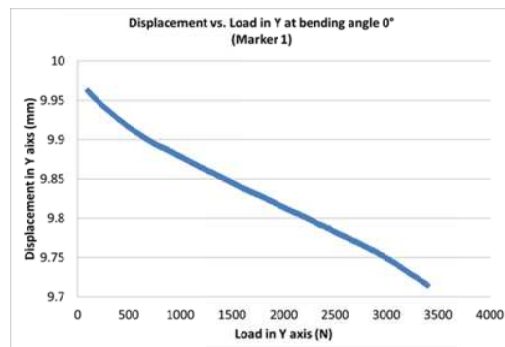
Figure 6-18. Simulation evaluation of the disk design for different sections: (a) the stress analysis of the disk of section 12 (the base stage); (b) the stress analysis of the disk of section 9 (the middle stage); (c) the stress analysis of the disk of section 6 (the middle stage); (d) the stress analysis of the disk of section 3 (the tip stage)

Further, the other parameters that need to be considered are the critical buckling load and the material yield of the compliant joints. Before the components were manufactured, a one-segment demonstrator was built along the same design with the last section of the 4<sup>th</sup> demonstrator (Section 12), as shown in Figure 6-19 (a). Since that section 12 takes the max backbone load, this demonstrator was tested on a universal test machine for measuring the joint performance. As shown in Figure 6-19 (b) to (e), it can be seen that the displacements of the joint (the max displacements are 0.27 mm, 0.31mm, 0.34mm and 0.45mm, respectively) were linear at different bending angles ( $0^\circ$ ,  $3^\circ$ ,  $6^\circ$ ,  $9^\circ$ ) against the load (0 up to 3.5kN) applied on the small

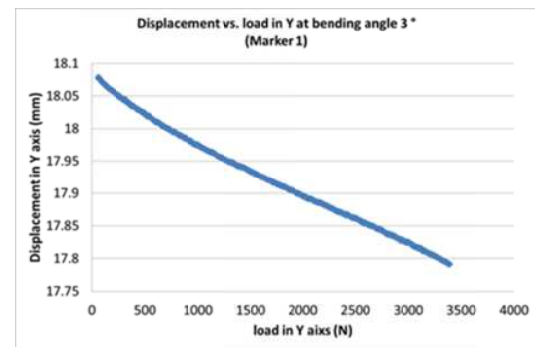
demonstrator. Therefore, the compliant joint can withstand the max load along the backbone (2956N) from both terms of joint buckling and material yield.



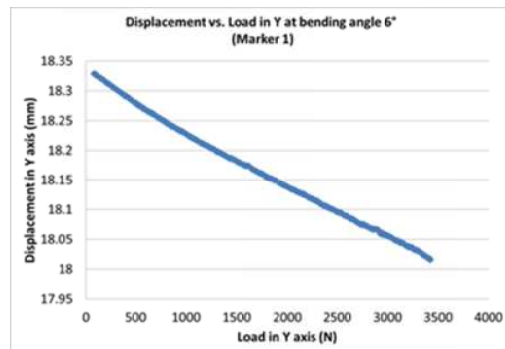
(a)



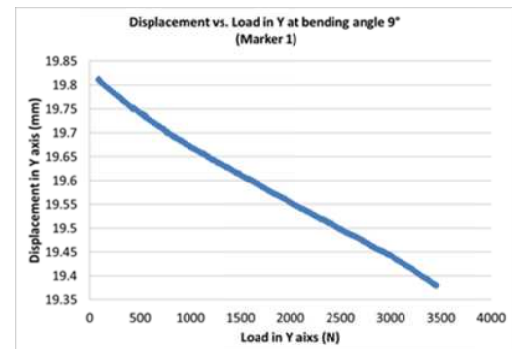
(b)



(c)



(d)



(e)

Figure 6-19. Trails of the buckling of compliant joint: (a) the setup of the experiment; (b) the test result of bending angle 0°; (c) the test result of bending angle 3°; (d) the test result of bending angle 6° (e) the test result of bending angle 9°;

#### 6.4.2. Actuation system

The actuation system of the 4<sup>th</sup> prototype consists of the following elements: (1) The base plates (the rotational mechanism), it allows the continuum robot can be coiled

and uncoiled on the outer casing by rotating the base plates, as shown in Figure 6-20; (2) Motor pack assembly, cable guide to the continuum robot (the same arrangement of the 3<sup>rd</sup> demonstrator) and electrical systems and mounting structure; (3) The outer casing.

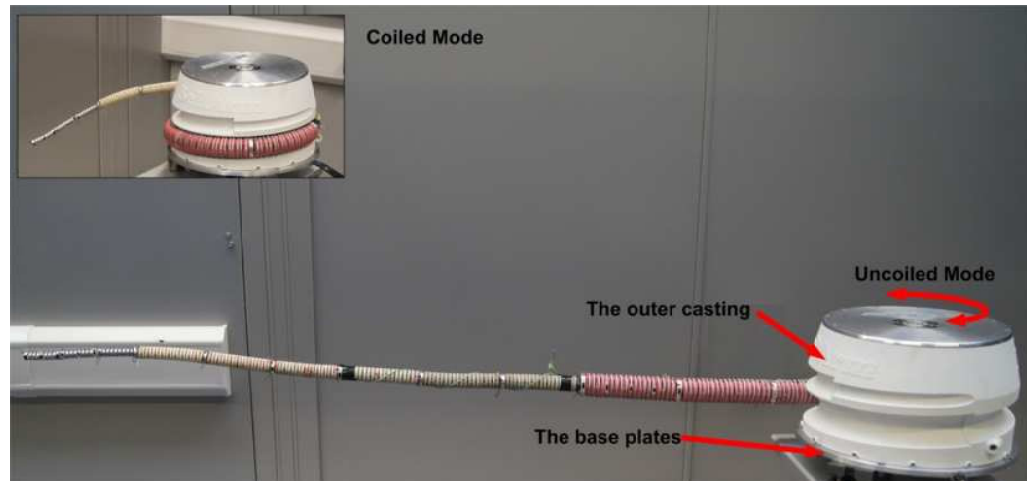


Figure 6-20. Coiled & uncoiled modes of the continuum robot;

The rotation mechanism is constructed to have as low a profile as possible, whilst being able to withstand and provide sufficient drive so that it can advance/retreat the continuum robot. The motor pack assembly and cable guide to the continuum robot is constructed along the same design with the previous prototype (Figure 6-13(a)). The close packing attachment of the motor pack assembly allows 24 individually controllable gearhead motors (P/N 468458) to be placed in the smallest possible space. Each motor can generate 4.5Nm torque and up to 647N for each of the 24 cable pairs. Further, each spool can provide a maximum stroke of +/-200mm, so it allows each section bend 90° and the continuum robot coil on the outer casing.

Figure 6-21 shows the assembled variable-stiffness continuum robot that is fully operational for movement. The system was designed to be a self-contained portable system, that is lightweight (<10Kg), and compact (base Ø300mm x 167mm in height). The home position of the continuum robot will be coiled up on the outside of the actuation pack allowing portability and effective integration onto the WakingHex

system. The outer covering layer of the continuum robot and the actual stiffening media will be added after an initial testing period is completed.



Figure 6-21. the assembly of the final full length continuum robot

## 6.5. Conclusions

In order to develop a variable stiffness continuum robot for in-situ repair of gas turbine engines, four prototypes were built to evaluate the concepts. Super-elastic NiTi was determined to be the backbone material of the continuum arm, according to the tests on the 1st demonstrator (continuum robot with segmented single backbone pivot). Then, a full length continuum robot with a novel double-compliant joint structure was built, which utilised the concept proposed in Chapter 3. Comparing with the previous demonstrator (utilising a conventional design: flexible backbone with cables as actuations), this design has following advantages which was validated in the experiments (Chapter 7.2):

- Less twisting angle along the longitudinal direction when it bends in horizontal plane;
- Better stiffness with a light weight construction;
- An appropriate accuracy for navigation;

---

However, it was found that anti-twisting ability and stiffness of the continuum arm needs to be further improved for the in-situ repair/maintenance application. Hence, a variable-stiffness three-section continuum robot with a novel twin-pivot backbone was constructed, which has following superiorities (see the trails in Chapter 7.3) comparing with double-pivot construction:

- Minimised twisting angle along the longitudinal direction;
- Controllable stiffness since it can equip with a variable stiffness system
- An appropriate accuracy allowing to active machining tasks, e.g. mechanically blending;
- Twin actuations for a single section;

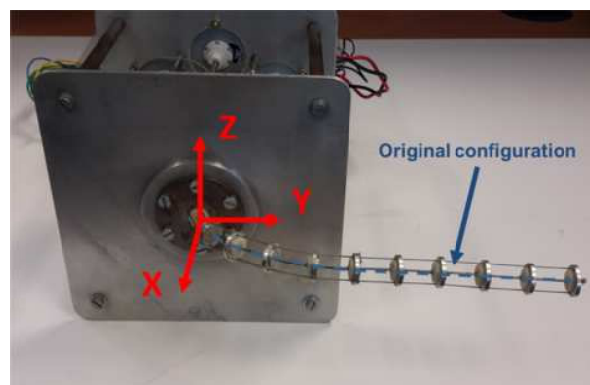
Finally, based on the concept of twin-pivot construction, the final continuum robot demonstrator was constructed to be able to take a 200g end load (e.g. a machining end-effector) and have an appropriate accuracy to be navigated to reach the low processor compressor of gas turbine engines (Rolls-Royce XWB) with a suitable length (more than 1.2m), diameters (tip diameter is no more than 15mm), a compact actuation system and variable stiffness system. The following trails prove the design can satisfy the stated requirements (chapter 7.4), except the variable stiffness system will be integrated with the continuum arm after finishing all the initial trails. However, it has been demonstrated on the previous demonstrator in the experiment (Chapter 7.3).

## Chapter 7 Experimental on the prototypes

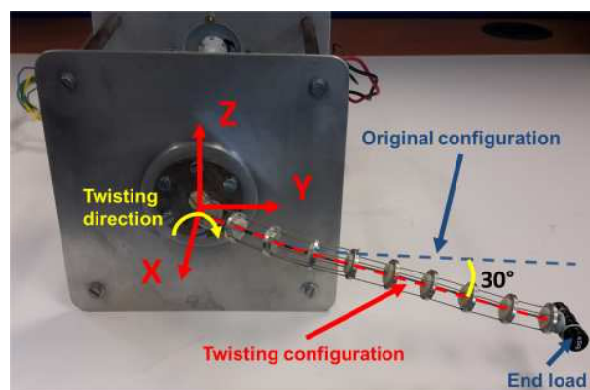
In the previous chapter, four prototypes of the continuum robots utilising the proposed concepts were designed and built. In this chapter, variable experiments, e.g. counter-twisting ability, control accuracy, repeatability, work volume, end load carrying and machining capabilities, have been undertaken to evaluate the hardware and the concepts.

### 7.1. Test of prototype 1

Since some experiments of the first demonstrator (Continuum robot with segmented single backbone pivot) have been illustrated in the previous chapter (Figure 6-2), which was utilised to test different designs and materials of the flexible backbones, thus they are not presented in the chapter in detail.



(a)



(b)

Figure 7-1. Twisting test of the first prototype: (a) 90° bend configuration without external load; (b) 90° bend with external load (20g);

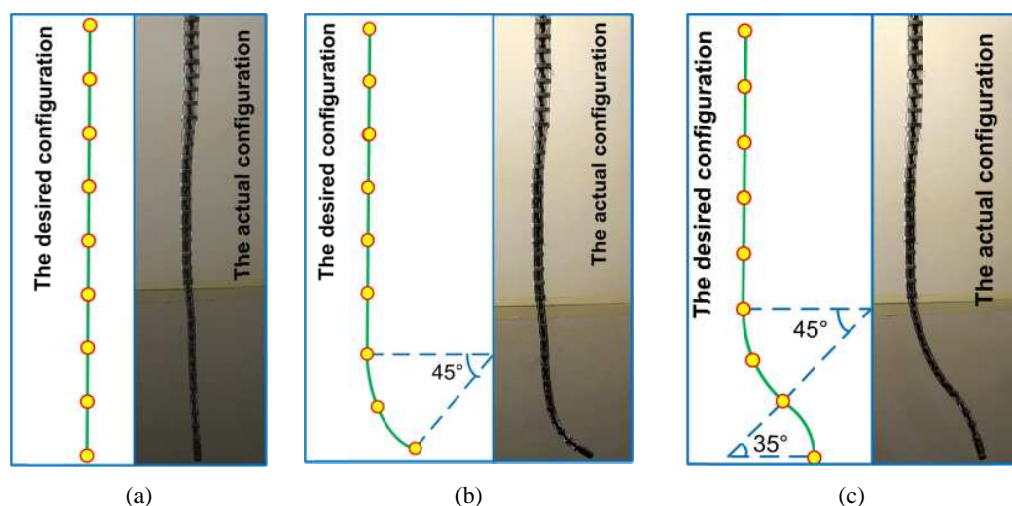
Further, the twisting problem (referring to the design challenge of flexible backbone continuum robot presented in chapter 3), was identified from this system, which utilised one of the conventional continuum robot designs (a NiTi rob/tube and steel cables are employed as backbone and actuation transmission mechanisms, respectively). In order to measure the max twisting angle, the base section bent  $90^\circ$  in the horizontal plane and the tip one kept straight, as shown in Figure 7-1(a), where the max torque can be applied to the base section of the arm with respect to a particular external load. According to the extensive experiments, it can be found that there is a significant twist (order of tens of degrees) of the system even at low (tens of grams) external loads. For example, the base section was twisted by  $30^\circ$  &  $45^\circ$  about X axis by 20 g & 36 g end load (Figure 7-1(b)), respectively, which significantly influences the control accuracy. Although the results were found not encouraging in reference to position inaccuracies when external load is applied, these findings enabled to take a decision on the development of a design solution to overcome this drawback (Chapter 3.2).

## **7.2. Test of prototype 2**

The second prototype (Full length continuum robot with single double-pivot backbone) was constructed with the concept of double-pivot construction (Chapter 3.2.1). Firstly, this system was setup for the trial of tip-following control algorithm [165]. The tip following approach is widely utilised for hyper-redundant robot navigations, especially for continuum robots. In particular, the strategy is that the very tip section of the continuum robot is considered as 'head' of the robot and the rest of the sections are considered as 'bodies'. When the robot is being navigated into a confined space, the 'bodies' follow the trajectory the 'head' generated, thus it allows a simpler inverse kinematics solution for navigating all the sections of the hyper-redundant robot (just one section is actively controlled by the operator and the other sections are passively controlled).

For navigation in a confined space, the continuum robot has two combined motions: one is the arm bends to variable configurations controlled by tip-following algorithm for avoiding the obstacles; the other is the whole system moves towards the target for feeding the arm into the desired space. Since there is no feeding mechanism in this system, the tip following was tested without combining the linear motion. Figure 7-2 illustrates an example of the tip-following experiments, where the left configurations show the desired shapes of the twelve-section continuum manipulator and the right ones are the actual performance of the robot. Specifically, the manipulator started to move from an initial configuration (Figure 7-2(a)), then formed a  $45^\circ$  curve, as shown in Figure 7-2(b); after that, the tip section bends  $35^\circ$  (Figure 7-2(c)) and next move straight forward for 300mm (Figure 7-2(d)); finally, the path ends up with a left  $30^\circ$  bend (Figure 7-2(e)).

Compared with the planned path, the max deviation of the manipulator is 14.7mm in the test and the max angular error per section is less than  $5^\circ$  (Table 7-1). According to the tests, it was found that the system has a great flexibility (bending capability) with an appropriate control accuracy to achieve the desired bending shapes for navigating [165].



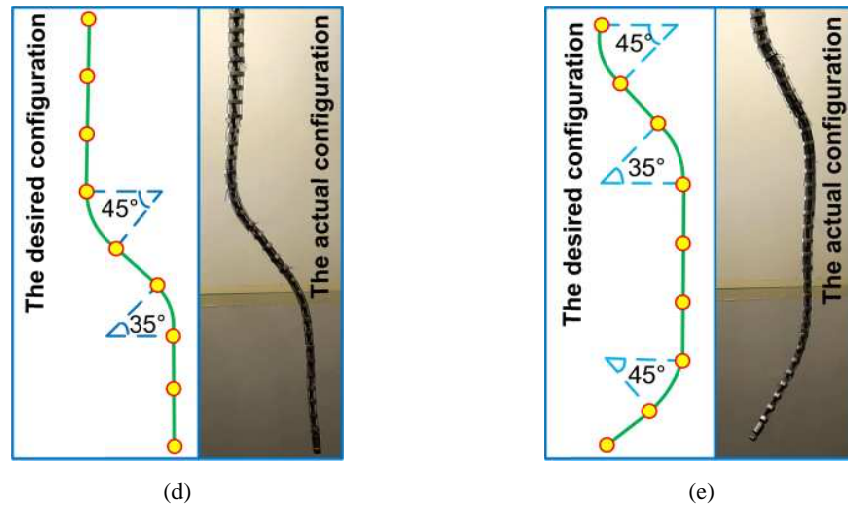


Figure 7-2. Navigation control trial of the 2nd prototype [165]

Table 7-1. Shape accuracy measurement results

Shape	section	Desired bending angle (°)	Actual bending angle (°)	Differences (°)	Note
1	11	10	9	-1	Figure 7-2(b)
1	12	35	40	5	Figure 7-2(b)
2	10	35	33	-2	Figure 7-2(c)
2	11	10	13	3	Figure 7-2(c)
2	12	-35	-36	1	Figure 7-2(c)
3	8	45	40	-5	Figure 7-2(d)
3	10	-35	-38	3	Figure 7-2(d)
4	5	45	41	-4	Figure 7-2(e)
4	7	-35	-36	1	Figure 7-2(e)
4	11	30	32	2	Figure 7-2(e)

Secondly, in order to compare the counter-twisting capability of the double-pivot design with the previous prototype (“continuum-style” segmented flexible backbone), the tip two sections of the 2<sup>nd</sup> system were utilised to measure the twisting angles when end loads applied. Since the first demonstrator and the bespoke sections of the

double-pivot demonstrator share the same dimensions in length (100 mm/section) and diameter (15mm), thus the comparison can be considered appropriate. In particular, the second section bent  $90^\circ$  in the horizontal plane and the tip section kept straight, which was the same configuration utilised for testing the first demonstrator. According to the test results, the second section of the double-pivot prototype has been twisted by  $7^\circ$  &  $15^\circ$  by 20g & 36g end load, respectively; this was considered an encouraging result when compared with the 1<sup>st</sup> prototype since it resulted in the decrease by 67% of the twist angles. The results show the counter-twisting capability of the double-pivot construction (family A) increases remarkably, compared with the conventional concept (“continuum-style” segmented flexible backbone demonstrator).

However, it was also found that the Archimedean spiral pattern of the actuation cable (Figure 6-4) significantly affects the navigation accuracy and the counter-twisting ability of this demonstrator, since it cannot maintain a constant cable tension. Specifically, two cables are attached on the same spool and both of them are coiled in the pattern of Archimedean spirals.

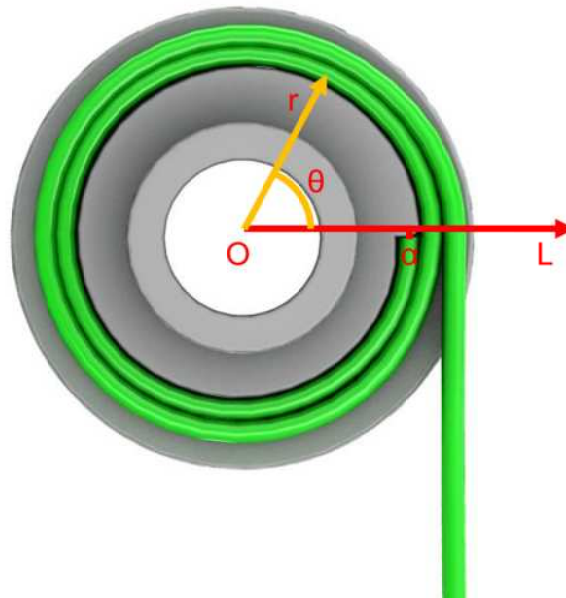


Figure 7-3. Schematic of the pattern of one actuation cable in polar coordinate

For each cable of a spool (Figure 7-3), in polar coordinates  $(r, \theta)$ , it can be described by the equation:

$$r = a + b\theta \quad (7.1)$$

Where  $a$  is the distance from the centre of the spool to the attached point of the cable and  $b$  is equal to the diameter of the cable.

When the motor rotates, one cable coils on the spool ( $r$  is increased) and the other uncoils ( $r$  is decreased), which causes different cable lengths are contracted and extended simultaneously (Table 7-2). But in order to maintain a constant cable tension, it requires the same lengths of cables to be contracted and extended for an arbitrary motor rotating angle. Hence, Archimedean spiral cable cannot enable a constant tension force, which remarkably affects the navigation accuracy (it is addressed (Chapter 6.3) by adoption of the cable coiling arrangement).

Table 7-2. Displacements of cables versus rotation angle of spool

Rotation angle of spool ( $^{\circ}$ )	Displacement of cable 1 (mm)	Displacement of cable 2 (mm)	Differences (mm)	Note
+90	21.3714	-18.9115	2.4599	
+60	13.9741	-12.8809	1.0932	
+30	6.8504	-6.5771	0.2733	$a = 6.5$
0	0	0	0	$b = 0.9$
-30	-6.5771	6.8504	0.2733	
-60	-12.8809	13.9741	1.0932	
-90	-18.9115	21.3714	2.4599	

Finally, according to all the experiment results, it can be concluded that the system has an appropriate control accuracy to achieve the desired bending shapes for navigating (max deviation is 14.71mm) and increased counter-twisting ability (the twisting angles are decreased by 67%) comparing with the conventional design (“continuum-style”

segmented flexible backbone demonstrator). However, since the aforementioned problem of the cable pattern, the mechanical design of spool needs to be optimised to enable a constant cable tension at an arbitrary rotation angle (the new design is shown in figure 13 of Chapter 6), which can enhance the control accuracy and counter-twisting ability.

### **7.3. Test of prototype 3**

The prototype (Three-section continuum robot with twin-pivot backbone) was built for evaluating the twin-joint construction, i.e. the more robust solution considered in this thesis, and demonstrating machining capability of a continuum robot built on this concept. Thus, more in-depth experimental works and reporting are associated to this demonstrator.

Firstly, the experiments for measuring the control accuracy and repeatability of the continuum robot were setup to validate the kinematics analysis. Further, the bending capability of each section was tested for evaluating the compliant joint design and the work volume analysis. Then, the twisting angles versus different end loads were measured to evaluate the counter-twisting ability of the twin-joint construction. After that, the end load carrying capability of the system was also tested, by applying different end loads at the tip of the arm. Next, the variable stiffness system was assembled on this demonstrator for comparing the differences of the arm stiffness when with/without the variable stiffness system. Finally, the machining trials were demonstrated on this system by blending different metal materials, e.g. aluminum and titanium.

#### **7.3.1. Accuracy and repeatability measurements**

In order to evaluate the control accuracy and the repeatability, a trial was setup, which employed a video gauge system [166] for tracking the trajectory of the arm, as shown in Figure 7-4(a). The video gauge system can provide a resolution of better than

1/200,000 of the visible area and a strain resolution of 5 micro-strain. The system was employed for measuring a single section (the visible area is around  $150\text{mm} \times 150\text{mm}$ ), hence, the displacement resolution is around  $7.5 \times 10^{-4}$  mm. In the test, twelve markers were placed along the continuum arm evenly for helping track the motion of the arm, as shown in Figure 7-4(b).

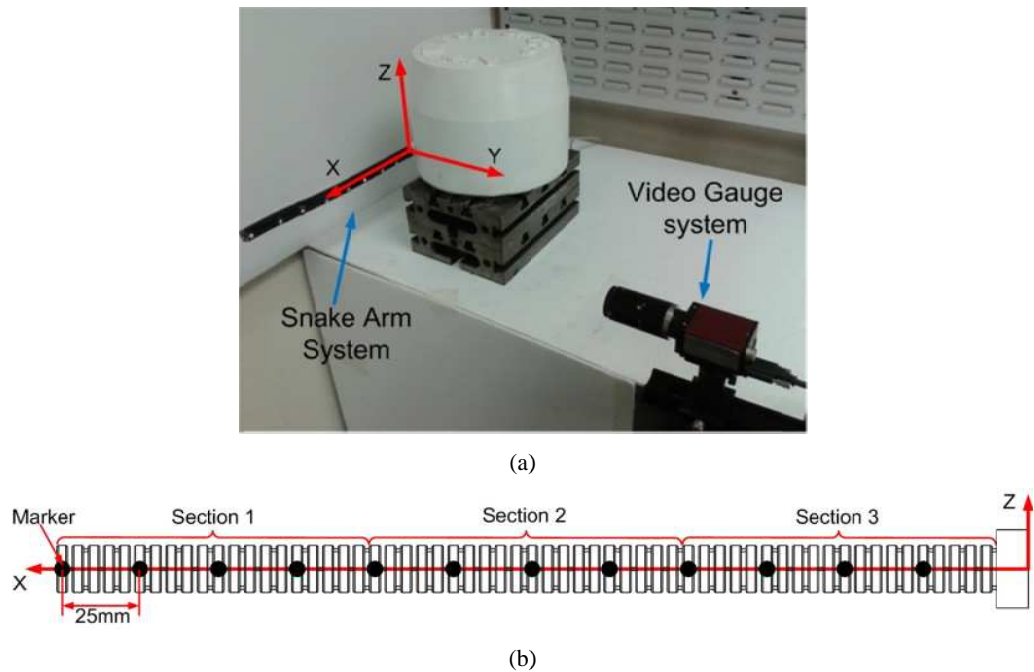


Figure 7-4. (a) The setup of the measurement system; (b) the arrangement of the markers

For doing in-situ repair in the turbine aero-engines, firstly, the continuum robot is navigated to reach an initial position in the target area based on the tip-following algorithm [165]. Secondly, the tip section of the robot is operated for active repairing tasks from this initial position, e.g. mechanical blade blending which generally requires the tip of the robot moves up and down repeatedly from the initial position to form a scallop trajectory. Since the system is deployed in a confined space, thus the operation range of each section is relatively small in the working environment. Hence, the continuum robot was tested to be operated to sweep in a  $\pm 5^\circ$  area (the initial positions were  $30^\circ$ ,  $45^\circ$  and  $60^\circ$ , respectively).

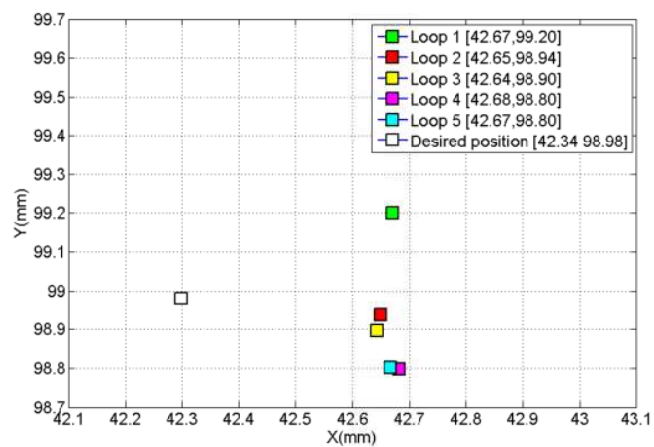
Table 7-3 illustrates the results of the experiment. It can be seen that the position error is less than 1 mm in translation.

Table 7-3. Position accuracy measurement results

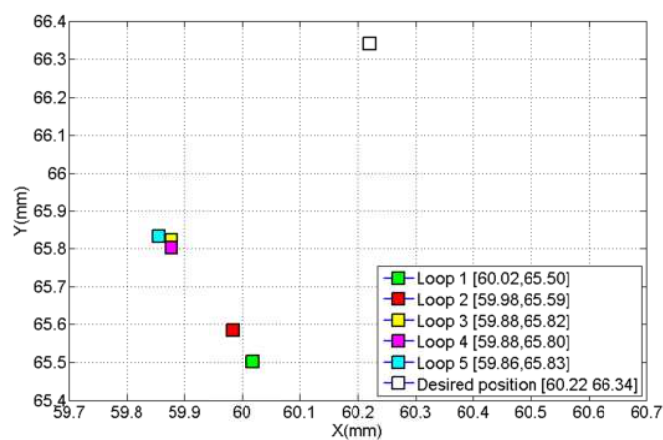
Bending Angle	Desired position (mm)		Actual position (mm)		Error (mm)	
	X	Z	X	Z	$\Delta X$	$\Delta Z$
25°	40.41	104.23	40.51	104.1	0.1	-0.13
27°	41.19	102.1	41.25	102.09	0.06	-0.01
29°	41.97	99.97	41.98	100.04	0.01	0.07
31°	42.75	97.91	42.76	97.95	0.01	0.04
33°	43.53	95.78	43.58	95.79	0.05	0.01
35°	44.31	93.65	44.46	93.77	0.15	0.12
Original position: [42.34mm, 98.98mm]; $\beta_{section\_III} = 30^\circ$ , $\beta_{section\_II} = 0^\circ$ , $\beta_{section\_I} = 0^\circ$ ;						
$\gamma_{section\_I} = \gamma_{section\_II} = \gamma_{section\_III} = 90^\circ$ ;						
40°	46.63	88.6	46.89	88.75	0.26	0.15
42°	47.88	86.47	47.92	86.78	0.04	0.31
44°	49.13	84.34	49.02	84.61	-0.11	0.27
46°	50.37	82.2	49.78	83.2	-0.59	1
48°	51.62	80.07	50.96	80.89	-0.66	0.82
50°	52.87	77.94	52.9	77.2	0.03	-0.74
Original position: [49.75mm, 83.28mm]; $\beta_{section\_III} = 45^\circ$ , $\beta_{section\_II} = 0^\circ$ , $\beta_{section\_I} = 0^\circ$ ;						
$\gamma_{section\_I} = \gamma_{section\_II} = \gamma_{section\_III} = 90^\circ$ ;						
55°	55.92	71.67	56.35	71.55	0.43	-0.12
57°	57.64	69.54	57.92	69.38	0.28	-0.16
59°	59.35	67.41	59.39	67.42	0.04	0.01
61°	61.07	65.27	60.85	65.5	-0.22	0.23
63°	62.78	63.14	62.45	63.68	-0.33	0.54
65°	64.5	61.01	64.04	62.01	-0.46	1
Original position: [60.22mm, 66.34mm]; $\beta_{section\_III} = 60^\circ$ , $\beta_{section\_II} = 0^\circ$ , $\beta_{section\_I} = 0^\circ$ ;						

$$\gamma_{section\_I} = \gamma_{section\_II} = \gamma_{section\_III} = 90^\circ ;$$

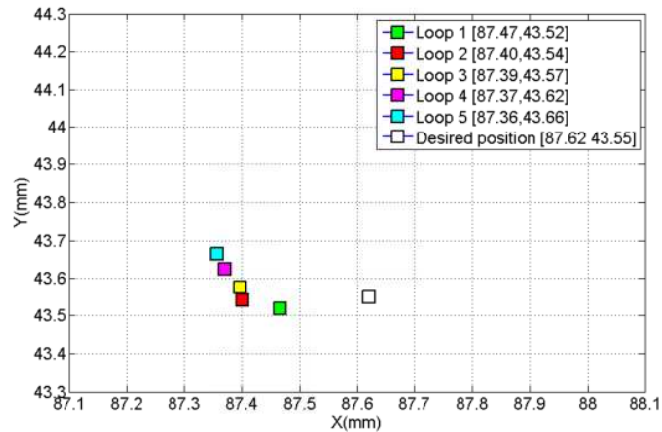
Further, the results of the repeatability trail are presented in Figure 7-5. In this test, the continuum robot was driven to bend from  $0^\circ$  to  $30^\circ$  ( $60^\circ$  and  $90^\circ$ ) and back  $0^\circ$  for 5 loops, in order to measure the repeatability of the system. It can be found that the repeatability error of system is less than 0.5mm in the work volume, as shown in Figure 7-5(a), (b) and (c). The small repeatability error also proves the tension of all the cables is kept well in the work volume of the system. Note: all these measurements for repeatability are made at the configurations of middle and base sections:  $0^\circ$  bend, direction angle:  $0^\circ$ .



(a)



(b)

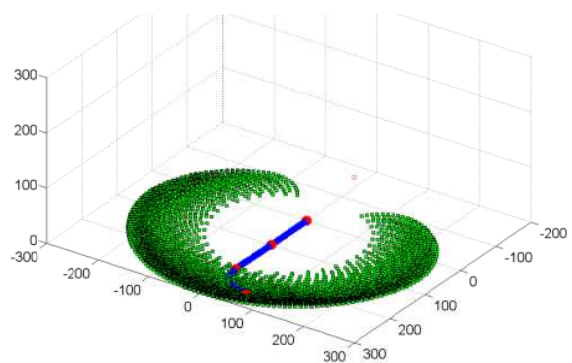
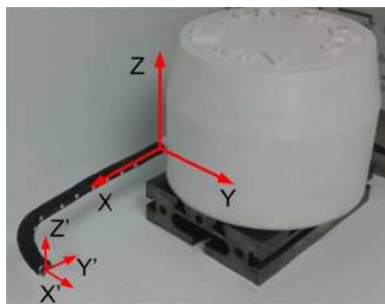


(c)

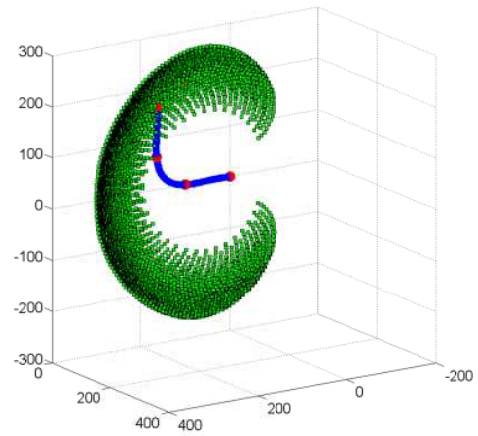
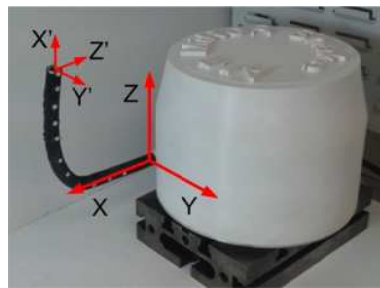
Figure 7-5. Repeatability of the three-section twin-pivot demonstrator: (a): repeatability test with respect to  $30^\circ$  [42.34mm, 98.98mm] bend (b): repeatability test with respect to  $60^\circ$  [60.22mm, 66.34mm] bend (c): repeatability test with respect to  $90^\circ$  [87.62mm, 43.55mm] bend (Note: One bend and return is called one loop)

### 7.3.2. Work volume validations

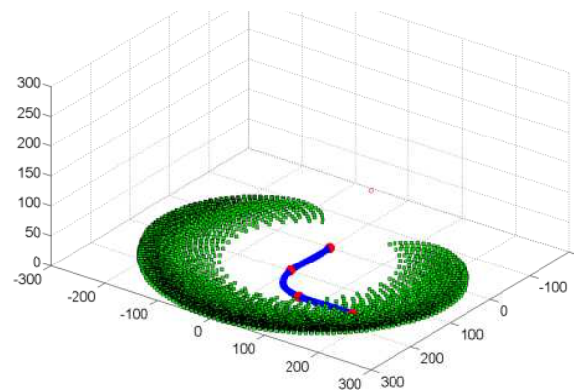
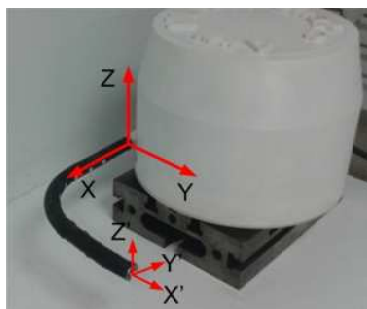
The size of the work volume is a key factor of a robot. Since the max bending of a single section was designed to be  $90^\circ$ , so each section was tested to bend to this limit for validating the flexibility of the compliant joints and work volume of the system. Figure 7-6 shows several examples of these trails. As shown in Figure 7-6(a), section three (the tip section) was bent  $90^\circ$  in plane XOY. Then the next section, section two (the middle section) was tested to bend  $90^\circ$  in both of planes XOY and XOZ (Figure 7-6 (b) & (c)). Section 1 (the base section) was bent to  $90^\circ$  in plane XOZ (Figure 7-6(d)).



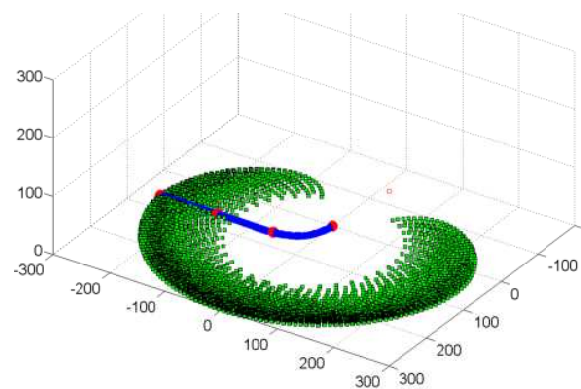
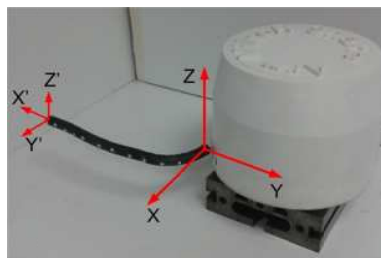
(a)



(b)



(c)



(d)

Figure 7-6. The 3rd demonstrator performing controlled motions for validating work volume

The results of the extensive trials demonstrate each section can bend up to  $90^\circ$  in an arbitrary direction, which validate the compliant joint design in terms of flexibility (chapter 6.3.1) and the work volume analysis (chapter 4.3.2).

### 7.3.3. Twisting angle measurements

In this demonstrator, one of the main emphases on the design aspect was given to minimize the twisting problem, thus, the trialing metrology system was setup to validate the counter-twisting ability of the design. Specifically, the twisting angle of this system was measured at the configuration where the max moment can be generated (the base section bends  $90^\circ$  in horizontal plane) which is the same to the previous two twisting angle measurement, as shown in Figure 7-7.

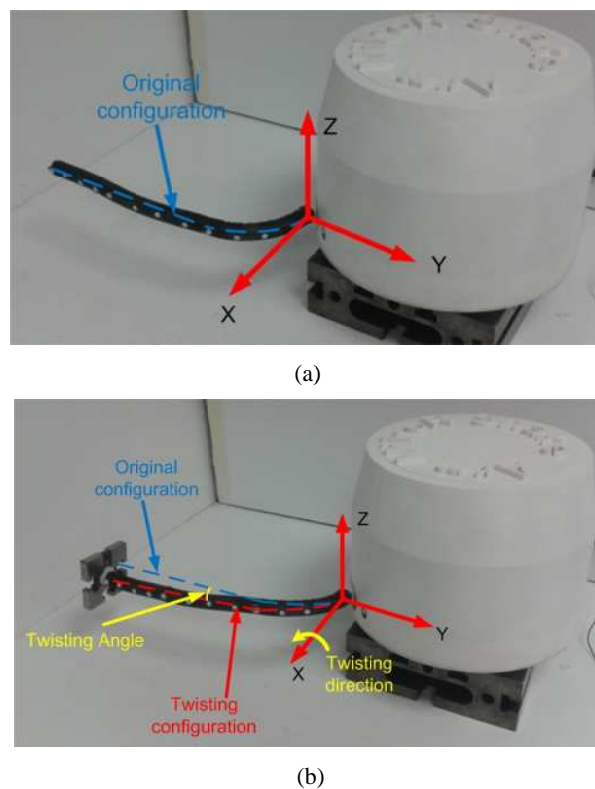


Figure 7-7. Twisting measurement of three section demonstrator: configuration for twisting measurement  
(a) original configuration without end load (b) twisting configuration

At this configuration, the twisting angles of the base section versus different end loads are presented in Table 7-4.

Table 7-4. Twisting angles of the base section versus end loads

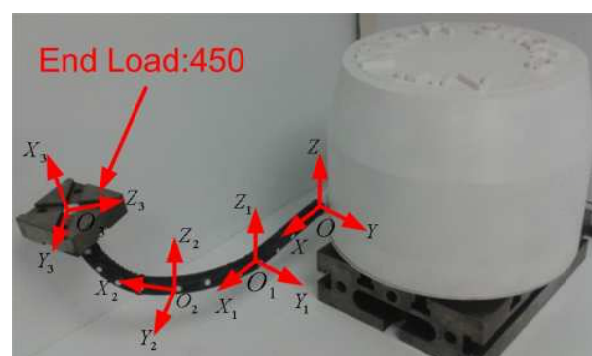
End load (g)	Twisting angle ( $^\circ$ )
100	0.34 $^\circ$
150	0.45 $^\circ$

200	0.61°
250	0.75°
300	0.91°
350	1.08°
400	1.21°
450	1.33°

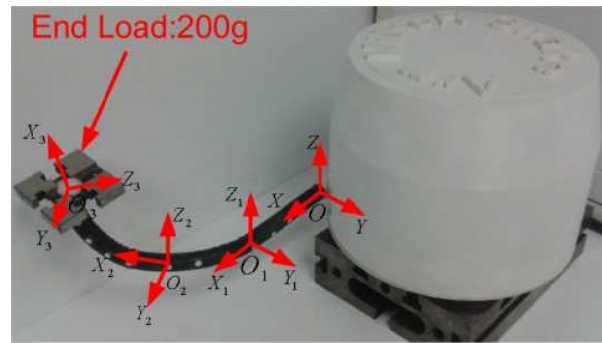
Compared with “continuum-style” segmented flexible backbone and the double-pivot demonstrator (they share the same diameter (15mm)), the twisting angle of the twin-pivot demonstrator is extremely decreased (twisting angle is decreased by 98.6% and 95.6%, respectively, even with heavier end load (200g) and longer moment arm (300mm) than the previous two demonstrators (36g end load & 200mm moment arm)).

#### 7.3.4. Load carrying capability measurements

In this trial, the end load carrying capability was tested on this prototype. Figure 7-8 illustrates several examples of the prototype carrying an end load with values (200g & 450g) of relevance for the end-effectors to be used for in-situ repair of gas turbine engines.



(a)



(b)

Figure 7-8. The 3rd demonstrator performing large load carrying capability: (a)200g end load; (b)450g end load

Further, the deflections of the continuum robot versus different end loads were measured. For example, the deflections of the arm at a particular configuration (section one (the base section) bends  $0^\circ$ ; section two (the middle section) bend  $30^\circ$  in plane  $X_1O_1Y_1$  with respect to coordinator  $X_1Y_1Z_1$ ; section three (the tip section) bends  $60^\circ$  in plane  $X_2O_2Z_2$  with respect to coordinate  $X_2Y_2Z_2$ . Coordinate  $X_1Y_1Z_1$ ,  $X_2Y_2Z_2$  and  $X_3Y_3Z_3$  are attached at the tips of the corresponding sections, respectively. The global coordinate is attached at the end of the base section) are presented in Table 7-5.

Table 7-5. Deflections of the arm versus end loads

Mass of the end load (g)	The deflection of TCP (mm)	Note
50	0.5	Configuration of Section 1:
100	1.2	Bending angle $0^\circ$
150	2.5	Direction angle $0^\circ$
200	4.0	Configuration of section 2:
250	6.2	Bending angle $30^\circ$
300	8.5	Direction angle $180^\circ$
350	11.5	Configuration of section 3:
400	16.1	Bending angle $60^\circ$
450	21.2	Direction angle $0^\circ$

According to the experiment results, the deflection is 4.0 mm when 200g end load is applied (the max end load of the research objective). This deflection is considerably large, however a light weight of machining tool is using for the mechanical blending application (45g). Therefore, a relatively small deflection is caused by the real design of the end effector (less than 0.5mm). Further, the machining operation is monitored and controlled via a camera attached at the tip of the arm by an operator, which enables desired machining shapes to be achieved.

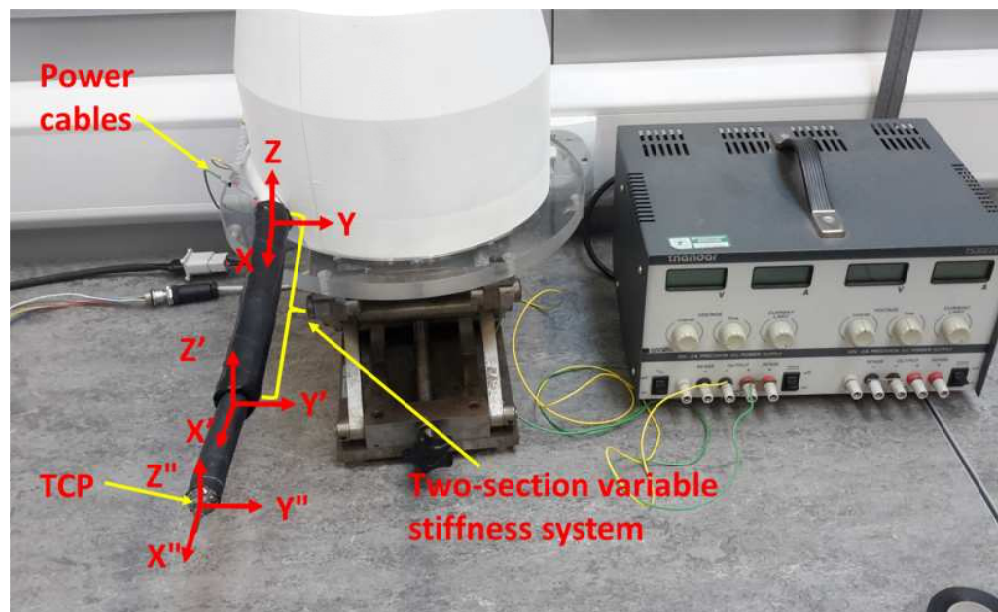


Figure 7-9. A three-section variable stiffness continuum robot

Next, a two-section variable stiffness system (chapter 6.3.2) was mounted on the base two sections of the arm in order to minimize the deflection caused by end loads, as shown in Figure 7-9. The continuum arm was driven to the previous configuration (Table 7-5) for comparing the deflection differences of the arm when equipped with/without a variable stiffness system and the deflections of the arm were presented in Table 7-6.

Table 7-6. Deflections of the variable stiffness continuum robot versus end loads

Mass of the end load (g)	The deflection of TCP (mm) (Soft state)	The deflection of TCP (mm) (Rigid state)	Percentage of the deflection decrease
--------------------------	---	--	---------------------------------------

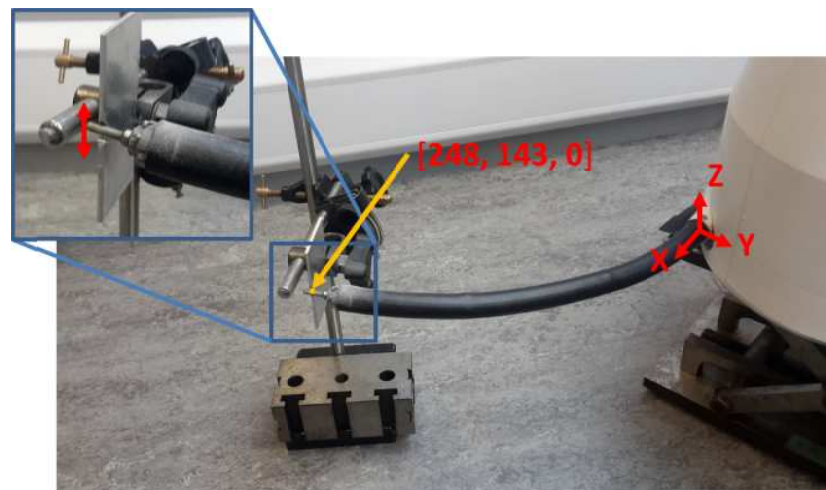
50	0.5	0.3	40%
100	1.0	0.7	30%
150	1.4	1.1	21%
200	2.0	1.4	30%
250	3.3	1.7	48%
300	5.3	2.0	43%
350	7.7	2.6	66%
400	8.8	3.0	65%
450	11.9	3.6	69%

The system can get flexible in 3 minutes by applying a 2A current via a NiCr wire (0.4mm in diameter) and get rigid in 20 minutes after turning off the power of the heating element. Comparing with Table 7-5 and Table 7-6, it can be found that the deflection was decreased by the variable stiffness system when in soft state, since an array of compliant joints are utilized for connecting the disks in the variable stiffness system which enhances the stiffness of the base two sections. Further, according to the results presented in Table 7-6, it can be seen that the deflection of the continuum robot in rigid state is much less than the soft state (decreased up to 69%), which proves the variable stiffness system can significantly increase the stiffness of the continuum robot.

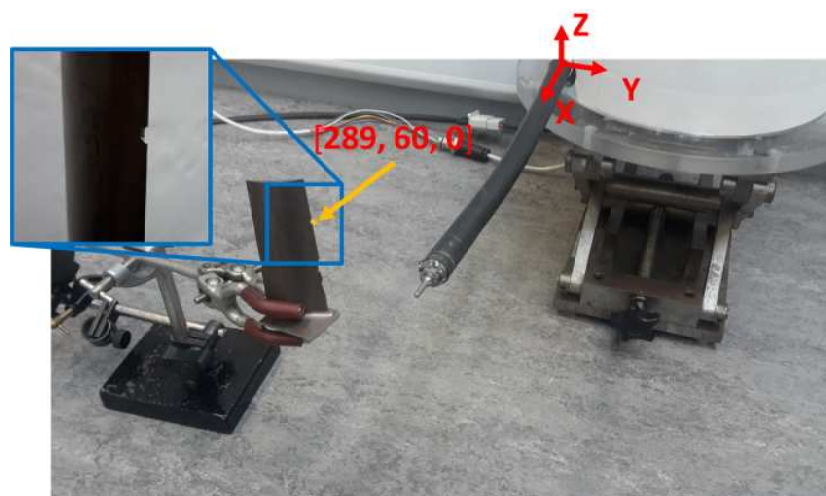
### 7.3.5. Machining trails

Finally, this demonstrator was utilised to demonstrate the machining capability of the twin-pivot design (since machining operations require all six DOFs of the three sections, thus the variable stiffness system was not employed in this trial). A blending tool is attached on the tip of the robot, which is actuated by a motor via a torque cable. The twin-pivot continuum robot was controlled to blend the edge of the metal plate/compressor blade and two types of material (Aluminium and Titanium) were utilised in the machining trial, as shown in Figure 7-10 (a) and (b). Specifically, in the

trail of blending the aluminium plate, the plate is placed at  $[248\text{mm}, 143\text{mm}, 0\text{mm}]$  with respect to the base coordinate attached at the end of the base section, which requires each section bend  $20^\circ$ . After the continuum robot reaches the desired position, the manipulator was controlled to make a scallop shape cut-off on the edge of the plate (see the insert of Figure 7-10). Likewise, in the case of the titanium blade trail, each section of the robot bends  $20^\circ$ ,  $0$  and  $-20^\circ$ , respectively, to reach the position  $[289\text{mm}, 60\text{mm}, 0\text{mm}]$  in the global coordinate. The results of the experiments prove that the three-section twin pivot demonstrator can provide an appropriate stiffness and control accuracy to stably blend metal materials, which includes the materials widely employed in the aerospace industry, e.g. aluminium and titanium.



(a)



(b)

Figure 7-10. Machining test of the 3rd demonstrator (a) the test on an aluminium plate; (b) the test on a titanium compressor blade

Finally, according to all the experiments undertaken on the three-section twin pivot demonstrator, the position control accuracy (the max error is less than  $\pm 1\text{mm}$  for sweeping in any  $\pm 5^\circ$  space in the work volume), repeatability (the max error is less than  $\pm 0.5\text{mm}$ ), counter-twisting ability (the twisting angle is  $0.61^\circ$  when  $200\text{g}$  end load),  $90^\circ$  bending ability at an arbitrary direction, end load carrying capability ( $200\text{g}$  end load with  $4\text{mm}$  deflection on the TCP and  $1.4\text{ mm}$  when integrating with a variable stiffness system on the base two sections) and machining abilities (aluminum and titanium plates) of this demonstrator have been demonstrated, which prove the design is reasonable. However, it is also found that a shape sensor needs to be integrated into the manipulator for compensating the deflection caused by the end effector and the reaction force of the repair tasks. However, this is beyond the scope of the current study and research aim of the group in the future.

#### **7.4. Test of prototype 4**

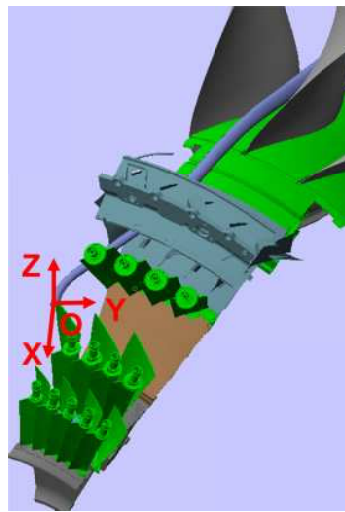
In this section, the experiments undertaken on the final twelve-section demonstrator (Full length continuum robot with twin-pivot backbone) are presented. The system was utilised to demonstrate the navigation in obstacle environment, work volume validation, coiling & uncoiling trials and end load carrying capability.

##### **7.4.1. Navigation trails of the twin-pivot demonstrator**

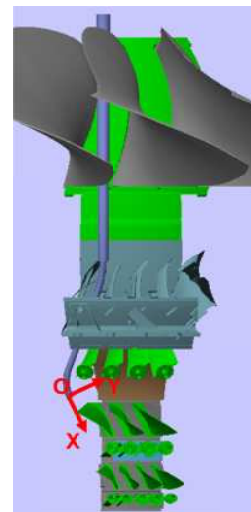
In order to inspect gas turbine engines, the continuum robot needs to be navigated to reach the first stage of LPC (Low pressure compressor). According to the construction of a gas turbine engine (Rolls-Royce Trent XWB), an example of navigation path is given (Figure 7-11(a), (b) & (c)):

1.  $19^\circ$  bend in  $+Z$  direction in the plane XOZ (arc length:  $132\text{mm}$ )
2. Straight path ( $280\text{ mm}$ ) with a  $19^\circ$  tilted angle
3.  $25^\circ$  bend in  $-Y$  direction in the plane XOY (the arc length:  $349\text{ mm}$ );
4. Straight path ( $300\text{ mm}$ ) with a  $19^\circ$  tilted angle;

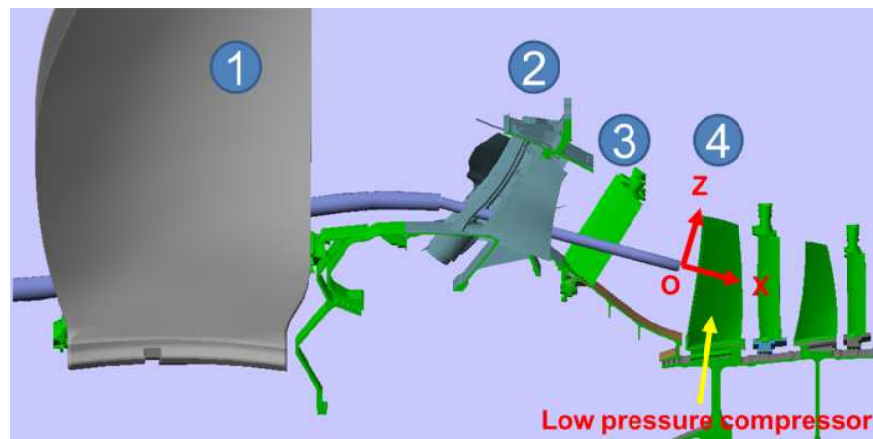
5.  $25^\circ$  bend in +Y direction in the plane XOY (the arc length: 100 mm);



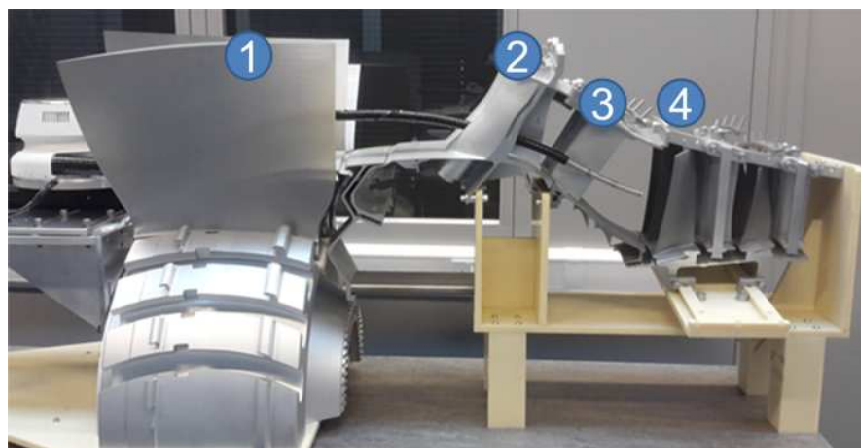
(a)



(b)



(c)



(d)

Figure 7-11. (a) An example of navigation paths in a gas turbine engines; (b) top view of the navigation path (c) front view of the navigation path (d) trial on a engine mock up (Rolls-Royce XWB)

In this test, the continuum robot was feed into the testing environment by a linear stage (1.5m long). Figure 7-11(d) illustrates that the continuum robot was navigated along the planned path in the desired confined space. And part 1 is engine fan blade, part 2 is engine section stators (ESS), part 3 is engine section rotors and part 4 is the first stage of low pressor compressor.

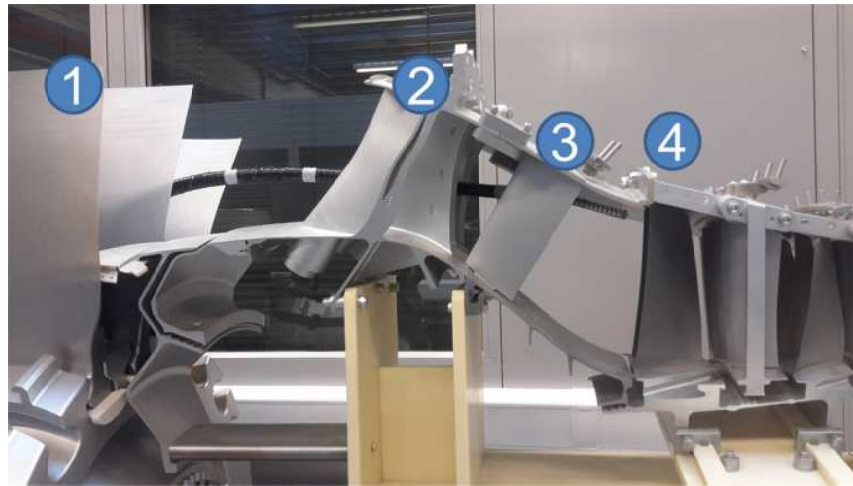


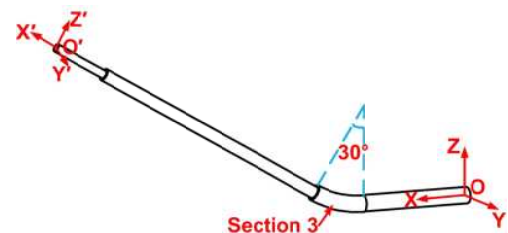
Figure 7-12. Another example of navigation tails in a gas turbine engines

As shown in Figure 7-12, another example of navigation tails into the engine mock-up was tested, which followed a path towards to the top of the compressor. According to the experiments, it has been proven that the full length twin-pivot continuum robot can be navigated to the desired position along a pre-planned path in the test environment. However, the control needs to be improved to minimize the deviation (currently  $\pm 10\text{mm}$ ) for more clutter environments (e.g. the other stages of low pressure compressor). Although the accuracy is appropriated for the application of this thesis, a shape sensor may need to be integrated into the system in the future, which can feed back the real-time shape of the continuum robot for increasing the control accuracy. Regarding the mechanical design, more sections may need to be built into the arm for minimising the deviation of navigation.

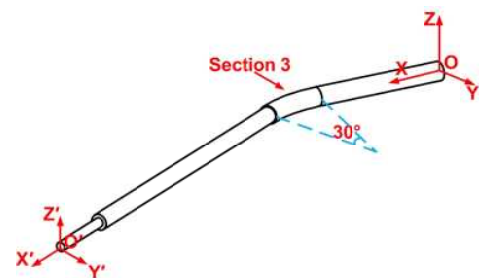
### 7.4.2. Work volume validation

In this part, the work volume of each section of the full length twin-pivot continuum robot was tested. Figure 7-13 illustrates several examples of the tests. Firstly, each section of the base stage was tested. For instance, section three bends  $30^\circ$  in different directions, respectively, as shown in Figure 7-13(a) & (b). Then six sections of the middle stage were tested separately. For example, Figure 7-13 (c) & (d) shows section six bends  $60^\circ$  in different planes. Further, one example of the tests of the tip stage (the tip three sections) is presented in Figure 7-13(e) & (f), which illustrates section ten bends  $90^\circ$  in variable directions.

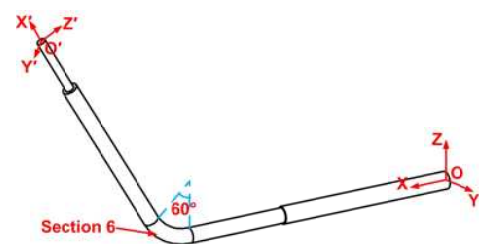
The trial result demonstrates the bending capability of the full length twin pivot system, which validates the designs of the compliant joints are reasonable in terms of flexibility (chapter 6.4.1).



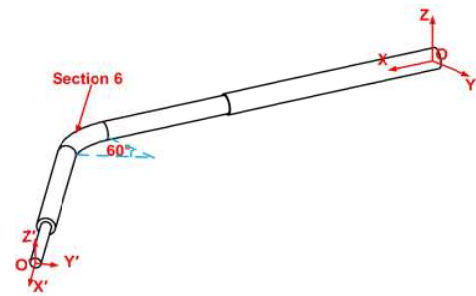
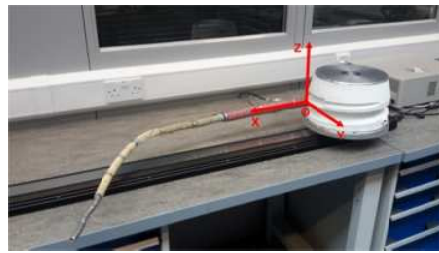
(a)



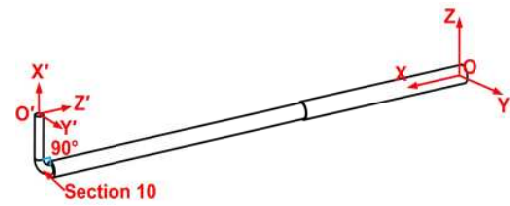
(b)



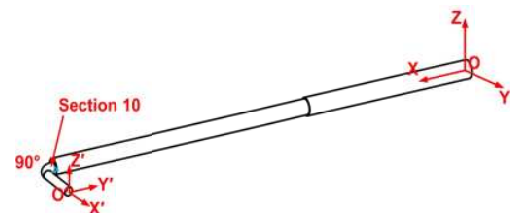
(c)



(d)



(e)



(f)

Figure 7-13. (a) 30° bend of section three in plane XOZ; (b) 30° bend of section three in plane XOY; (c) 60° bend of section six in plane XOZ; (d) 60° bend of section six in plane XOY; (e) 90° bend of section ten in plane XOZ; (f) 90° bend of section ten in plane XOY;

### 7.4.3. Coiling and uncoiling trails

Furthermore, another trail was setup for testing coiling and uncoiling motion on the casing of the actuation system, as shown in Figure 7-14. At the coiled configuration, the robot was coiled in a 275mm diameter profile (each section of the base stage (section 1~3; 144mm in length) bends 60.0°; each of section 4 to 6 (122mm in length) bends 50.8°; each of section 7 to 9 bends 42.5°). When the robot is fully coiled, the system is very compact enabling the system to be easily packed in a transport casing and safely shipped between different working places. Also, coiling & uncoiling ability enables the arm to be navigated into/out from clutter environments without requiring a

linear feeding system (e.g. a linear stage), which allows the system to be operated on the top of the walking hexapod robot (chapter 1.3).



(a)



(b)

Figure 7-14. Coiling and uncoiling trials of the 4th demonstrator

#### 7.4.4. Load carrying capability measurements

Finally, the end load carrying capability was tested on this prototype. Figure 7-15 illustrates an example of the motion of the manipulator carrying an end load (200g). It proves that the design can achieve the goal of the 200g end load carrying.

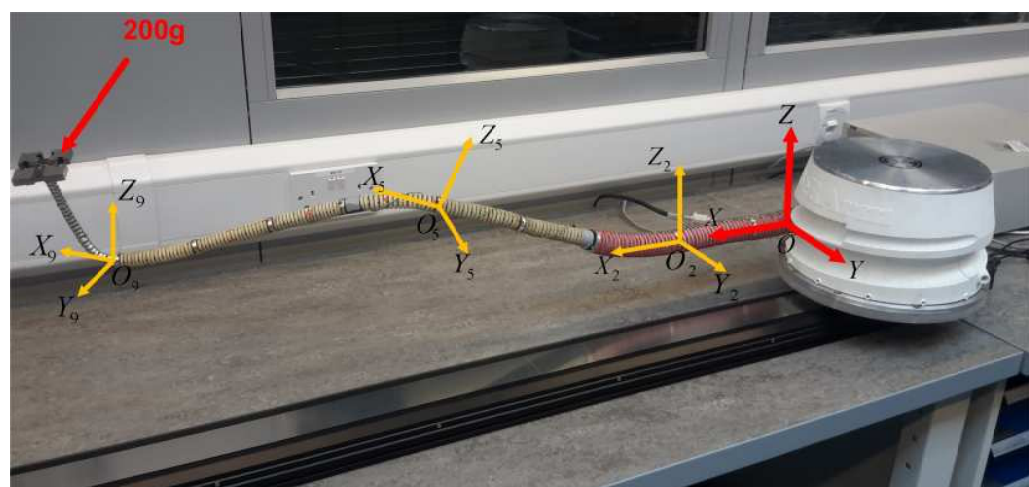


Figure 7-15. End load carrying capability trial

Since the twin-pivot continuum robot is a flexible and slender construction, a deflection is generated when applied an end load. For example, the deflection versus different end loads at a particular configuration (as shown in Figure 7-15, section three bends  $30^\circ$  in plane XOZ (direction angle  $90^\circ$ ); section six bend  $45^\circ$  in direction angle  $210^\circ$  ( $O_5Y_5$  is direction angle  $0^\circ$ ) with respect to coordinate  $X_5Y_5Z_5$  which is attached on the TCP of the 5<sup>th</sup> section; section ten bends  $70^\circ$  in plane  $X_9O_9Z_9$  with respect to coordinate  $X_9Y_9Z_9$  which is attached on the TCP of the 9<sup>th</sup> section; all of the rest sections bends  $0^\circ$ ) are presented in Table 7-7. It can be found that the deflection of the arm is 21.1mm when 200g end load is applied. However, there are two ways to minimize the position error of the arm TCP caused by the deflection. One way is to employ a light weight end effector (the current design is 45g (the same to the one employed in the three section twin-pivot system), so the deflection is less than 5.4mm); the other way is to monitor and control the tip position via a camera attached at the tip of the arm by the operator, which has been demonstrated on the three-section twin-pivot demonstrator.

Table 7-7. Deflections of the full length arm versus end loads

Mass of the end load (g)	The deflection of TCP (mm)
50	5.4
100	10.3
150	15.7
200	21.1

Finally, the full length twelve-section continuum robot (1266mm in length) was built and tested in the aforementioned experiments, e.g. navigation trail ( $\pm 10$ mm deviation), work volume test, coiling & uncoiling and end load carrying capability (200g end load with 21.1 mm deflection at the tip). It proves the demonstrator has an appropriate

flexibility, stiffness and diameter/length ratio for inspecting in a confine space. Further, a trial for demonstrating the machining ability of this demonstrator will be undertaken.

However, some problems were identified from this prototype. One is the control accuracy needs to be further enhanced (currently the deviation compared with the pre-planned path is  $\pm 10\text{mm}$ ) by integrating a shape sensor for feeding back the actual bending shape of the manipulator. Alternatively, position sensors can be integrated into the head of each section, which enables the actual bending shape of the system can be calculated. However, it is difficult to implement, when the section diameter is small. Further, the equations for computing the deflection of the manipulator when acting an end load/force/torque at the tip of the manipulator need to be studied in the further research, which will enable more precise control when the system carries a heavy end effector.

## 7.5. Conclusions

In this chapter, the trials undertaken on the four demonstrators are introduced. The first demonstrator was setup to evaluate the backbone materials and according to the test, super-elastic Nitinol was determined to be employed for building the further systems as the source of generating the bending motion.

Further, a twisting problem of the conventional flexible backbone continuum robot was identified from the continuum-style segmented flexible backbone prototype ( $45^\circ$  twisting angle respect to 36g end load). In order to study this problem, the twisting angles were measured from the double-joint ( $15^\circ$  twisting angle respect to 36 g end load) and twin-joint constructions ( $0.61^\circ$  twisting angle respect to 200g end load), respectively. It was seen that the twin-joint construction has a better counter-twisting capability.

Furthermore, the accuracy (error is less than  $\pm 1$  mm for sweeping in any  $\pm 5^\circ$  area in the work volume) and repeatability (error is less than  $\pm 0.5$  mm) of the three-section

twin-pivot demonstrator were measured. It was also proved that each section of the demonstrator can bend  $90^\circ$  at an arbitrary direction. Next, the three-section continuum robot was equipped with a two-section variable stiffness system and it was found that up to 69% of the tip deflection was decreased by employing the variable stiffness system. Several machining trials (aluminium & titanium plates) were undertaken on this system for demonstrating the machining capability.

Finally, the full length twin pivot demonstrator was tested to be navigated along a pre-planned path (based on the construction of Rolls-Royce Trent XWB) into a confined space (max deviation  $\pm 10\text{mm}$ ), which proves the demonstrator has an appropriate control accuracy for inspecting a gas turbine engine. The work volume test and coiling & uncoiling trial prove the designs of the compliant joints are reasonable in terms of flexibility. The load carrying trial demonstrates the system is able to carry 200g end load, which enables a wide range of repair tools to be delivered into an engine.

---

## Chapter 8 Conclusion and future works

In this chapter, the overall outcomes and achievements of the thesis are discussed emphasising how these address the current limitations in the field. Based on both academic and technology achievements of this research, this chapter also provides possible future research directions in designing and modelling approaches which can be utilised to advance the capabilities of a wide range of continuum robots.

### 8.1. Discussing challenges in continuum robots vs project objectives

In this part, the challenges of this research are discussed in terms of design and modelling so that the achievements of the PhD research can be put into a wider academic and technology context.

The aim of this thesis was focused on developing a novel continuum robot comprising an appropriate diameter/length ratio continuum arm and a tubular variable-stiffness system for in-situ repair of gas turbine engine (Rolls-Royce Trent XWB); this has not been achieved by any other systems so far, hence, the novelty claimed by this work. For achieving this goal, the continuum arm needs to be able to wave between the blades to reach desired positions in the engine while the adjustable-stiffness unit allows the arm to have a proper flexibility for navigating in the working environment and increase its stiffness (of particular sections) when activating machining tasks. Moreover, further challenges aroused from the fact that, being a part of FP7 project MiRoR (Miniaturised Robotic systems for holistic in-situ Repair and maintenance works in restrained and hazardous environments), the robot needs to combine with a walking-hexapod system for inspection in nuclear stations; this resulted in the need for the system to have a compact size and be light weight (especially the actuation system) for allowing the hexapod able to carry it in a limited space. Hence, not only the robot needed to have a high number of degrees of freedom, to be slim and able to selectively rigidize sections but also to be very compact so that it could be carried on the top of the walking hexapod (subject of another PhD thesis at Univ. of Nottingham).

According to a wide range of literature review, although some of the existing continuum robots have been demonstrated in several key applications, e.g. minimally invasive surgery (MIS) and rapid handling, there are several limitations of these systems identified, which need to be addressed for in-situ repair applications in this research:

- The accessibility of a continuum robot in confined spaces is depended on several factors, e.g. flexibility (it can be found that flexible backbone continuum robots have better accessibility in a crowded environment, comparing with rigid backbone ones (Chapter 3.1)), diameter/length ratio and stiffness. Since most of the existing systems were not developed for the applications in highly constrained and large work environments as gas turbine engines, the designs was not given a consideration to all of these three factors simultaneously; *therefore, the thesis aimed at proposing a new mechanical design solution for structuring a flexible backbone continuum robot, which has a small diameter, long length, appropriate stiffness and flexibility;*
- In order to perform in-situ repair, it requires the continuum robot to have a relatively great stiffness of its arm needs to support end loads, especially reaction force/torque of machining. However, the existing flexible backbone continuum robots were generally designed for MIS and rapid handling by using the advantage of safe robot-human/objective interaction (since the flexible construction), which renders the backbone difficult to maintain the TCP when activating desired tasks in this research, e.g. mechanical blade blending. *Hence, the research in the PhD thesis sought to develop a mechanical solution for enhancing the arm stiffness when activating machining tasks.*
- Based on the experiment undertook on the first demonstrator built in this thesis (continuum robot with segmented single backbone pivot), another

drawback of the conventional designs was found: the central located flexible backbone is twisted along the longitudinal axis by end load and its own weight when bending in the horizontal plane (Chapter 7.1). In particular,  $45^\circ$  twisting angle was generated at the base section of two-section demonstrator (employing a conventional design concept: a super-elastic NiTi rod is located in the centre of disk as backbone and articulated by cables) by 36g end load when the base section bent  $90^\circ$  and the tip one kept straight, which leads to poor control accuracy. *Since the continuum robot needed to carry an appropriate end load when navigating into the engine, which is very likely to have several bends in horizontal plane, thus the research in the PhD thesis aimed to address this problem.*

In this research, since some unique concepts of continuum robots were proposed, the following fundamental modelling, including kinematics, actuation force, compliant joint bulking and stiffness analyses, needed to be studied for the design and control of these new constructions.

- Regarding continuum robots kinematics, the research topic can be divided into two levels: the first one is the mapping between task space to joint space (e.g. computing the position and orientation of each section tip, based on a given desired position for robot TCP: tip-following algorithm [165]); the second one is the mapping between joint to actuation space (e.g. calculate the actuation displacements by the configurations of each section obtained from the first mapping, according to the geometry of section mechanism) [135]. In this thesis, the research focused on the second mapping of kinematics, because it had to be developed based on the design of the robot. *Since new structures were introduced in this research, so their kinematics models needed to be investigated to enable their precise control. Further, the aforementioned*

*challenge of inverse kinematics (Chapter 3.1) also aimed to be addressed in this research.*

- Model for calculating actuation force of cables is required to be developed for assisting the hardware design. Comparing with kinematics, this field was less considered by the existing researches. Principle of virtual work was utilised in previous studies, which focused on the static analysis of rod-driven continuum robot (elastic rods can pull and push) [32, 167, 168]. The analysis for cable-driven system is dissimilar since different actuation media is utilised which makes different interaction to the structure (cables can only pull). *The research in this PhD thesis aimed to introduce a static approach for calculating actuation force of cable-driven continuum robot.*
- Flexible rods are employed as the compliant joints of continuum robots. Because of the elastic property, they can be buckled if overloaded. However, this has not been seen from the existing researches. *Hence, the max buckling load of compliant joint sought to be studied. Further, stiffness of the new constructions was needed to be introduced for guiding the design of the hardware.*

## **8.2. Academic findings and engineering validations**

A new approach of in-situ repair for gas turbine engine has been developed by employing continuum robots to deliver machining tools and vision system to desired places, which cannot be reached by conventional tools or human being without disassembling the engines, bringing the benefits on decreasing repair time and cost significantly.

In the following the main achievements of the PhD research have been summarized.

### 8.2.1. Unique designs of continuum robots

With regard to the identified limitations, two families of unique continuum robot design concepts have been proposed for structuring a “slender” continuum robot with appropriate stiffness and flexibility.

One employs two compliant joints connected in series in a segment (double-pivot compliant joint) and a single section consists of multiple segments for enabling high bending capability (Chapter 3.2).

The other, more advanced concept that has been materialised in two working prototypes, utilizes two orthogonal groups of twin parallel elastic rods/sheets, which are connected in series, as compliant joints (twin-pivot compliant joint) in a segment and couples of segments are built into a single section (Chapter 3.2).

These two families of concepts bring various options for continuum robot designs, which have the following advantages:

- Unlike the existing designs (“pure” continuum backbone/ continuum arm with segmented backbone), the designs enable the robot to have high flexibility (great bend capability:  $90^\circ$  per section), small diameter/length ratio (two full length continuum robots’ average diameter/length ratios are 0.02 and 0.023, respectively; the smallest diameter/length ratio of the existing long continuum robots is 0.03 [33]) and an appropriate stiffness simultaneously (the deflection of the final full length prototype is less than 5.4mm when carrying an end load (50g)). Compared with the existing solutions, the continuum robots developed in this PhD research (with 200g loading capability for 1.2m long) represent a step-change in the development of the families of such system.
- The twisting angle along the longitudinal direction can be decreased by both of the concepts significantly; this allows a slender continuum robot have a precise position control, when bending in the horizontal plane (for example, comparing with one of conventional designs continuum robot with segmented

single backbone pivot), the twisting angles of double and twin-pivot compliant joint concepts are decreased by 67% and 98.6%, respectively. See chapter 7 for details). These results proved not only a significant advancement in the field but also a critical enabler for improving the positioning accuracy especially when dealing with a long continuum robots (that are likely to be needed for “far away” invasive interventions such as those within gas turbine engines).

- Based on the cable tension analysis, both concepts of continuum arm design enable two pairs of cables employed in one single section with constant tension force at any arbitrary configuration, giving the opportunity to minimise the size and weight of actuation pack (at least 95% of original tension force is able to be maintained at arbitrary configuration (Chapter 4.1 & 4.2)). Up to now, most of continuum robots have been using linear actuators (to minimise the slippages in spools) or simple spooling systems with tensioning mechanism that resulted in significantly bulky constructions. With a smart spooling design, the present research work proved that the actuation pack can be so compact (275mm in diameter; 25 motors packed in it) that is can be a truly portable robotic system; no similar achievements have been reported.

Based on these new concepts, three demonstrators (i.e. a three-section continuum robot with twin-pivot backbone - 300 mm in length) and two full length ones with double and twin-pivot backbone (no less than 1.2m in length), respectively) were designed and built (Chapter 6).

According to the preliminary experiments, it was found that twin-pivot compliant joint structure can provide better stiffness and minimise the twisting angle (twisting angle is decreased by 95.9%), comparing with double-pivot compliant joint structure. Hence, the concept of twin-pivot compliant joint was selected for building the final prototype.

In the machining trials, it has been proven that the three-section continuum robot with twin-pivot backbone can provide an appropriate stiffness (the deflection of the arm is less than 0.5mm when carrying 50g end load, which is heavier than the end effector using on this demonstrator), control accuracy ( $\pm 1$ mm error for sweeping in any  $\pm 5^\circ$  area in the work volume) and repeatability ( $\pm 0.5$  mm error in the whole work volume), enabling the system to blend metal materials stably, e.g. aluminium and titanium, which are the materials widely employed in the aerospace industry (Chapter 7.3).

Accessing in gas turbine engines has been realised by the final full length continuum robot (1266mm). It has been proven that the system has an appropriate control accuracy to be navigated to reach the first stage of LPC (low pressure compressor) of a gas turbine engine (Rolls-Royce XWB) by following a pre-planned path, since HLC via vision is still under development by a project partner (Chapter 7.4). Further, a machining trial will be demonstrated on this full length continuum robot in the near future (the machining code is being prepared). According to the test, TRL of the final full length continuum robot can be defined as Level 4.

### **8.2.2. Modelling of continuum robots**

In this thesis, several fundamental analyses were achieved, e.g. kinematics, buckling analysis of compliant joint, actuation force and stiffness. As aforementioned, there were two families of novel continuum robot constructions proposed in this research, thus new kinematics models were needed to be developed for in order to precisely control them (Chapter 4).

- Based on an algebra approach, a straightforward kinematic model for the family of double-pivot compliant joint concepts (flexible cable actuated mechanism) was presented in this thesis. Unlike the conventional approach making a projection on section's bending plane which transfers the 3D problem to 2D, the new method directly projects cables on the backbone and remarkably simplifies the derivation. In this model, compliant joint was

assumed as a virtual universal joint, which also can simplify the calculation. Further, a simulation model was built in ANSYS for cross-validation, which proves the kinematics model able to provide a small position (max 0.017 mm) and angular error (max  $1.04 \times 10^{-4}$  in radian), comparing with the simulation results (Chapter 4.1);

- Regarding the concept of twin-pivot compliant joint (flexible cable actuated mechanism), a new kinematic model was also developed based on a combination of D-H method and geometry approach. In this model, the short compliant joint was assumed as a virtual conventional revolute joint, which simplified the analysis (Chapter 4.2). Two sub-bending plane was utilised for deriving forward kinematics, since the conventional geometry approach cannot be deployed here by projecting on section's overall bending plane, due to the construction. Further, the kinematics challenge of inverse kinematics (Chapter 3.1) has been corrected by an iterative approach based on forward kinematics in this model. According to the trial results of the three-section demonstrator, the position control error of single section is less than  $\pm 1$  mm in translation for sweeping in any  $\pm 5^\circ$  operation area in the work volume. The max error of single section repeatability is less than  $\pm 0.5$  mm in the work volume (Chapter 7.3) that fulfils the requirements of machining in a confined space. It can be applied to a wider range of continuum robots, if the flexible rod is built in the model.
- A method for calculating work volume of multiple-section continuum robots has been developed by considering the geometry of the robot and the material property of compliant joints (Chapter 4.3). Because the design employed elastic material as compliant joints which needed to be bent to a small bending radius for generating an appropriate bending angle during the operation. However, this factor was neglected in the existing researches. The model was

---

based on forward kinematics with a search procedure to find out the location of the section tip against different bending angles.

- Unlike the previous researches employing principle of virtual work, a static method was developed for calculating actuation forces of a continuum robot developed on the concepts proposed in this thesis (Chapter 5.1), which built the static equilibrium by considering end load, weight of robot, cable tension, force for bending flexible backbone and the interaction from distal sections' cables. It allows designers to calculate the actuation force of an arbitrary section of a multiple-section continuum robot for any bending angle in the work volume. An interface was built in MATLAB, which is able to compute actuation force based on the parameters of a robot (e.g. section diameter, length, weight, compliant joint size and bending angles, etc.).
- Since compliant joint is relatively flexible comparing with conventional rigid joint, the joint can be buckled if overloaded, which can cause poor control accuracy and even physically fail the whole system. Therefore, buckling analysis of compliant joint was introduced for providing designers with a methodology to calculate the max load which a joint can withstand (Chapter 5.2); and it can also provide the dimensions of the compliant joint (e.g. length and diameter) when the load along the backbone is given. It was utilised in designing the compliant joints of the demonstrators and the experiments proven the joint designs are reasonable.
- Stiffness matrix of a single multi-compliant section was achieved. In this model, actuation cables and compliant joint were considered as the compliance resource. Jacobian matrix of a single section was also analysed for supporting the derivation of stiffness matrix. Finally, the analysis has been validated by simulations in ANSYS with max 7% error in the whole work volume of a single section (Chapter 5.3 & 5.4).

---

### **8.2.3. An unique design of variable stiffness system as ancillary for continuum robots**

In this thesis, a concept of unique variable stiffness system was developed for enhancing the stiffness of a continuum robot when it activates machining tasks and being flexible enough to allow the robot move freely when navigating into target areas. By employing a thermoplastic material to fill the space for the joint movement, the system can be switched into a soft state at a low temperature (60°C) by applying an electrical current via a heating element (NiCr wire) for melting the bespoke material and get rigid by air when the electrical power is switched off.

Based on this idea, a two-section stiffness-controllable system was built, which also employed twin-pivot compliant joint structure and the space between adjacent disks are filled with polymorph (melting temperature is 60°C). It was able to be mounted on the outside of the three-section continuum robot as a sleeve, which can significantly decrease the deflection caused by end loads (Chapter 6.3). Specifically, the system can get flexible in 3 minutes by applying a 2A current via a NiCr wire (0.4mm in diameter) and get rigid in 20 minutes after turning off the power of the heating element. It was found that the deflection of the arm TCP in rigid state can be decreased by up to 69%, comparing with that in soft state, which proves the stiffness was increased dramatically by the variable stiffness system; the continuum robot was also flexible enough to move in a soft state (Chapter 7.3).

### **8.3. Future work**

The proposed design concepts and modelling of continuum robots has been validated based on both simulations and physical demonstrators in this thesis. However, some further challenges that could be materialised in future research directions have been identified and are discussed per separate topics in the following.

### 8.3.1. Towards next-generation design of continuum robots

- According to the literature review, it can be found that there is a trend for taking flexible rods as the actuation media for continuum robots, especially for the system used in MIS. One advantage of rod actuation is that it can push and pull, thus the backbone takes less compressive load compared with wire-actuation system, so it does not suffer buckling problem. The other one is rod can give the construction better stiffness. However, up to now, rod-actuation continuum robots have been built with max three sections [169, 170], which limit it to be utilised in large highly confined space. One possible reason is that the shape of a proximal section is depended on the overall stiffness of rods running through this section [135], thus it makes more difficult to bend a proximal section if there are more actuation rods of distal sections passing through it. Therefore, it is valuable to compare between different actuation methods (i.e. cable and flexible rod) for structuring a small diameter and long continuum robot, in terms of bending capability/section, stiffness and control accuracy.
- The size of the work volume is a critical parameter for continuum robot design. To date, the researches in this area focused on the design of symmetric continuum robots which have symmetric work space. However, for some application cases, the workspace of the system does not need necessarily to be symmetric in all directions. In some applications, e.g. machining, inspecting and surgery operations, the objective only appears on one side of the system, so that one side of the work volume needs to be increased and the other side does not really help on the operation, so it could be decreased. Likewise, the stiffness of the continuum robot also can be asymmetric, thus it can provide the advantage of higher stiffness in desired directions. Therefore, the design solutions need to be searched in the future studies.

### 8.3.2. Modelling

- According to the experiments, it was found that shape of a single section affected by the frictions between actuation cables and guide holes. A trail is required for comparing the kinematics differences against different amounts of friction, in order to identify how the friction affects the kinematics performance. In order to minimise this influence, a mechanical approach is probably needed to be found for reducing the friction in the future;
- In this thesis, an approach for calculating the critical buckling load of single compliant joint was introduced and validated by both simulation and physical test (Chapter 5&6). However, the equations for obtaining critical buckling loads of single and multiple sections were not achieved, but valuable to be investigated, which may include other elements of the system, e.g. cables and disks. Because the buckling problem affects the straight configuration of the robot, generally utilised as the initial position for calibrating continuum robots, which inevitably affects the position control. Further, the critical buckling load of compliant joints in bent configurations is also worth to be investigated, since the flexible structure maybe even more likely to be buckled in curved shapes, which has not been studied.
- In this thesis, a 2D stiffness matrix was obtained, which can calculate the deflection in 2 DoFs directions when a torque is applied. However, a 6D stiffness matrix and deflection compensation approach needs to be developed for the proposed designs, since end effector/reaction force/torque cause a deflection of a continuum robot, which can affect the position control accuracy. Further, the stiffness of the variable-stiffness mechanism also needs to be investigated, so it can provide the deflection in both soft and stiff states for evaluating it when designing the hardware.

### 8.3.3. Control and calibration

- Furthermore, in order to minimize the control error, a shape sensor may need to be integrated into the continuum arm which can feed back the actual shape of the system. Alternatively, the actual lengths of all the cables can be measured in real time, and calculate the TCP of each section from the proximal to distal accordingly by forward kinematics.
- A method for calibrating the continuum robot (e.g. initial configurations, including bending and direction angles of each section; tension force of cables) needs to be developed. There are various ways can be utilised, e.g. optical camera, strain gauge and fibre optic techniques (see: <http://lunainc.com/>).

## References:

- [1] *Oxford dictionary*. Available: <http://www.oxforddictionaries.com/definition/english/robot>
- [2] B. Siciliano and O. Khatib, *Springer handbook of robotics*: Springer Science & Business Media, 2008.
- [3] *International Federation of Robotics (IFR)*. Available: <http://www.ifr.org/>
- [4] *Industrial robots*. Available: <http://www.ifr.org/industrial-robots/>
- [5] *Types of industrial robots*. Available: <http://www.ifr.org/industrial-robots/products/>
- [6] *Articulated robots*. Available: <http://new.abb.com/products/robotics/industrial-robots/irb-120>
- [7] *SCARA robot*. Available: <http://robots.epson.com/products/1>
- [8] *CARTESIAN ROBOT*. Available: <http://www.parker.com/portal/site/PARKER/menuitem.7100150cebe5bbc2d6806710237ad1ca/?vgnextoid=f5c9b5bbec622110VgnVCM10000032a71dacRCRD&vgnextdiv=687362&vgnnextcatid=3155045&vgnnextcat=CARTESIAN++ROBOTS&Wtky=>
- [9] *parallel kinematic robot*. Available: <http://new.abb.com/products/robotics/industrial-robots/irb-360>
- [10] *Service Robots*. Available: <http://www.ifr.org/service-robots/>
- [11] NASA. (2015). *Mars Exploration Rovers*. Available: <http://mars.jpl.nasa.gov/>
- [12] *OpenROV | Underwater Exploration Robots*. Available: <http://www.openrov.com/>
- [13] *SeeByte*. Available: <http://www.seebyte.com/>
- [14] *Aerial robotics for the society*. Available: <http://sparc-robotics.eu/aerial-robotics-for-the-society/>
- [15] *AIRBORNE ROBOTICS*. Available: <http://www.airborne-robotics.com/en>
- [16] *Mining Robots*. Available: <http://www.superdroidrobots.com/shop/custom.aspx/mining-robots/65/>
- [17] *ASI*. Available: <http://www.asirobots.com/>
- [18] *RESCUE ROBOTS-Machines Play Vital Roles in Disaster Relief*. Available: [http://web-japan.org/trends/09\\_sci-tech/sci100909.html](http://web-japan.org/trends/09_sci-tech/sci100909.html)
- [19] *Lego Mindstorms*. Available: <http://www.lego.com/en-us/mindstorms/?domainredir=mindstorms.lego.com>
- [20] *da Vinci Surgery*. Available: <http://www.davincisurgery.com/>
- [21] (2002). *Surgeon uses Zeus Robotic Surgical System*. Available: <http://www.vision-systems.com/articles/2002/01/surgeon-uses-zeus-robotic-surgical-system.html>
- [22] *Versatrax 300*. Available: <http://www.inuktun.com/crawler-vehicles/versatrax-300.html>
- [23] *Alstom Inspection Robotics*. Available: <http://www.inspection-robotics.com/site/index.cfm>
- [24] *Vacuum Cleaning Robot*. Available: <http://www.irobot.co.uk/>
- [25] *IRB 140*. Available: <http://new.abb.com/products/robotics/industrial-robots/irb-140>
- [26] *Absolute accuracy industrial robot option*. Available: [https://library.e.abb.com/public/931fcb281dbe7fecc1257b1300579a6a/AbsAc cPR10072EN\\_R5.pdf](https://library.e.abb.com/public/931fcb281dbe7fecc1257b1300579a6a/AbsAc cPR10072EN_R5.pdf)
- [27] "IRB 140."
- [28] *710 Kobra*. Available: <http://www.irobot.com/For-Defense-and-Security/Robots/710-Kobra.aspx>
- [29] *Titan Medical Inc*. Available: <http://www.titanmedicalinc.com/>
- [30] *Medrobotics*. Available: <http://medrobotics.com/>

- [31] *Hansen Medical*. Available: <http://www.hansenmedical.com/us/en>
- [32] N. Simaan, R. Taylor, and P. Flint, "A dexterous system for laryngeal surgery," in *Robotics and Automation, 2004. Proceedings. ICRA'04. 2004 IEEE International Conference on*, 2004, pp. 351-357.
- [33] T. Ota, A. Degani, D. Schwartzman, B. Zubiante, J. McGarvey, H. Choset, *et al.*, "A highly articulated robotic surgical system for minimally invasive surgery," *The Annals of thoracic surgery*, vol. 87, pp. 1253-1256, 2009.
- [34] R. Buckingham, V. Chitrakaran, R. Conkie, G. Ferguson, A. Graham, A. Lazell, *et al.*, "Snake-arm robots: a new approach to aircraft assembly," SAE Technical Paper2007.
- [35] *OCRobotics*. Available: <http://www.ocrobotics.com/>
- [36] *MiRoR*. Available: <http://www.mirror.eu/>
- [37] I. D. Walker and M. W. Hannan, "A novel elephant's trunk'robot," in *Advanced Intelligent Mechatronics, 1999. Proceedings. 1999 IEEE/ASME International Conference on*, 1999, pp. 410-415.
- [38] B. Hazel, J. Côté, Y. Laroche, and P. Mongenot, "In-situ robotic interventions in hydraulic turbines," in *Applied Robotics for the Power Industry (CARPI), 2010 1st International Conference on*, 2010, pp. 1-6.
- [39] R. Bogue, "Robots in the nuclear industry: a review of technologies and applications," *Industrial Robot: An International Journal*, vol. 38, pp. 113-118, 2011.
- [40] *Qantas Flight 32*. Available: [http://en.wikipedia.org/wiki/Qantas\\_Flight\\_32#Cause](http://en.wikipedia.org/wiki/Qantas_Flight_32#Cause).
- [41] *United Airlines Flight 232*. Available: [http://en.wikipedia.org/wiki/United\\_Airlines\\_Flight\\_232#cite\\_note-ntsb-1](http://en.wikipedia.org/wiki/United_Airlines_Flight_232#cite_note-ntsb-1).
- [42] *On site repairs - Diesel engine repair maintenance*. Available: [http://www.sudmoteurs.fr/on\\_site\\_repairs/on\\_site\\_repairs\\_en.php](http://www.sudmoteurs.fr/on_site_repairs/on_site_repairs_en.php)
- [43] *In-Situ Laser Cladding*. Available: <http://www.hardwear.com.au/>
- [44] *BLENDING SCOPE-AN ESSENTIAL KEY TO SUPERIOR AIRCRAFT FLEET PERFORMANCE*. Available: <http://www.blending-scope.com/>
- [45] D. Reintsema, K. Landzettel, and G. Hirzinger, "DLR's advanced telerobotic concepts and experiments for on-orbit servicing," in *Advances in Telerobotics*, ed: Springer, 2007, pp. 323-345.
- [46] *MIRO - Versatile Robot Arm for Surgical Applications*. Available: [http://www.dlr.de/rmc/rm/en/desktopdefault.aspx/tabid-3795/16616\\_read-40535/](http://www.dlr.de/rmc/rm/en/desktopdefault.aspx/tabid-3795/16616_read-40535/)
- [47] A. Albu-Schäffer, S. Haddadin, C. Ott, A. Stemmer, T. Wimböck, and G. Hirzinger, "The DLR lightweight robot: design and control concepts for robots in human environments," *Industrial Robot: An International Journal*, vol. 34, pp. 376-385, 2007.
- [48] S. Klanke, D. Lebedev, R. Haschke, J. Steil, and H. Ritter, "Dynamic path planning for a 7-dof robot arm," in *Intelligent Robots and Systems, 2006 IEEE/RSJ International Conference on*, 2006, pp. 3879-3884.
- [49] L. Zollo, B. Siciliano, C. Laschi, G. Teti, and P. Dario, "An experimental study on compliance control for a redundant personal robot arm," *Robotics and Autonomous systems*, vol. 44, pp. 101-129, 2003.
- [50] C. W. Kennedy and J. P. Desai, "Modeling and control of the Mitsubishi PA-10 robot arm harmonic drive system," *Mechatronics, IEEE/ASME Transactions on*, vol. 10, pp. 263-274, 2005.
- [51] E. S. Conkur and R. Buckingham, "Clarifying the definition of redundancy as used in robotics," *Robotica*, vol. 15, pp. 583-586, 1997.
- [52] R. Menasri, A. Nakib, H. Oulhadj, B. Daachi, P. Siarry, and G. Hains, "Path planning for redundant manipulators using metaheuristic for bilevel optimization and maximum of manipulability," in *Robotics and Biomimetics (ROBIO), 2013 IEEE International Conference on*, 2013, pp. 145-150.

- [53] J. Sullivan and A. Pipe, "Path planning for redundant robot manipulators: a global optimization approach using evolutionary search," in *Systems, Man, and Cybernetics, 1998. 1998 IEEE International Conference on*, 1998, pp. 2396-2400.
- [54] J. M. Hollerbach and K. Suh, "Redundancy resolution of manipulators through torque optimization," *Robotics and Automation, IEEE Journal of*, vol. 3, pp. 308-316, 1987.
- [55] G. S. Chirikjian and J. W. Burdick, "Hyper-redundant robot mechanisms and their applications," in *Intelligent Robots and Systems' 91. Intelligence for Mechanical Systems, Proceedings IROS'91. IEEE/RSJ International Workshop on*, 1991, pp. 185-190.
- [56] R. V. Bostelman, J. S. Albus, R. E. Graham, and L. Grey Pilgrim, "Robocrane and EMMA applied to waste storage tank remediation," in *American Nuclear Society Seventh Topical Meeting on Robotics and Remote Systems*, 1997, pp. 708-713.
- [57] S. Ma, S. Hirose, and H. Yoshinada, "Development of a hyper-redundant multijoint manipulator for maintenance of nuclear reactors," *Advanced robotics*, vol. 9, pp. 281-300, 1994.
- [58] V. C. Anderson and R. C. Horn, "Tensor arm manipulator design," in *MECHANICAL ENGINEERING*, 1967, pp. 54-&.
- [59] S. Ma, H. Yoshinada, and S. Hirose, "CT ARM-I: Coupled tendon-driven manipulator model I-design and basic experiments," in *Robotics and Automation, 1992. Proceedings., 1992 IEEE International Conference on*, 1992, pp. 2094-2100.
- [60] G. Robinson and J. B. C. Davies, "Continuum robots-a state of the art," in *Robotics and Automation, 1999. Proceedings. 1999 IEEE International Conference on*, 1999, pp. 2849-2854.
- [61] V. C. Anderson, "Tensor arm manipulator," 1970.
- [62] M. W. Hannan and I. D. Walker, "Analysis and experiments with an elephant's trunk robot," *Advanced Robotics*, vol. 15, pp. 847-858, 2001.
- [63] M. W. Hannan and I. D. Walker, "Analysis and initial experiments for a novel elephant's trunk robot," in *Intelligent Robots and Systems, 2000.(IROS 2000). Proceedings. 2000 IEEE/RSJ International Conference on*, 2000, pp. 330-337.
- [64] M. Hannan and I. Walker, "The elephant trunk'manipulator, design and implementation," in *Advanced Intelligent Mechatronics, 2001. Proceedings. 2001 IEEE/ASME International Conference on*, 2001, pp. 14-19.
- [65] I. A. Gravagne and I. D. Walker, "Kinematic transformations for remotely-actuated planar continuum robots," in *Robotics and Automation, 2000. Proceedings. ICRA'00. IEEE International Conference on*, 2000, pp. 19-26.
- [66] I. A. Gravagne and I. D. Walker, "On the kinematics of remotely-actuated continuum robots," in *Robotics and Automation, 2000. Proceedings. ICRA'00. IEEE International Conference on*, 2000, pp. 2544-2550.
- [67] M. W. Hannan and I. D. Walker, "Kinematics and the implementation of an elephant's trunk manipulator and other continuum style robots," *Journal of Robotic Systems*, vol. 20, pp. 45-63, 2003.
- [68] N. Lobontiu, *Compliant mechanisms: design of flexure hinges*: CRC press, 2010.
- [69] *Snake-arm robots for aircraft assembly*. Available: <http://www.ocrobotics.com/applications--solutions/aerospace/aerospace-case-study/>
- [70] *JetSnake: Snake-arms for tunnel boring machines*. Available: <http://www.ocrobotics.com/applications--solutions/construction/construction-case-study-jetsnake/>
- [71] R. O. Buckingham and A. C. Graham, "Link assembly for a snake like robot arm," 2009.

- [72] R. O. Buckingham and A. C. Graham, "Robotic arms with coaxially mounted helical spring means," 2011.
- [73] J. He, R. Liu, K. Wang, and H. Shen, "The mechanical design of snake-arm robot," in *Industrial Informatics (INDIN), 2012 10th IEEE International Conference on*, 2012, pp. 758-761.
- [74] S. Ma, S. Hirose, and H. Yoshinada, "Design and experiments for a coupled tendon-driven manipulator," *Control Systems, IEEE*, vol. 13, pp. 30-36, 1993.
- [75] S. Ma, I. Kobayashi, S. Hirose, and K. Yokoshima, "Control of a multijoint manipulator" Moray arm", *Mechatronics, IEEE/ASME Transactions on*, vol. 7, pp. 304-317, 2002.
- [76] Y.-J. Kim, S. Cheng, S. Kim, and K. Iagnemma, "A Stiffness-Adjustable Hyperredundant Manipulator Using a Variable Neutral-Line Mechanism for Minimally Invasive Surgery," *Robotics, IEEE Transactions on*, 2014.
- [77] P. Dario, M. C. Carrozza, M. Marcacci, S. D'Attanasio, B. Magnani, O. Tonet, *et al.*, "A novel mechatronic tool for computer-assisted arthroscopy," *Information Technology in Biomedicine, IEEE Transactions on*, vol. 4, pp. 15-29, 2000.
- [78] O. Robotics, "Snake-arm robots access the inaccessible," *Nuclear Technology International*, vol. 1, pp. 92-94, 2008.
- [79] A. Degani, H. Choset, A. Wolf, and M. A. Zenati, "Highly articulated robotic probe for minimally invasive surgery," in *Robotics and Automation, 2006. ICRA 2006. Proceedings 2006 IEEE International Conference on*, 2006, pp. 4167-4172.
- [80] H. M. Choset, A. Wolf, and M. A. Zenati, "Steerable, follow the leader device," 2005.
- [81] H. ZHU. (2003). *Single Motor Driven Hyper-Redundant Manipulator*. Available: <http://www.imdl.gatech.edu/haihong/Arm/Arm.html>
- [82] Y. Li, P. Ma, C. Qin, X. Gao, J. Wang, and H. Zhu, "Design and study of a novel hyper-redundant manipulator," *Robotica*, vol. 21, pp. 505-509, 2003.
- [83] D. P. Noonan, G. P. Mylonas, J. Shang, C. J. Payne, A. Darzi, and G.-Z. Yang, "Gaze contingent control for an articulated mechatronic laparoscope," in *Biomedical Robotics and Biomechatronics (BioRob), 2010 3rd IEEE RAS and EMBS International Conference on*, 2010, pp. 759-764.
- [84] J. Shang, D. P. Noonan, C. Payne, J. Clark, M. H. Sodergren, A. Darzi, *et al.*, "An articulated universal joint based flexible access robot for minimally invasive surgery," in *Robotics and Automation (ICRA), 2011 IEEE International Conference on*, 2011, pp. 1147-1152.
- [85] E. Paljug, T. Ohm, and S. Hayati, "The JPL Serpentine Robot: a 12-DOF system for inspection," in *Robotics and Automation, 1995. Proceedings., 1995 IEEE International Conference on*, 1995, pp. 3143-3148.
- [86] E. Shamma, A. Wolf, and H. Choset, "Three degrees-of-freedom joint for spatial hyper-redundant robots," *Mechanism and machine theory*, vol. 41, pp. 170-190, 2006.
- [87] A. Wolf, H. B. Brown, R. Casciola, A. Costa, M. Schwerin, E. Shamas, *et al.*, "A mobile hyper redundant mechanism for search and rescue tasks," in *Intelligent Robots and Systems, 2003.(IROS 2003). Proceedings. 2003 IEEE/RSJ International Conference on*, 2003, pp. 2889-2895.
- [88] M. Mori and S. Hirose, "Three-dimensional serpentine motion and lateral rolling by active cord mechanism ACM-R3," in *Intelligent Robots and Systems, 2002. IEEE/RSJ International Conference on*, 2002, pp. 829-834.
- [89] H. Yamada and S. Hirose, "Development of practical 3-dimensional active cord mechanism ACM-R4," *Journal of Robotics and Mechatronics*, vol. 18, p. 305, 2006.

- [90] S. Yu, S. Ma, B. Li, and Y. Wang, "An amphibious snake-like robot: design and motion experiments on ground and in water," in *Information and Automation, 2009. ICIA'09. International Conference on*, 2009, pp. 500-505.
- [91] R. Behrens, C. Kuchler, T. Forster, and N. Elkmann, "Kinematics analysis of a 3-DOF joint for a novel hyper-redundant robot arm," in *Robotics and Automation (ICRA), 2011 IEEE International Conference on*, 2011, pp. 3224-3229.
- [92] R. Behrens, M. Poggendorf, E. Schulenburg, and N. Elkmann, "An Elephant?? s Trunk-Inspired Robotic Arm?? Trajectory Determination and Control," in *Robotics; Proceedings of ROBOTIK 2012; 7th German Conference on*, 2012, pp. 1-5.
- [93] (2012). *BROMMI : TAK biomimetic elephant's trunk kinematic*. Available: [http://www.biorobotiklabor.de/ourwork\\_robotics.html](http://www.biorobotiklabor.de/ourwork_robotics.html)
- [94] I. Boblan, A. Schulz, A. Tuchscherer, I. Perfilov, and B. Bertrand, "A Compliant Lightweight Universal Joint Cascadable to a Multi-joint Kinematics-Tripedale Alternanzkaskade, TAK," presented at the In 6th International Symposium on Adaptive Motion of Animal and Machines, Darmstadt, Germany, 2013.
- [95] K. Otsuka and C. M. Wayman, *Shape memory materials*: Cambridge university press, 1999.
- [96] M. Ho, A. B. McMillan, J. M. Simard, R. Gullapalli, and J. P. Desai, "Toward a meso-scale SMA-actuated MRI-compatible neurosurgical robot," *Robotics, IEEE Transactions on*, vol. 28, pp. 213-222, 2012.
- [97] M. Ho, M. Koltz, J. M. Simard, R. Gullapalli, and J. P. Desai, "Towards a MR image-guided SMA-actuated neurosurgical robot," in *Robotics and Automation (ICRA), 2011 IEEE International Conference on*, 2011, pp. 1153-1158.
- [98] V. A. Sujan and S. Dubowsky, "Design of a lightweight hyper-redundant deployable binary manipulator," *Journal of Mechanical Design*, vol. 126, pp. 29-39, 2004.
- [99] E. Ayvali and J. P. Desai, "Towards a discretely actuated steerable cannula," in *Robotics and Automation (ICRA), 2012 IEEE International Conference on*, 2012, pp. 1614-1619.
- [100] E. Ayvali, C.-P. Liang, M. Ho, Y. Chen, and J. P. Desai, "Towards a discretely actuated steerable cannula for diagnostic and therapeutic procedures," *The International journal of robotics research*, vol. 31, pp. 588-603, 2012.
- [101] (2000). *West Valley Demonstration Project Waste Management Area #3-Closure Alternative I*. Available: <http://www.wipp.energy.gov/NAMP/EMLLegacy/reports/eml609.pdf>
- [102] G. Immega, "Tentacle-like manipulators with adjustable tension lines," 1994.
- [103] G. Immega and K. Antonelli, "The KSI tentacle manipulator," in *Robotics and Automation, 1995. Proceedings., 1995 IEEE International Conference on*, 1995, pp. 3149-3154.
- [104] G. Immega, K. Antonelli, and J. Ko, "Teleoperation of the KSI Tentacle Manipulator for hot cell decontamination," in *Systems, Man and Cybernetics, 1995. Intelligent Systems for the 21st Century., IEEE International Conference on*, 1995, pp. 2133-2136.
- [105] I. D. Walker, "Continuous Backbone "Continuum" Robot Manipulators," *ISRN Robotics*, vol. 2013, 2013.
- [106] W. Taylor, D. Lavie, and I. Esat, "A curvilinear snake arm robot with gripper-axis fibre-optic image processor feedback," *Robotica*, vol. 1, pp. 33-39, 1983.
- [107] R. Cieslak and A. Morecki, "Elephant trunk type elastic manipulator-a tool for bulk and liquid materials transportation," *Robotica*, vol. 17, pp. 11-16, 1999.

- [108] I. A. Gravagne and I. D. Walker, "Uniform regulation of a multi-section continuum manipulator," in *Robotics and Automation, 2002. Proceedings. ICRA'02. IEEE International Conference on*, 2002, pp. 1519-1524.
- [109] C. Li and C. D. Rahn, "Design of continuous backbone, cable-driven robots," *Journal of Mechanical Design*, vol. 124, pp. 265-271, 2002.
- [110] I. A. Gravagne, C. D. Rahn, and I. D. Walker, "Large deflection dynamics and control for planar continuum robots," *Mechatronics, IEEE/ASME Transactions on*, vol. 8, pp. 299-307, 2003.
- [111] Festo. (2011). *Bionic Tripod 3.0*. Available: [http://www.festo.com/cms/en\\_corp/11371.htm](http://www.festo.com/cms/en_corp/11371.htm)
- [112] K. Xu and N. Simaan, "Actuation compensation for flexible surgical snake-like robots with redundant remote actuation," in *Robotics and Automation, 2006. ICRA 2006. Proceedings 2006 IEEE International Conference on*, 2006, pp. 4148-4154.
- [113] R. Webster, A. M. Okamura, and N. J. Cowan, "Toward active cannulas: Miniature snake-like surgical robots," in *Intelligent Robots and Systems, 2006 IEEE/RSJ International Conference on*, 2006, pp. 2857-2863.
- [114] P. E. Dupont, J. Lock, B. Itkowitz, and E. Butler, "Design and control of concentric-tube robots," *Robotics, IEEE Transactions on*, vol. 26, pp. 209-225, 2010.
- [115] D. M. Lane, J. B. C. Davies, G. Robinson, D. J. O'Brien, J. Sneddon, E. Seaton, *et al.*, "The AMADEUS dextrous subsea hand: design, modeling, and sensor processing," *Oceanic Engineering, IEEE Journal of*, vol. 24, pp. 96-111, 1999.
- [116] K. Suzumori, S. Iikura, and H. Tanaka, "Development of flexible microactuator and its applications to robotic mechanisms," in *Robotics and Automation, 1991. Proceedings., 1991 IEEE International Conference on*, 1991, pp. 1622-1627.
- [117] D. Lane, J. Sneddon, D. O'Brien, J. Davies, and G. Robinson, "Aspects of the design and development of a subsea dextrous grasping system," in *OCEANS'94. 'Oceans Engineering for Today's Technology and Tomorrow's Preservation. Proceedings*, 1994, pp. II/174-II/181 vol. 2.
- [118] J. Davies, D. Lane, G. Robinson, D. O'Brien, M. Pickett, M. Sfakiotakis, *et al.*, "Subsea applications of continuum robots," in *Underwater Technology, 1998. Proceedings of the 1998 International Symposium on*, 1998, pp. 363-369.
- [119] M. Sfakiotakis, D. Laue, and B. C. Davies, "An experimental undulating-fin device using the parallel bellows actuator," in *Robotics and Automation, 2001. Proceedings 2001 ICRA. IEEE International Conference on*, 2001, pp. 2356-2362.
- [120] W. McMahan, V. Chitrakaran, M. Csencsits, D. Dawson, I. D. Walker, B. A. Jones, *et al.*, "Field trials and testing of the OctArm continuum manipulator," in *Robotics and Automation, 2006. ICRA 2006. Proceedings 2006 IEEE International Conference on*, 2006, pp. 2336-2341.
- [121] D. Braganza, D. M. Dawson, I. D. Walker, and N. Nath, "A neural network controller for continuum robots," *Robotics, IEEE Transactions on*, vol. 23, pp. 1270-1277, 2007.
- [122] FESTO. (2010). *Bionic Handling Assistant—flexible and compliant movement*. Available: [http://www.festo.com/cms/en\\_corp/9655\\_10219.htm](http://www.festo.com/cms/en_corp/9655_10219.htm)
- [123] T. Mahl, A. Hildebrandt, and O. Sawodny, "A variable curvature continuum kinematics for kinematic control of the bionic handling assistant," *Robotics, IEEE Transactions on*, vol. 30, pp. 935-949, 2014.
- [124] M. De Volder, A. Moers, and D. Reynaerts, "Fabrication and control of miniature McKibben actuators," *Sensors and Actuators A: Physical*, vol. 166, pp. 111-116, 2011.

- [125] Y. Bailly and Y. Amirat, "Modeling and control of a hybrid continuum active catheter for aortic aneurysm treatment," in *Robotics and Automation, 2005. ICRA 2005. Proceedings of the 2005 IEEE International Conference on*, 2005, pp. 924-929.
- [126] V. A. Sujjan, M. D. Lichter, and S. Dubowsky, "Lightweight hyper-redundant binary elements for planetary exploration robots," in *Advanced Intelligent Mechatronics, 2001. Proceedings. 2001 IEEE/ASME International Conference on*, 2001, pp. 1273-1278.
- [127] N. Simaan, R. Taylor, and P. Flint, "High dexterity snake-like robotic slaves for minimally invasive telesurgery of the upper airway," in *Medical Image Computing and Computer-Assisted Intervention—MICCAI 2004*, ed: Springer, 2004, pp. 17-24.
- [128] M. Csencsits, B. A. Jones, W. McMahan, V. Iyengar, and I. D. Walker, "User interfaces for continuum robot arms," in *Intelligent Robots and Systems, 2005.(IROS 2005). 2005 IEEE/RSJ International Conference on*, 2005, pp. 3123-3130.
- [129] Y. Bailly, A. Chauvin, and Y. Amirat, "Control of a high dexterity micro-robot based catheter for aortic aneurysm treatment," in *Robotics, Automation and Mechatronics, 2004 IEEE Conference on*, 2004, pp. 65-70.
- [130] G. S. Chirikjian, "Theory and applications of hyper-redundant robotic manipulators," California Institute of Technology, 1992.
- [131] G. S. Chirikjian and J. W. Burdick, "A modal approach to hyper-redundant manipulator kinematics," *Robotics and Automation, IEEE Transactions on*, vol. 10, pp. 343-354, 1994.
- [132] K. Xu and N. Simaan, "Analytic formulation for kinematics, statics, and shape restoration of multibackbone continuum robots via elliptic integrals," *Journal of Mechanisms and Robotics*, vol. 2, p. 011006, 2010.
- [133] S. Neppalli and B. A. Jones, "Design, construction, and analysis of a continuum robot," in *Intelligent Robots and Systems, 2007. IROS 2007. IEEE/RSJ International Conference on*, 2007, pp. 1503-1507.
- [134] B. A. Jones and I. D. Walker, "Kinematics for multisection continuum robots," *Robotics, IEEE Transactions on*, vol. 22, pp. 43-55, 2006.
- [135] R. J. Webster and B. A. Jones, "Design and kinematic modeling of constant curvature continuum robots: A review," *The International Journal of Robotics Research*, 2010.
- [136] H. Mochiyama, E. Shimemura, and H. Kobayashi, "Direct kinematics of manipulators with hyper degrees of freedom and Frenet-Serret formula," in *Robotics and Automation, 1998. Proceedings. 1998 IEEE International Conference on*, 1998, pp. 1653-1658.
- [137] H. Mochiyama, E. Shimemura, and H. Kobayashi, "Shape correspondence between a spatial curve and a manipulator with hyper degrees of freedom," in *Intelligent Robots and Systems, 1998. Proceedings., 1998 IEEE/RSJ International Conference on*, 1998, pp. 161-166.
- [138] S. Cobos-Guzman, D. Palmer, and D. Axinte, "Kinematic model to control the end-effector of a continuum robot for multi-axis processing," *Robotica*, pp. 1-17.
- [139] X. Dong, M. Raffles, S. C. Guzman, D. Axinte, and J. Kell, "Design and analysis of a family of snake arm robots connected by compliant joints," *Mechanism and Machine Theory*, vol. 77, pp. 73-91, 2014.
- [140] *Snake-arm robots- robots for confined space*. Available: <http://www.ocrobotics.com/>
- [141] J. Peirs, H. Van Brussel, D. Reynaerts, and G. De Gerssem, "A flexible distal tip with two degrees of freedom for enhanced dexterity in endoscopic robot surgery," in *Proceedings of the 13th micromechanics europe workshop*, 2002, pp. 271-274.

- [142] E. Brown, N. Rodenberg, J. Amend, A. Mozeika, E. Steltz, M. R. Zakin, *et al.*, "Universal robotic gripper based on the jamming of granular material," *Proceedings of the National Academy of Sciences*, vol. 107, pp. 18809-18814, 2010.
- [143] N. G. Cheng, M. B. Lobovsky, S. J. Keating, A. M. Setapen, K. I. Gero, A. E. Hosoi, *et al.*, "Design and analysis of a robust, low-cost, highly articulated manipulator enabled by jamming of granular media," in *Robotics and Automation (ICRA), 2012 IEEE International Conference on*, 2012, pp. 4328-4333.
- [144] A. Jiang, G. Xynogalas, P. Dasgupta, K. Althoefer, and T. Nanayakkara, "Design of a variable stiffness flexible manipulator with composite granular jamming and membrane coupling," in *Intelligent Robots and Systems (IROS), 2012 IEEE/RSJ International Conference on*, 2012, pp. 2922-2927.
- [145] A. Sadeghi, L. Beccai, and B. Mazzolai, "Innovative soft robots based on electro-rheological fluids," in *Intelligent Robots and Systems (IROS), 2012 IEEE/RSJ International Conference on*, 2012, pp. 4237-4242.
- [146] N. G. Cheng, "Design and analysis of active fluid-and-cellular solid composites for controllable stiffness robotic elements," Massachusetts Institute of Technology, 2009.
- [147] N. Cheng, G. Ishigami, S. Hawthorne, H. Chen, M. Hansen, M. Telleria, *et al.*, "Design and analysis of a soft mobile robot composed of multiple thermally activated joints driven by a single actuator," in *Robotics and Automation (ICRA), 2010 IEEE International Conference on*, 2010, pp. 5207-5212.
- [148] M. J. Telleria, M. Hansen, D. Campbell, A. Servi, and M. L. Culpepper, "Modeling and implementation of solder-activated joints for single-actuator, centimeter-scale robotic mechanisms," in *Robotics and Automation (ICRA), 2010 IEEE International Conference on*, 2010, pp. 1681-1686.
- [149] *Transport® Endoscopic Access Device - Retroflex*. Available: <http://usgimedical.com/eos/components-transport.htm>
- [150] Y.-J. Kim, S. Cheng, S. Kim, and K. Iagnemma, "A novel layer jamming mechanism with tunable stiffness capability for minimally invasive surgery," *Robotics, IEEE Transactions on*, vol. 29, pp. 1031-1042, 2013.
- [151] S. Zuo, T. Ohdaira, K. Kuwana, Y. Nagao, S. Ieiri, M. Hashizume, *et al.*, "Developing essential rigid-flexible outer sheath to enable novel multi-piercing surgery," in *Medical Image Computing and Computer-Assisted Intervention—MICCAI 2012*, ed: Springer, 2012, pp. 26-33.
- [152] T. Dohi, K. Masamune, S. Zuo, and N. Yamanaka, "Flexibility/rigidity adjustable apparatus," ed: Google Patents, 2013.
- [153] K. Iijima, K. Masamune, T. Tokumiya, and S. Zuo, "Medical tube and flexibility-variable mechanism with the same," ed: Google Patents, 2013.
- [154] S. Zuo, K. Iijima, T. Tokumiya, and K. Masamune, "Variable stiffness outer sheath with "Dragon skin" structure and negative pneumatic shape-locking mechanism," *International journal of computer assisted radiology and surgery*, pp. 1-9, 2014.
- [155] G. S. Chirikjian and J. W. Burdick, "Kinematically optimal hyper-redundant manipulator configurations," *Robotics and Automation, IEEE Transactions on*, vol. 11, pp. 794-806, 1995.
- [156] D. Trivedi, A. Lotfi, and C. D. Rahn, "Geometrically exact models for soft robotic manipulators," *Robotics, IEEE Transactions on*, vol. 24, pp. 773-780, 2008.
- [157] W. McMahan, B. Jones, and I. D. Walker, "Design and implementation of a multi-section continuum robot: Air-Octor," in *Intelligent Robots and Systems, 2005.(IROS 2005). 2005 IEEE/RSJ International Conference on*, 2005, pp. 2578-2585.
- [158] J. S. Beggs, *Kinematics*: CRC Press, 1983.

- 
- [159] K. Xu and N. Simaan, "An investigation of the intrinsic force sensing capabilities of continuum robots," *Robotics, IEEE Transactions on*, vol. 24, pp. 576-587, 2008.
- [160] N. Lobontiu, *Compliant mechanisms: design of flexure hinges*: CRC press, 2002.
- [161] C. Gosselin, "Stiffness mapping for parallel manipulators," *Robotics and Automation, IEEE Transactions on*, vol. 6, pp. 377-382, 1990.
- [162] D. Chakarov, "Study of the passive compliance of parallel manipulators," *Mechanism and Machine Theory*, vol. 34, pp. 373-389, 1999.
- [163] *Monocoil*. Available: <http://www.armorassociates.us/Monocoil.cfm>
- [164] I. DYNALLOY. Available: <http://www.dynalloy.com/index.php>
- [165] D. Palmer, S. Cobos-Guzman, and D. Axinte, "Real-time method for tip following navigation of continuum snake arm robots," *Robotics and Autonomous Systems*, vol. 62, pp. 1478-1485, 2014.
- [166] *Video Gauge™ Technology - Imetrum*. Available: <http://www.imetrum.com/>
- [167] N. Simaan, "Snake-like units using flexible backbones and actuation redundancy for enhanced miniaturization," in *Robotics and Automation, 2005. ICRA 2005. Proceedings of the 2005 IEEE International Conference on*, 2005, pp. 3012-3017.
- [168] W. S. Rone and P. Ben-Tzvi, "Mechanics Modeling of Multisegment Rod-Driven Continuum Robots," *Journal of Mechanisms and Robotics*, vol. 6, p. 041006, 2014.
- [169] A. Bajo and N. Simaan, "Kinematics-based detection and localization of contacts along multisegment continuum robots," *Robotics, IEEE Transactions on*, vol. 28, pp. 291-302, 2012.
- [170] R. E. Goldman, A. Bajo, and N. Simaan, "Compliant motion control for multisegment continuum robots with actuation force sensing," *Robotics, IEEE Transactions on*, vol. 30, pp. 890-902, 2014.
-